FALL 2025

GEMS & GEMOLOGY

VOLUME LXI

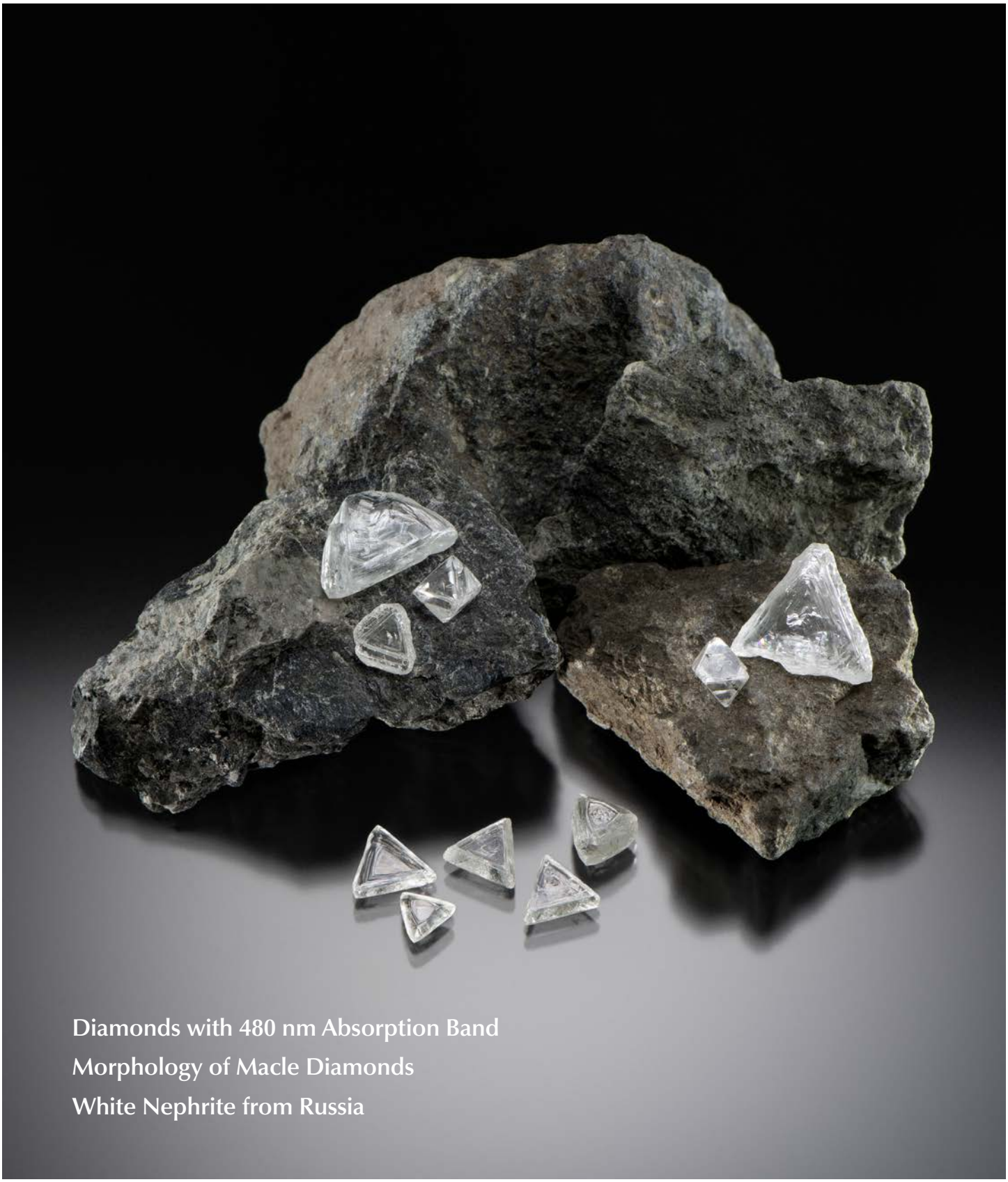

Diamonds with 480 nm Absorption Band

Morphology of Macle Diamonds

White Nephrite from Russia

THE QUARTERLY JOURNAL OF THE GEMOLOGICAL INSTITUTE OF AMERICA

GEMS & GEMOLOGY®
Fall 2025
VOLUME 61, No. 3

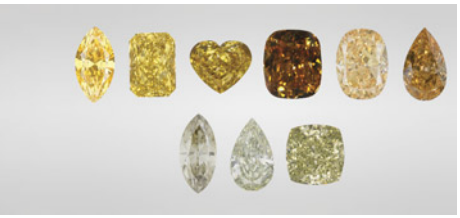
p. 233


p. 271


p. 296

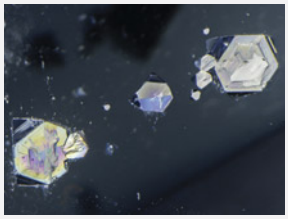
p. 305


p. 312

Editorial

231 Diamonds with the 480 nm Absorption Band, the Morphology of Macle Diamonds, and Russian White Nephrite's Distinctive "Orange Peel" Texture
Duncan Pay

Feature Articles

232 A Guide to Diamonds with the 480 nm Absorption Band
Mei Yan Lai
Summarizes the features of 480 nm band diamonds, including chameleon diamonds and those with unmodified orange hues, for rapid identification or advanced gemological testing.

250 External Morphology and Internal Zonal Structure of Macle Diamond
Ahmadjan Abduriyim and Masao Kitamura
Investigates the morphological changes of macle diamonds during the growth process by exploring their three-dimensional internal zonal structure.

270 Characterization of "Orange Peel" Surface Microstructure of White Nephrite from Russia: A Unique Pseudomorph Pattern
Meiyu Shih, Guanghai Shi, and Biqian Xing
Examines correlations between surface microstructures and the orange peel effect in Russian white nephrite, proposing a formation model and revealing distinctive microfeatures specific to the material.

Regular Features

288 2025 *G&G* Challenge Winners

290 Lab Notes
Extraordinary large bicolor natural rough diamond • Pink diamond with mottled appearance • Starburst cloud inclusions in diamond • Type IIa/IaB diamond showing transient type IIb responses • Prismatic bicolor dumortierite crystal • Quench-crackled and dyed laboratory-grown sapphire • Two assembled pearls • Low-heft hollow natural pearl with an opening

302 *G&G* Micro-World
"UFO" in diamond • Cristobalite stars and snowflakes in devitrified glass • Natural opal with unusual play-of-color pattern • "Melon" pearl • Gersdorffite in quartz • 3D radial fissures in a heated Mong Hsu ruby • Suspended pargasite crystal in pink spinel • Quarterly Crystal: Almandine-pyrope garnet in diamond

308 Diamond Reflections
Showcases the diverse natural shapes of rough diamonds and explores how geological processes create their unique forms.

316 Gem News International
Palaeoclavaria burmitis inclusions in Burmese amber • Trapiche pattern formation of grossular garnets • Gaseous carbon dioxide phases in Paraíba tourmaline • Large peridot from Myanmar with an eight-rayed star • Blue color in quartz caused by elbaite inclusions • Unusual yellow diamond with a complex growth history • Diamond ring prize from an arcade-style claw game • Low-temperature heat treatment of corundum and the behavior of the 3161 cm^{-1} infrared band • Erratum

GEMS & GEMOLOGY®

gia.edu/gems-gemology

Customer Service
(760) 603-4200
gandg@gia.edu

Subscriptions
Copies of the current issue may be purchased for $35.95 plus shipping. Subscriptions are $95.99 for one year (4 issues) in the U.S. and $119.99 elsewhere. Canadian subscribers should add GST. Discounts are available for renewals, group subscriptions, GIA alumni, and current GIA students. To purchase print subscriptions, visit store.gia.edu or contact Customer Service. For institutional rates, contact Customer Service.

Database Coverage
Gems & Gemology's impact factor is 2.6, according to the 2024 Journal Citation Reports by Clarivate Analytics (issued June 2025). *G&G* is abstracted in Thomson Reuters products (Current Contents: Physical, Chemical & Earth Sciences and Science Citation Index—Expanded, including the Web of Knowledge) and other databases. For a complete list of sources abstracting *G&G*, go to gia.edu/gems-gemology, and click on "Publication Information."

Manuscript Submissions
Gems & Gemology, a peer-reviewed journal, welcomes the submission of articles on all aspects of the field. Please see the Author Guidelines at gia.edu/gems-gemology or contact the editors (gandgeditorial@gia.edu). Letters on articles published in *G&G* are also welcome. Please note that Field Reports, Lab Notes, Gem News International, Micro-World, Colored Stones Unearthed, Diamond Reflections, Charts, and In the Spotlight are not peer-reviewed sections but do undergo technical and editorial review.

Gems & Gemology is published quarterly by the Gemological Institute of America, a nonprofit educational organization for the gem and jewelry industry.

Postmaster: Return undeliverable copies of *Gems & Gemology* to GIA, The Robert Mouawad Campus, 5345 Armada Drive, Carlsbad, CA 92008.

Our Canadian goods and service registration number is 126142892RT.

About the Cover

An assortment of colorless macle and octahedral diamond crystals, ranging in size from 0.52 to 2.53 ct, are pictured against samples of kimberlite host rock. The back cover features a closer look at the largest macle specimen. One of this issue's feature articles investigates the morphological changes of contact-twinned macle diamonds during the growth process. Photos by Kevin Schumacher. Kimberlite from Kelsey Lake, Colorado, gift of Dr. James E. Shigley; 0.52 ct octahedral diamond gift of Dr. D. Vincent Manson; 1.77 ct octahedral crystal gift of George Kaplan; other diamonds from the GIA Museum collection.

Printing is by L+L Printers, Carlsbad, CA.

GIA World Headquarters The Robert Mouawad Campus 5345 Armada Drive Carlsbad, CA 92008 USA

ISSN 0016-626X

Diamonds with the 480 nm Absorption Band, the Morphology of Macle Diamonds, and Russian White Nephrite's Distinctive "Orange Peel" Texture

Recently I had the privilege to attend Converge—a unique event uniting GIA's research and education with our sister organization the American Gem Society's professional development opportunities—and see firsthand there's a real appetite for well-curated, relevant gemological information. People packed into talks focused on gemstone treatments, field gemology, colored diamonds, diamond origin, and more. If you're a subscriber or online reader of *Gems & Gemology*, you'll know these are all topics we cover regularly, and our Fall 2025 issue is no exception!

"...there's a real appetite for well-curated, relevant gemological information."

Our lead article by GIA's Dr. Mei Yan Lai offers a perspective on natural diamonds with a broad absorption band centered at 480 nm in the visible spectrum. This category deserves more attention as it includes rare and sought-after pure orange and color-change chameleon diamonds. Dr. Lai summarizes the properties of these unique gems.

The flattened triangular shapes of diamond macles are some of the natural world's most recognizable crystals. In our next article, Drs. Ahmadjan Abduriyim and Masao Kitamura examine the morphology, internal structure, and growth mechanisms of natural macle diamonds using scanning electron microscopy and cathodoluminescence imaging.

In our final paper, three researchers from China—Drs. Meiyu Shih, Guanghai Shi, and Biqian Xing—deliver a study on the potentially diagnostic "orange peel" surface microstructure of white nephrite from Russia, which is similar to that seen in jadeite jade. This texture results from nephrite replacing carbonate grains to produce a distinctive pattern supporting a Russian geographic origin determination.

There's truly something for everyone in our regular features. *Lab Notes* draws on reports from GIA's global labs, including an extraordinary large bicolor natural rough diamond, a dumortierite crystal with color zoning reminiscent of watermelon tourmaline, and a quench-crackled and dyed laboratory-grown sapphire resembling Paraíba tourmaline.

As always, *Micro-World* illuminates the inner beauty of gemstones. Some of the intriguing contributions this time include a UFO-shaped feather in a yellow diamond, a remarkable play-of-color pattern resembling a turtle shell in Ethiopian opal, and a rare almandine-pyrope garnet crystal in a diamond octahedron from South Africa.

Our *Gem News International* section highlights interesting studies from all over the globe, such as two Burmese amber specimens containing fungal inclusions, three blue quartz spheres colored by elbaite, and a low-temperature heat treatment study of natural corundum analyzing the behavior of the 3161 cm^{-1} infrared band.

We come full circle with *Diamond Reflections*, which showcases highly unusual and interesting crystal morphologies from a unique collection of rough diamonds. They demonstrate that Earth's natural processes have the power to sculpt the hardest mineral into remarkable shapes that can resemble animals or familiar objects. These distorted crystals offer a window into our dynamic planet's turbulent interior.

Thank you for being a subscriber or online reader of *G&G*. Welcome to our Fall issue!

Duncan Pay | Editor-in-Chief | dpay@gia.edu

A Guide to Diamonds with the 480 nm Absorption Band

Mei Yan Lai

In the gemological research community, diamonds with a broad absorption band centered at roughly 480 nm in the visible spectrum are referred to as "480 nm band diamonds." Despite the 480 nm absorption band being one of the few causes of yellow bodycolor, diamonds with this feature are relatively scarce and not as widely recognized as those colored by the N3 defect, single substitutional nitrogen defect, or H3 defect. Yet 480 nm band diamonds deserve more attention because they account for the vast majority of rare diamonds with unmodified orange hues, as well as all chameleon diamonds—diamonds with a reversible color-change property. However, the global abundance and distribution of 480 nm band diamonds are currently unknown. To date, only mines in Russia and Canada are known to produce these diamonds, but other sources likely exist. Understanding their gemological and spectroscopic characteristics will help the mining industry and the gem trade identify these obscure treasures. This article summarizes the features of 480 nm band diamonds for rapid identification or advanced gemological testing.

Though natural diamond is composed of carbon, atomic impurities and vacancies commonly occur in the diamond crystal structure, attributed to the incorporation of extrinsic elements and strain induced during diamond growth. Post-growth irradiation and plastic deformation can also produce vacancies in the diamond structure (Van Enckevort and Visser, 1990; Fisher, 2009). Consequently, the otherwise perfectly ordered arrangement of carbon atoms in the diamond crystal structure is disturbed. Some structural defects absorb light in the visible spectrum—the portion of the electromagnetic spectrum that the human eye can perceive—producing different bodycolors in diamonds. The defects responsible for color in many diamonds have been well documented, with the majority associated with nitrogen (e.g., Collins, 2001; De Weerdt and Van Royen, 2001; Kanda, 2007; Shigley and Breeding, 2013).

Yellow is one of the most common bodycolors of diamond. The majority of yellow diamonds—known as "cape" diamonds in the gem trade—are colored by the N3 defect (with a structure of three nitrogen atoms surrounding a vacancy) and associated absorptions including the N2 defect (a vibronic transition of N_3V) (Breeding et al., 2020). Yellow color in a significant number of diamonds can also come from single substitutional nitrogen (C-center) or from the H3 defect (a vacancy between two nitrogen atoms).

In Brief

- Diamonds exhibiting a broad absorption band centered around 480 nm in the visible spectrum are known as "480 nm band diamonds."
- This category includes rare and highly sought-after pure orange diamonds and chameleon diamonds with a reversible color-change property.
- Key gemological features of 480 nm band diamonds include strong fluorescence responses (yellow, orange, or a combination of yellow and blue) to long-wave UV and the presence of micrometer-sized dark inclusion clusters.

A subset of yellow diamonds also contain nitrogen yet are primarily colored by a broad absorption band centered at about 480 nm in the visible spectrum. The 480 nm absorption band has been tentatively attributed to substitutional oxygen (Gali et al., 2001; Hainschwang et al., 2020), and diamonds with this

See end of article for About the Authors and Acknowledgments.
Gems & Gemology, Vol. 61, No. 3, pp. 232–248,
http://dx.doi.org/10.5741/GEMS.61.3.232

Figure 1. Yellow is the most common color in 480 nm band diamonds and can occur in different tones and saturations (top row, three on the left). The 480 nm band diamond family also includes those with brown and orange colors (top row, three on the right), as well as chameleon diamonds with a green color component (bottom row). Photos by GIA staff.

absorption feature are termed "480 nm band diamonds" in the gemological research community. This absorption band has only been observed in natural diamonds, and the defect(s) associated with it have not been produced in natural or synthetic diamonds by commercial treatments (Collins, 2001).

Among all yellow diamonds submitted to GIA in the last decade, <5% have been 480 nm band diamonds. These diamonds have not received much attention in the gem trade because of their relative scarcity. However, it is notable that the 480 nm absorption band is not restricted to diamonds with primarily yellow color but also occurs in a variety of colored diamonds, including some of the most valuable orange and chameleon diamonds. Chameleon diamonds are those with a reversible color-change property, typically turning from a green to a more intense yellow or orange color when they are heated mildly or kept in the dark for a significant period of time (Fryer et al., 1981, 1982; Hainschwang et al., 2005; Fritsch et al., 2007a; Fritsch and Delaunay, 2018). Exposure to ambient light or cool temperatures restores the original color. While the documentation of chameleon diamonds is sparse, it is possible that many of these diamonds have not been evaluated and recognized due to a lack of awareness of their properties. This article provides detailed descriptions of the gemological and spectroscopic properties of the diverse and dynamic 480 nm band diamonds to facilitate their identification in the gem and mining industries.

COLOR VARIETIES AND CORRESPONDING VISIBLE ABSORPTION SPECTRA

The broad absorption band with a maximum at approximately 480 nm extends from violet to green in the visible spectrum, producing a yellow to orange color in diamond. Depending on the range and intensity of this absorption band, 480 nm band diamonds can have a variety of tones and saturations (figure 1). Generally, diamonds with Fancy Vivid, Fancy Intense, or Fancy Deep orange, orangy yellow, or yellowish orange color grades have the strongest 480 nm absorption band (figure 2, A and B). In contrast, chameleon diamonds usually have a much weaker 480 nm absorption band (figure 2C) (Lai et al., 2024a). The cause of green color in chameleon diamonds differs from that in green or blue-green diamonds colored by the GR1 defects (neutral vacancies). GR1 defects can be produced by natural or artificial radiation, and produce a green bodycolor in diamonds that have a yellow hue (Breeding et al., 2018). The green color in chameleon diamonds has been attributed to a transmission window between 500 and 600 nm produced by a combination of the 480 nm absorption band and the additional broad absorption band extending from

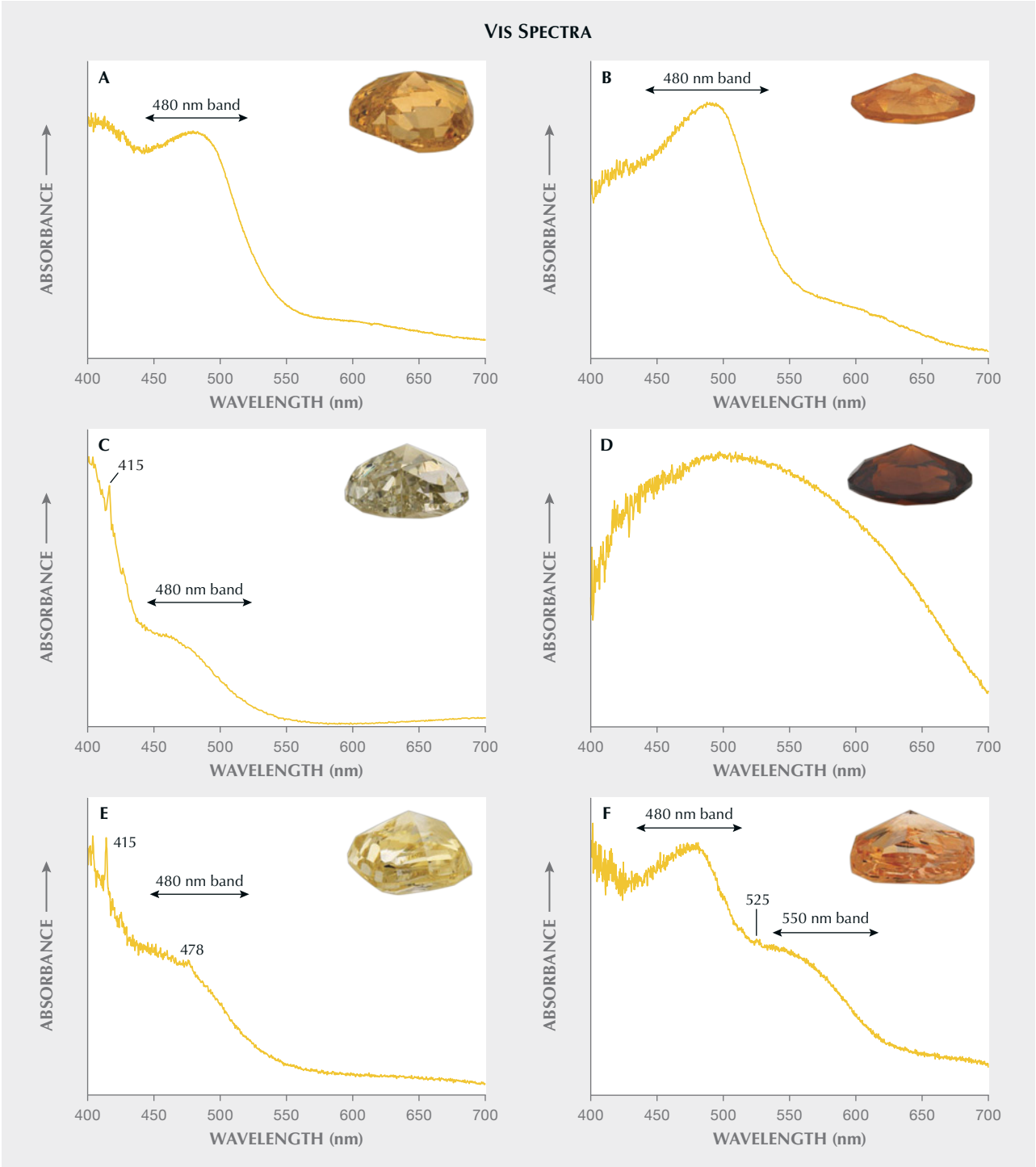

Figure 2. Visible absorption spectra of 480 nm band diamonds with a variety of colors showing single or a combination of color-causing defects. A: An orangy yellow diamond with a 480 nm absorption band. B: An orange diamond with an intense 480 nm absorption band. C: A chameleon diamond with a combination of the N3 defect (415 nm) and a weak 480 nm absorption band. D: An orangy brown diamond with a continuous absorption that increases from the red end of the visible spectrum and reaches a maximum near 500 nm, which usually masks the 480 nm absorption band. Other gemological and spectroscopic features were used to confirm the association with the 480 nm absorption band. E: A yellow diamond with a combination of cape defects (N3 and N2 defects, 415 and 478 nm, respectively) and a weak 480 nm absorption band. F: A brownish orange diamond with a combination of 480 nm and 550 nm absorption bands. Visible absorption spectra were collected at ~77 K. Photos by GIA staff.

approximately 600 nm to the near-infrared region (Hainschwang et al., 2005; Fritsch et al., 2007a). The majority of chameleon diamonds also have an absorption peak at 415 nm corresponding to the N3 defect (figure 2C), whereas this absorption feature is far less common in non-chameleon 480 nm band diamonds.

The occurrence of additional structural defects can modify 480 nm band diamonds' colors. For example, single substitutional nitrogen frequently occurs in these diamonds, which could add an orangy or brownish tint to their primary colors. In addition, vacancy clusters in the diamond structure are also a common cause of brown coloration in diamonds (Fisher et al., 2009). In some 480 nm band diamonds with dominant brown bodycolor there is a continuous absorption that increases from the red end of the visible spectrum and reaches a maximum near 500 nm (figure 2D). This increasing absorption may mask the 480 nm absorption band, increasing the difficulty of identifying 480 nm band diamonds based solely on their visible absorption spectra. In this case, other gemological and spectroscopic features are required to detect the existence of the 480 nm absorption band.

On very rare occasions, some non-chameleon 480 nm band diamonds contain absorption features typically observed in cape diamonds (figure 2E), with absorption peaks at 415 and 478 nm corresponding to the N3 and N2 absorptions, respectively (Altobelli and Johnson, 2014). Unlike chameleon diamonds (which frequently show N3 absorption in addition to the 480 nm absorption band), non-chameleon 480 nm band diamonds with N3 and N2 absorptions generally have yellow or orangy yellow bodycolors without a green component, and N2 absorption has not been observed in chameleon diamonds. Another group of uncommon 480 nm band diamonds contains an additional broad absorption band centered at about 550 nm and a minor absorption peak at 525 nm (Lall et al., 2024). This broad absorption band is the cause of the pink color associated with plastic deformation in most pink diamonds (Collins, 1982, 2001). Diamonds of this variety with a relatively stronger 480 nm absorption band generally have an orange color (figure 2F), whereas those with a more intense 550 nm band tend to have a pink color.

Irregular color zoning is often observed in 480 nm band diamonds when they are viewed microscopically—some zones have a more saturated color, while other zones have lower color saturation and/or are near-colorless. In some extreme cases, the color zoning can be distinct enough that a 480 nm band diamond will appear bicolored or even tricolored (figure 3). A notable example is a chameleon diamond with one half graded Fancy Dark orangy brown and the other half graded Fancy Dark brown greenish yellow; a color-change reaction was observed only in the brown–greenish yellow portion when the diamond was heated (figure 3, right; Lai and Eaton-Magaña, 2023).

RAPID IDENTIFICATION BASED ON GEMOLOGICAL FEATURES

Fluorescence. A quick preliminary screening of diamonds can be achieved using a handheld long-wave ultraviolet (UV) flashlight with an excitation wavelength of 365 nm. Most 480 nm band diamonds have moderate to strong yellow fluorescence, generally corresponding to an asymmetric broad band with maximum intensity at about 540 nm in the

Figure 3. Some 480 nm band diamonds may have distinct color zoning and appear bicolored. Photos by GIA staff.

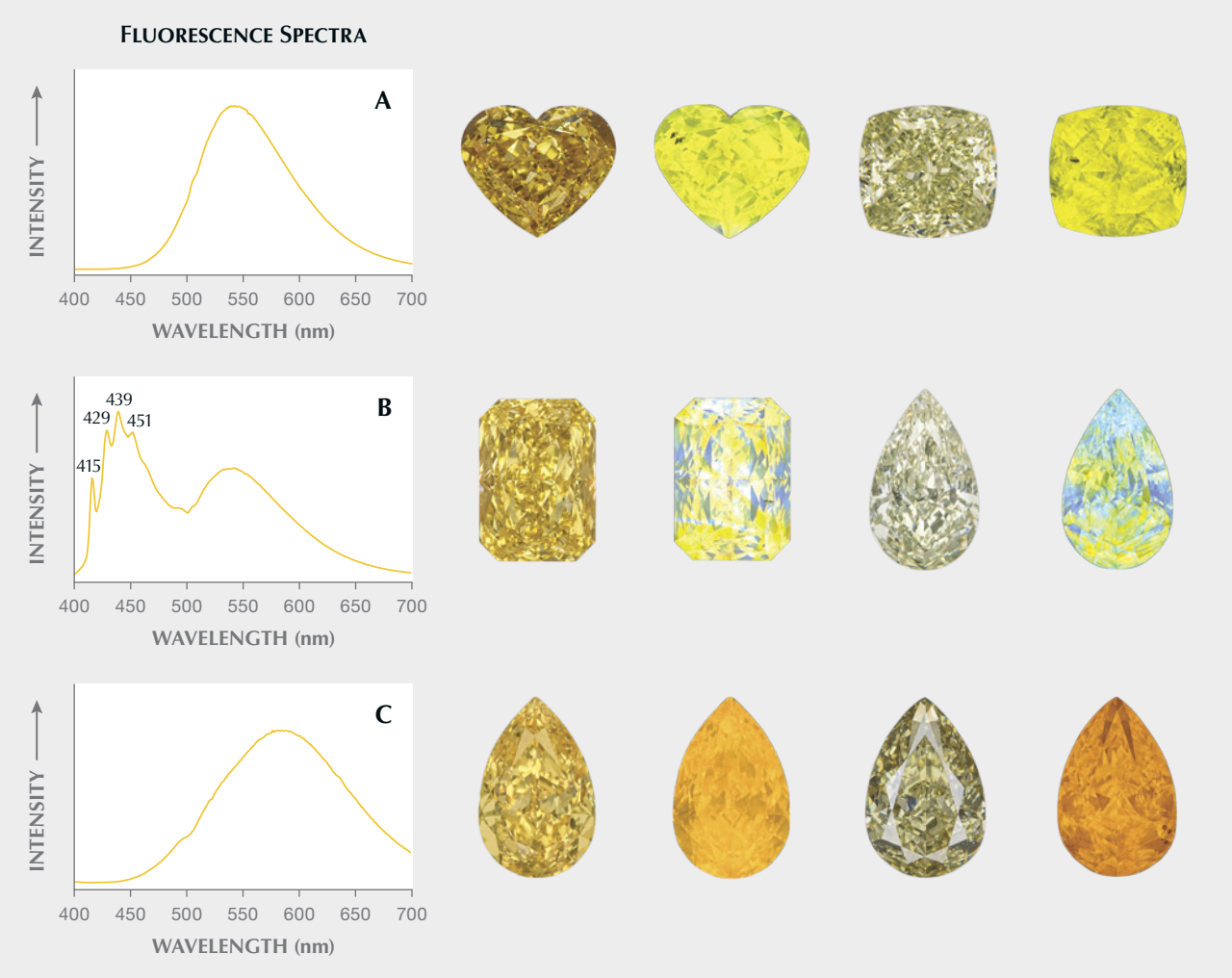

Figure 4. Fluorescence of 480 nm band diamonds excited by a long-wave (365 nm) UV LED light source. A: An orangy yellow diamond and a chameleon diamond showing yellow fluorescence. B: A yellow diamond and a chameleon diamond showing a mixture of yellow and blue fluorescence. C: An orangy yellow diamond and a chameleon diamond showing orange fluorescence. Fluorescence spectra were collected at room temperature. Photos by Rhonda Wilson.

fluorescence spectrum excited by the long-wave UV source (figure 4A). It is also fairly common for 480 nm band diamonds to have heterogeneous distributions of yellow and blue fluorescence, where the blue fluorescence is detected in the fluorescence spectrum as a broad band between 400 and 500 nm with overlaying peaks at 415, 429, 439, and 451 nm, all of which are associated with the N3 defect (figure 4B). Moderate to strong orange fluorescence is occasionally observed in 480 nm band diamonds, which is detected in the fluorescence spectrum as a broad band extending from approximately 450 nm to the near-infrared region, centered at about 585 nm (figure 4C).

Excitation wavelengths can affect the observed color and intensity of fluorescence in diamonds. For example, if the UV light source produces light with multiple wavelengths instead of a single wavelength at 365 nm, or if the excitation wavelength is significantly shifted from 365 nm (Luo and Breeding, 2013), the fluorescence will be impacted, potentially enough to be visually observed. This is because fluorescence associated with certain structural defects could be more effectively excited by light with wavelengths outside the intended excitation wavelength. Shortwave UV with an excitation wavelength of 254 nm is also typically used for testing 480 nm band diamonds with a green component, and in order for these dia-

Figure 5. A chameleon diamond changes color from grayish green (left) to yellow (right) after heating. Photos by Robert Weldon.

monds to receive a "chameleon" classification on GIA grading reports, they must exhibit phosphorescence after exposure to short-wave UV (Breeding et al., 2018). All 480 nm band diamonds with a green component and phosphorescence can be tested for color change through mild heating (figure 5). However, phosphorescence is not limited to chameleon diamonds, as it has also been observed in 480 nm band diamonds without a green component.

Inclusions. Clusters of dark inclusions are often observed in 480 nm band diamonds under the microscope (figure 6). The clusters are usually oriented in three directions and appear highly reflective when viewed at certain angles. Within each cluster, the dark inclusions are generally less than 10 μm and extremely thin, either with rounded or well-defined hexagonal shapes (figure 6D). Notably, these inclusions are unique to 480 nm band diamonds and are a

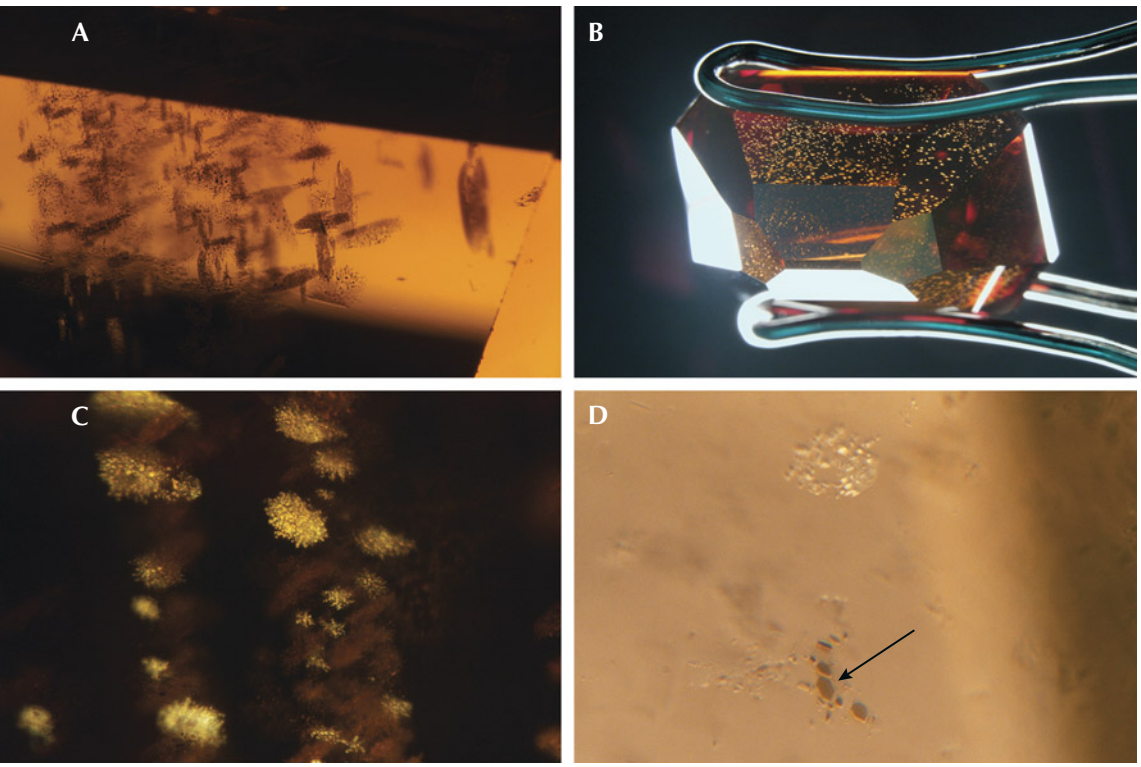

Figure 6. Clusters of micrometer-sized dark inclusions observed in a single 480 nm band diamond. They are oriented in three directions (A) and appear highly reflective when observed at certain angles (B and C). The dark inclusions are platy and extremely thin, either with rounded or well-defined hexagonal shapes (indicated by an arrow in D). Photomicrographs by Mei Yan Lai; fields of view 2.34 mm (A), 14.52 mm (B), 1.58 mm (C), and 0.64 mm (D).

diagnostic identification criterion. In 480 nm band diamonds with noticeable color zoning, such as those with a combination of colorless or near-colorless and yellow color zones, these micrometer-sized inclusions are observed only in zones with yellow color. Since the 480 nm absorption band is detected only in the yellow color regions in these zoned diamonds, the absence of the micrometer-sized dark inclusions in the colorless or near-colorless regions indicates that these inclusions are likely associated with the formation of the structural defects responsible for the 480 nm absorption band.

The micrometer-sized dark inclusions are very similar to those observed in brown diamonds containing carbon dioxide (Hainschwang et al., 2008, 2020; Barannik et al., 2021; Shiryaev et al., 2023; Lai and Schwartz, 2023) (figure 7). Diamonds containing carbon dioxide are rarely encountered in the gem trade, and only five have been submitted to GIA for analysis since 2022. These brown carbon dioxide–bearing diamonds have a much higher density of dark inclusions, which tend to be larger (up to 50 µm) than those observed in 480 nm band diamonds lacking detectable carbon dioxide. In one of these carbon dioxide–bearing diamonds analyzed by the author, the largest dark inclusions were identified as graphite (or graphene layers), with a characteristic Raman peak at 1583 cm^{-1}, consistent with the analytical result obtained with transmission electron microscopy on similar inclusions from brown carbon dioxide–bearing diamonds from a previous study (Shiryaev et al., 2023). Apart from having clusters of micrometer-sized graphite inclusions, these carbon dioxide–bearing brown diamonds also produce yellow fluorescence in response to long-wave UV, as well as surface fluorescence patterns (excited by deep-UV with wavelengths <230 nm) and spectroscopic features closely resembling those of typical 480 nm band diamonds, which will be discussed in the following section. The similarity in gemological and spectroscopic features suggests a possible genetic relationship between brown carbon dioxide–bearing diamonds and typical 480 nm band diamonds (Hainschwang et al., 2008; Lai and Schwartz, 2023).

ADVANCED GEMOLOGICAL TESTING

Surface Fluorescence Imaging. The DiamondView instrument is commonly used in gemological laboratories for surface fluorescence imaging of diamonds. The system uses a deep-UV light source. Since the energy of this light source is similar to or greater than diamond's intrinsic band gap, diamonds strongly absorb the deep-UV light and generate fluorescence very close to the surface, thus producing surface fluorescence patterns that reveal the growth texture (Welbourn et al., 1996).

Most 480 nm band diamonds have irregular surface fluorescence patterns composed of blocky zones (figure 8A). In these diamonds, the dominant fluorescence color is generally yellow or greenish yellow associated with the 480 nm absorption band, with blocky blue fluorescence zones associated with the

Figure 7. Left: A 1.03 ct Fancy Dark brown diamond containing carbon dioxide showing a high density of dark inclusion clusters. Right: The dark inclusions are larger (up to 50 µm) than those observed in typical 480 nm band diamonds without detectable carbon dioxide (generally <10 µm). Photos by Mei Yan Lai; field of view 1.26 mm (right).

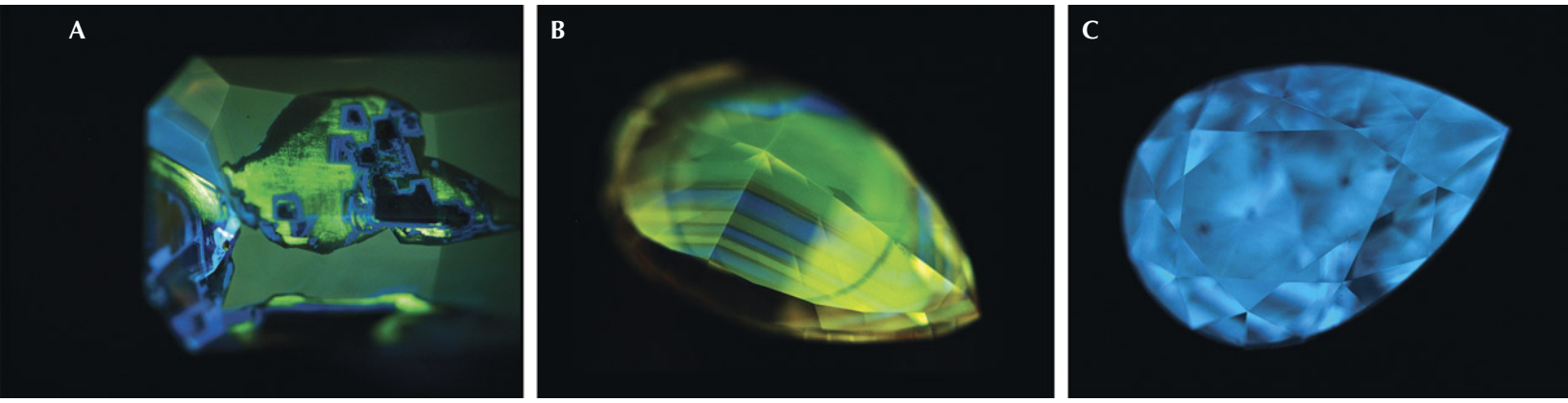

Figure 8. Surface fluorescence patterns in 480 nm band diamonds include those with blocky fluorescence zones (A), alternating blue and yellow fluorescence bands (B; the dark circle in the image is the DiamondView instrument's sample holder), and evenly distributed blue fluorescence (C). Images by Mei Yan Lai.

N3 defect. These blocky zones can have sharp or diffuse boundaries, and the sharp boundaries may be inert to UV and appear as dark rims. Clusters of quadrilateral blocks are occasionally observed within the blue fluorescence zones. Intersecting lines of bright green fluorescence (attributed to the H3 defect) often occur with the blue fluorescence zones.

Another type of surface fluorescence pattern often observed in 480 nm band diamonds is characterized by alternating blue and yellow (or greenish yellow) fluorescence bands, either throughout the entire diamond or limited to a small region (figure 8B). Similar to the blocky type, these fluorescence bands may have sharp boundaries with thin dark lines between the blue and yellow fluorescence zones. The thickness of the alternating fluorescence bands varies within diamonds.

Some 480 nm band diamonds may not have clear surface fluorescence zoning. Most diamonds in this category appear to have evenly distributed blue (figure 8C), yellow, or greenish yellow fluorescence, and a small number of them have orange fluorescence. Generally, blue fluorescence is more frequently observed in chameleon diamonds, whereas yellow or greenish yellow fluorescence is more common for non-chameleon 480 nm band diamonds.

Fourier-Transform Infrared (FTIR) Absorption Spectroscopy. At GIA's laboratories, the infrared absorption features of faceted diamonds are usually detected using an FTIR spectrometer equipped with a diffuse reflectance (DRIFTS) accessory. This bulk analytical technique measures the integrated absorption signal of a diamond. Nitrogen is detected in all 480 nm band diamonds; thus, they are classified as type I (i.e., nitrogen-bearing). Both single substitutional nitrogen atoms (i.e., C-centers, with characteristic absorption peaks at 1130 and 1344 cm^{-1}, commonly accompanied by minor absorption peaks at 1353, 1358, and 1363 cm^{-1}) and nitrogen aggregates in the forms of nitrogen pairs (i.e., A-centers, with representative absorption peak at 1282 cm^{-1}) and groups of four nitrogen atoms around a vacancy (i.e., B-centers, with representative absorption peak at 1175 cm^{-1}) have been observed in these diamonds (Breeding and Shigley, 2009). However, the nitrogen aggregation states in 480 nm band diamonds are usually low, where A-centers (the less aggregated form) are more abundant, and the proportions of B-centers (the more aggregated form) generally do not exceed 45% relative to the total concentration of A-, B-, and C-centers (Lai et al., 2024a). Platelets (i.e., aggregates of interstitial carbon atoms that possibly also contain nitrogen atoms; Woods, 1986; Gu et al., 2020) are occasionally detected in these diamonds, with an absorption peak in the range of 1353–1370 cm^{-1}.

The total concentrations of A-, B-, and C-centers in 480 nm band diamonds are usually low to moderate, typically lower than 300 ppma, calculated based on the integrated nitrogen absorption of the entire diamond (Lai et al., 2024a), although some growth zones may have significantly higher concentrations of these nitrogen defects than others due to the diamonds' highly heterogeneous defect distribution. Many 480 nm band diamonds have an irregular one-phonon region (400–1332 cm^{-1}) where they show an unusual absorption band (centered at about

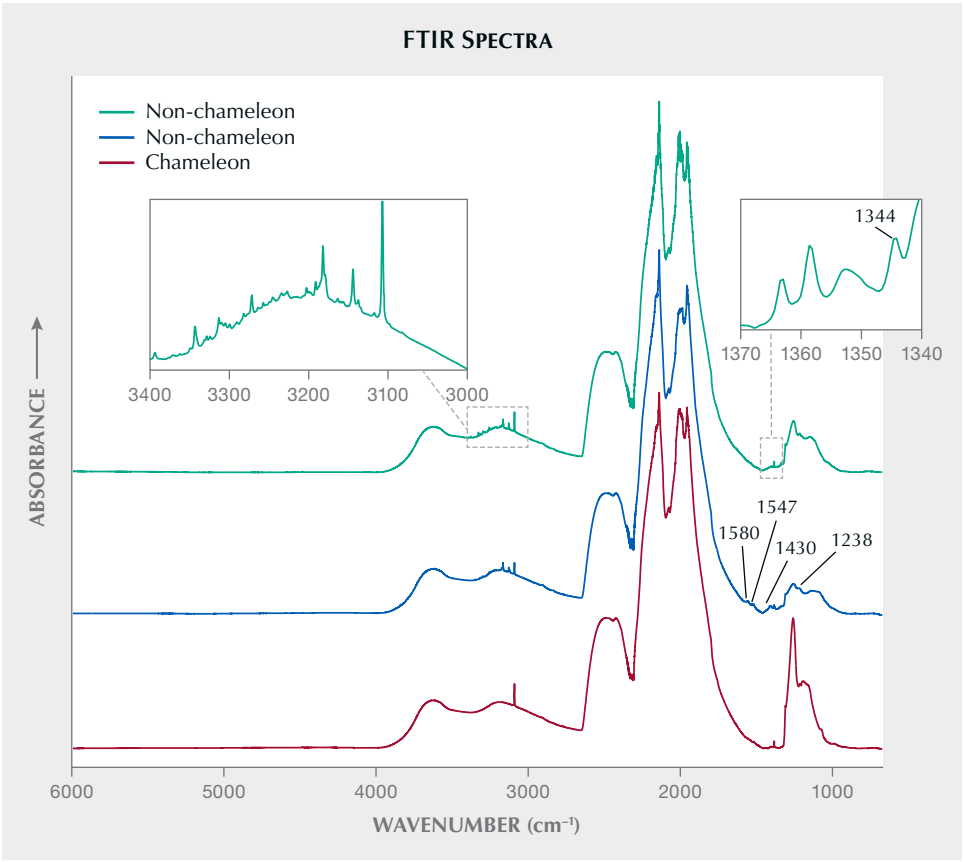

Figure 9. Typical FTIR absorption spectra of 480 nm band diamonds. Non-chameleon 480 nm band diamonds tend to have a more distorted one-phonon region (400–1332 cm^{-1}), and those with detectable single substitutional nitrogen tend to have more hydrogen-related peaks in the 3100–3400 cm^{-1} range, compared to chameleon diamonds. Other infrared absorption features frequently observed in 480 nm band diamonds include a peak at 1238 cm^{-1} and an absorption band centered at 1424–1445 cm^{-1} together with two adjacent bands at 1537–1556 and 1574–1591 cm^{-1}. FTIR absorption spectra were collected at room temperature. Spectra are offset vertically for clarity.

1145–1150 cm^{-1}) (Hainschwang et al., 2012) in addition to the A-, B-, or C-centers (figure 9, green and blue lines). The origin of this additional absorption feature has not been determined, but it was previously observed in some diamonds containing C-centers and referred to as the Y-center (Hainschwang et al., 2012). Notably, non-chameleon 480 nm band diamonds tend to have a more distorted one-phonon region compared to chameleon diamonds (figure 9). Within the one-phonon region, a peak at 1238 cm^{-1} is also frequently observed, which might be correlated with the 480 nm absorption band (Collins and Mohammed, 1982).

Occasionally, an absorption band centered at 1424–1445 cm^{-1} is coupled with two adjacent bands at 1537–1556 and 1574–1591 cm^{-1} in 480 nm band diamonds (figure 9, blue line), all of which have been suggested to be hydrogen-related, but the structure of the defect has not been determined (Hainschwang et al., 2005). A hydrogen-related defect (N_3VH^0; three nitrogen atoms adjacent to a vacancy and a hydrogen atom), with the characteristic absorption peak at 3107 cm^{-1} and the associated absorption at 1405 cm^{-1} (Goss et al., 2014), is detected in all 480 nm band diamonds. Apart from the 3107 cm^{-1} peak, a series of hydrogen-related absorptions with low intensities is detected in the spectral range beyond 2700 cm^{-1} (Fritsch et al., 2007b; Day et al., 2024). Compared to chameleon diamonds, non-chameleon 480 nm band diamonds, especially those with detectable single substitutional nitrogen, tend to have more hydrogen-related peaks in the range of 3100–3400 cm^{-1} (Lai et al., 2024a). Hence, most of these peaks might be associated with hydrogen-related defects comprising single substitutional nitrogen, which become unstable when isolated nitrogen atoms proceed to form nitrogen aggregates, as they are observed only in diamonds with single substitutional nitrogen (Hainschwang et al., 2012; Breeding et al., 2020; Day et al., 2024).

Visible/Near-Infrared (Vis-NIR) Absorption Spectroscopy. Apart from the characteristic broad absorption band centered at around 480 nm, a rare group of 480 nm band diamonds show oscillatory absorption features in the Vis-NIR spectrum (figure 10, red line), which may contribute to their body-color. These diamonds have two series of absorption peaks that exhibit an oscillatory pattern in the range of 600–750 nm. The most prominent peaks are 610,

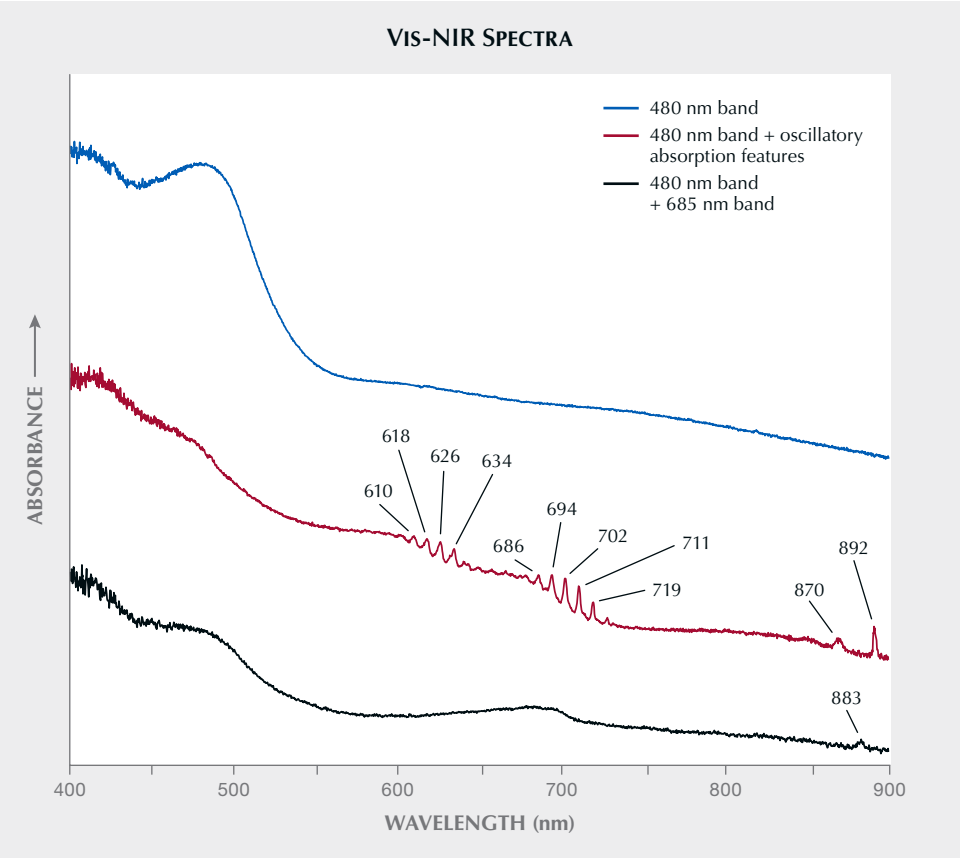

Figure 10. A typical Vis-NIR absorption spectrum of a 480 nm band diamond compared to diamonds that also show oscillatory absorption features in the 600–750 nm range or a broad absorption band at about 685 nm, in addition to the 480 nm broad absorption band. Vis-NIR absorption spectra were collected at ~77 K. Spectra are offset vertically for clarity.

618, 626, and 634 nm (approximately 26 meV apart) in the first series, and 686, 694, 702, 711, and 719 nm (approximately 21 meV apart) in the second series. Between these two series, absorption peaks with much lower intensities may also be detected in some 480 nm band diamonds in this group (figure 10, red line). Relatively strong absorption peaks at 870 and 892 nm almost always accompany the oscillatory features. These oscillatory features have been previously reported for only 10 natural green to yellow diamonds (some of which are likely 480 nm band diamonds based on their FTIR and UV-Vis-NIR absorption spectra) among thousands of colored diamonds analyzed, again highlighting their scarcity (Reinitz et al., 1998). Most 480 nm band diamonds in this category show medium to strong orange fluorescence to long-wave UV and medium to strong yellow or orange fluorescence to short-wave UV; a few diamonds show strong yellow fluorescence to long-wave UV and weak to medium yellow fluorescence to short-wave UV.

Another absorption feature that has been observed, yet is also uncommon in 480 nm band diamonds, is an asymmetrical broad band extending from 600 to 730 nm, centered at approximately 685 nm (figure 10, black line). The 685 nm broad absorption band has been attributed to nickel-related defects and frequently occurs with the absorption peak at 883 nm (Lawson and Kanda, 1993; Wang et al., 2007; Dobrinets et al., 2013). The 883 nm absorption peak corresponds to the well-documented 1.4 eV optical center attributed to a defect comprising an interstitial nickel at the center of a di-vacancy (i.e., a pair of vacancies) in the diamond structure (Iakoubovskii and Davies, 2004; Thiering and Gali, 2021). Another nickel-related absorption feature that has been detected along with the 685 nm band is the peak at 794 nm, attributed to a defect comprising nickel in a di-vacancy position surrounded by four nitrogen atoms (Nadolinny et al., 1999). Point defects in the diamond structure that absorb light generally also emit light at an identical wavelength, corresponding to a spectral feature known as the zero-phonon line (ZPL) (see review by Green et al., 2022). The 794 and 883 nm peaks are both ZPLs; thus, they can also be detected with photoluminescence (PL) spectroscopy as luminescence peaks, with the 883 nm peak resolvable as the 883/885 nm doublet in PL spectra (Wang et al., 2007).

Photoluminescence Spectroscopy. The majority of 480 nm band diamonds have a highly heterogeneous distribution of structural defects, as revealed by their surface fluorescence patterns with distinct zones (again, see figure 8A). Blue fluorescence zones are not directly associated with the 480 nm absorption band, and in many cases, they correspond to the much paler colored or near-colorless zones of 480 nm band diamonds (figure 11). Typically, the most prominent PL feature detected within blue fluorescence zones is the N3 center with a ZPL at 415 nm. In contrast to the blue fluorescence zones, the yellow or greenish yellow fluorescence zones (directly correlated with the 480 nm absorption band) show complex PL spectra, in which approximately 200 PL peaks have been documented (Lai et al., 2024a). The most frequently observed PL features within the yellow or greenish yellow fluorescence zones are reported below, and many of these features are unique to 480 nm band diamonds. As certain peaks can be better resolved by particular laser wavelengths due to selective excitation of defects (Green et al., 2022), the PL features reported here were excited by multiple laser wavelengths, including 455, 532, 633, and 785 nm, which cover a combined PL spectral range of 457–1059 nm.

When 480 nm band diamonds are excited at 455 nm, the most prominent PL peaks include 459, 468, 470, 489, 497, 512, and 518 nm. The 489 and 497 nm peaks are ZPLs of the nickel-related defects, known as the S2 and S3 centers, respectively (Nadolinny and Yelisseyev, 1994). The S2 and S3 centers have the same basic structure of three (for the S2 center) or two (for the S3 center) nitrogen atoms in the first coordination sphere surrounding a nickel ion in the diamond structure (Lang et al., 2004; Yelisseyev and Kanda, 2007).

When 480 nm band diamonds are excited at 532 nm, a broad PL band is always centered at 650–685 nm (figure 12). This broad band is the most crucial feature for the identification of 480 nm band diamonds, as it is the vibronic emission associated with the 480 nm absorption band (Collins and Mohammed, 1982). Typically, the intensity of the broad PL band increases with the 480 nm absorption band and hence tends to be weaker in chameleon diamonds. The PL band is often overlain by small oscillatory bands that have an interval of approximately 10 nm in the 600–690 nm range (figure 12). These oscillatory features are more commonly observed in non-chameleon 480 nm band diamonds than in chameleon diamonds.

Figure 11. A plate cut and polished from a yellow 480 nm band diamond showing color zoning (left). The yellow color zones, with greenish yellow fluorescence, show the 480 nm absorption band in the visible absorption spectrum, while the near-colorless zones, with blue fluorescence, show an absorption peak at 415 nm (right; analyzed spots and corresponding spectra are indicated by yellow and blue dots, respectively). Visible absorption spectra were collected at room temperature. Spectra are offset vertically for clarity. Images by Mei Yan Lai.

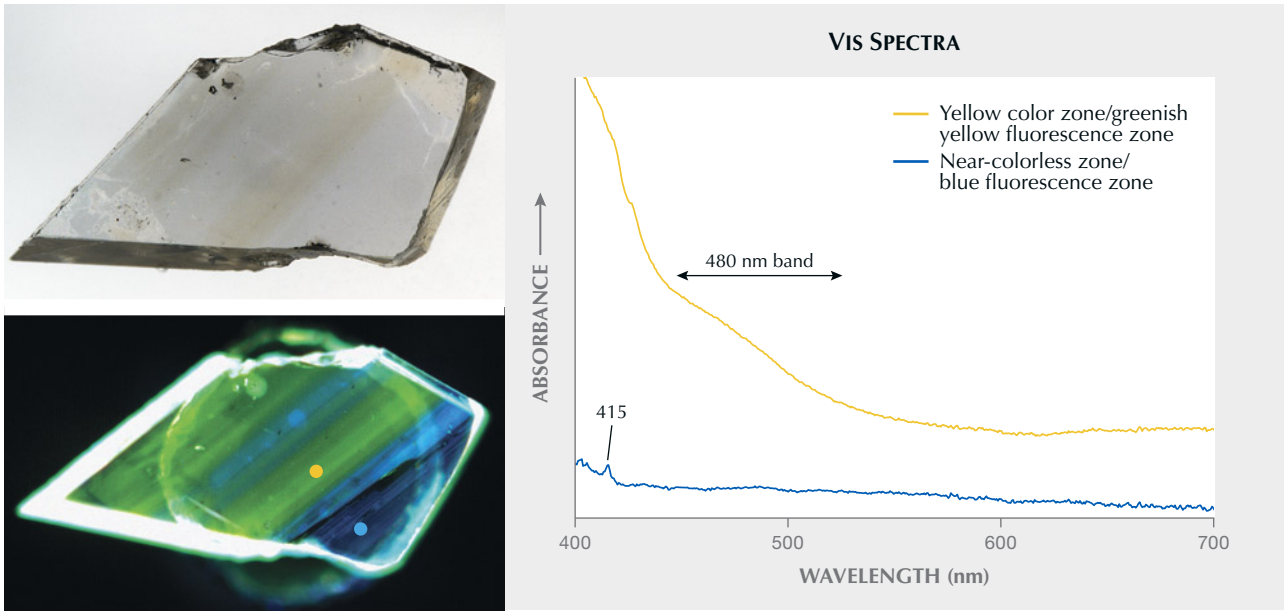

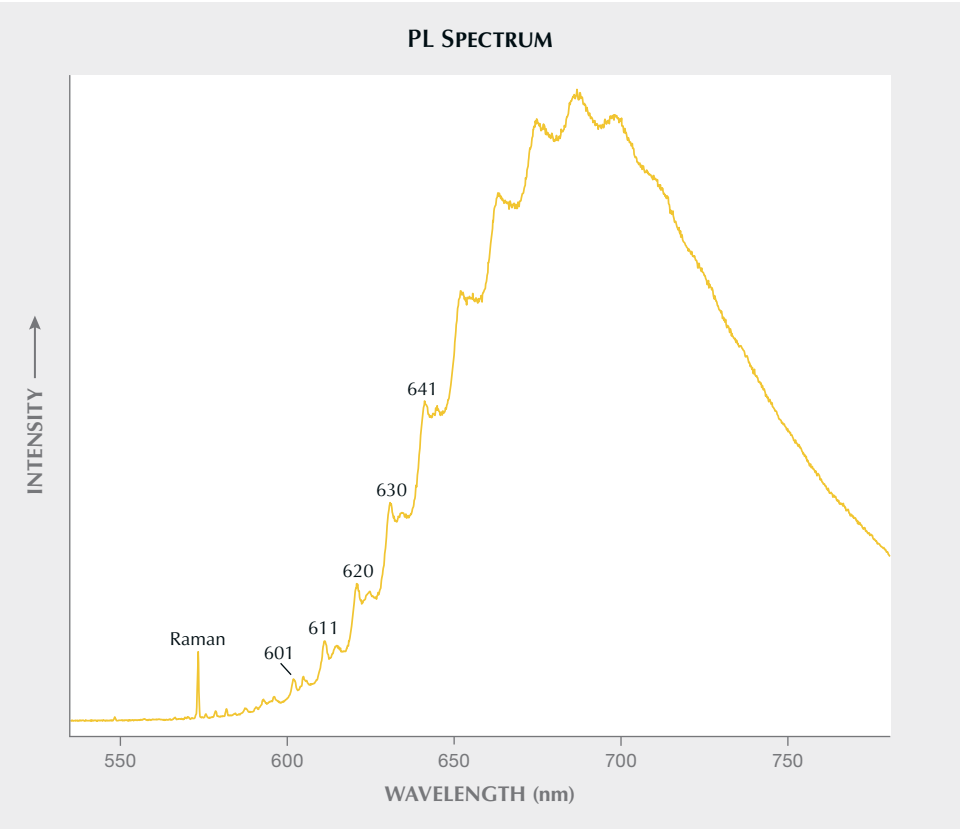

Figure 12. PL spectrum of a 480 nm band diamond excited at 532 nm showing a broad emission band centered at about 685 nm, a diagnostic feature directly associated with the 480 nm absorption band. The broad band is overlain by two sets of small oscillatory bands in the 600–690 nm range. PL spectrum was collected at ~77 K.

The intense PL band generally also shows a secondary set of oscillatory bands, which are about 3 nm away from the primary oscillatory bands and have lower intensities. Other frequently observed PL peaks excited by a 532 nm laser are 566, 575, 578, 581, and 590 nm.

When 480 nm band diamonds are excited at 633 nm, the commonly detected PL peaks include 677, 688, 699, 759, 783, and 794 nm. The 759 nm peak is a doublet that comprises two adjacent peaks at 758.7 and 759.4 nm, where the 758.7 nm peak is always more intense. The two peaks in this doublet might not be well resolved if the diamond has experienced plastic deformation (evidenced by the presence of deformation lines), in which case the doublet might become a single peak due to peak broadening. Peak broadening occurs in diamond with strain that is often associated with plastic deformation (Lai et al., 2024a,b), and the effect is more severe for peaks associated with vacancy-related defects (Fisher et al., 2006). This suggests that the 759 nm doublet corresponds to a structural defect involving a vacancy. The intensity of the 759 nm doublet is positively correlated with two bands centered at 774 and 791 nm, which are likely the phonon sidebands of the doublet. The peak at 759 nm has been attributed to a nickel-related defect and considered a feature of untreated natural diamonds (Dobrinets et al., 2013).

When 480 nm band diamonds are excited at 785 nm, the most frequently observed PL peaks are 799, 819, 838, 846, 859, 869, and 883/885 nm. The relative intensities between the 799 and 819 nm peaks can potentially be used to classify chameleon and non-chameleon 480 nm band diamonds (Lai et al., 2024a; Hardman et al., 2025). Most chameleon diamonds (with a green component) have a relatively stronger 819 nm peak, whereas the non-chameleon 480 nm band diamonds (without a green component) generally have a relatively stronger 799 nm peak, suggesting that the relative intensities between these two peaks may be related to the concentrations of certain structural defects responsible for the bodycolor and thus the color-change property of 480 nm band diamonds. The 838, 846, and 859 nm peaks are strongly correlated with the 819 nm peak; thus, they might all be related to the same defect (Lai et al., 2024a).

OCCURRENCE OF 480 NM ABSORPTION BAND WITHIN SMALL YELLOW COLOR ZONES

Irregularly shaped or cuboid yellow color zones caused by the 480 nm absorption band have been observed in several colorless and pink diamonds (figure 13) (Sohrabi et al., 2023; Lai et al., 2024b; Hardman et al., 2025). In most of these diamonds, the yellow color zones are volumetrically minor compared to the rest of the diamond. Consequently, the 480 nm absorption band is usually not detected when the bulk diamond is measured using Vis-NIR absorption spectroscopy. Instead, PL spectroscopy is a highly sensitive *in situ* technique that has been used to confirm that the yellow color zones in these diamonds contain PL features associated with the 480 nm absorption band (Lai et al., 2024b; Hardman et al., 2025).

Similar to typical 480 nm band diamonds, yellow color zones in colorless and pink diamonds have medium to strong yellow fluorescence when exposed to long-wave UV, whereas the colorless or pink color zones have blue fluorescence (figure 13). When examined with the DiamondView instrument, yellow color zones generally show much weaker yellow fluorescence compared to that produced by long-wave UV. This is partly because the yellow color zones are small and/or are only partially located on the surface of these diamonds; occasionally the yellow color zones are completely beneath the diamonds' surfaces, in which case a yellow fluorescence response cannot be detected by surface fluorescence imaging using the DiamondView. For diamonds with subsurface yellow color zones, PL depth profiling (collecting PL spectra as a function of depth) has demonstrated the ability to detect the zone where the PL features associated with the 480 nm absorption band are the strongest, hence estimating the depth and thickness of the yellow color zones (Lai et al., 2024b). The occurrence of diamonds containing yellow color zones further emphasizes the dynamic environments in which 480 nm band diamonds may grow.

SOURCES

The global abundance and distribution of 480 nm band diamonds are presently unknown. These diamonds are not commonly reported by the mining industry or geological research fields, due in part to their scarcity (and that they are not found in all diamond mines) and/or that these industries are not aware of their features. To date, only two localities are confirmed to produce 480 nm band diamonds: the Chidliak kimberlite field in Canada (Lai et al., 2020) and the kimberlites of the Siberian Platform in Russia (Titkov et al., 2014). Other localities that likely also contain 480 nm band diamonds are Botswana's Orapa kimberlite cluster (Timmerman et al., 2018) and Canada's Lake Timiskaming kimberlite cluster (Van Rythoven et al., 2022), based on the interpretation of FTIR spectra and surface fluorescence patterns of the reported yellow diamonds from these localities that are similar to 480 nm band diamonds.

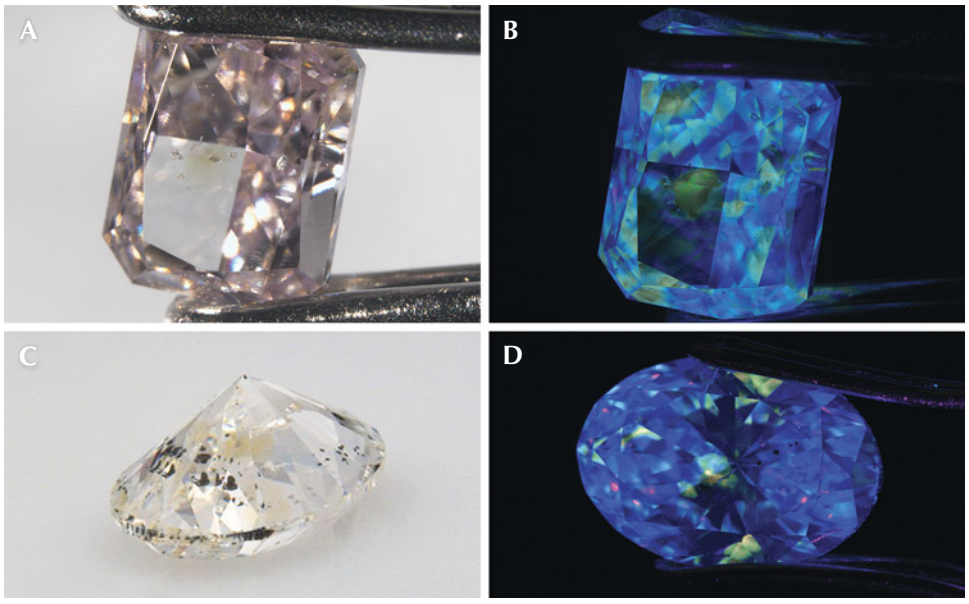

Figure 13. Yellow zones colored by the 480 nm absorption band have been observed in pink (A) and colorless (C) diamonds. B and D: When exposed to long-wave UV, the yellow color zones in the pink and colorless diamonds show yellow fluorescence, while the remaining areas of the diamonds show blue fluorescence. Photos by Mei Yan Lai.

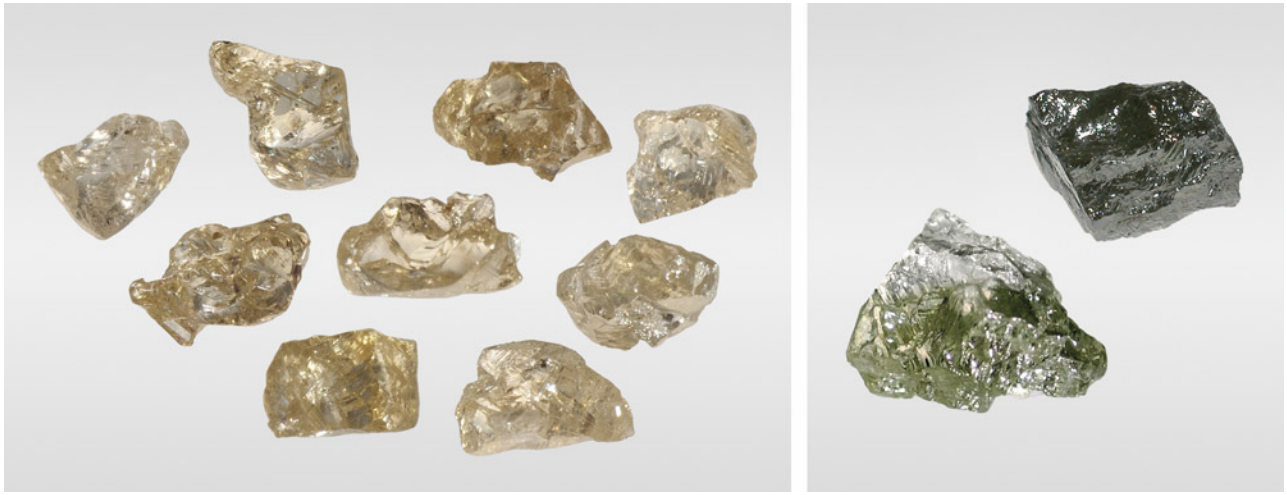

Figure 14. Left: Rough yellow 480 nm band diamonds from the Chidliak kimberlite field in Canada. Right: Rough chameleon diamonds submitted to GIA for analysis. All of these diamonds have irregular morphologies. Photos by Mei Yan Lai (left) and GIA staff (right).

MORPHOLOGY OF ROUGH 480 NM BAND DIAMONDS

Rough 480 nm band diamonds commonly have irregular morphology, lacking any well-defined octahedral or cuboid crystal faces. This morphological characteristic is observed among 480 nm band diamonds from the Chidliak kimberlite field in Canada (figure 14, left) (Lai et al., 2020). Over the past few years, GIA has received several rough 480 nm band diamonds, including chameleon diamonds, for analysis (figure 14, right). Similar to the Chidliak diamonds, none showed any well-defined octahedral or cuboid crystal faces. Another submitted rough diamond exhibited both trigons and tetragons on the same face (figure 15). Trigons and tetragons are etched features restricted to the octahedral and cuboid crystal faces, respectively, formed on the surface of diamond from the interaction with fluids in Earth's mantle or during kimberlite eruption. This suggests that the diamond has a combination of octahedral and cuboid growth habits, probably resulting from crystallization under dynamic geological conditions. While most 480 nm band diamonds submitted to GIA are faceted and hence the original morphologies are unknown, occasionally etch features are preserved within indented naturals, which reveal the growth habits of these diamonds (e.g., Lai and Hardman, 2023).

Figure 15. Tetragons (left) and trigons (right) were observed on the same side of this rough 480 nm band diamond, indicating a combination of octahedral and cuboid growth habits. Photomicrographs by Mei Yan Lai; fields of view 2.41 mm (left) and 0.73 mm (right).

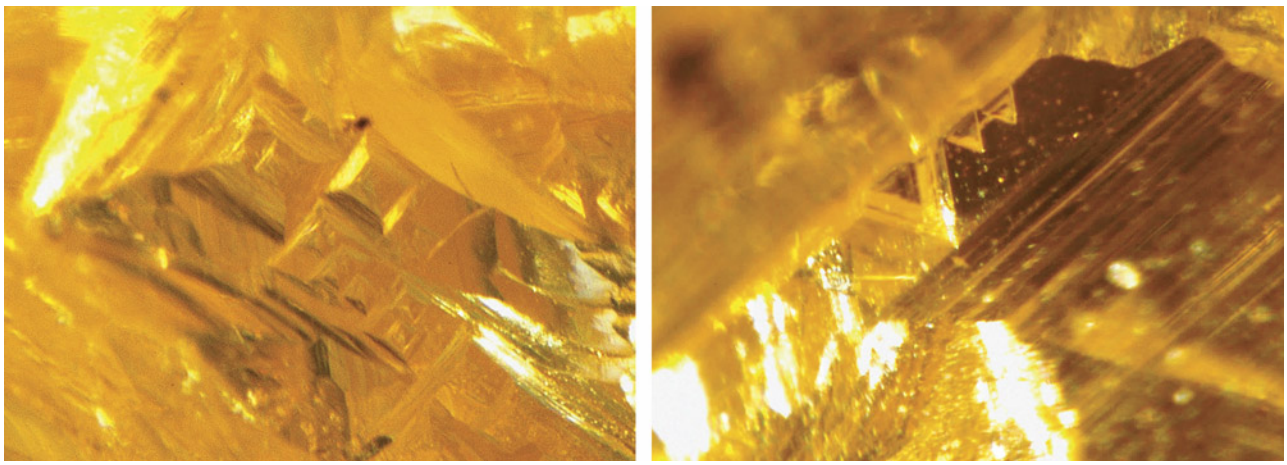

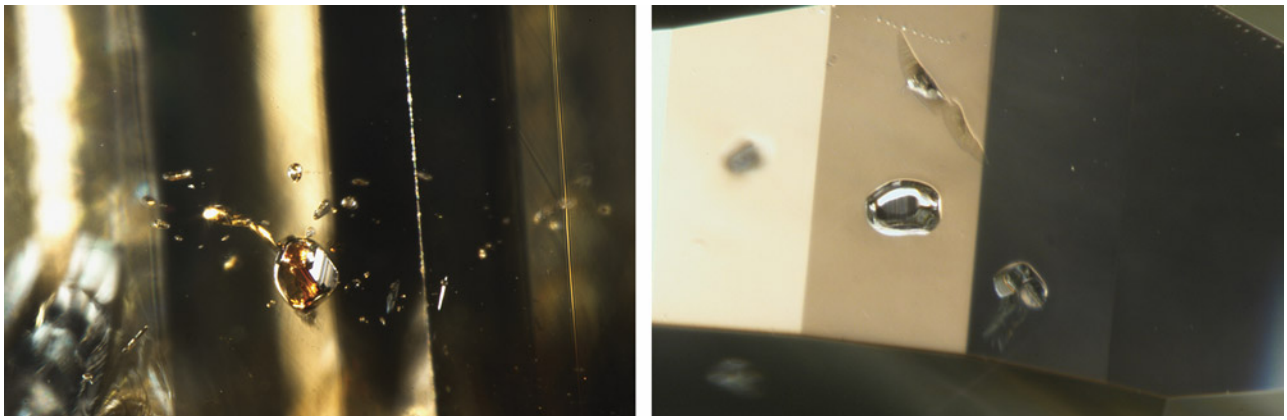

Figure 16. Pyrope-almandine-grossular garnet (left) and omphacite (right) are the most common mineral inclusions observed in 480 nm band diamonds. (The tan areas in the right photo are reflections from the girdle facets.) Photomicrographs by Mei Yan Lai; fields of view 1.76 mm (left) and 0.93 mm (right).

MINERAL INCLUSIONS

Often minerals from mantle rocks are encapsulated by diamonds during growth. These mineral inclusions can be used to interpret the mantle rock from which they were derived, and hence the rock in which the diamond may have grown. Mineral inclusions observed in 480 nm band diamonds include pyrope-almandine-grossular garnet, omphacite, rutile, graphite, and sulfide minerals. Pyrope-almandine-grossular garnet ($(Mg,Fe,Ca)_3Al_2Si_3O_{12}$), omphacite ($(Ca,Na)(Mg,Fe,Al)Si_2O_6$), and rutile ($TiO_2$) are minerals associated with eclogite—a major host rock for diamond in the lithospheric mantle (figure 16). Based on the observation that most, if not all, inclusion-bearing 480 nm band diamonds submitted to GIA are eclogitic, it is inferred that these diamonds are more likely to be found in mines that predominantly produce eclogitic diamonds. However, this does not preclude the possibility that 480 nm band diamonds can also form in peridotite—another major diamond host rock in the lithospheric mantle comprised predominantly of olivine ($(Fe,Mg)_2SiO_4$), orthopyroxene ($(Mg,Fe)_2Si_2O_6$), and chromium-rich diopside ($(Ca,Cr)MgSi_2O_6$).

CONCLUSIONS

Diamonds colored by the 480 nm absorption band have attracted little attention in the mining industry and gem trade, due in part to their scarcity and therefore unfamiliarity with their properties. While most 480 nm band diamonds have a saturated yellow bodycolor similar to that generated by other diamond defects, these diamonds also occur in a variety of additional colors, including the highly sought-after pure orange diamonds and color-change chameleon diamonds.

Rapid diamond screening can be achieved by exposing them to long-wave UV, as 480 nm band diamonds generally emit medium to strong yellow fluorescence, a mixture of yellow and blue fluorescence, or (occasionally) orange fluorescence. The presence of micrometer-sized dark inclusion clusters—identified as graphite—are a diagnostic gemological feature of 480 nm band diamonds. These platy inclusions are extremely thin and highly reflective when viewed at certain angles, with rounded or well-defined hexagonal shapes. Other characteristic features of 480 nm band diamonds include irregular surface fluorescence patterns, anomalous absorption in the one-phonon region of the FTIR spectrum, and a broad PL band centered at 650–685 nm when the diamond is excited by lasers with wavelengths in the range of, for example, 488–532 nm.

Currently, no known commercial treatments or synthetic growth methods can create the defect(s) associated with the 480 nm absorption band or the color-change property associated with chameleon diamonds. However, it is certainly possible to artificially create other defects in 480 nm band diamonds to alter their colors (e.g., laboratory irradiation treatments to produce a green bodycolor); therefore, advanced gemological testing may be required to ensure that the diamonds are naturally colored. Finally, care must be taken when examining colorless or pink diamonds, as small yellow color zones caused by the 480 nm absorption band may occur in these diamonds and affect their color grades.

ABOUT THE AUTHORS
Dr. Mei Yan Lai is a metrologist and former postdoctoral research associate at GIA in Carlsbad, California.

ACKNOWLEDGMENTS
The author is grateful to Matthew Hardman for many helpful suggestions and comments on the first draft of the manuscript. George Rossman (California Institute of Technology) is sincerely thanked for providing access to a UV-Vis-NIR microspectrometer. Thank you to Christopher M. Breeding and Sally Eaton-Magaña for their guidance on this research and providing helpful comments on the manuscript. Paul Johnson, Kyaw Moe, and Virginia Schwartz and her team are acknowledged for providing data and identifying the diamonds for this study. Simon Lawson and three reviewers are thanked for reviewing the manuscript and providing constructive comments.

REFERENCES

Altobelli M., Johnson P. (2014) Lab Notes: Mixed-type cape diamond. *G&G*, Vol. 50, No. 3, p. 237.

Barannik E.P., Shiryaev A.A., Hainschwang T. (2021) Shift of CO_2-I absorption bands in diamond: A pressure or compositional effect? A FTIR mapping study. *Diamond and Related Materials*, Vol. 113, article no. 108280, http://dx.doi.org/10.1016/j.diamond.2021.108280

Breeding C.M., Shigley J.E. (2009) The "type" classification system of diamonds and its importance in gemology. *G&G*, Vol. 45, No. 2, pp. 96–111, http://dx.doi.org/10.5741/gems.45.2.96

Breeding C.M., Eaton-Magaña S., Shigley J.E. (2018) Natural-color green diamonds: A beautiful conundrum. *G&G*, Vol. 54, No. 1, pp. 2–27, http://dx.doi.org/10.5741/gems.54.1.2

——— (2020) Naturally colored yellow and orange gem diamonds: The nitrogen factor. *G&G*, Vol. 56, No. 2, pp. 194–219, http://dx.doi.org/10.5741/gems.56.2.194

Collins A.T. (1982) Colour centres in diamond. *Journal of Gemmology*, Vol. 18, No. 1, pp. 37–75.

——— (2001) The colour of diamond and how it may be changed. *Journal of Gemmology*, Vol. 27, No. 6, pp. 341–359.

Collins A.T., Mohammed K. (1982) Optical studies of vibronic bands in yellow luminescing natural diamonds. *Journal of Physics C: Solid State Physics*, Vol. 15, No. 1, pp. 147–158, http://dx.doi.org/10.1088/0022-3719/15/1/012

Day M.C., Jollands M.C., Novella D., Nestola F., Dovesi R., Pamato M.G. (2024) Hydrogen-related defects in diamond: A comparison between observed and calculated FTIR spectra. *Diamond and Related Materials*, Vol. 143, article no. 110866, http://dx.doi.org/10.1016/j.diamond.2024.110866

De Weerdt F., Van Royen J. (2001) Defects in coloured natural diamonds. *Diamond and Related Materials*, Vol. 10, No. 3-7, pp. 474–479, http://dx.doi.org/10.1016/s0925-9635(00)00521-5

Dobrinets I.A., Vins V.G., Zaitsev A.M. (2013) *HPHT-Treated Diamonds: Diamonds Forever*. Springer, Heidelberg, 257 pp.

Fisher D. (2009) Brown diamonds and high pressure high temperature treatment. *Lithos*, Vol. 112S, pp. 619–624, http://dx.doi.org/10.1016/j.lithos.2009.03.005

Fisher D., Evans D.J.F., Glover C., Kelly C.J., Sheehy M.J., Summerton G.C. (2006) The vacancy as a probe of the strain in type IIa diamonds. *Diamond and Related Materials*, Vol. 15, No. 10, pp. 1636–1642, http://dx.doi.org/10.1016/j.diamond.2006.01.020

Fisher D., Sibley S.J., Kelly C.J. (2009) Brown colour in natural diamond and interaction between the brown related and other colour-inducing defects. *Journal of Physics: Condensed Matter*, Vol. 21, No. 36, article no. 364213, http://dx.doi.org/10.1088/0953-8984/21/36/364213

Fritsch E., Massi L., Rossman G.R., Hainschwang T., Jobic S., Dessapt R. (2007a) Thermochromic and photochromic behaviour of "chameleon" diamonds. *Diamond and Related Materials*, Vol. 16, No. 2, pp. 401–408, http://dx.doi.org/10.1016/j.diamond.2006.08.014

Fritsch E., Hainschwang T., Massi L., Rondeau B. (2007b) Hydrogen-related optical centers in natural diamond: An update. *New Diamond and Frontier Carbon Technology*, Vol. 17, No. 2, pp. 63–89.

Fritsch E., Delaunay A. (2018) What truly characterises a chameleon diamond? An example of an atypical 25.85 ct stone. *Journal of Gemmology*, Vol. 36, No. 2, pp. 142–151.

Fryer C., Crowningshield R., Hurwit K.N., Kane R.E. (1981) Lab Notes: "Chameleon" diamond. *G&G*, Vol. 17, No. 4, p. 227.

——— (1982) Lab Notes: "Chameleon" diamond. *G&G*, Vol. 18, No. 4, p. 228.

Gali A., Lowther J.E., Deak P. (2001) Defect states of substitutional oxygen in diamond. *Journal of Physics: Condensed Matter*, Vol. 13, No. 50, article no. 11607, http://dx.doi.org/10.1088/0953-8984/13/50/319

Goss J.P., Briddon P.R., Hill V., Jones R., Rayson M.J. (2014) Identification of the structure of the 3107 cm^{-1} H-related defect in diamond. *Journal of Physics: Condensed Matter*, Vol. 26, No. 14, article no. 145801, http://dx.doi.org/10.1088/0953-8984/26/14/145801

Green B.L., Collins A.T., Breeding C.M. (2022) Diamond spectroscopy, defect centers, color, and treatments. *Reviews in Mineralogy and Geochemistry*, Vol. 88, No. 1, pp. 637–688, http://dx.doi.org/10.2138/rmg.2022.88.12

Gu T., Ritterbex S., Tsuchiya T., Wang W. (2020) Novel configurations of VN_4 and VN_4H defects in diamond platelets: Structure, energetics and vibrational properties. *Diamond and Related Materials*, Vol. 108, article no. 107957, http://dx.doi.org/10.1016/j.diamond.2020.107957

Hainschwang T., Simic D., Fritsch E., Deljanin B., Woodring S., DelRe N. (2005) A gemological study of a collection of chameleon diamonds. *G&G*, Vol. 41, No. 1, pp. 20–35, http://dx.doi.org/10.5741/gems.41.1.20

Hainschwang T., Notari F., Fritsch E., Massi L., Rondeau B., Breeding C.M., Vollstaedt H. (2008) HPHT treatment of CO_2 containing and CO_2-related brown diamonds. *Diamond and Related Materials*, Vol. 17, No. 3, pp. 340–351, http://dx.doi.org/10.1016/j.diamond.2008.01.022

Hainschwang T., Fritsch E., Notari F., Rondeau B. (2012) A new defect center in type Ib diamond inducing one phonon infrared absorption: The Y center. *Diamond and Related Materials*, Vol. 21, pp. 120–126, http://dx.doi.org/10.1016/j.diamond.2011.11.002

Hainschwang T., Notari F., Pamies G. (2020) A defect study and classification of brown diamonds with non-deformation-related color. *Minerals*, Vol. 10, No. 10, article no. 914, http://dx.doi.org/10.3390/min10100914

Hardman M.F., Lai M.Y., Breeding C.M., Eaton-Magaña S., Schwartz V.A. (2025) A statistical evaluation of the spectroscopic features in natural diamonds with the 480 nm absorption band. *Diamond and Related Materials*, Vol. 155, article no. 112277, http://dx.doi.org/10.1016/j.diamond.2025.112277

Iakoubovskii K., Davies G. (2004) Vibronic effects in the 1.4–eV optical center in diamond. *Physical Review B*, Vol. 70, article no. 245206, http://dx.doi.org/10.1103/physrevb.70.245206

Kanda H. (2007) Nonuniform distributions of color and luminescence of diamond single crystals. *New Diamond and Frontier Carbon Technology*, Vol. 17, No. 2, pp. 105–116.
Lai M.Y., Eaton-Magaña S. (2023) Lab Notes: Rare natural bicolor diamond. *G&G*, Vol. 59, No. 4, pp. 486–487.
Lai M.Y., Hardman M.F. (2023) Lab Notes: Etch features reveal the morphology of diamond. *G&G*, Vol. 59, No. 3, pp. 356–357.
Lai M.Y., Schwartz V. (2023) Lab Notes: Carbon dioxide in a brown diamond. *G&G*, Vol. 59, No. 4, pp. 487–488.
Lai M.Y., Stachel T., Breeding C.M., Stern R.A. (2020) Yellow diamonds with colourless cores–evidence for episodic diamond growth beneath Chidliak and the Ekati Mine, Canada. *Mineralogy and Petrology*, Vol. 114, pp. 91–103, http://dx.doi.org/10.1007/s00710-020-00693-0
Lai M.Y., Hardman M.F., Eaton-Magaña S., Breeding C.M., Schwartz V.A., Collins A.T. (2024a) Spectroscopic characterization of diamonds colored by the 480 nm absorption band. *Diamond and Related Materials*, Vol. 142, article no. 110825, http://dx.doi.org/10.1016/j.diamond.2024.110825.
Lai M.Y., Myagkaya E., Hardman M.F., Eaton-Magaña S., Breeding C.M., Sohrabi S., Collins A.T. (2024b) Spectroscopic characterization of rare natural pink diamonds with yellow color zones. *Diamond and Related Materials*, Vol. 148, article no. 111428, http://dx.doi.org/10.1016/j.diamond.2024.111428
Lall A., Ruan S., Johnson P. (2024) Lab Notes: Natural orange diamond with unusual absorption features. *G&G*, Vol. 60, No. 1, pp. 59–60.
Lang A.R., Yelisseyev A.P., Pokhilenko N.P., Steeds J.W., Wotherspoon A. (2004) Is dispersed nickel in natural diamonds associated with cuboid growth sectors in diamonds that exhibit a history of mixed-habit growth? *Journal of Crystal Growth*, Vol. 263, No. 1-4, pp. 575–589, http://dx.doi.org/10.1016/j.jcrysgro.2003.11.116
Lawson S.C., Kanda H. (1993) Nickel in diamond: An annealing study. *Diamond and Related Materials*, Vol. 2, No. 2-4, pp. 130–135, http://dx.doi.org/10.1016/0925-9635(93)90043-2
Luo Y., Breeding C.M. (2013) Fluorescence produced by optical defects in diamond: Measurement, characterization, and challenges. *G&G*, Vol. 49, No. 2, pp. 82–97, http://dx.doi.org/10.5741/gems.49.2.82
Nadolinny V.A., Yelisseyev A.P. (1994) New paramagnetic centres containing nickel ions in diamond. *Diamond and Related Materials*, Vol. 3, No. 1-2, pp. 17–21, http://dx.doi.org/10.1016/0925-9635(94)90024-8
Nadolinny V.A., Yelisseyev A.P., Baker J.M., Newton M.E., Twitchen D.J., Lawson S.C., Yuryeva O.P., Feigelson B.N. (1999) A study of ^{13}C hyperfine structure in the EPR of nickel-nitrogen-containing centres in diamond and correlation with their optical properties. *Journal of Physics: Condensed Matter*, Vol. 11, article no. 7357, http://dx.doi.org/10.1088/0953-8984/11/38/314
Reinitz I.M., Fritsch E., Shigley J.E. (1998) An oscillating visible light optical center in some natural green to yellow diamonds. *Diamond and Related Materials*, Vol. 7, No. 2-5, pp. 313–316, http://dx.doi.org/10.1016/s0925-9635(97)00268-9
Shigley J.E., Breeding C.M. (2013) Optical defects in diamond: A quick reference chart. *G&G*, Vol. 49, No. 2, pp. 107–111, http://dx.doi.org/10.5741/gems.49.2.107
Shiryaev A.A., Chesnokov Y., Vasiliev A.L., Hainschwang T. (2023) Exsolution of oxygen impurity from diamond lattice and formation of pressurized CO_2-I precipitates. *Carbon Trends*, Vol. 11, article no. 100270, http://dx.doi.org/10.1016/j.cartre.2023.100270
Sohrabi S., Lai M.Y., Eaton-Magaña S. (2023) Lab Notes: Yellow zoning in pink diamonds. *G&G*, Vol. 59, No. 2, pp. 211–212.
Thiering G., Gali A. (2021) Magneto-optical spectra of the split nickel-vacancy defect in diamond. *Physical Review Research*, Vol. 3, article no. 043052, http://dx.doi.org/10.1103/physrevresearch.3.043052
Timmerman S., Chinn I.L., Fisher D., Davies G.R. (2018) Formation of unusual yellow Orapa diamonds. *Mineralogy and Petrology*, Vol. 112, pp. 209–218, http://dx.doi.org/10.1007/s00710-018-0592-9
Titkov S.V., Mineeva R.M., Zudina N.N., Sergeev A.M., Ryabchikov I.D., Shiryaev A.A., Speransky A.V., Zhikhareva V.P. (2014) The luminescent nature of orange coloration in natural diamonds: Optical and EPR study. *Physics and Chemistry of Minerals*, Vol. 42, pp. 131–141, http://dx.doi.org/10.1007/s00269-014-0705-x
Van Enckevort W.J.P., Visser E.P. (1990) Photoluminescence microtomography of diamond. *Philosophical Magazine B*, Vol. 62, No. 6, pp. 597–614, http://dx.doi.org/10.1080/13642819008215258
Van Rythoven A.D., Schulze D.J., Stern R.A., Lai M.Y. (2022) Composition of diamond from the 95-2 pipe, Lake Timiskaming kimberlite cluster, Superior Craton, Canada. *Canadian Mineralogist*, Vol. 60, No. 1, pp. 67–90, http://dx.doi.org/10.3749/canmin.2000104
Wang W., Hall M., Breeding C.M. (2007) Natural type Ia diamond with green-yellow color due to Ni-related defects. *G&G*, Vol. 43, No. 3, pp. 240–243, http://dx.doi.org/10.5741/gems.43.3.240
Welbourn C.M., Cooper M., Spear P.M. (1996) De Beers natural versus synthetic diamond verification instruments. *G&G*, Vol. 32, No. 3, pp. 156–169, http://dx.doi.org/10.5741/gems.32.3.156
Woods G.S. (1986) Platelets and the infrared absorption of type Ia diamonds. *Proceedings of the Royal Society of London A*, Vol. 407, No. 1832, pp. 219–238, http://dx.doi.org/10.1098/rspa.1986.0094
Yelisseyev A., Kanda H. (2007) Optical centers related to 3d transition metals in diamond. *New Diamond and Frontier Carbon Technology*, Vol. 17, No. 3, pp. 127–178.

Introducing Jewelry Services

Our legacy of trust,
now available for jewelry.

GIA®

New GIA Jewelry Services

For generations, the world has trusted GIA to provide accurate reports for loose gems.

Now, we're bringing our global leadership to new horizons by providing jewelry services.

Expect the same rigorous GIA standards, deep expertise, and advanced technology to add confidence and credibility to every jewelry report.

GIA.edu/jewelryservices

Jewelry provided courtesy of The Clear Cut.

External Morphology and Internal Zonal Structure of Macle Diamond

Ahmadjan Abduriyim and Masao Kitamura

Contact-twinned crystals of natural diamond rough, known as "macle," typically exhibit a flattened triangular shape, which has been attributed to preferential growth at re-entrant corners where two crystals mutually contact. The influence of the re-entrant corner effect on the morphological alteration of macle diamond may be closely linked to the conditions of carbon supersaturation. However, no detailed investigation has been conducted regarding the possibility of preferential growth on the opposite side of the re-entrant corner, which is referred to as a "salient corner" in this study. The four external and internal growth morphologies (I, II, III, and IV) of contact-twinned macle diamonds with four different corresponding re-entrant corner shapes (i, ii, iii, and iv) were analyzed by examining the surface features of each corner and the zonal growth structure through scanning electron microscopy–cathodoluminescence images. The study confirmed that morphological changes and the flatness of macle diamonds resulted from preferential growth at both re-entrant and salient corners. To our knowledge, this is the first reporting of group III and IV macle crystals characterized by an apex covered by high-index {hhk} faces as well as the salient corner effect. Additionally, the variations in morphology appear to correlate with fluctuations in carbon supersaturation conditions in the diamonds' growth medium.

The most distinctive type of contact-twinned crystals are the triangular *macle* (French for "twin") diamonds (figure 1). These diamonds consist of two octahedral crystals in contact with each other on the (111) octahedral face, with the twin plane parallel to the octahedral <111> direction. These crystals often grow significantly larger than the sum of the two single octahedral diamond crystals would be, displaying the characteristic morphology of a flattened triangular shape (Sinkankas, 1964; Orlov, 1977; Tappert and Tappert, 2011). Due to dissolution, macle diamonds may also lose their sharp edges and develop a rounded habit. In some South African diamond mines, an average of 10–15% of diamonds are macle crystals (Harris et al., 1975). Twinning also occurs in synthetic diamonds grown by chemical vapor deposition (CVD), with the contact twin mechanism originating from the formation of a hydrogen-terminated four-carbon atom cluster on the {111} surface during polycrystalline diamond growth (Battaile et al., 1998; Butler and Oleynik, 2008).

See end of article for About the Authors and Acknowledgments.
Gems & Gemology, Vol. 61, No. 3, pp. 250–269,
http://dx.doi.org/10.5741/GEMS.61.3.250

The crystal faces {111} are crystallographically equivalent in single octahedral diamonds (figure 2, A and B), and there is no difference in the growth rates of these {111} faces. Additionally, there is no change in growth morphology under stable growth conditions (Hartman, 1956). Therefore, estimating changes in growth conditions is quite challenging. However, in the case of contact-twinned crystals, the growth rates of the {111} faces are not equivalent.

In Brief

- "Macle" refers to a twinned diamond with a flat triangular shape, formed when two single diamonds contact each other during the growth process.
- Morphologies of macle diamonds with different re-entrant corner shapes are classified into distinct morphology groups (I, II, III, and IV) with corresponding re-entrant corner shapes (i, ii, iii, and iv). These morphologies are explained by preferential growth effects at the corners.
- The flatness and changes in the morphology of macle diamonds are directly related to preferential growth occurring at the re-entrant and salient corners under different carbon supersaturation conditions.

Figure 1. Examples of contact-twinned macle diamond crystals from South Africa. Left to right: a flat triangular macle with limited resorption (sample 11; 0.357 ct); an extensively resorbed variant of a flat triangular macle (sample 12; 0.411 ct); a very elongated flat macle with stacking growth layers on the octahedral faces, showcasing sharp edges and pointed apex corners (sample 13; 0.553 ct); a six-pointed star-shaped, poorly resorbed flat macle (sample 14; 0.747 ct). Photo by Tetsuya Chikayama; courtesy of Suwa & Son, Inc.

The octahedral {111} faces are categorized into three types depending on their relation to the twin boundary (junction): (1) faces *r* and *r**, which are not parallel to the twin plane and form re-entrant corners with an interfacial angle of 141.06°; (2) faces *s* and *s**, which are not parallel to the twin plane and form salient corners with an interfacial angle of 218.94° (figure 2D); and (3) faces *n* and *n**, which do not contact re-entrant and salient corners and are parallel to the twin plane.

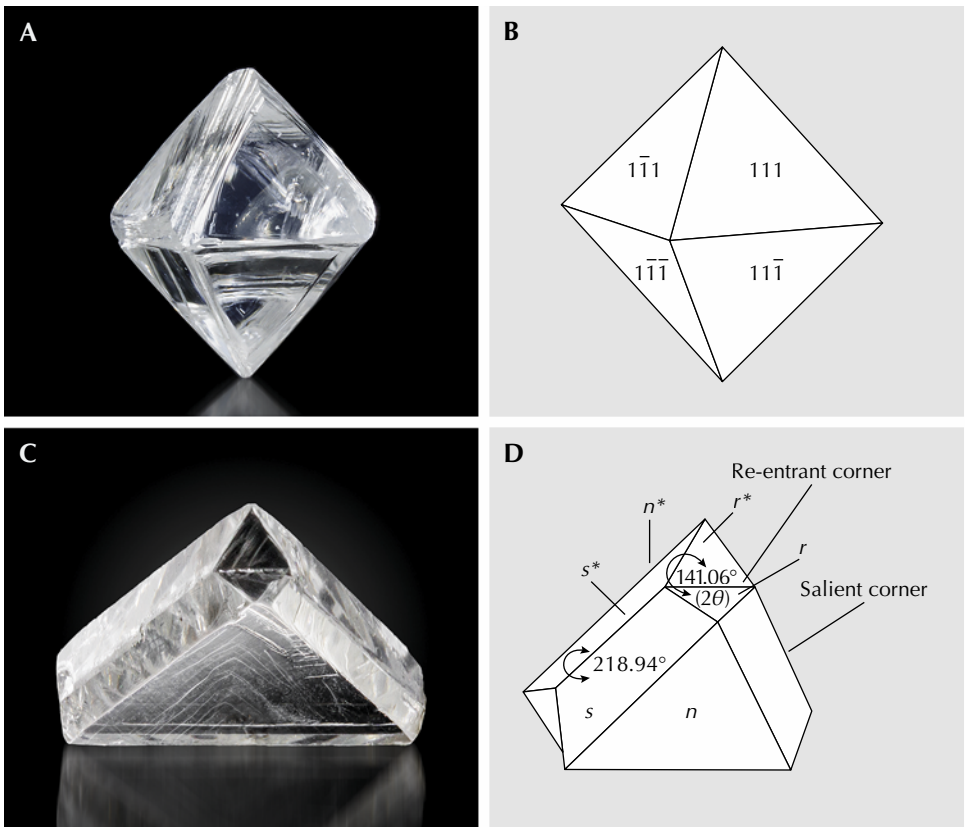

*Figure 2. A: A natural single octahedral crystal diamond bounded by {111} faces (3.51 × 3.50 × 6.18 mm). B: Illustration of an octahedral diamond. All of the {111} faces are crystallographically equivalent. C: A contact-twinned macle diamond, characterized by its {111} faces (7.74 × 7.63 × 2.86 mm). D: Illustration of a contact twin. The {111} faces are categorized into three types (*r *and* r*, s *and* s*, *and* n *and* n*) *according to their relationship with the twin boundary. Photos by Tetsuya Chikayama; courtesy of Suwa & Son, Inc. (C).*

The characteristic morphology of twinned crystals has been studied based on the re-entrant corner effect resulting from preferential nucleation at the corner (Becke, 1911; Chudoba, 1927; Stranski, 1949; Hartman, 1956), as well as the "pseudo-re-entrant corner" effect attributed to the concentration of screw dislocations on the twin boundary at the corner. These studies aim to explain the distinctive morphologies of twinned crystals (Kitamura et al., 1979). The preferential growth at the re-entrant corners has also been emphasized to elucidate the flattened morphology of contact-twinned crystals, including the parallel axes of contact-twinned spinel and macle diamond, the inclined axes of heart-shaped Japan law–twinned quartz, the V-shaped twin of amethyst, the V-shaped twin of rutile, the swallowtail-shaped twin of gypsum, the butterfly-shaped twin of calcite, and the Brazil law twin of hematite (figure 3) (Sunagawa, 1975; Sunagawa et al., 1979; Sunagawa and Yasuda, 1983; Sunagawa and Lu, 1987; Ming and Sunagawa, 1988; Kitamura et al., 1992; Hirabayashi et al., 1993). However, to our knowledge, no detailed study has been conducted on the potential for preferential growth at the salient corners of macle diamond crystals.

In this study, the authors aim to introduce a model that facilitates understanding of the morphological changes of contact twins based on the growth rates of octahedral faces {111} *r* and *r** at the re-entrant corners, *s* and *s** at the salient corners, and *n* and *n** that do not interact with these corners. Specifically, the study presents detailed results regarding the morphological changes of macle diamonds during the growth process by exploring their three-dimensional internal zonal structure, which chronicles the morphological changes during crystal formation and estimates the growth rate ratios based on growth zoning. The fluctuation in carbon supersaturation conditions during crystallization can be influenced by the addition of a carbon source to the growth system or a significant change in pressure and temperature conditions. The increase or decrease in carbon supersaturation conditions is also estimated in this study based on the observed morphological changes.

MATERIALS AND METHODS

Samples. Fourteen selected rough macle diamonds from South Africa (samples 1–14) were used in this study. The crystals ranged in weight from 0.118 to 0.747 ct, with one side length varying from 2.4 to 6.3 mm and colors spanning from colorless to light yellow and very light pink. Samples 1–10 were provided by the Department of Geology and Mineralogy at Kyoto University. Samples 11–14 were loaned by Suwa & Son, Inc. and were used only to study the external morphology.

Microscopic Observation. The external morphology and surface microtopography of these macle diamonds were examined using an Olympus SZX optical microscope equipped with a 0.8× objective lens and an Olympus BX51 differential interference contrast microscope (DICM). Photographs were taken using a Nikon DS-Ri2 camera.

Scanning Electron Microscopy–Cathodoluminescence (SEM-CL). To investigate the internal zonal structure and morphological changes during the growth process, four samples (1, 3, 6, and 10) were prepared for SEM-CL observation. These four crystals were sliced with a diamond saw (ref 1002, Bettonshop Israel Ltd.) in one direction through the center of the re-entrant corner, perpendicular to the twinning plane and parallel to a (110) plane. The cut surfaces were polished using a diamond polishing machine (Imahashi FAC-8) and carbon coated in a vacuum evaporation process. The polished surfaces were subsequently examined under a scanning electron microscope with cathodoluminescence mode (Kitamura et al., 1992; Ponahlo, 1992). The polishing and SEM-CL observation processes were repeated to achieve a surface cut through the crystal's growth center.

Measurement of Growth Band Widths. Based on the zonal structure appearance of the polished surfaces of the four samples, schematic drawings of the growth bands were carefully sketched from the CL image of each crystal; then the growth band widths of each {111} face (*r*, *n*, *s* at the left side and *r**, *n**, *s** at the right side of the twin) were measured. Because the first growth region in the core area of the twin showed a very complex zonal structure and the last growth region at the rim area showed a dissolved curved band, only the mantle region (between the rim and central core) was measured in detail in order to obtain reliable data in this study.

RESULTS

Classification of Re-Entrant Corners and External Morphology of Macle Diamonds. All the macle diamond crystals studied exhibit a flattened triangular morphology with either concave or convex

Figure 3. Representative shapes of contact-twinned flat triangular spinel (0.244–3.422 ct), heart-shaped Japan law–twinned quartz (16.212 ct), V-shaped Japan law–twinned amethyst (69.603 ct), V-shaped contact-twinned rutile (5.176 ct), swallowtail-shaped contact-twinned gypsum (314.02 ct), butterfly-shaped contact-twinned calcite (117.55 ct), and heart-shaped contact-twinned hematite (298.81 ct). Photos by Tetsuya Chikayama.

(apex) shapes at the re-entrant corners (figure 4). Among them, various forms depend on the degree of flatness and types of re-entrant corners. Except for the extremely rounded corners and edges of samples 12 and 13, the other crystals display nearly flat octahedral faces with straight, sharp corners and edges. This suggests that these crystals underwent limited dissolution, indicating that they nearly retained their original as-grown forms (again, see figure 1). Sample 14 resembles a six-pointed star, known as the "Star of David twin," which presents an intergrowth of two macle crystals oriented in opposite directions, featuring well-formed re-entrant and salient surface corners (again, see figure 1).

The morphologies of macle diamond crystals are determined by the four different shapes of the re-entrant corners (i, ii, iii, and iv). These macle morphologies are primarily characterized by growth layers generated at the twin boundaries of the re-entrant corners, and fall into four groups: I, II, III, and IV (figure 5, top).

- Group I morphology consists of nearly flat {111} surfaces and features a concave shape at the re-entrant corners (figure 5, bottom). Samples 1 and 2 (figure 4, A and B) and sample 11 (figure 1) exhibit this re-entrant corner shape (i).
- Group II morphology has a concave re-entrant corner and is defined by two {111} surfaces stacked with a few lamellae growth layers formed at the twin boundary of the re-entrant corners (shape ii). This group includes samples 3 and 4 (figure 4, C and D).
- Group III morphology is characterized by the stacking of thick growth layers formed at the twin boundary, which leads to the formation of four high-index {hhk} faces surrounding a small

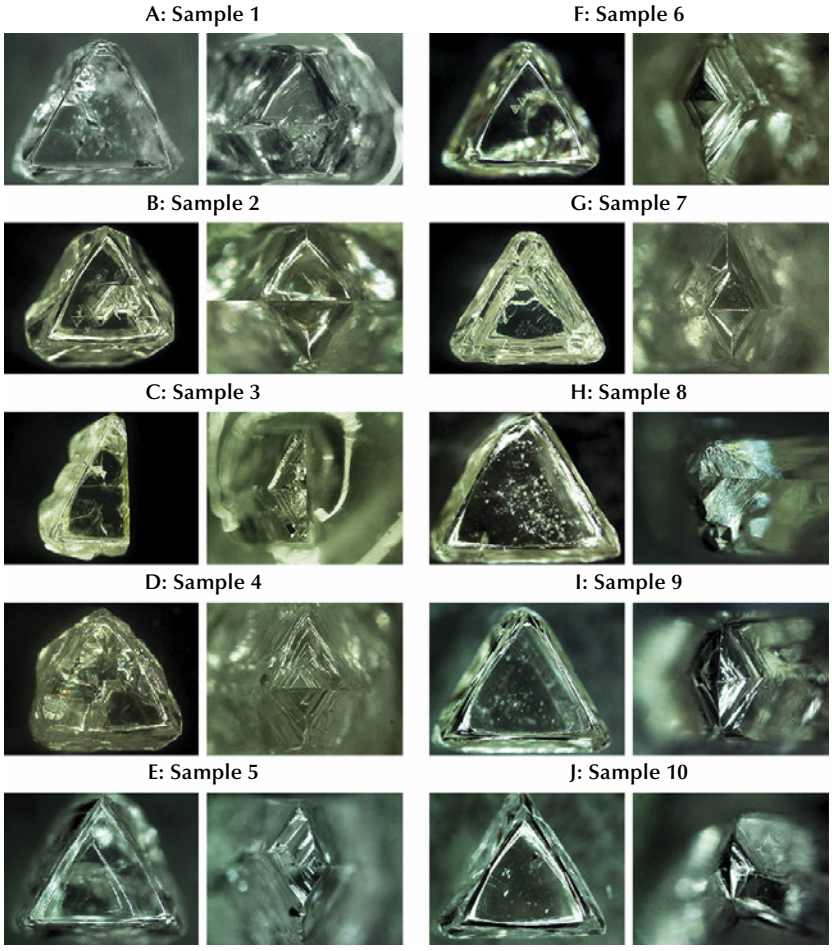

Figure 4. Outlines and distinct shapes of re-entrant corners from macle samples 1–10, with weights ranging from 0.118 to 0.185 ct, sourced from South Africa. Photos by Ahmadjan Abduriyim. Fields of view for the right images of each sample: 2.63 (A), 1.93 (B), 2.49 (C), 2.04 (D), 1.32 (E), 1.67 (F), 1.56 (G), 1.70 (H), 1.70 (I), and 2.10 (J) mm.

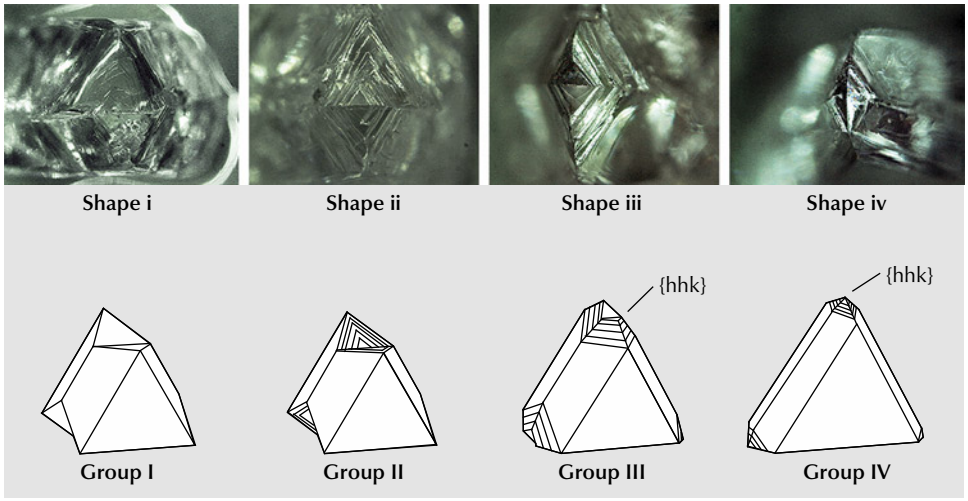

Figure 5. The four re-entrant corner shapes (i, ii, iii, and iv) and illustrations of the external morphologies (I, II, III, and IV) of macle crystals. Photomicrographs by Ahmadjan Abduriyim; fields of view 2.67 mm, 2.40 mm, 1.76 mm, and 2.22 mm, respectively.

concave re-entrant corner (shape iii). This group includes samples 5–7 (figure 4, E–G).

- Group IV morphology is marked by a convex (apex) corner formed by smooth curved surfaces or stepped surfaces, made up entirely of a stack of growth layers at the re-entrant corners (shape iv). This group comprises six crystals: samples 8–10 (figure 4, H–J) and samples 12–14 (figure 1).

External Morphology and Flatness. Samples 1 and 2 exhibit a flattened triangular form with three re-entrant corners, referred to as morphology group I (figure 4, A and B). They have relatively flat {111} faces with slightly rounded corners and edges at the re-entrant corners, along with some growth layers forming on the *s* (*s**) and *n* (*n**) faces. At a prominent corner, the growth layers on the face *s* can be seen protruding to the opposite side. The degree of flatness is 1, based on equation A-1 (see box A).

Samples 3 and 4 display nearly pointed corners and straight edges, but the *r* and *r** surfaces are covered by a few stacking lamellae growth layers at the re-entrant corners, as illustrated in morphology group II (figure 4, C and D). A few developed growth hillocks were observed on the *s* (*s**) and *n* (*n**) surfaces. The degree of flatness is 1.1.

Sample 5 has nearly pointed corners and straight edges, showcasing a flattened triangular shape with three small re-entrant corners, as seen in morphology group III (figure 4E). The growth layers on both {111} faces at the re-entrant corners extend outward from the twin boundaries. During the growth process, the re-entrant corners tend to fill with growth layers, resulting in an apex corner that features four high-index {hhk} faces. Well-developed growth layers are also present on the *s* (*s**) and *n* (*n**) surfaces. The degree of flatness is 1.4. Samples 6 and 7 also belong to the shape III group but have slightly rounded corners and edges and consist of four high-index {hhk} faces with stepped surfaces at the re-entrant corners (figure 4, F and G). Their morphology is significantly flatter than that of sample 5, and the degree of flatness for both crystals is 2.2.

Sample 8 has re-entrant corners fully covered by four high-index {hhk} faces with stepped lamellae growth layers, forming three apexes instead of re-entrant corners, resembling morphology group IV (figure 4H). At the salient corners, well-developed growth layers were observed around the twin boundary (plane). The degree of flatness is 2.4. Samples 9 and 10 also belong to the shape IV group, and the four high-index {hhk} faces exhibit a very smooth curved surface feature (figure 4, I and J). The development of growth layers around the twin boundary at the salient corner was noted. The degree of flatness for both crystals is 3.3.

These results indicate that the value of the flatness indicator (equation A-1; see box A) increases as the flatness of contact-twinned macle diamonds increases.

Surface Microtopography. The surface microtopography of octahedral faces varies significantly from crystal to crystal and even from face to face on a single crystal. The 12 octahedral {111} faces (6 faces at the re-entrant corners and 6 faces at the salient corners) of most samples exhibit mirror-smooth, uniform surfaces and sharp edges characterized by stacked triangular growth layer lamellae of progressively diminishing size. Some faces display a pronounced blocky stepped growth structure. These mirror-smooth growth layers and sharp stepped

BOX A: MEASUREMENT OF MACLE DIAMOND FLATNESS

To indicate the flatness of contact-twinned crystals, the ratio of the sum of the height of a triangular octahedral face (h) and the height of an edge of the apex corner (h') to the thickness (d) of the crystal is defined as the flatness indicator (f) of external morphology (as illustrated in figure A-1):

$$f = \frac{(h+h')}{d} \qquad \text{(A-1)}$$

When two regular octahedral crystals contact each other, the calculated degree of flatness is $3\sqrt{2}/8$. In contrast to this ideal morphology, the heights of the n face (h), the edge of the apex corner (h'), and the thickness (d) of samples 1–10 were measured. (Note: Samples 11–14 were not measured for their flatness.)

*Figure A-1. Macle crystals with ideal morphology illustrating how to measure the flatness of the contact-twinned crystals. The flatness indicator variables (*h, h', l, d*), and the* θ *and* α *angles are labeled, where* h *is the height of the triangular octahedral face;* h' *is the height of the apex corner edge;* l *is the length of the apex corner edge;* d *is macle thickness;* θ *is the internal angle between the twin plane and face* r*; and* α *is the internal angle between the re-entrant corner edge and face* n*.*

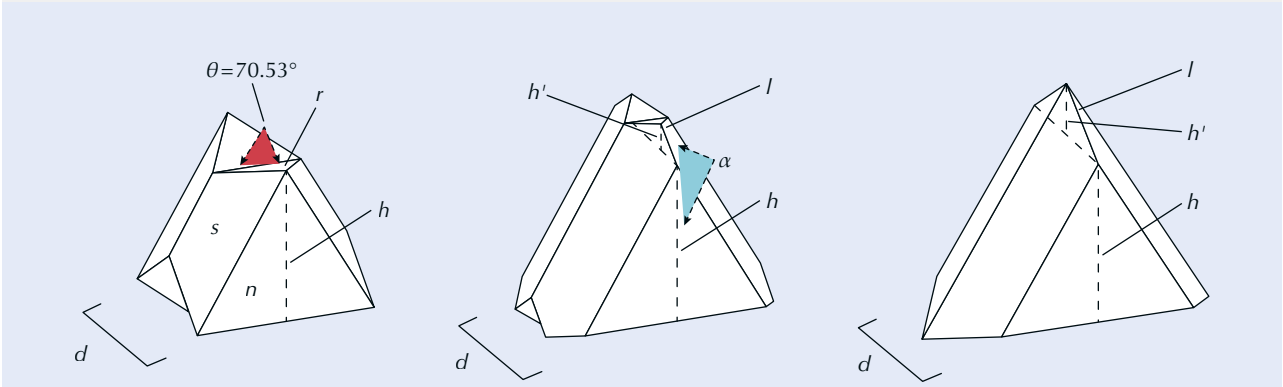

growth structures retain nearly all original as-grown features. The corners and edges of a few samples exhibit slightly rounded forms, with curved faces and deep etch pits known as trigons on their surfaces, indicating that these crystals underwent mild dissolution. Based on the analysis of microtopography, the characteristic morphologies of growth layers on the octahedral faces can be categorized into two types, depending on the generation of growth layers around twin boundaries or on the surfaces of the octahedral faces. The first type consists of spiral-stepped stacked lamellae growth layers that develop at the center of small r faces and large n faces, alongside polycentric stacked lamellae growth layers on the trapezoid-shaped s faces (figure 6). The second type involves the formation of single large mirror-smooth growth layers on the large n faces, stacked lamellae growth layers on the small r faces around the twin boundary of the re-entrant corners, and several thick stepped block growth layers on the trapezoid-shaped s faces near the twin boundary of the salient corners (figure 7). As a result of the observations of the microtopography surface structure, the surfaces r and r^* at the three re-entrant corners and the surfaces s and s^* at the three salient corners of the morphology group I and II macle crystals demonstrate very smooth, flat growth layers. Compared to morphology groups I and II, group III reveals two types of growth layer structures: one involves thick lamellae growth layers developing or originating from the twin boundary at the re-entrant and salient corners, while the other features spiral-stepped growth layers forming at the center of r and r^* and s and s^* surfaces. In morphology group IV, the growth layer structure of faces r and r^* at the re-entrant corner is unobservable, as it has been replaced by an apex corner, with very thick blocky lamellae layers emerging from the twin boundary at the salient corner being predominant.

Distribution of Trigons. The octahedral faces almost invariably display triangular depressions (trigons) that are oriented opposite the triangles of the octahedral faces. These trigons arise from dissolution (Frank et al., 1958), primarily at dislocation outcrops

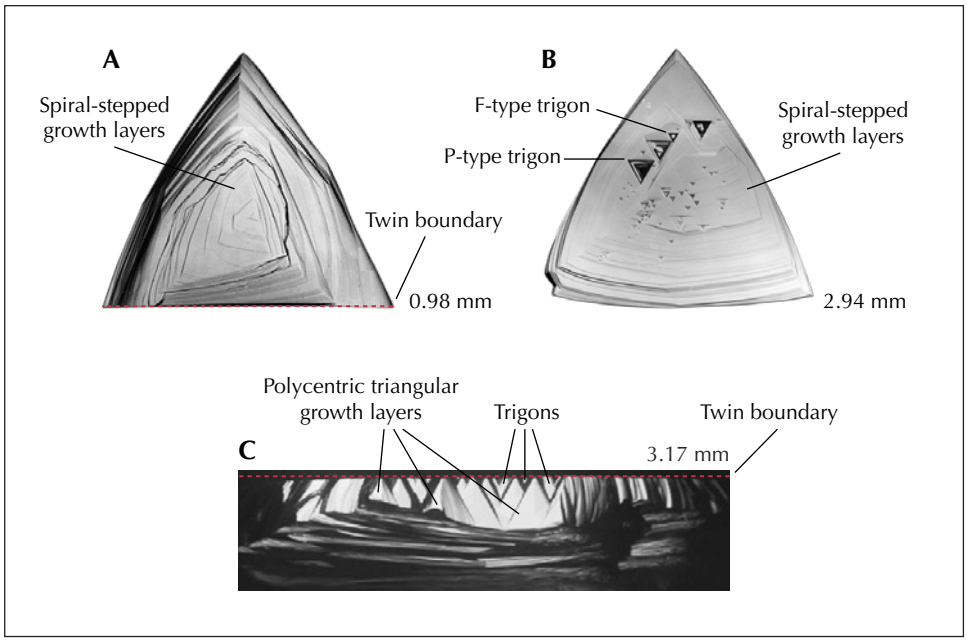

Figure 6. A: The micro-surface structure of a contact-twinned macle diamond features well-developed stacked triangular spiral-stepped laminae growth layers on an r *face. B: The spiral-stepped (shield-shaped) laminae growth layers are generated on face* n*. The features of the P-type (pointed bottom) trigon and F-type (flat bottom) trigon are preserved on this surface. C: Face* s *displays a distinct poly-centric development of small triangular stacked growth layers. Photos by Ahmadjan Abduriyim.*

(Lang, 1964). There is a one-to-one correlation between screw-type dislocation outcrops and the centers of growth layers (Sunagawa et al., 1984). This shows that natural diamonds' stacked lamellae growth layers develop through a spiral growth mechanism under low supersaturation conditions. Consequently, the well-defined growth layers on the octahedral faces or twin boundaries are affected by the density of screw dislocations protruding from the surfaces.

Trigons were noted on most octahedral faces and twin boundaries, although this does not necessarily mean that all octahedral faces have trigons. The number of trigons on a single face varies between crystals and from face to face. The two primary types of trigons are pointed-bottomed (P-type) and flat-bottomed (F-type).

Trigon density was assessed on all octahedral faces and at the twin boundaries of samples 1 (morphology group I), 3 (morphology group II),

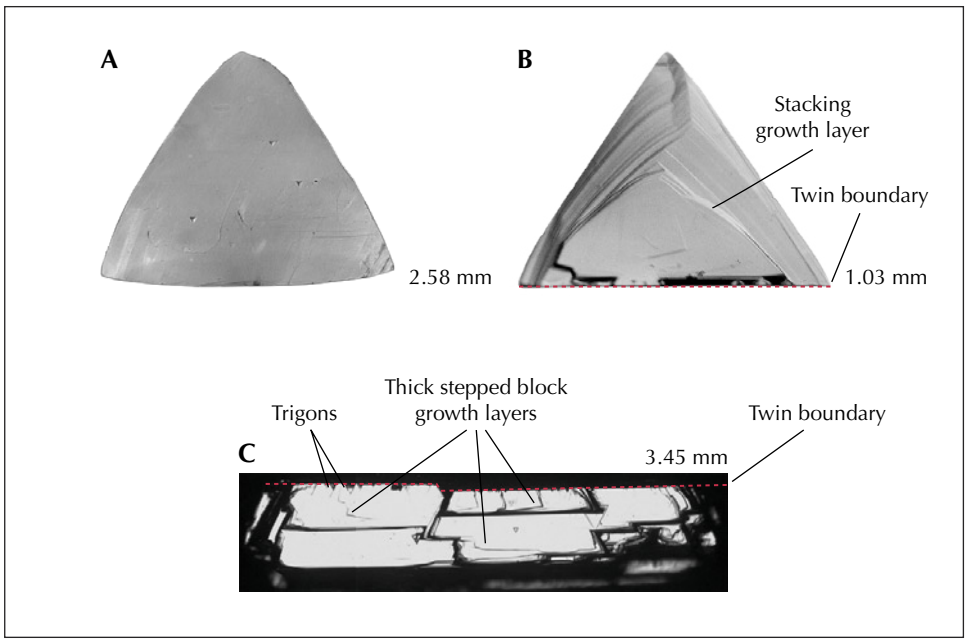

Figure 7. A: The micro-surface structure of face n *is characterized by a featureless (or mirror-like) surface. B: Triangular stacking lamellae growth layers on face* r *originated from the twin boundary at the re-entrant corner. C: Thick stepped block growth layers originated from the twin boundary at the salient corner. Photos by Ahmadjan Abduriyim.*

6 (morphology group III), and 10 (morphology group IV). The number of trigons on one face differs from locality to locality within a face and from face to face. The number of trigons observed on the surfaces and at the twin boundaries of each group, along with the density of trigons per unit area (number/mm^2), is illustrated in figure 8.

The data from samples 1 to 10 clearly reveal an increase in the number and density of trigons at the *s* and *s** face of salient corners and the twin boundaries. Sample 1 exhibits a higher density of trigons at the *r* and *r** surface and twin boundaries than at the *s* and *s** surface. The trigon density at each face of re-entrant and salient corners and twin boundaries shows an increasing trend from samples 4 to 6. For sample 10, we could not account for the trigons at the re-entrant corners due to coverage by high-index {hhk} faces. The density of trigons at the *s* and *s** faces gradually increases from samples 1 to 10, with the highest density noted at the *n* and *n** faces.

For morphology group I, surface microtopographical features such as growth layers and trigons do not significantly appear on salient corners; therefore, a highly flattened morphology cannot be anticipated. In contrast, the macle diamonds in morphology group IV demonstrate a markedly higher density than those in the other groups. This suggests that preferential growth can be expected from the screw dislocations on such surfaces, and the flatness is much more pronounced.

Internal Zonal Structure and Morphological Changes of Macle Diamonds During Growth. Natural diamonds are known to exhibit a well-defined zonal structure during their crystallization process. This growth zoning provides significant insights into the morphological changes in crystals, revealing their growth history. Several studies have clarified contact-twinned diamond crystals' internal structure and growth history (Kitamura, 1990; Yacoot et al., 1998; Abduriyim and Kitamura, 2002). The following subsections individually describe the zonal structures of four crystals from four morphology groups defined in this paper.

Observation of Internal Zonal Structure. Mosaic photographs of CL images show two successive polished surfaces sliced on the (110) plane of sample 1. One of the sliced planes is believed to be the center of the macle crystal, as illustrated in figure 9A, with a detailed schematic drawing based on the zonal structure observed in the CL image. This zonal structure features oscillatory zones characterized by alternating light and dark growth bands.

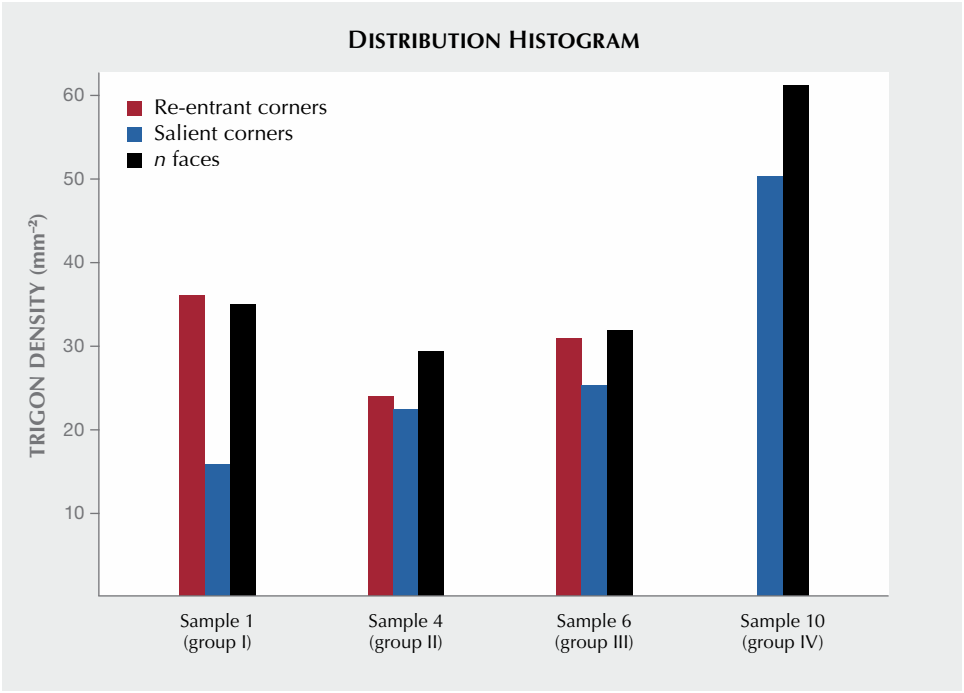

Figure 8. This distribution histogram shows the density (number/mm^2) of trigons found on faces n *and* n* *in re-entrant corners and in salient corners of samples 1, 4, 6, and 10 from morphology groups I, II, III, and IV, respectively.*

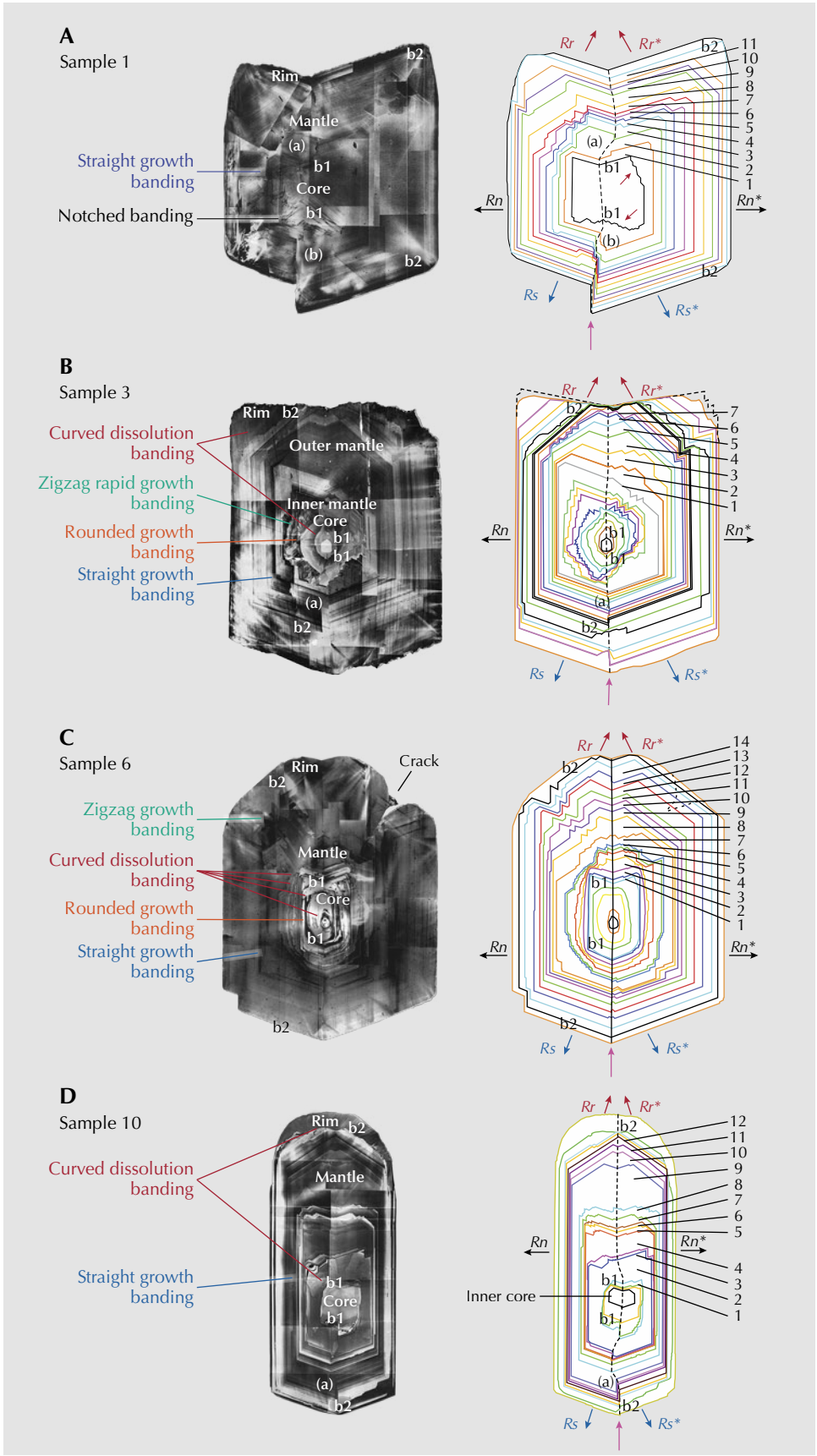

Figure 9. Left: CL images of a plane cutting through the center of samples 1 (A), 3 (B), 6 (C), and 10 (D) reveal a zonal growth structure. The growth stages are divided into three regions, where the growth bands exhibit rounded characteristics that are interrupted by a dissolution process during the growth period. The boundaries are labeled "b1" between the core and mantle and "b2" between the mantle and rim. Right: Illustrations of the growth banding corresponding to the zonal structure. An arrow indicates the direction of the normal growth rate on each face.

According to the CL image of the sliced plane, the crystal displays twinning from its initial growth stage. The entire growth stage can be divided into three zones: core, mantle, and rim, separated by the discordant bands b1 and b2.

In the core zone, a contact twin forms a re-entrant corner with an angle of 141° between the two smooth growth bands of the *r* and *r** {111} faces. However, at the salient corner, the growth bands are marked by zigzag banding (as indicated by the red arrows in figure 9A, right), and some areas of the core may have cracked and broken away during the initial growth stage.

In the mantle zone, the zoning exhibits the typical shape of contact-twinned crystals bounded by {111} faces, creating perfect re-entrant corners. The growth bands of face *r** (as shown in figure 9A, labeled "a" in the illustration) grew larger than those of face *r*, causing the twin boundary to lean to the right. As a result, both faces *r* and *r** became thicker than the other faces, transforming the re-entrant corner from shape i to shape iii. This morphology consists of high-index {hhk} faces with stepped growth layers surrounding a small re-entrant corner at the top, ultimately ending in a thicker, flattened triangular form with the re-entrant corner reverting to shape i. At the salient corner, face *s** (figure 9A, right, labeled "b") grew larger than face *s*, leading to the right crystal being larger and protruding farther than the left. Based on microscopic observations, a significant number of trigons originate at the stacked lamellae growth layers on the *s** surface, indicating preferential spiral growth facilitated by these cooperative screw dislocations on the *s** surface.

In the rim zone (where the border between the mantle and rim is labeled "b2"), the edge of each corner of the {111} face displays a slightly rounded band but develops a perfect concave re-entrant corner resembling shape i. This macle crystal underwent a low degree of dissolution in the final stage.

Sample 3 was sliced into four planes, and the CL image of the center plane is displayed in figure 9B. In the core zone, labeled "b1," the small core shows a high CL intensity, presenting a smooth rounded surface with an apex corner instead of a concave re-entrant corner. This rounded apex corner can be understood as having formed through a dissolution process following the completion of growth on the re-entrant corners during the initial growth stage of this contact-twinned macle crystal. The mantle zone is further divided into two parts; the inner mantle part exhibits a highly complex zonal structure. Several curved growth layers cover the core zone and extend outward in succession. Following this stage, distinct zigzag-shaped step zonings appear, indicating that anti-skeletal faces develop under conditions of high carbon supersaturation. The crystal shows a flattened morphology in the outer mantle with clearly defined straight zoning lines. Faces *r* and *r** in the re-entrant corner grew faster than the other faces (*n* and *n** and *s* and *s**), resulting in the transformation of the re-entrant corner from shape i to shape iv and the formation of a perfect apex corner bounded by {111} faces during the growth stage. In the salient corner, faces *s* and *s** grew in competition, with face *s* (figure 9B, labeled "a") growing larger than face *s** and protruding slightly. A dissolution texture was again noted between the outer mantle and rim (labeled "b2"). In the rim zone, the crystal gradually formed a re-entrant corner once more, covered by several zonings of the {111} face under relatively high carbon supersaturation conditions. In the salient corner, face *s** grew larger, ultimately becoming equal to the growth layer of face *s*. The protrusion of the growth bands did not occur in the final growth stage.

Sample 6 was sliced into three planes, and the CL image of the central plane of the crystal is shown in figure 9C. The core zone displays several rounded growth band morphologies, with the curved surfaces resulting from multiple dissolution processes during the early stages of crystallization. The crystal began twinning from the initial growth stage, with the twin boundary running through the center of all zones. In the mantle, thin stepped lamellae growth layers developed on the curved {111} faces and transitioned from a rounded shape to a flattened morphology with a re-entrant corner. Subsequently, faces *r* and *r** at the re-entrant corners grew faster than the other faces, transforming the re-entrant corner into an apex corner, which was nearly covered by zigzag and stepped {111} *r** faces, along with a very smooth {111} *r* face. However, a small concave re-entrant corner remains at the top until the latest growth stage. Faces *s* and *s** grew almost equally on the salient corner side. In the rim zone, each corner displays a slightly rounded habit, but the plane surface of each {111} face shows no curved structure, indicating that this macle crystal underwent a low degree of dissolution. A crack was observed on the right side of the crystal.

Sample 10 was sliced and polished multiple times into six planes. The CL image of the central plane and a schematic drawing are shown in figure 9D. The core zone displays a bright CL image, with the inner

part characterized by a morphology defined by smooth {111} faces featuring a re-entrant corner (red arrows). In the mantle zone, the crystal exhibits the most flattened morphology with distinct growth bands. Faces *r* and *r** in the re-entrant corner developed more rapidly than the other faces, gradually transforming the re-entrant corner from shape i to shape iv. On the salient corner side, faces *s* and *s** grew in competition, with the growth layers of face *s** in the right domain developing faster and larger than those in the left, causing a shift of the twin plane to the left side and an outward protrusion of the growth bands. During the later growth stage of the mantle zone, preferential growth occurred at face *s*, which developed faster and larger than face *s**. As a result, the twin boundary tilted to the right side. The twin boundary plane that spans the entire crystal is not straight but features a downwardly curved twin plane. In the rim zone is a very flattened and elongated twin crystal with a slightly rounded apex corner, bounded by curved {111} faces that have been somewhat altered by dissolution action. Comparing the four crystals from the four groups, sample 10 is significantly flatter than the other crystals.

Morphological Variation. Because the core and rim exhibit a complex zonal structure that prevents reliable data acquisition, only four samples' mantle zones were studied in detail. The width of growth banding from each face in the mantle zone was measured using the CL image, and the value was adjusted according to the actual size of sample 1 (table 1). The ratios *Rr*/*Rn* (the growth rate of face *r* versus the growth rate of face *n*) and *Rs*/*Rn* (the growth rate of face *s* versus the growth rate of face *n*) of the mantle zone in each twin were estimated by measuring the growth band widths (box B).

The growth rate ratio data (*Rr*/*Rn* and *Rs*/*Rn*) were collected from growth bands 1 to 11 in the mantle zone of sample 1 and are plotted in figure 10A. A small red circle marks the left side of the macle crystal, while a blue circle represents the right side. The arrow's direction indicates the plot sequence from bands 1 to 11.

Most of the data is plotted within the range between *Rr*/*Rs* = 1 and 2. The ratios display a slightly different trend in both single crystals. The ratios (*Rr*/*Rn* and *Rs*/*Rn*) gradually increase to the area where *Rr*/*Rs* > 1 from the initial data plot, indicating that the preferential growth at the re-entrant corner is slightly faster than the growth at the salient corner, resulting in a large re-entrant corner. Then both ratios decrease to a level close to the lower range of *Rr*/*Rn* < 0.5 and *Rs*/*Rn* < 0.5. The last few plotted points show that the ratios increase briefly and then stabilize near the region where *Rr*/*Rn* = 1 and *Rs*/*Rn* = 1.

TABLE 1. Width of growth banding (in μm) from each face in the mantle zone from sample 1.

	r	*r**	*n*	*n**	*s*	*s**	*Rr*/*Rn*	*Rr**/*Rn**	*Rs*/*Rn*	*Rs**/*Rn**
Band 1	43.15	69.58	49.65	88.95	41.47	79.02	0.8690	0.7822	0.8352	0.8883
Band 2	215.60	94.48	57.13	74.27	61.75	78.74	4.4039	1.2721	1.0807	1.0602
Band 3	57.06	93.22	41.96	38.39	34.97	57.13	1.3600	2.4281	0.8333	1.4881
Band 4	31.61	45.17	35.31	57.76	24.27	34.06	0.8950	0.7821	0.6871	0.5896
Band 5	22.45	37.34	30.91	108.50	27.97	32.59	0.7262	0.4430	0.9050	0.3004
Band 6	29.93	29.93	35.03	63.57	34.97	31.40	0.8543	0.4708	0.9980	0.4939
Band 7	64.62	64.62	39.44	90.14	44.41	47.62	1.6383	0.7168	1.1259	0.5283
Band 8	87.55	102.70	50.63	92.24	76.43	62.24	1.7293	1.1130	1.5096	0.6747
Band 9	50.84	50.84	30.56	48.25	32.66	48.25	1.6636	1.0536	1.0686	1.0000
Band 10	34.69	34.69	38.32	35.59	31.82	35.80	0.9051	0.9745	0.8303	1.0059
Band 11	40.83	40.87	31.54	32.03	36.36	36.22	1.2945	1.2759	1.1530	1.1310

BOX B: ESTIMATION OF GROWTH RATE RATIO BY MEASURING THE GROWTH BAND

A natural crystal is bound by a set of flat faces that relate to one another through symmetry. The forms that crystals take result from the conditions under which they grow. The same crystal may exhibit different morphologies depending on the growth rates in different crystallographic directions throughout the growth process (figure B-1). Fluctuations in growth rates are recorded as variations in perfection and homogeneity, such as growth sectors and growth banding. Additionally, the ratio of growth rates at any given time cannot be directly estimated from the crystal's external form. Therefore, linear growth rates can be inferred by measuring the widths of growth bands that appear as alternating light and dark bands in the zonal structure of the crystal using this simplified model:

$$\textit{width of growth band} = [\textit{growth rate}] \times [\textit{time}] \qquad \text{(B-1)}$$

The growth rate ratio from different growth faces that belong to the same isochronous face can be expressed as follows, where *R1* = growth rate 1 and *R2* = growth rate 2:

$$\frac{\textit{width of growth band 1}}{\textit{width of growth band 2}} = \frac{(R1) \times \textit{time}}{(R2) \times \textit{time}} = (R1/R2) \qquad \text{(B-2)}$$

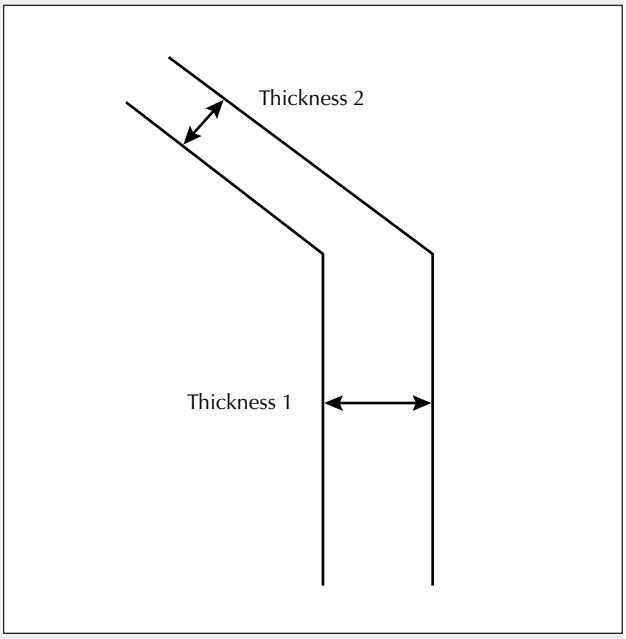

Figure B-1. Illustration of two growth bands showing varying thicknesses on different surfaces belonging to one growth phase.

In sample 3, the core, inner mantle, and rim zones display curved dissolution banding and a complex zigzag zonal structure, enabling the measurement of growth band widths from 1 to 7 in the outer mantle area. The ratios from bands 1 to 5 were plotted within the field of $Rr/Rs > 2$, while the ratios of bands 6 and 7 were plotted in the range between $Rr/Rs = 2$ and $Rr/Rs = 1$ in figure 10B. The left side of the macle crystal is marked with a red circle, while the right is labeled with a blue circle. The ratios for both sides of the twin exhibit a similar trend. The ratios (*Rr*/*Rn* and *Rr**/*Rn**) initially rise significantly to the range where $Rr \geqq 2Rs$, where the growth rates (*Rr* and *Rr**) at the re-entrant corner are prominent, causing the re-entrant corner to transform into an apex corner, which is bounded only by {111} faces during the growth process.

The ratios then decrease repeatedly to the lower range of $Rr/Rs < 2$, where the effects at both the re-entrant and salient corners were not anticipated. These trends suggest that carbon supersaturation diminished at the beginning of crystal growth in the initial stage of this outer mantle zone, with the re-entrant corner effect playing a significant role in forming an apex corner and shaping the twin into a flattened form. During the latter half of the growth stage of the mantle zone, carbon supersaturation increased significantly, leading to growth on every face of the crystal, with two-dimensional nucleation preferentially occurring near the crystal's edges to create a large surface of *n*, *s*, and *r*, thus recreating a re-entrant corner similar to shape ii.

Figure 10C plots the 14 data points of band width from bands 1 to 14 in the mantle zone of sample 6. Most data points are plotted in the range where $Rr/Rn > 1$ and $Rs/Rn > 1$. The ratios in both sides of the twin show a consistent trend. The ratios first increase to the range where $Rr > 2Rs$, indicating a tendency for the re-entrant corner to transition into an apex corner due to preferential growth at the re-entrant corner under relatively low carbon supersaturation conditions. Simultaneously, the ratio of *Rs*/*Rn* also shows a high value of 1.6, suggesting that the preferential growth at the salient corner is expected to produce a unidirectionally flattened shape. Subsequently, both ratios (*Rr*/*Rn* and *Rs*/*Rn*) decline rapidly to the range where $Rr/Rn < 1$ and $Rs/Rn < 1$ from bands 3 to 5, where the effects of the re-entrant and salient corners were not anticipated. The ratios from bands 6 to 8 display a similar pattern,

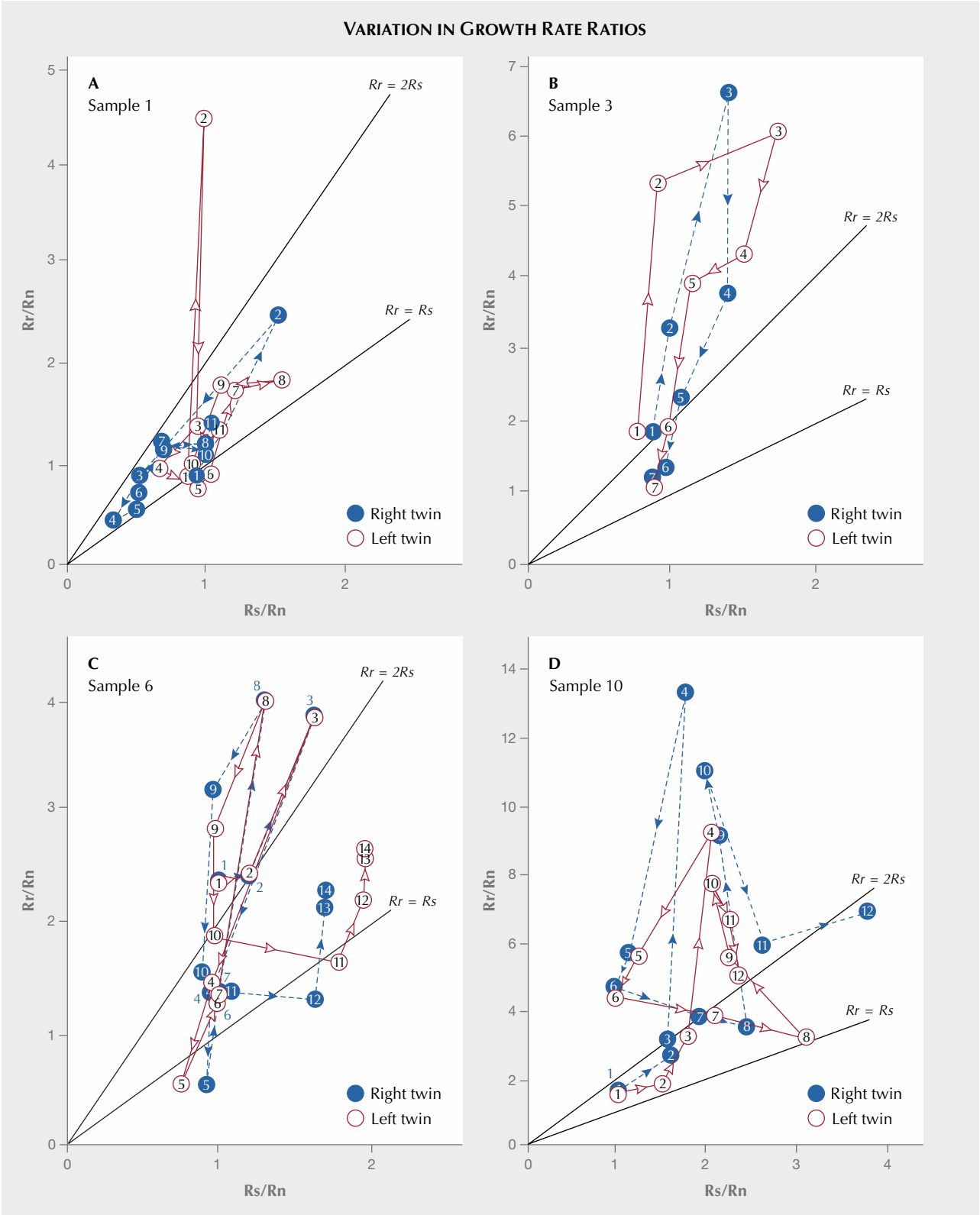

Figure 10. The ratios Rr/Rn *and* Rs/Rn*, indicated by red circles, are calculated based on the growth banding observed in the left twin of samples 1, 3, 6, and 10. Meanwhile, the growth rate ratios* Rr*/Rn* *and* Rs*/Rn*, represented by solid blue circles, are derived from the growth banding in the right twin. The lines for* Rr = Rs *(or* Rr/Rs = *1) and* Rr = 2Rs *(or* Rr/Rs = *2) are also displayed.*

increasing again to the range of $Rr > 2Rs$ and reaching a peak value of $Rr/Rn = 4$, resulting in the re-entrant corner becoming almost concealed by stacking growth layers on the {111} faces over time. However, the ratios from bands 9 to 10 quickly decreased to the range between $Rr/Rs = 1$ and 2, and the ratios (Rs/Rn) from bands 11 and 12 for both twins showed a significant change from values of unity (1) to 1.97 and 1.63, respectively, dropping below the $Rr < Rs$ line, where preferential growth on the salient corner became dominant, forming thick growth banding that enhanced the flatness of the twin. In the final stage of the mantle zone, the ratios Rr/Rn and Rs/Rn from bands 13 and 14 increased again.

The data for the Rr/Rn and Rs/Rn ratios from bands 1 to 12 in the mantle zone of sample 10 are plotted in figure 10D. Most of the data fall within the range where $Rr/Rn > 1$ and $Rs/Rn > 1$. The ratios from bands 1 to 4 initially increased to the range of $Rr \geqq 2Rs$, with anticipated effects from both the re-entrant and salient corners. The ratio of Rr/Rn reaches its peak of 13, marking the transition from the re-entrant corner to the apex corner. Conversely, the expected preferential growth at the salient corner led to face s^* growing thicker and larger than face s, causing the twin boundary to shift to the left side. Subsequently, both ratios decreased to Rr/Rn of 4.3 and Rs/Rn of 1. At this juncture, the preferential growth at the re-entrant corner gradually weakened, while the growth at the salient corner was entirely unexpected. Following this growth stage, the ratio of Rs/Rn (from bands 7 to 8) shows a significant rise, and the anticipated preferential growth at the salient corner is expected to create thick growth bands (layers) on faces s and s^*. Consequently, the morphology of this macle crystal is noticeably flatter than that of macle crystals from other groups. In the final stage of the mantle zone, the Rr/Rn ratio (bands 9 to 10) increased again. The {111} face completely covers the re-entrant corner, showcasing a perfect apex corner and corresponding to the shape iv form of a re-entrant corner. However, the Rr/Rn ratio (bands 11 to 10) decreased rapidly, while the Rs/Rn ratio continued to trend upward, indicating a preference for growth at the salient corner, forming a highly elongated macle crystal.

DISCUSSION

Establishing a Model of Morphological Variation for Contact Twins. When a twinned crystal forms in its initial stage and the normal growth rates of the r, s, and n faces—designated Rr, Rs, and Rn—remain consistent throughout the growth process, a morphological variation model is geometrically represented by two ratios: Rr/Rn and Rs/Rn (figure 11). When all octahedral faces exhibit identical growth rates ($Rr/Rn = 1$, $Rs/Rn = 1$; see figure 11), the morphology features both re-entrant and salient corners, appearing flatter than those formed by two regular octahedra ($Rr/Rn = 0.5$, $Rs/Rn = 0.75$; see figure 12).

An increase in the ratios Rr/Rn or Rs/Rn indicates preferential growth at re-entrant corners or salient corners, respectively. A rise in both ratios leads to a flatter morphology. Previous studies have not explored preferential growth at salient corners (Rs/Rn) in contact-twinned macle diamonds (Becke, 1911; Chudoba, 1927; Stranski, 1949; Hartman, 1956, Sunagawa, 1975; Sunagawa et al., 1979; Sunagawa and Yasuda, 1983; Sunagawa and Lu, 1987). In the range where $Rr \geq 2Rs$, re-entrant corners disappear and transform into apexes covered by neighboring s and s^* faces. In this case, morphology is influenced solely by the ratio of Rs/Rn. When Rr is less than $2Rs$, re-entrant corners begin to appear. The overall shape can display various morphologies depending on the ratio of Rr/Rs. These include shapes with small re-entrant corners at the apexes, well-developed re-entrant corners, and re-entrant corners formed by trapezoidal faces. When $Rr = Rs$ ($Rr/Rs = 1$), the formation of re-entrant corners and salient corners is equal.

Relationship Between the Ratio of Growth Rate and External Morphology. We proposed the following equations to connect the growth rate ratio with the flatness of the external morphology of the macle crystals:

$$\frac{Rr}{Rn} = \frac{4}{3}\frac{h}{d}\sin\theta - \cos\theta + \frac{2l}{d}\sin\alpha \quad (1)$$

$$\frac{Rs}{Rn} = \frac{2}{3}\frac{h}{d}\sin\theta + \cos\theta + \frac{2l}{d}\sin\alpha \quad (2)$$

where h is the height of face n, d is the thickness of the crystal, l is the length of the edge at the re-entrant corner, θ is the interfacial angle between face n and face r, and α is the interfacial angle between the edge of the re-entrant corner and face n (again, see these flatness indicators in box A, figure A-1). The ratios Rr/Rn and Rs/Rn of the 10 studied crystals from the four morphology groups were estimated based on the flatness of their external morphology. They are plotted in figure 12 and labeled with diamond markers in different colors for each group of crystals.

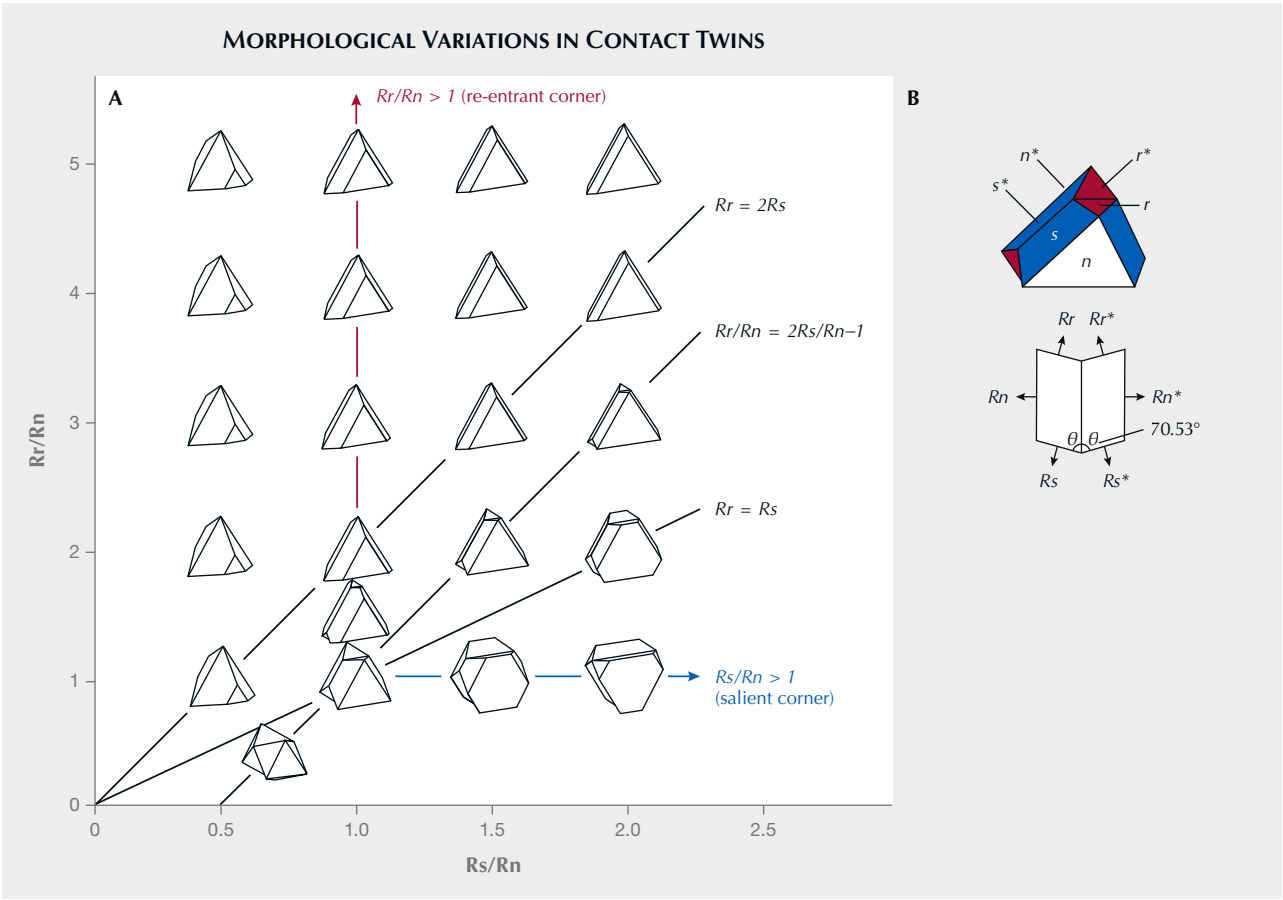

Figure 11. A: Schematic illustration of the model of morphological variations in contact twins caused by changes in the ratios Rr/Rn *and* Rs/Rn. *The lines for* Rr = Rs *(or* Rr/Rs = *1),* Rr = 2Rs *(or* Rr/Rs = *2), and* Rr/Rn = 2Rs/Rn–1 *are also shown. The re-entrant effect is expected if* Rr/Rn > *1. Additionally, if* Rs/Rn *exceeds 1, the salient corner effect can be anticipated. B: Illustration of a contact twin. Three types of {111} faces (*r *and* r*, s *and* s*, *and* n *and* n**) along with the normal growth rate of each face (left side of twin:* Rr, Rn, Rs*; right side of twin:* Rr*, Rn*, Rs**) are labeled.*

The macle crystals with shape i and shape ii re-entrant corners show morphologies indicating minimal or no preferential growth at re-entrant and salient corners, with growth morphologies expected to form within the $1 \leq Rr/Rs < 2$ range. Morphology groups III and IV are plotted close to or within the range of line *Rr = 2Rs*. The morphologies of the contact twins feature apex corners but may or may not have re-entrant corners. This aligns with the expectation that preferential growth occurs at both re-entrant and salient corners. The apex corners of morphology group IV discussed here are not covered by flat {111} faces but by high-index {hhk} stepped lamellae faces instead (again, see figure 4, H–J). Group III crystals, characterized by small re-entrant corners, clearly show the stacking of thick growth layers formed at the twin boundary (again, see figure 4, E–G). This suggests that the formation of the high-index faces likely occurs under conditions similar to those required for apex formation by neighboring {111} faces. However, the stacking of these growth layers may result from impurity trapping. Samples 9 and 10 exhibit slightly curved apex corners and underwent low levels of dissolution after completing their growth.

As observed in figure 12, the preferential growth at salient corners does not dominate the growth at re-entrant corners. Nevertheless, it clearly influences the growth of morphology. Two main effects can be considered in this context. The first effect relates to the diffusion fields surrounding the crystals. Salient corners protrude more than the *n* and *n** faces, resulting in higher carbon supersaturation conditions at these corners. Despite this, the preferential growth at salient corners is significantly linked to the re-entrant corner effect, suggesting that the preferential growth of the *s* and *s** faces is primarily controlled by surface kinetics. Therefore, the impact of diffusion fields on

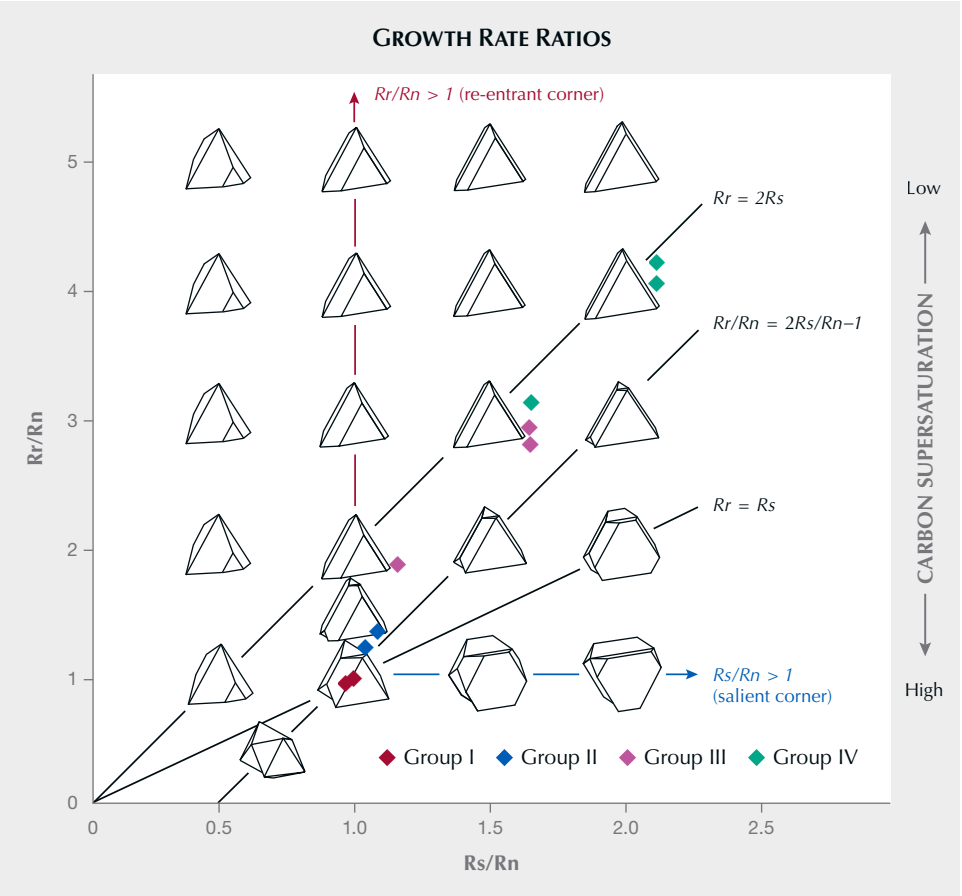

Figure 12. The growth rate ratios of 10 macle crystals from four morphology groups are estimated based on the flatness of their external morphologies. A macle crystal's flatness is strongly related to preferential growth at the re-entrant and salient corners. The relationship between carbon supersaturation and the effects of the re-entrant and salient corners is presented.

preferential growth may be relatively minor. The second effect involves the role of screw dislocations at the twin boundary. When screw dislocations at the twin boundary of salient corners are more abundant than those in the *n* and *n** faces, preferential growth can be expected at the twin boundary, similar to the pseudo re-entrant corner effect (Kitamura et al., 1979). Based on microtopographical surface observations, the surfaces at re-entrant and salient corners in morphology group I and II crystals exhibit predominantly flat growth layers. In contrast, well-defined growth layers extending two-dimensionally outward from the twin boundary of the re-entrant and salient corners were observed in group III and IV crystals. The density and number of trigons at salient corners are more pronounced than in the morphology I and II groups. This indicates that preferential growth at salient corners is primarily driven by screw dislocations generated at the twin boundary. Consequently, groups III and IV exhibit greater morphology flatness than groups I and II.

The Carbon Supersaturation Condition. Under conditions of high carbon supersaturation, growth particles can easily form two-dimensional nuclei across the surface before settling on the most energetically favorable sites. This occurs because the likelihood of growth particles reaching the growing surface significantly increases due to the high carbon supersaturation. Consequently, all sites appear to have a similar capacity to adsorb growth particles, leading to two-dimensional nucleation occurring almost universally on the surface. Considering the Berg effect (Berg, 1938), two-dimensional nucleation is more likely to occur near the crystal's edges. As a result, the re-entrant corner effect is not expected to function at all under conditions of high carbon supersaturation.

Conversely, the normal growth rate of a crystal face is influenced by the number of cooperative screw dislocations. Spiral growth preferentially occurs at energetically favorable sites, but this occurs under low, rather than high, carbon supersaturation conditions (Burton et al., 1949; Hartman, 1956). Thus, the re-entrant and salient corner effects can be anticipated only under relatively low carbon supersaturation conditions. The ratio *Rr*/*Rn* indicates changes in carbon supersaturation during crystal

growth (Kitamura et al., 1979). An increasing value of *Rr*/*Rn* signifies a decrease in carbon supersaturation. In contrast, when *Rr* is less than *Rn*, it indicates increased carbon supersaturation. In this study, the values of *Rr*/*Rn* and *Rs*/*Rn* illustrate the relative differences in growth conditions of four crystals, as shown in figure 13.

It can be inferred that sample 1 formed under conditions of higher carbon supersaturation compared to the other crystals, while sample 10 formed under the lowest carbon supersaturation conditions. Additionally, samples 1 and 3 show a trend of increasing carbon supersaturation during the final stages of growth. Samples 6 and 10 show a decreasing trend in the later stages of growth. As mentioned earlier, we suggest that the carbon supersaturation in the four types of crystals decreased and then increased repeatedly during the growth stage of their mantle zones. In natural crystallization, crystal growth is expected to reduce carbon supersaturation in a closed system, assuming there are no external influences from environmental conditions such as pressure, temperature, or external fluids. Consequently, our data on the varying growth rates indicate that carbon supersaturation does not change in a simple, consistent manner as traditionally believed; rather, it can fluctuate during the growth process. Therefore, introducing additional carbon into the growth environment or significantly changing pressure and temperature conditions may explain the observed increases in carbon supersaturation during certain growth stages of the specimens we studied.

Figure 13. Diagram illustrating the estimated changes in carbon supersaturation during the crystal growth of contact-twinned macle diamonds. It emphasizes the relationship between carbon supersaturation and growth rate (growth band) in the crystal's mantle zones, particularly focusing on the preferential growth effect at the re-entrant corner. Four macle crystals—samples 1 (group I), 3 (group II), 6 (group III), and 10 (group IV)—show distinct fluctuations in carbon supersaturation throughout their growth period. The horizontal axis represents the distance from the first to the last growth banding in the crystal's mantle zone.

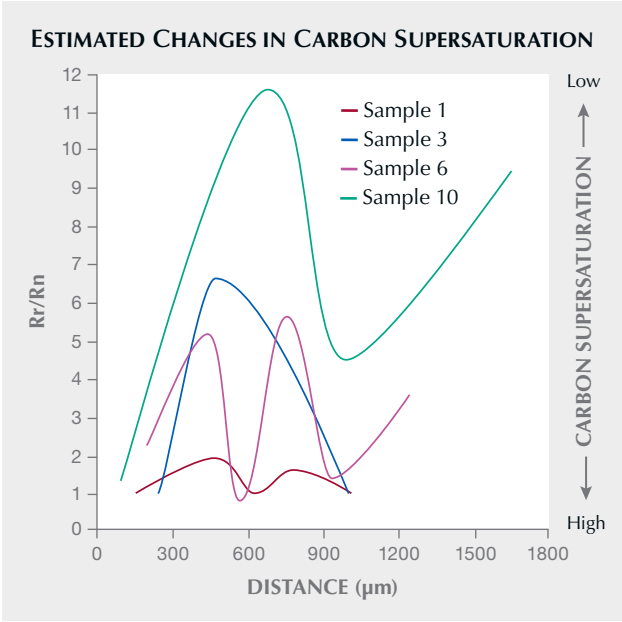

CONCLUSIONS

Based on observations of external morphology, surface microtopography, and internal zonal structure of contact-twinned natural macle diamonds, their re-entrant corners can be classified into four distinct shapes (i, ii, iii, and iv) determined by modifications from growth layers. Morphology groups I and II have been previously identified and are characterized by either very flat {111} surfaces or a few thicker growth layers at the re-entrant corners. However, this study reports morphology groups III and IV (figure 14) for the first time. Groups III and IV are distinguished by the accumulation of thick growth layers at the twin boundaries of the re-entrant corners, leading to the formation of four high-index {hhk} faces surrounding a small re-entrant corner or being completely covered by smooth or stepped {hhk} surfaces, rather than exhibiting a re-entrant corner. The four macle diamond crystal morphology groups are more flattened than a twin formed solely by the contact of two regular octahedra bounded by {111} faces. The effects of re-entrant and salient corners play a significant role in their growth. The macle crystals from groups III and IV are flatter than those from groups I and II. The growth mechanism can be explained by preferential growth occurring not only at the re-entrant corners but also significantly influencing the salient corners of the contact-twinned macle diamonds.

Macle crystals' internal zonal growth structure reveals distinct morphological changes during growth. The zonal structure of four sliced and polished macle crystals indicates that growth begins with a morphology featuring re-entrant corners. Over time, this morphology transforms into one with apex corners that gradually become covered by {111} faces, replacing the re-entrant corners.

Figure 14. A gold pendant adorned with four flattened triangular macle rough diamonds with re-entrant corners belonging to morphology groups III and IV, weighing 0.945 total carats. Photo by Tetsuya Chikayama.

At the end of the growth process, a flattened contact twin may form, which can revert to a morphology with re-entrant corners or result in a very flattened form ending with a smooth or curved apex corner. It should be noted that dissolution can occur during the growth stage and lead to a curved zonal structure of growth banding.

The flatness of the external morphology of macle diamonds is closely linked to the preferential growth occurring at the re-entrant and salient corners. The changes in the morphology of macle diamonds can be interpreted as fluctuations in carbon supersaturation conditions during the crystallization process. By measuring the width of the growth bands in these crystals, we estimated that the growth conditions of macle diamonds fluctuated, indicating that carbon supersaturation levels decreased and increased repeatedly throughout their growth. Large, flattened, thin triangular macle diamonds, characterized by apex corners, are believed to form under relatively lower carbon supersaturation than crystals with a thick triangular morphology featuring concave re-entrant corners.

To our knowledge, this study is the first to provide a comprehensive understanding of the crystal growth of natural macle diamonds, revealing the complex growth processes that occur deep within the earth.

ABOUT THE AUTHORS

Dr. Ahmadjan Abduriyim is president of Tokyo Gem Science and director of GSTV Gemological Laboratory in Tokyo. Dr. Masao Kitamura is emeritus professor of the Division of Earth and Planetary Sciences, Department of Geology and Mineralogy at the Graduate School of Science, Kyoto University, Japan.

ACKNOWLEDGMENTS

The authors would like to sincerely thank Norimasa Shimobayashi of Kyoto University for critically reading the manuscript and for productive discussions, encouragement, and guidance throughout this study. We also greatly appreciate the technical assistance and insightful discussions provided by our former colleagues Junichi Minato, Jun Kawano, and Yusuke Seto in the Department of Geology and Mineralogy at the Graduate School of Science, Kyoto University.

REFERENCES

Abduriyim A., Kitamura M. (2002) Growth morphology and change in growth conditions of a spinel-twinned natural diamond. *Journal of Crystal Growth*, Vol. 237–239, pp. 1286–1290, http://dx.doi.org/10.1016/S0022-0248(01)02146-7

Battaile C.C., Srolovitz D.J., Butler J.E. (1998) Atomic-scale simulations of chemical vapor deposition on flat and vicinal diamond substrates. *Journal of Crystal Growth*, Vol. 194, No. 3-4, pp. 353–368, http://dx.doi.org/10.1016/S0022-0248(98)00685-X

Becke F. (1911) Über die ausbildung der zwillingskristalle. *Fortschritte der Mineralogie, Kristallographi und Petrographie*, Vol. 1, pp. 48–65.

Berg W.F. (1938) Crystal growth from solutions. *Proceedings of the Royal Society A*, Vol. 164, No. 916, pp. 79–95, http://dx.doi.org/10.1098/rspa.1938.0006

Burton W.K., Cabrera N., Frank F.C. (1949) Role of dislocations in crystal growth. *Nature*, Vol. 163, pp. 398–399.

Butler J.E., Oleynik I. (2008) A mechanism for crystal twinning in the growth of diamond by chemical vapour deposition. *Philosophical Transactions of the Royal Society A*, Vol. 366, No. 1863, pp. 295–311, http://dx.doi.org/10.1098/rsta.2007.2152

Chudoba K. (1927) Zwillingspersistenzen. *Zeitschrift für Kristallographie*, Vol. 65, pp. 225–237.

Frank F.C., Puttick K.E., Wilks E.M. (1958) Etch pits and trigons on diamond: 1. *Philosophical Magazine*, Vol. 3, No. 35, pp. 1262–1272, http://dx.doi.org/10.1080/14786435808233308

Harris J.W., Hawthorne J.B., Oosterveld M.M., Wehmeyer E. (1975) A classification scheme for diamond and a comparative study of South African diamond characteristics. *Physics and Chemistry of the Earth*, Vol. 9, pp. 765–783, http://dx.doi.org/10.1016/B978-0-08-018017-5.50053-5

Hartman P. (1956) On the morphology of growth twins. *Zeitschrift für Kristallographie – Crystalline Materials*, Vol. 107, No. 1-6, pp. 225–237, http://dx.doi.org/10.1524/zkri.1956.107.16.225

Hirabayashi K., Kimura T., Hirose Y. (1993) Morphology of flattened diamond crystals synthesized by the oxy-acetylene flame method. *Applied Physics Letters*, Vol. 62, pp. 354–356, http://dx.doi.org/10.1063/1.108955

Kitamura M. (1990) Growth history of spinel-twinned diamond. *Proceedings of the Third Topical Meeting on Crystal Growth Mechanism* (Tokyo), pp. 95–98.

Kitamura M., Hosoya S., Sunagawa I. (1979) Re-investigation of the re-entrant corner effect in twinned crystals. *Journal of Crystal Growth*, Vol. 47, No. 1, pp. 93–99, http://dx.doi.org/10.1016/0022-0248(79)90162-3

Kitamura M., Fudaki M., Shwin K., Shimobayashi N. (1992) A cathodoluminescence microscope and its application to the study of growth zoning of minerals. *Mineralogical Journal*, Vol. 16, No. 2, pp. 108–116, http://dx.doi.org/10.2465/minerj.16.108

Lang A.R. (1964) Dislocations in diamond and the origin of trigones. *Proceedings of the Royal Society of London A*, Vol. 278, No. 1373, pp. 234–242, http://dx.doi.org/10.1098/rspa.1964.0057

Ming N.-B., Sunagawa I. (1988) Twin lamellae as possible self-perpetuating step sources. *Journal of Crystal Growth*, Vol. 87, No. 1, pp. 13–17, http://dx.doi.org/10.1016/0022-0248(88)90339-9

Orlov Y.L. (1977) *The Mineralogy of the Diamond*. John Wiley & Sons, New York.

Ponahlo J. (1992) Cathodoluminescence (CL) and CL spectra of De Beers experimental synthetic diamonds. *Journal of Gemmology*, Vol. 23, No. 1, pp. 3–18.

Sinkankas J. (1964) *Mineralogy for Amateurs*. Van Nostrand Reinhold Company, Princeton, New Jersey, pp. 96–105.

Stranski L.N. (1949) General discussion. *Discussions of the Faraday Society*. No. 5, pp. 66–69.

Sunagawa I. (1975) Mechanism of formation of growth twins, and their macro- and micro-morphology. *Journal of the Mineralogical Society of Japan*, Vol. 12, No. 2, pp. 117–131, http://dx.doi.org/10.2465/gkk1952.12.117 [in Japanese]

Sunagawa I., Takahashi J., Aonuma K., Takahashi M. (1979) Growth of quartz crystals twinned after Japan law. *Physics and Chemistry of Minerals*, Vol. 5, pp. 53–63, http://dx.doi.org/10.1007/BF00308168

Sunagawa I., Yasuda T. (1983) Apparent re-entrant corner effect upon the morphologies of twinned crystals; A case study of quartz twinned according to Japanese twin law. *Journal of Crystal Growth*, Vol. 65, No. 1-3, pp. 43–49, http://dx.doi.org/10.1016/0022-0248(83)90034-9

Sunagawa I., Tsukamoto K., Yasuda T. (1984) Surface microtopographic and X-ray topographic study of octahedral crystals of natural diamond from Siberia. In I. Sunagawa, Ed., *Materials Science of the Earth's Interior*. Terra Scientific Publishing, Tokyo, and Reidel, Boston, pp. 331–349.

Sunagawa I., Lu T. (1987) Apparent re-entrant corner effect due to impurities in ribbon-like morphology of hematite twins. *Mineralogical Journal*, Vol. 13, No. 6, pp. 328–346, http://dx.doi.org/10.2465/minerj.13.328

Tappert R., Tappert M.C. (2011) *Diamonds in Nature: A Guide to Rough Diamonds*. Springer-Verlag, Berlin, pp. 15–42.

Yacoot A., Moore M., Machado W.G. (1998) Twinning in natural diamond. I. Contact twins. *Journal of Applied Crystallography*, Vol. 31, pp. 767–776, http://dx.doi.org/10.1107/S0021889898005317

Characterization of "Orange Peel" Surface Microstructure of White Nephrite from Russia: A Unique Pseudomorph Pattern

Meiyu Shih, Guanghai Shi, and Biqian Xing

The term *orange peel effect* is often used to refer to the uneven appearance of the polished surface of jadeite, which arises due to the hardness anisotropy of its mineral grains arranged in different directions. The unusual orange peel effect observed on white nephrite from Russia has been preliminarily recognized in the commercial sphere, but minimal description of the underlying causes for the effect exists in the literature. In this investigation, this orange peel surface feature, which includes granular pits and bumps, pseudo-rhombic microstructure, and subparallel fissures, was explored using gemological and petrographic microscopes, an electron probe microanalyzer with backscattered electron imaging, and cathodoluminescence imaging. The observed surface feature, related to pseudomorphs, results from metasomatism where nephrite (tremolite) replaces rhombic carbonate (dolomite) mineral grains while preserving their original microstructure. Petrographic observations show that the pseudo-rhombs on these pseudomorphs are intersected by a network of veins, similar to the framework of cleavage patterns of calcite or dolomite. The pseudo-rhombs ranged from 100 to 500 μm in width, consisting of a thin vein outline and an inside region composed of fine compacted fibers, with a relatively less compact central domain. This study demonstrates that this effect is largely dependent on the nephrite's adopted microstructure rather than its chemical composition or mineral components. Derived from these results, a formation model of this distinctive microstructure is proposed, arising from fluid flow and precipitation accompanied by volume shrinkage reactions during replacement progress. Based on the review of the microstructures of available white nephrite samples from other localities, the pattern of pseudomorphs with pseudo-rhombs and claw lineation is a unique feature of Russian nephrite.

Nephrite is mainly composed of aggregates of tremolite-actinolite. According to Bradt et al. (1973), high-quality nephrite is characterized by felted, matted, interwoven, and recrystallized microstructures and thus typically has high toughness. As a gemstone and ornamental material, nephrite played important roles in ancient Asian cultures and continues to do so in modern China. It has been considered a symbol of power and wealth, as well as a symbol of desirable moral qualities, including kindheartedness, righteousness, wisdom, courage, and purity, throughout history in Chinese culture (e.g., Cha, 2011). Because of its cultural meaning, white has been regarded by the Chinese as the most valuable color variety of nephrite. For instance, during the Song Dynasty of China, Emperor Zhenzong (997–1022) used a "white nephrite album of slips" (*yùcè* 玉册), a jade tablet that resembles an ancient bamboo scroll and is inscribed with Chinese characters, to worship and communicate with heaven in order to affirm his divine mandate and reinforce his imperial authority.

Nephrite colors are associated with its two mechanisms of formation: metasomatic replacement of

See end of article for About the Authors and Acknowledgments.
Gems & Gemology, Vol. 61, No. 3, pp. 270–288,
http://dx.doi.org/10.5741/GEMS.61.3.270

Figure 1. A high-quality Russian white nephrite bracelet, measuring approximately 58 × 13 × 7 mm, with the orange peel effect observable in its reflective areas. Photo by Zuojiang Chen.

serpentinite (S-type) and metasomatic replacement of dolomite (D-type) (Yui and Kwon, 2002; Harlow and Sorensen, 2005; Liu et al., 2011a,b). S-type is predominantly dark green or green, while D-type is often white, yellow, celadon, or gray (see box A). White nephrite forms exclusively via the metasomatic replacement of dolomite crystals.

The main sources of white nephrite in the Chinese market are China, Russia, and South Korea (Ling et al., 2013). White nephrite from various localities differs in value even if of similar quality. Hence, a method to distinguish the origin of white nephrite is critical in the marketplace as consumers demand this information. Furthermore, origin determination of white nephrite artifacts can be crucial in archaeological provenance studies.

White nephrite from different localities may have very slightly different characteristic appearances. Some experienced collectors and connoisseurs can identify specific sources of nephrite with the unaided eye based on appearance (Wang and Sun, 2013; Chen et al., 2020). As an example, according to Hu et al. (2011) and Wang and Sun (2013), nephrite with a linear "water line" that is more transparent and denser than the adjacent matrix, and that has relatively high overall transparency, typically originates from Qinghai, China. Geochemical methods, including analyzing hydrogen and oxygen isotopes in mineralizing fluids associated with nephrite formation, can also aid in identification of their sources (e.g., Gao et al., 2020; Shih et al., 2024). However, such identification methods may damage the samples and cannot be widely applied.

Recently, the authors found an unexpected orange peel effect in Russian white nephrite jade (figures 1 and 2). The effect looks similar to that associated with Burmese jadeite but has its own distinctive pattern. While inspecting white nephrite samples from

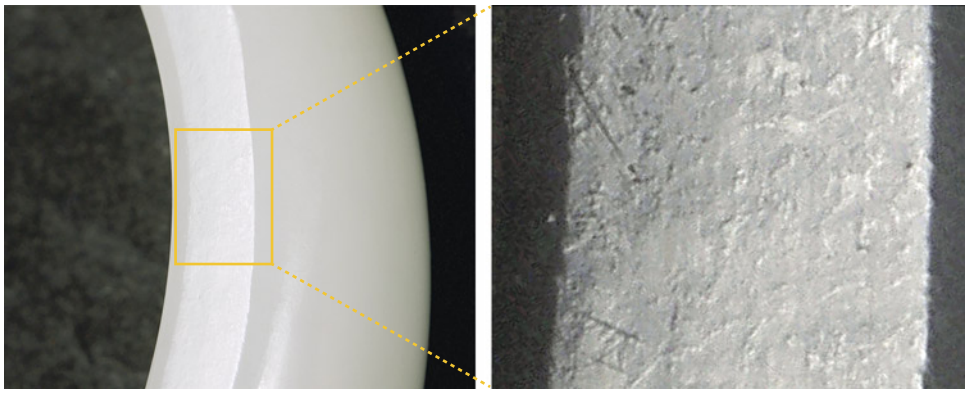

Figure 2. A section of a high-quality Russian white nephrite bracelet shows the distinctive orange peel effect, with lenticular contour ranging in size from 300 to 500 μm viewed under oblique illumination. Photo by Guanghai Shi.

Box A: Terminology Related to Jade Microstructure

Figure A-1. The orange peel effect on the surface of jadeite from Guatemala (left) and nephrite from Russia (right) viewed under oblique illumination. Photomicrographs by Meiyu Shih; field of view 6 mm.

Microstructure: The small-scale arrangement of geometric mineralogical elements within a rock (Hobbs et al., 1976). The term also refers to a structure observed on a thin section or smaller scale (Brodie et al., 2002).

Orange peel effect: A term that refers to the uneven surface of jade resembling that of an orange peel or lemon peel (Manutchehr-Danai, 2009). In the jade market, the orange peel effect is typically considered a feature of polished phanerocrystalline jadeite jade and is commonly observed. In this investigation, we find that such an effect can be observed on polished white nephrite (D-type) from Russia but not in green nephrite (S-type) from Russia (figure A-1).

Pseudomorph: A mineral or mineral aggregate that has undergone a chemical or structural transformation while retaining the external shape of the original material. This process often involves replacement (substitution) or alteration, resulting in a new mineral composition while preserving the original mineral's external geometry (Blazek, 1979).

Figure A-2. A schematic diagram showing fissures within and between pseudomorphs.

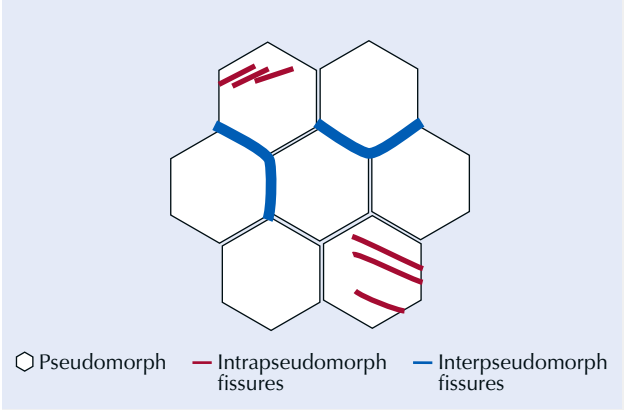

Intrapseudomorph fissures: Fissures within a pseudomorph that are displayed as subparallel lines or curves, following the pseudomorph's internal structure (figure A-2).

Interpseudomorph fissures: Fissures occurring along a boundary between pseudomorphs that appear as unclosed curves, following the outer contour and surrounding structure of the pseudomorphs (figure A-2).

Claw lineation: A trade term used by nephrite jade dealers to describe the lineation observed on nephrite exclusively from Russia. Viewed under oblique illumination, this lineation loosely resembles crab claws (figure A-3). According to the lineation's distribution, it is more likely associated with major intrapseudomorph fissures than with interpseudomorph fissures.

Figure A-3. A simple sketch showing the claw lineation pattern. The red lines represent claw lineation, and the outlined gray particles represent the granular microstructure (pseudomorphs) of nephrite.

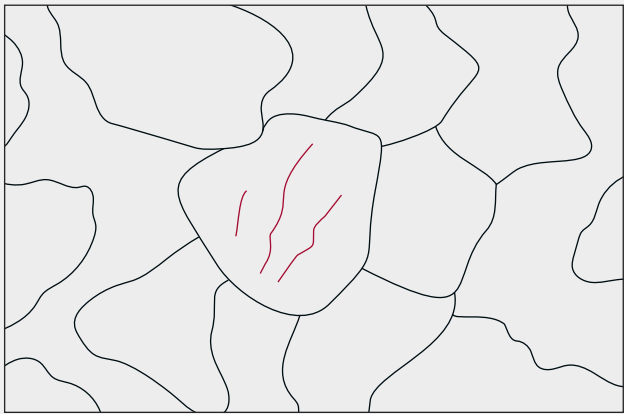

other localities, we were unable to find this effect on material from outside Russia. After discussing this characteristic with many experienced collectors and dealers and making a broad comparison with microstructures of white nephrite from other localities (e.g., Zhang et al., 2001; Zhou et al., 2008; Pei et al., 2011; Gao et al., 2019a; Zhang et al., 2022), we report that to our knowledge, only white nephrite from Russia has this feature. This finding may have significant implications for origin determination of Russian white nephrite jade. This unique microstructure also reveals a distinctive formation mechanism of this gem.

In Brief

- A distinctive orange peel effect identified in many samples of Russian white nephrite is characterized by granular pits and bumps, a pseudo-rhombic microstructure, and subparallel fissures.
- This orange peel effect can be recognized through unaided visual inspection or verified using cathodoluminescence instrumentation.
- Together, the processes of metasomatism and precipitation from fluid to replace precursor dolomite crystals with tremolite are evident in the orange peel effect of Russian white nephrite.

The distinctive ripples and dimple-like surface features on polished jadeite jade are similar to those on the surface of an orange peel or lemon peel. This effect is often a key factor in the separation of jadeite from its imitations or treated equivalents; however, it is rarely mentioned for the identification of nephrite (e.g., Read, 2008; Manutchehr-Danai, 2009; Hansen, 2022). It is assumed that the orange peel effect of jadeite jade is strongly correlated with its microstructure, and specific white and colorless jadeite jades with almost identical chemical compositions and mineral constituents may have varying microstructures (Shi et al., 2009). As white nephrite from various localities differ slightly in appearance, their microstructures may also differ. However, descriptions of microstructure (e.g., felted) in white nephrite are quite similar in the literature (Hou et al., 2010; Jiang et al., 2020; Wang and Shi, 2020). Apparently, the differences in white nephrite microstructures have been overlooked.

Given the potential significance of microstructure, the present study was conducted to investigate correlations between microstructures and the orange peel effect in Russian white nephrite, including its impact on appearance, as well as other gemological implications.

MATERIALS AND METHODS

In this study, white nephrite samples from Russia were provided by a nephrite trading company with the help of Yu Ming at the Chinese Jade Culture Research Center, Central Academy of Fine Arts in Beijing. This company trades with Russian mines and provided 60 white Russian nephrite jade remnants from commercial cutting for this study. Large quantities of raw Russian white nephrite have reportedly been imported from Russia to the Chinese market (approximately 3,500 to 4,000 tons annually between 2019 and 2021; Wang, 2022).

Three representative Russian white nephrite samples (figure 3) were randomly chosen from the 60-piece study set (see appendix 1 at https://www.gia.edu/-gems-gemology/fall-2025-white-nephrite); all three had a uniform appearance, were translucent and white, and varied slightly in grain size. Standard gemological testing was conducted on the three samples, including examination with a 10× loupe, determination of refractive index and specific gravity (using the hydrostatic method), and observation

Figure 3. Three representative samples of Russian white nephrite: ELS13 (4.0 × 2.5 × 0.9 cm; A), ELS24 (3.8 × 20.0 × 0.8 cm; B), and ELS27 (3.6 × 2.5 × 0.7 cm; C). Photos by Meiyu Shih.

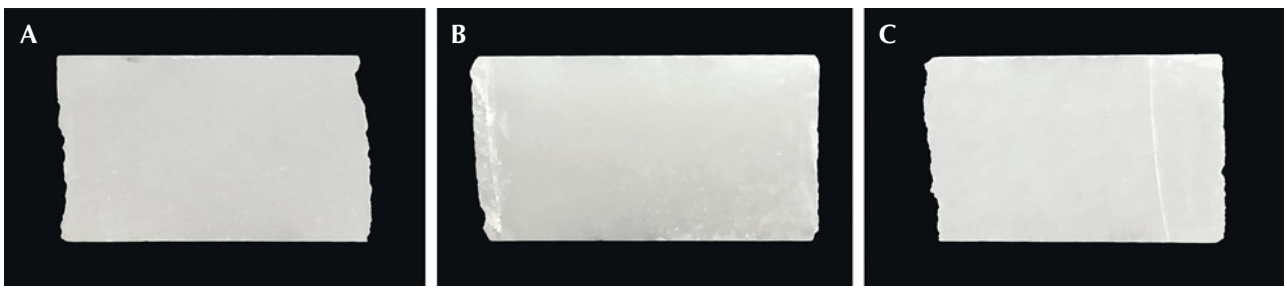

of the reaction to long-wave (365 nm) and short-wave (254 nm) ultraviolet light. Afterward, thin sections for electron probe microanalyses were prepared by cutting a small piece of each sample, gluing them to a glass plate with resin, and then grinding and polishing each sample to a thickness of approximately 70 μm.

Petrographic observations and photomicrographs were obtained with an Olympus BX51 polarizing microscope at the Gemological Center, China University of Geosciences in Beijing (CUGB). Cathodoluminescence (CL) images were acquired with an MK-CL-5200 cathodoluminescence microscope equipped with a Nikon DS-Fi3 microscope camera at the Resources Exploration Laboratory, CUGB, under conditions of 10 s exposure time, gain setting ×20, 250 μA stable current, and 0.003 mbar vacuum.

Backscattered electron (BSE) images and chemical compositions were acquired using a Shimadzu EPMA-1720 electron probe microanalyzer at the Geological Lab Center, CUGB, with a voltage of 15 kV, a beam current of 10 nA, a beam diameter with a spot size of approximately 1–3 μm, and a detection limit for a single element of ±0.01 wt.%. All electron probe microanalysis (EPMA) data processing utilized the ZAF correction method, a standard procedure that accounts for factors affecting the accuracy of elemental analysis: Z (atomic number effect), A (absorption effect), and F (fluorescence effect). The EPMA standards include the following minerals: andradite for silicon and calcium, rutile for titanium, corundum for aluminum, hematite for iron, eskolaite for chromium, rhodonite for manganese, bunsenite for nickel, periclase for magnesium, albite for sodium, K-feldspar for potassium, and barite for barium. The analytical errors for the major oxide content of the minerals were within ±1.5 wt.%, and the formula was calculated according to Shi et al. (2024). The ferric iron contents of the mineral phases were determined using the AX program (Holland, 2009).

The micro X-ray fluorescence (micro-XRF) mapping images were acquired using a Bruker M4 Tornado micro-XRF spectrometer at the National Infrastructure of Mineral, Rock and Fossil Resources for Science and Technology (NIMRF), CUGB, with the tube operating at 50 kV and 300 μA, a pixel size of 20 μm, and a time of 10 ms/pixel. Individual element maps for silicon, calcium, magnesium, aluminum, manganese, sodium, potassium, iron, sulfur, and titanium were detected using the instrument's software.

RESULTS

Gemological Properties. The standard gemological properties determined for the three Russian white nephrite samples are summarized in table 1.

TABLE 1. Gemological properties of three representative Russian white nephrite samples.

	ELS13	ELS24	ELS27
Color	White	White	White
Transparency	Translucent	Translucent	Translucent
Granularity of pseudomorph	Fine to medium	Fine to medium	Medium to coarse
Cracks observed under a 10× loupe	Few	Few	Few to some
Granularity (mm)	~0.8–1.7	~0.8–1.7	~1.7–2.5
Size (cm)	4.0 × 2.5 × 0.9	3.8 × 2.0 × 0.8	3.6 × 2.5 × 0.7
Refractive index	1.62	1.62	1.62
Specific gravity	3.01	2.93	2.93
UV responses	Inert	Inert	Inert

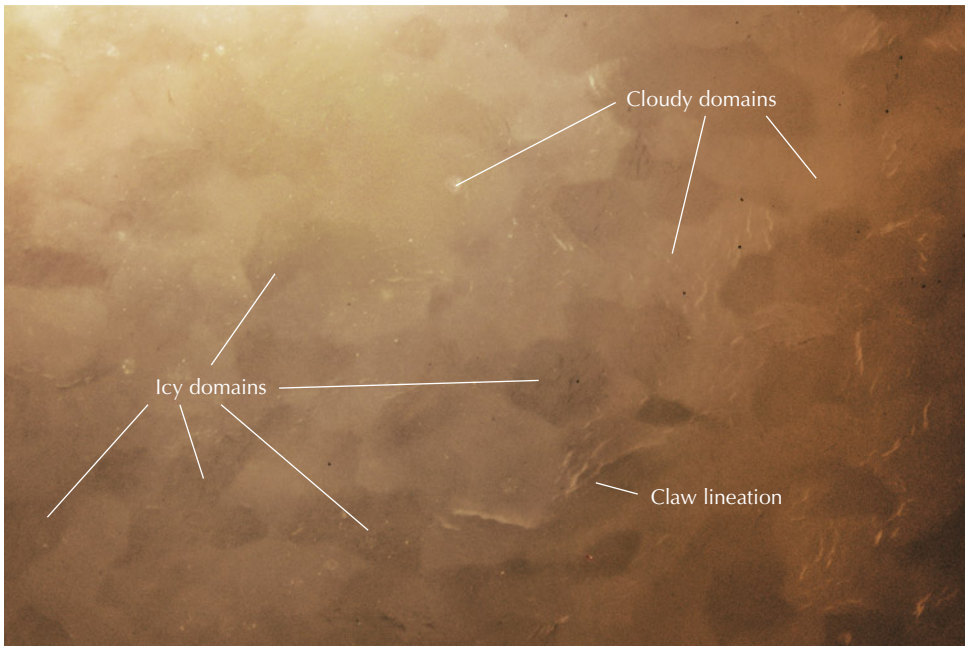

Figure 4. The polished surface of Russian white nephrite sample ELS27 showed icy domains (darker grains), cloudy domains (lighter grains), and claw lineation under oblique illumination with a sodium light source. Photomicrograph by Meiyu Shih; field of view 6.90 mm.

Magnification. Magnification of the polished surfaces of the specimens revealed a mosaic-like granular microstructure. This microstructure is characterized by grain-like domains that appear darker under reflected illumination but exhibit greater transparency under transmitted illumination than the lighter granular domains (figure 4). These darker domains resembled ice blocks and thus were referred to as "icy domains." The other grain-like domains were whiter under reflected illumination and less opaque under transmitted illumination, resembling clouds, and were consequently called "cloudy domains." Both of these domains form granular pits and bumps on the nephrite's surface under oblique illumination, similar to a magnified picture of the surface of an orange peel.

Variations in icy and cloudy domains in the same area of nephrite can be observed when the angle of the incident light changes (figure 5). Each whiter or darker domain appears as an entire grain. Each grain is not a single crystal but is composed of numerous

Figure 5. Nephrite sample ELS27 illuminated laterally by a flashlight. B is a magnified view of the area indicated by the rectangle in A, showing clearer contours of the grains, while C further outlines the grain shapes with yellow dashed lines. Photos by Meiyu Shih; fields of view 2.73 cm (A) and 0.774 mm (B and C).

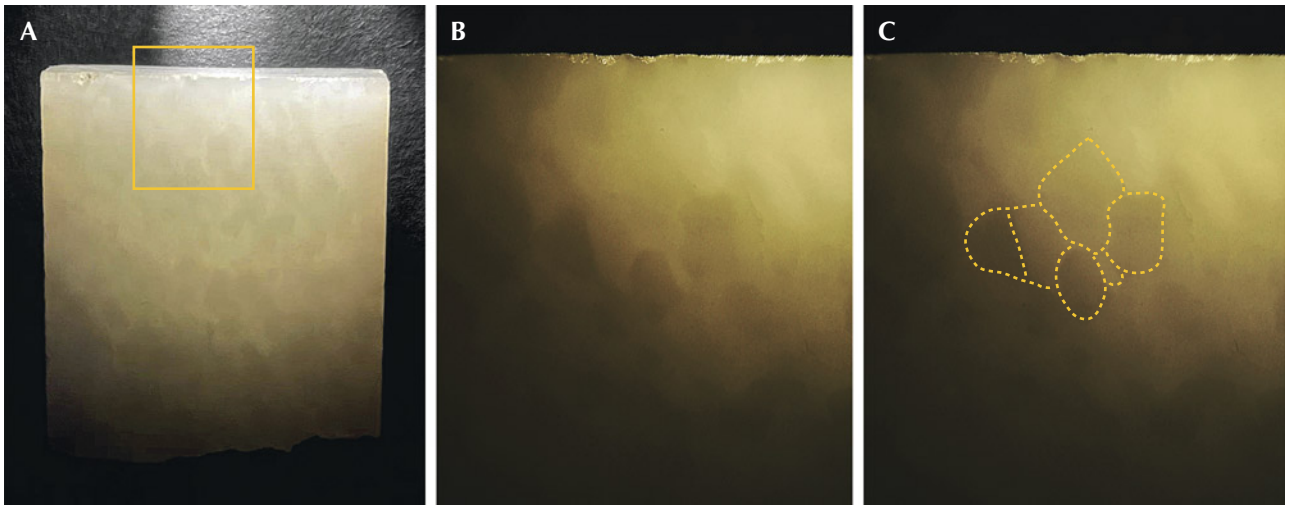

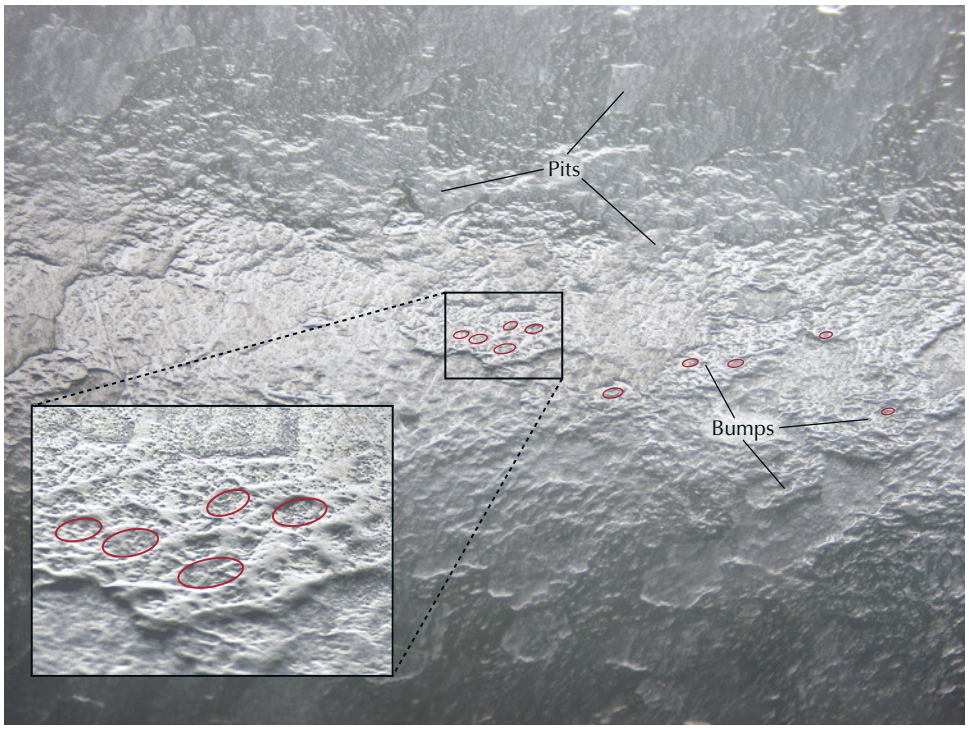

Figure 6. Sample ELS27 under reflective illumination displaying pseudo-rhombic microstructure on the granular pits and bumps of the surface. The inset shows an enlarged section of the surface to better demonstrate its unevenness. Small lenticular contours located on the depressions of the granular pits and bumps are outlined in red. These lenticular contours may either interconnect to form a network or remain dispersed, constituting a pseudo-rhombic microstructure. Photomicrograph by Meiyu Shih; fields of view 17.79 mm and 1.18 mm (inset).

small crystals with sizes less than 2 μm. The whole grain can be regarded as a pseudomorph. With higher magnification, several lenticular contours (figure 6, outlined in red) could be observed within the grains, each with a length not exceeding 700 μm. These lenticular contours may either interconnect to form a network or remain dispersed, constituting a pseudo-rhombic microstructure. In addition, subparallel lineations that together resembled a claw were observed (again, see figure 4).

Chemical Composition. The white nephrite samples studied consist of an almost pure tremolite end member according to EPMA data and Leake et al.'s formula calculations (1997) (figure 7 and table 2). The chemical formula for amphibole is $AB_2{}^{VI}C_5{}^{IV}T_8O_{22}W_2$. The meanings of the notations are as follows: A = A-site cations (including Na^+, K^+, or vacancies); B = large cations in the B-site; T = tetrahedral site cations; C = octahedral site cations; W = anions such as OH^-, F^-, or Cl^- (Leake et. al., 1997).

Figure 7. Mg/(Mg + Fe^{2+}) and Na + K + 2Ca diagrams for amphibole classification (modified from Leake et al., 1997) with the sample compositions plotted in orange.

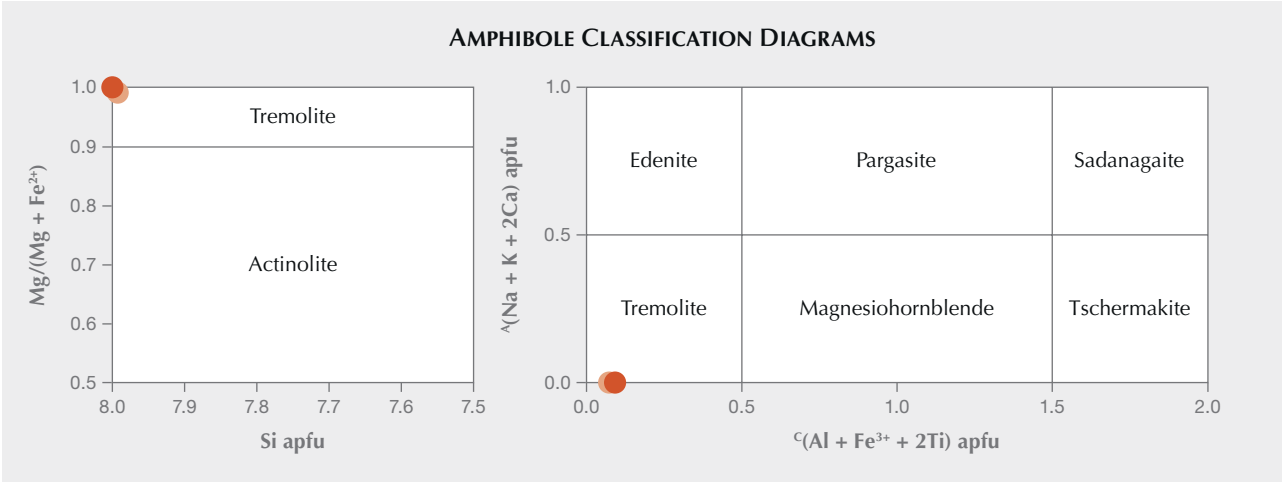

TABLE 2. Chemical composition (in wt.%) of three Russian white nephrite samples, analyzed by EPMA.

	ELS27	ELS24	ELS13-1	ELS13-2
SiO_2	58.46	58.79	58.69	58.58
TiO_2	bdl[a]	0.05	0.04	0.01
Al_2O_3	0.50	0.60	0.60	0.62
Cr_2O_3	bdl	0.04	bdl	bdl
Fe_2O_3	bdl	bdl	bdl	0.16
FeO	0.17	0.18	0.32	0.15
MnO	bdl	0.06	0.01	0.08
MgO	24.61	24.70	24.57	24.42
CaO	13.02	13.23	12.80	13.06
Na_2O	0.09	0.09	0.10	0.40
K_2O	0.07	0.10	0.08	0.12
F	0.34	0.51	0.41	0.32
NiO	bdl	0.01	0.07	0.06
Totals	97.26	98.36	97.70	97.95
H_2O_{calc}	2.19*	2.20*	2.10*	2.20*
	Calculated stoichiometry (apfu)[b]			
T_{Si}	8.001	8.002	8.017	7.992
T_{Al}	0.000	0.000	0.000	0.000
T_{Ti}	0.000	0.005	0.004	0.001
T_{sum}	8.001	8.008	8.021	7.993
C_{Al}	0.080	0.096	0.097	0.100
$C_{Fe^{3+}}$	0.000	0.000	0.000	0.000
C_{Cr}	0.000	0.004	0.000	0.000
C_{Ni}	0.000	0.001	0.008	0.006
C_{Mg}	5.022	5.012	5.004	4.967
$C_{Fe^{2+}}$	0.000	0.000	0.000	0.000
C_{sum}	5.102	5.114	5.108	5.073
$B_{Mn^{2+}}$	0.000	0.007	0.001	0.009
$B_{Fe^{2+}}$	0.019	0.020	0.037	0.033
B_{Ca}	1.918	1.937	1.878	1.917
B_{Na}	0.110	0.093	0.119	0.154
B_{sum}	2.047	2.058	2.035	2.113

[a]*bdl = below detection limit; indicates values below 0.01 wt.%.*
[b]*Stoichiometries were calculated on the basis of 23 oxygen atoms to account for fluorine and chlorine replacing hydroxyl. Ferric iron content was estimated based on charge balance. The atoms per formula unit values were calculated and normalized to ensure charge balance, maintaining overall electrical neutrality in the formula.*

TABLE 2 (continued). Chemical composition (in wt.%) of three Russian white nephrite samples, analyzed by EPMA.

	ELS27	ELS24	ELS13-1	ELS13-2
A_{Ca}	0.000	0.000	0.000	0.000
A_{Na}	0.000	0.000	0.000	0.000
A_{sum}	0.000	0.000	0.000	0.000
W_{OH}	2.000	2.000	2.000	2.000
W_{F}	0.129	0.199	0.157	0.119
W_{Cl}	0.000	0.000	0.000	0.000
$W_{O^{2-}}$	0.000	0.000	0.000	0.000
W_{sum}	2.129	2.199	2.157	2.119
$Mg^{2+}/(Mg^{2+}Fe^{2+})$	0.996	0.996	0.993	0.993
ΣSi	8.001	8.002	8.017	7.992

[a]*bdl = below detection limit; indicates values below 0.01 wt.%.*
[b]*Stoichiometries were calculated on the basis of 23 oxygen atoms to account for fluorine and chlorine replacing hydroxyl. Ferric iron content was estimated based on charge balance. The atoms per formula unit values were calculated and normalized to ensure charge balance, maintaining overall electrical neutrality in the formula.*

Due to the presence of hydroxyl groups, the total EPMA content of the amphibole group is usually less than 100 wt.% (e.g., Jiang et al., 2020; Yang et al., 2022; Zhang et al., 2022). Due to the low signal intensity, the chlorine content was not detected. Assuming two hydroxyl groups (2(OH)) for our theoretical calculations, the water (H_2O) contents of ELS27, ELS24, ELS13-1, and ELS13-2 were calculated as 2.19, 2.20, 2.19, and 2.20 wt.%, respectively, and the total compositions summed to 99.45, 100.56, 99.89, and 100.15 wt.%, respectively. These deviations were within an acceptable range of ±1.5 wt.% from the ideal 100 wt.% composition.

The BSE images of the white nephrite samples were uniform (figure 8), suggesting a nearly homogeneous chemical composition without other apparent mineral components, although minimal calcite and apatite have been reported in Russian white nephrite (Zhang and Zhao, 2012). All the available element map images show nearly homogeneous colors (figure 9), except for the iron map image, in which the darker areas in the intact pseudomorphs indicate richer iron content, whereas the brighter areas in the incomplete pseudomorphs indicate lower iron content, possibly due to slight iron contamination during later-stage growth.

Microstructure. *Metasomatic pseudomorph microstructure.* Polygonal pseudomorphs were observed in the Russian white nephrite samples (figure 10). They reached 2.0 mm in size and were not single crystals. Instead, each one was an aggregate of many tiny tremolite crystals. Each individual pseudomorph showed flat contact with its neighbors. Together they formed an isogranular mosaic microstructure with respect to the whole nephrite, provided that each pseudomorph was considered a separate grain. This flat contact indicated that the original grain boundaries of the precursor rock were

Figure 8. BSE image of Russian white nephrite sample ELS27. The similar contrast levels across the image indicate a nearly homogeneous chemical composition. Image by Qingqing Deng.

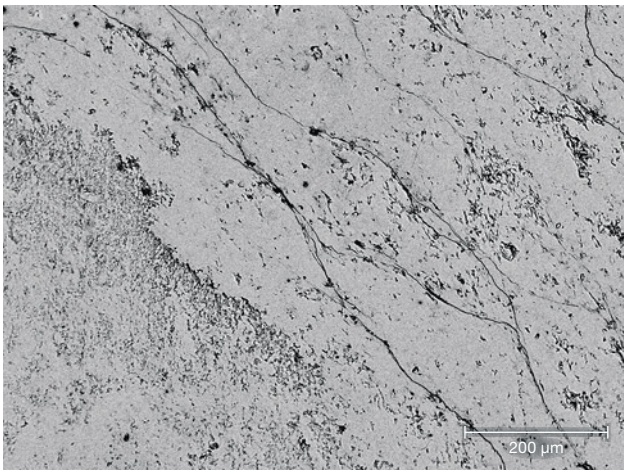

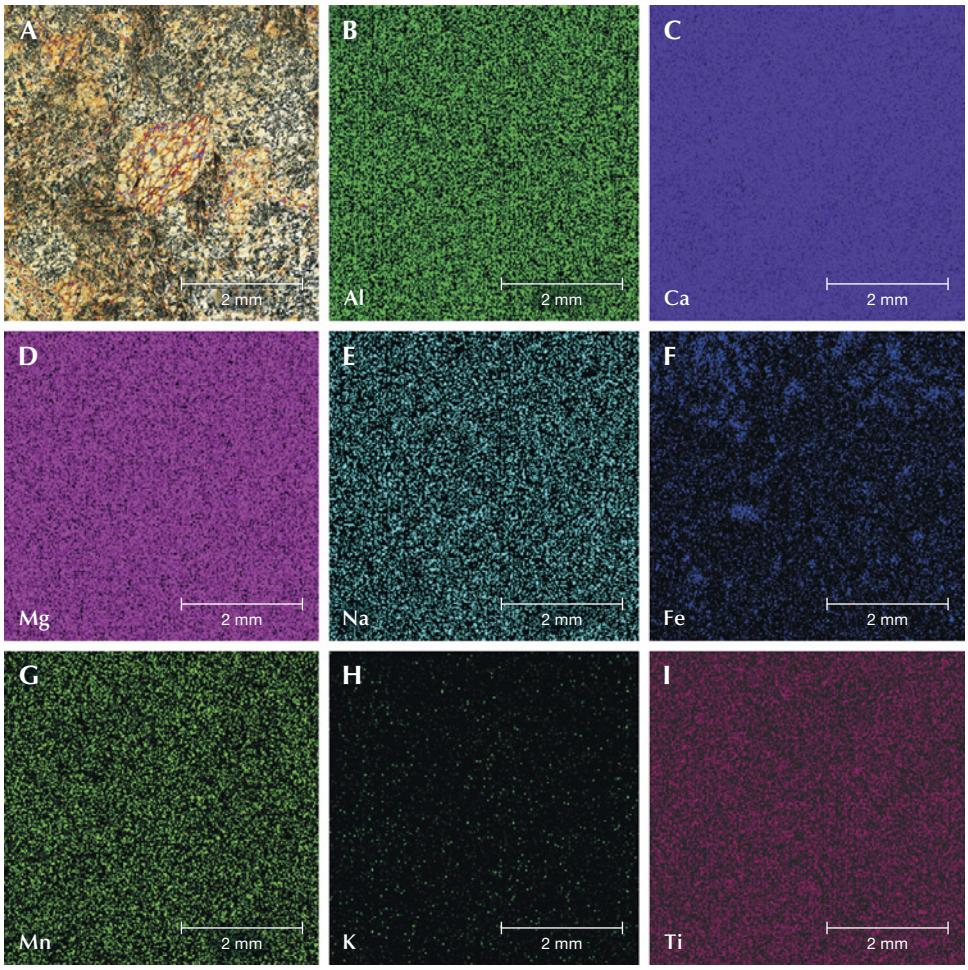

Figure 9. Photomicrograph and corresponding micro-XRF elemental maps of the same area of white nephrite sample ELS27. A: The analyzed domain of the white nephrite (cross-polarized illumination). Photomicrograph by Meiyu Shih; field of view 5 mm. B–I: Element maps of aluminum, calcium, magnesium, sodium, iron, manganese, potassium, and titanium, respectively. According to A, the observed heterogeneity in the iron content in F may indicate the occurrence of a late-stage filling phase. Other element maps indicate a nearly homogeneous chemical composition within the same area of the thin section.

preserved during the metasomatic process. The microstructure exhibited by the pseudomorphs resembles that of a coarse-grained dolomitic marble, which is considered the precursor parent rock. This resemblance suggests that the pseudomorphs formed through metasomatic replacement of dolomite by tremolite. Thus, each pseudomorph was interpreted to be equivalent to a precursor marble crystal from the dolomitic marble parent rock. Notably, the flat contacts between neighboring pseudomorphs were seamless and compact, even under magnification.

Inside an individual pseudomorph, long and dense tremolite fiber veins form an interconnected network, referred to as the "vein net" (figure 10). The veins intersect and extend across almost one entire pseudomorph, forming connected pseudo-rhombs

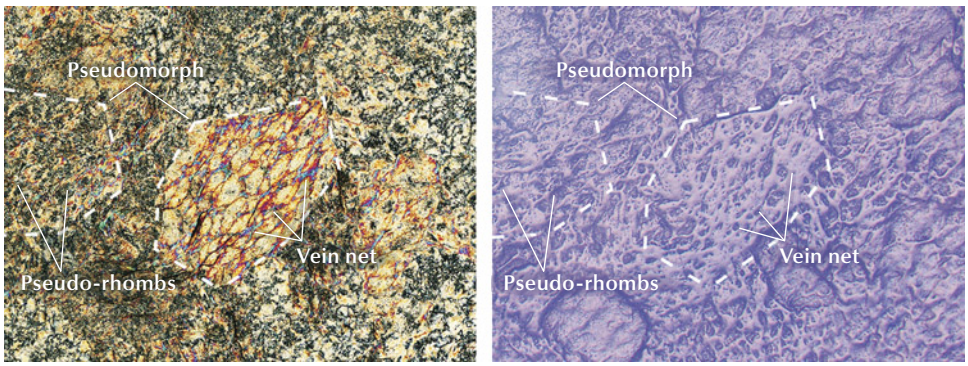

Figure 10. White nephrite sample ELS27 showing a metasomatic pseudomorph microstructure of numerous tiny tremolite grains. Crossed-polarized illumination (left) and reflected darkfield illumination (right). Photomicrographs by Meiyu Shih; field of view 4.18 mm.

inside as a result of the replacement of dolomite in the marble by tremolite. Within these veins, tremolite fibers are distributed almost parallel to the vein walls and exhibit nearly identical interference colors and extinction directions. The pseudo-rhombs range from 100 to 500 μm in length and exhibit similar interference colors and extinction directions. Within each pseudo-rhomb is an inner region, mainly composed of fine and compacted fibers, approximately 200 μm in width, and a central domain that may be relatively less compact or even empty (figure 11). The arrangement of these pseudo-rhombs displays a pattern similar to the three typical sets of cleavage planes and twin planes in calcite, dolomite, or both.

The fibers or tiny crystals inside each pseudo-rhomb did not show clear boundaries, and adjacent crystals appeared to be connected. In the central domain, tiny empty spaces often occurred among the tremolite fibers (figure 11). Based on the microstructure, inner region fibers formed under the guidance of the veins. The fibers terminated at the core or reached the other side of the same pseudo-rhomb (figure 11), suggesting a formation sequence of the pseudo-rhomb: from the vein net to the fibrous inner region and then to the central domain. Although the formation sequence was somewhat complicated, the precursor rock had been thoroughly replaced by tremolite, as no carbonate minerals could be detected in the white nephrite studied.

Microstructure Due to Fissures. Two types of fissures exist in the studied samples: intrapseudomorphs and interpseudomorphs (see box A). The former occur within pseudomorphs and mainly developed along the long fiber veins, and some even bifurcated when crossing the intersecting veins (figure 12). In contrast, the latter occur occasionally between pseudomorphs and developed along the pseudomorph boundary. No fissures were observed to cut through a pseudo-rhomb. The fissures ranged from 0.2 to 1.5 mm long. Notably, ductile deformation and dynamic recrystallization dominating the microstructure of jadeite jade from Myanmar (e.g., Shi et al., 2009) were not obvious in the Russian white nephrite due to the flat contacts between the pseudomorphs (figure 10). The direction of the lineation was closely related to its growth microstructure. Some domains in the aggregation were more compact than others (e.g., the centers of some pseudomorphs or some pseudo-rhombs), and microfissures were more likely to occur at the weak edges of these aggregations, forming the intrapseudomorph and interpseudomorph fissures (figure 11). The intrapseudomorph fissures were likely to be the main contributors to claw lineation, which usually occurs on a small scale and is not easily observed without magnification.

Cathodoluminescence Imaging. CL imaging revealed the presence of vein nets and pseudo-rhombs in the Russian white nephrite. In sample ELS27 (figure 13), the representative vein net exhibits strong pink luminescence, highlighting many pseudo-rhombs with pink to violet light (figure 13). The fissures appeared light pink due to the reflective cathodoluminescence. Notably, figure 13 (right) reveals that the variation in the long-axis directions of the pseudo-rhombs suggests the presence of several pseudomorphs.

DISCUSSION

Microstructure Formation. White nephrite from Russia was reportedly hosted by carbonate rocks and formed through the replacement of dolomitic marble by skarn metasomatism (e.g., Harlow and Sorensen, 2005; Burtseva et al., 2015). Although not all replaced phases have the same microstructure as the precursor rock, the original microstructure was well preserved in the white nephrite studied. The flat

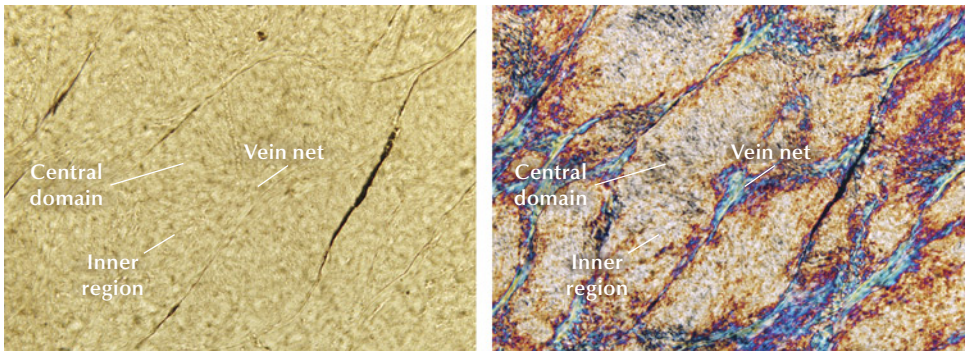

Figure 11. Microstructure of the interior of a pseudomorph with a vein net, inner region, and central domain (sample ELS27). Plane-polarized illumination (left) and cross-polarized illumination (right). Photomicrographs by Meiyu Shih; field of view 262 μm.

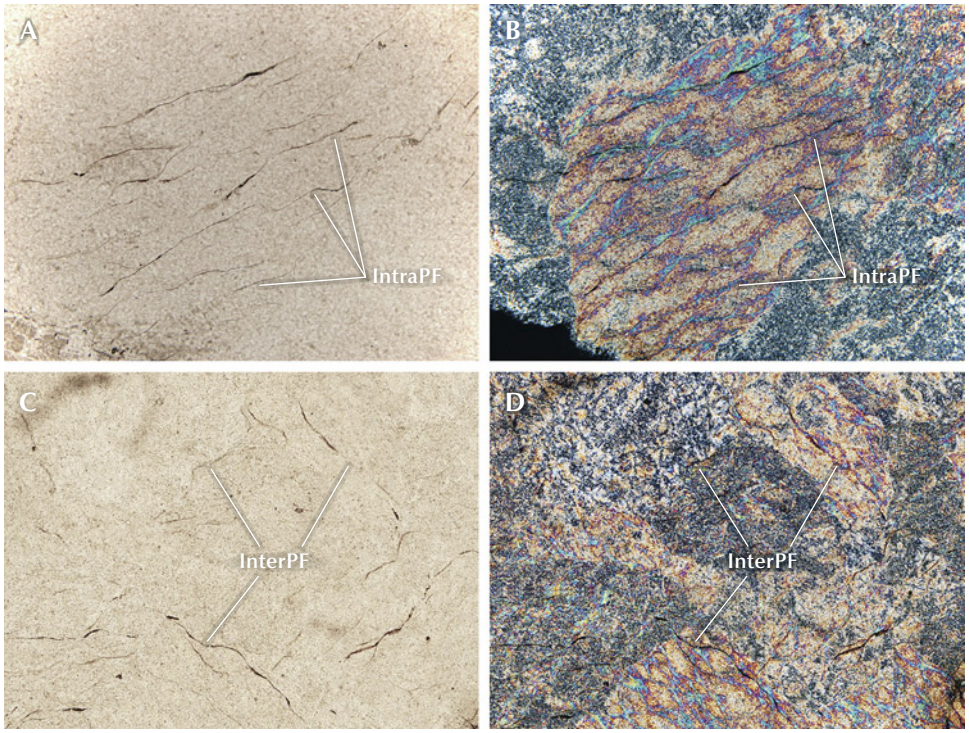

Figure 12. Two fissure types in sample ELS27. A and B: Intrapseudomorph fissures (IntraPF) were curved rather than flat, mainly developed along the long fiber veins, and some even bifurcated when crossing the intersecting veins. C and D: Interpseudomorph fissures (InterPF) were rarely observed and developed along the pseudomorph boundary. Plane-polarized illumination (A and C) and cross-polarized illumination (B and D). Photomicrographs by Meiyu Shih; fields of view 1.75 mm (A and B) and 3.50 mm (C and D).

boundaries between the large pseudomorphs in the studied nephrite reveal that its precursor rock, dolomitic marble with an isogranular mosaic microstructure, was likely formed by static metasomatism rather than dynamic metamorphism.

Dolomite has three sets of well-developed cleavages, and twin planes easily develop during the diagenetic process. These well-developed planes could have separated and formed pseudo-rhombs inside a single dolomite crystal. Such pseudo-rhombs are similar to the outlines of the vein nets in the pseudomorphs in the studied nephrite. This similarity was interpreted to mean that the vein net outlines were the pseudo-rhomb bodies inherited from the prior dolomite crystal grains. This interpretation is supported by the previously formed parallel vein net that linked the entire pseudomorph, suggesting that an early phase of tremolite precipitation occurred as the fluids penetrated through existing channels induced by the cleavage plane inside the precursor dolomite crystal.

The microstructure of the pseudo-rhombs of the Russian white nephrite showed that the replacement of dolomite by tremolite took place from the rim to the core inside an individual pseudo-rhomb. Since no residual dolomite or calcite was retained inside the pseudo-rhombs and all the reactant products were

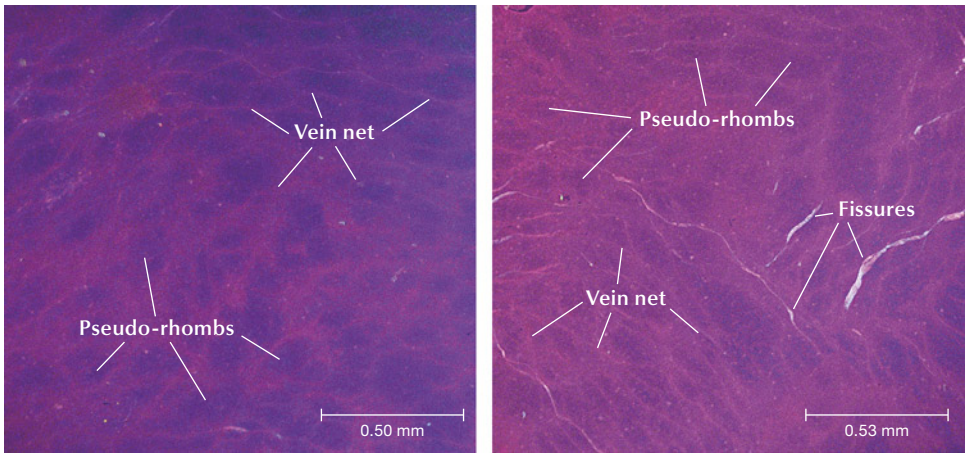

Figure 13. Cathodoluminescence images of sample ELS27. Left: Classic pattern of pseudo-rhombs and vein net in the pseudomorphs. Right: Fissures along the vein net between the pseudo-rhombs. Images by Biqian Xing.

tremolite without any other phases, the replacement is inferred to be complete, as indicated in reaction 1:

$$5CaMg(CO_3)_2 + 4H_2O + 8SiO_2(aq) \rightarrow Ca_2Mg_5[Si_4O_{11}]_2(OH)_2 \downarrow + 3Ca(HCO_3)_2 + 4CO_2 \quad (1)$$

This reaction implied a sufficient fluid supply for metasomatism. Based on the observations, a formation model of Russian white nephrite by fluid flow within a single carbonate crystal (figure 14) is proposed.

Before metasomatism occurred, transmission channels for fluid flow had already developed through the interconnected planes (i.e., grain boundaries and cleavage planes) in the dolomite of the precursor marble, induced by factors such as abrupt temperature changes or tectonic events. These channels allowed the nascent pseudo-rhombs to be produced. During metasomatism, the fluid then infiltrated along the connected plane net as the carbonate crystals were immersed, and an early-stage tremolite (Tr-I) precipitated by occupying the intersecting plane net, forming the pseudo-rhomb framework of tremolite. This constituted the first formation stage of tremolite and was associated with a precipitation mechanism, as evidenced by the vein nets of the pseudomorph framework having a similar crystallographic orientation (vein net in figures 10 and 11 and Tr-I in figure 14). The initial tremolite framework served to reinforce and emphasize the pseudo-rhombs and was further modified during the metasomatic process. Afterward, middle-stage tremolite (Tr-II) formed through metasomatism and grew from the base of the framework toward the interior of each pseudo-rhomb, as evidenced by the tremolite fibers oriented perpendicular to the outline of each pseudo-rhomb (figure 11, inner region, and figure 14). A late-stage tremolite (Tr-III) formed as tiny fiber-shaped crystal aggregates around the core of an individual pseudo-rhomb, forming a microstructure similar to that of fully encircling agate (e.g., Zhou et al., 2021).

A possible reason for the homogeneous chemical composition of Russian white nephrite is the absence of intermediate phases such as calcite and diopside during metasomatism. Another possible reason is the sufficient fluid supply passing through the pseudo-rhombs, which serve as interconnected fluid pathways and facilitate complete metasomatism, as exemplified by reaction 1.

Pattern of the Orange Peel Effect and Interpretations. Our observations clearly showed that microfeatures among pseudomorphs in the nephrites were distinctive. Within a specific pseudomorph, the separate patterns of the higher-relief vein net and lower-relief central domain observed under reflected illumination correspond directly to the microstructural framework revealed under cross-polarized illumination (figure 15). Moreover, the relief pattern shown in figure 15 (A and C) corresponds to the lenticular contours outlined in figure 6. Possible reasons for the seemingly higher-relief and lower-relief areas on the well-polished surface of the nephrite might involve orientation discrepancies in the tremolite fibers coupled with differences in their refractive indices and

Figure 14. A formation model of the specific microstructure of Russian white nephrite generated by fluid flow within a single carbonate crystal. Stage 1: Fluid (orange line) flowing along the channels of the weak planes (black lines), which are assumed to be cleavages or twinning planes of the carbonate crystal, initially precipitated the early-stage tremolite (Tr-I) and established a rhombic framework (blue lines). This early-stage tremolite (Tr-I) deposited before the metasomatic process began and further developed during metasomatism. Stage 2: The entire carbonate crystal was immersed in the fluid, and the middle-stage tremolite (Tr-II, curved thin gray lines) grew on the foundation of the Tr-I vein net. Stage 3: Tr-II and late-stage tremolite (Tr-III, red dots) formed inward within the pseudo-rhomb, around its center. The finely crystalline Tr-III may or may not grow in the form of fibrous crystals.

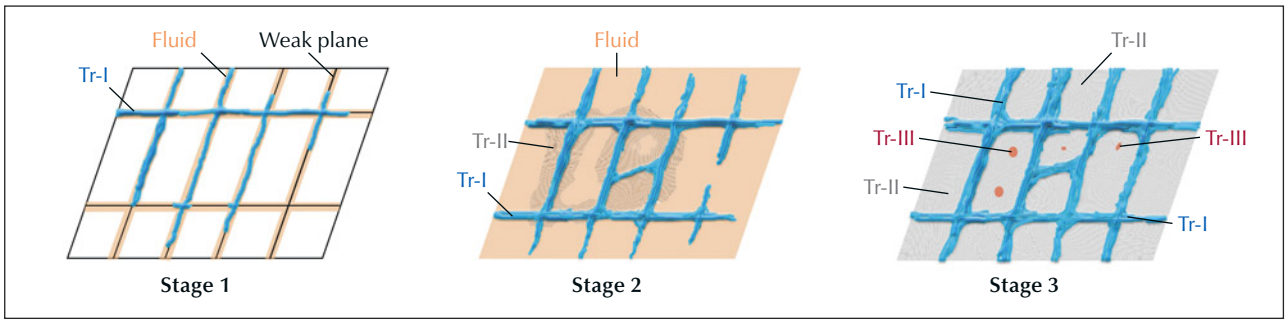

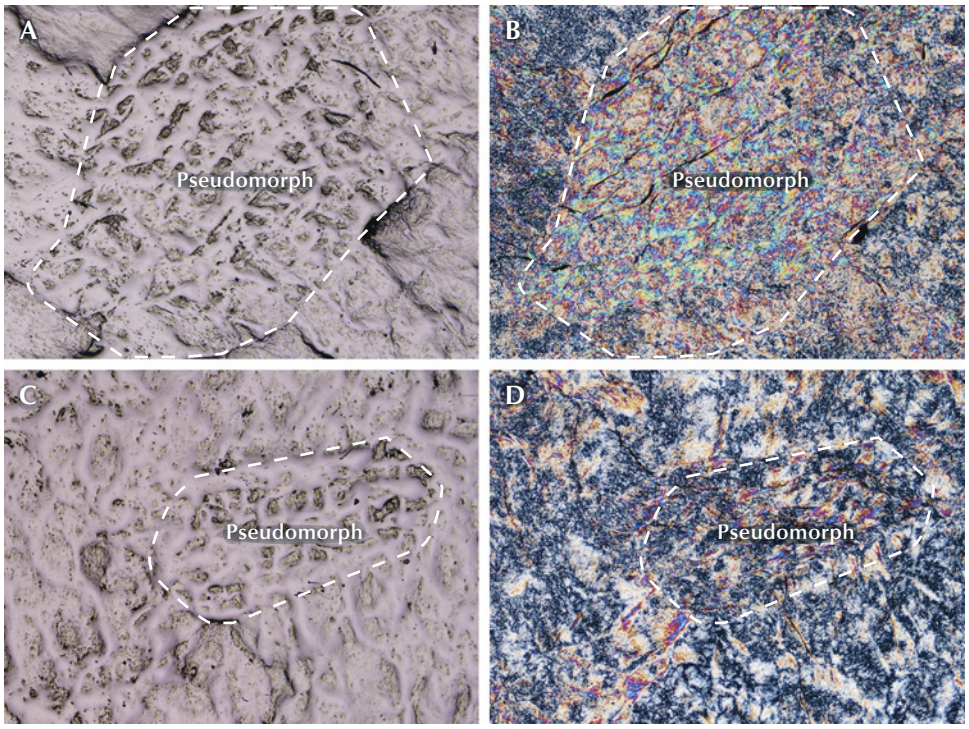

Figure 15. Correlation between textural pattern and microstructural framework in pseudomorphs from sample ELS27. A and C: Reflected darkfield illumination images showing the separate textural patterns of higher-relief vein nets and lower-relief central domains. B and D: Cross-polarized transmitted light images of the same areas shown in A and C, respectively, revealing the corresponding microstructural framework. Dashed lines outline the pseudomorph boundaries. Photomicrographs by Meiyu Shih; field of view 2.8 mm.

dense or less compact configurations. Notably, this visual effect was associated with a relatively flat plane rather than any real topography on the surface (again, see figure 6). The size and shape of the icy and cloudy domains correspond to those of the isogranular mosaic microstructure, with each domain very likely representing one pseudomorph. In figure 5, if the direction of the incident light were changed, then the brightness and transparency of these pseudomorphs may differ. Thus, these differences were associated with the isogranular mosaic microstructure of the precursor dolomite marble before the formation stage of the nephrite.

Microstructural observations of the individual pseudomorphs revealed that the vein net consisted of long tremolite fibers with almost the same orientation distributed along three cleavage planes, forming a three-dimensional network system of pseudo-rhomb frameworks by replacement of a precursor dolomite crystal. A schematic diagram illustrates the approximate orientation of tremolite; conoscopic interference images (featuring characteristic extinction patterns called isogyres) of Tr-I, Tr-II, and Tr-III indicate that the *c*-axis of tremolite (Tr-I) is subparallel to the cleavage plane of the replaced carbonate (figure 16). According to the optical indicatrix of tremolite (Verkouteren and Wylie, 2000; Deer et al., 2013), the maximum refractive index of tremolite was almost parallel to the long tremolite fiber orientation, and most oblique and vertical fiber sections had greater birefringence. This may explain why the vein net looked higher than the adjacent area. Furthermore, as the pseudo-rhomb may consist of either Tr-II alone or of a combination of Tr-II and Tr-III, the former, consisting of similarly oriented Tr-II, tends to appear relatively flat with minimal light scattering, and the latter, composed of variously oriented Tr-II and Tr-III, develops uneven surface relief that increases light scattering.

The central domain had an indistinct empty space between the tremolite fibers, indicating that the replacement of dolomite by tremolite resulted in volume shrinkage. A calculation based on reaction 1 can reveal the volume change. If the magnesium in dolomite were assumed to be relatively immobile and all the magnesium remained during the replacement of dolomite by tremolite, the volume of ideally calculated tremolite would be ~13% less than that of the replaced dolomite. For a specific pseudo-rhomb, assuming that the vein net framework had been consolidated, the process of forming tremolite would not fully occupy the central domain. This indicates that tremolite formation would require a greater volume of dolomite to be replaced. In this situation, if the earlier tremolite formation resulted in a consolidated framework, such as a vein net, then empty space would consequentially appear, similar to what has been revealed near the central pseudo-rhomb.

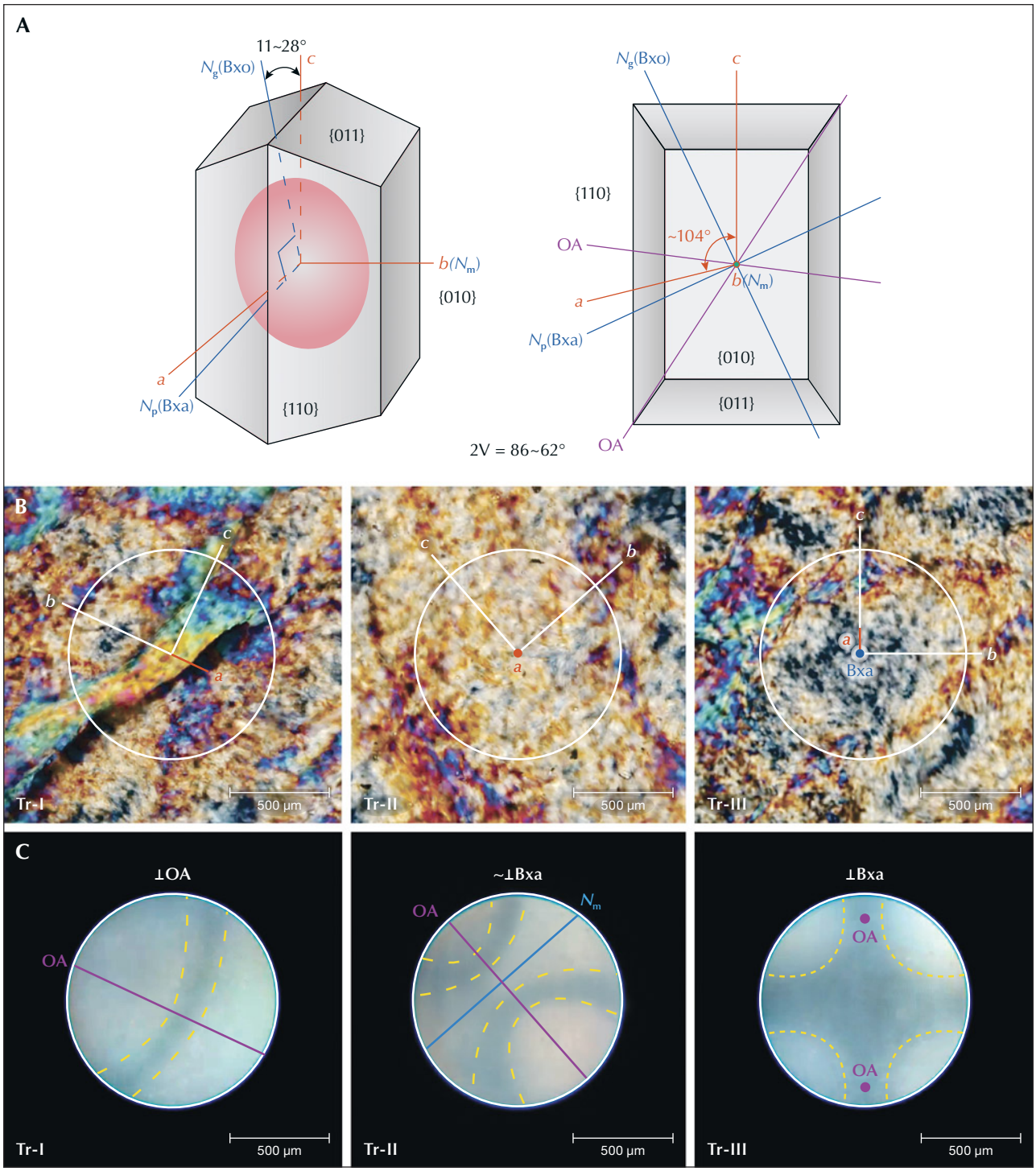

*Figure 16. A: Schematic diagram of the optical orientation of tremolite. The red oval represents the optical indicatrix, which is biaxial negative; the purple lines represent the optical axes (OA); the orange lines represent the crystallographic axes (*a, b, *and* c*); and the blue lines represent the optic principal axes (Bxa, Bxo, N_m) and the corresponding minimum (N_p; 1.599–1.612), intermediate (N_m; 1.614–1.626), and maximum (N_g; 1.625–1.637) refractive indices. B: Photomicrographs of Tr-I, Tr-II, and Tr-III in cross-polarized light. The orange lines and orange dot denote the possible orientations of the* a*-axis and correspond to the OA, while the white lines represent the possible orientations of the* b- *and* c*-axes. The blue dot marks the orientation of Bxa. C: Conoscopic interference images of Tr-I, Tr-II, and Tr-III. The yellow dashed lines outline the isogyre, the purple lines and purple dots correspond to the OA, and the white circle is the visual area size of the conoscope. Images by Meiyu Shih (B) and Biqian Xing (C).*

Ideally, in the case of individual dolomite grains, when the replacement by tremolite is initiated along the rhomb frame and subsequently formed a framework, the porous interior inside each pseudo-rhomb framework (again, see figures 11B, 13, and 14) could be the consequence of such volume loss to some degree, and a quantity of void space might accommodate further tremolite precipitation, as the precipitation of tremolite occurs widely in both dolomite-replacement and serpentine-replacement nephrites (e.g., Harlow and Sorensen, 2005; Zhang et al., 2022; Shi et al., 2024).

Causes of the Intrapseudomorph and Interpseudomorph Fissures. There are several possible causes for the development of intrapseudomorph and interpseudomorph fissures: volume-reducing replacement, displacement along the weak plane, uneven thermal expansion, or a gradual decrease in formation temperature of the nephrite. The volume-reducing replacement of dolomite by tremolite is regarded as the predominant reason. However, this volume reduction was more or less counteracted by the unique microstructure of the Russian white nephrite. In addition, the replacement occurred at a higher temperature than that during fissure development. This precludes synchronous formation of fissures, as the fissure is assumed to be coeval with the replacement and would have been occupied by precipitation of the fluids. The reason for displacement along the weak plane of the relevant rock and minerals by later tectonic activity, which could have involved carbonate cleavages or mechanical twinning retained during nephritization, the rerupture of veined Tr-III, or deflection along rigid bodies such as pseudomorph boundaries, was proposed by Brown and Macaudiére (1984), Tullis and Yund (1992), and Kushnir et al. (2015). However, flat and undeformed or very slightly deformed boundaries between neighboring pseudomorphs, well-preserved pseudomorphs, and their pseudo-rhombs showed no obvious evidence of this influence. Uneven thermal expansion caused by external forces might have induced fissures. Several Russian nephrite mines are located at elevations between 1000 and 1500 m with seasonal changes involving freezing and thawing, and the anisotropy of thermal expansion in randomly oriented grains might have caused fissures to grow. However, fissures, especially intrapseudomorph fissures, occurred exclusively along the vein of the pseudo-rhombs in the Russian white nephrite samples. Hence, the fissures were considered to be independent of uneven thermal expansion.

The most likely reason for the fissures was a gradual decrease in the formation temperature of the nephrite. For a specific rock body, if its microstructure is homogeneous, then volume shrinkage induced by a temperature drop might occur homogeneously. Some long hexagonal basalt prisms are good examples of this phenomenon (Xu et al., 2020). Although Russian white nephrite is a monomineral aggregate, its microstructure is inhomogeneous, even in an individual pseudomorph. The fissure morphology indicates gradual propagation rather than brittle failure, as evidenced by its selective occurrence along the boundaries among the pseudomorphs and the vein net inside the pseudomorphs. Therefore, such fissure characteristics that correlated with the inhomogeneous microstructure of the Russian white nephrite were interpreted as unique features. Thus, the lineation (especially the claw lineation) in Russian white nephrite has implications for locality identification.

Although lineation similar to that described in this paper has only been found in white nephrite from China (Xinjiang), South Korea, and Russia (e.g., Hou et al., 2010; Jiang et al., 2020), the lineation features in Xinjiang and South Korean nephrite show a long, densely oriented pattern or a long, slightly curved pattern and have been subjected to dynamic deformation.

Gemological Implications. Although all white nephrite from Russia, China, and South Korea are hosted by carbonate rocks and formed through the replacement of dolomitic marble (e.g., Yui and Kwon, 2002; Harlow and Sorensen, 2005; Burtseva et al., 2015; Gao et al., 2019b; Zhang et al., 2022), their appearance characteristics (such as transparency, luster, homogeneity, and compactness) are quite similar. However, this study reveals distinctive microfeatures specific to Russian white nephrite.

In particular, among 60 samples of Russian white nephrite, when seven samples with poor transparency and polish were excluded, we determined that 100% exhibited pits and bumps, 88% showed pseudo-rhombic microstructure, 81% displayed icy and cloudy domains, and 68% manifested claw lineation. Compared to the Russian samples studied here, reports from the literature and observations by experienced dealers (e.g., Zhang et al., 2001; Pei et al., 2011) indicate that white nephrite from other localities, including Qinghai, China, and Chuncheon, South Korea, does not exhibit such distinctive pseudomorphs with pseudo-rhombs. Therefore, this pattern of pseudomorphs with pseudo-rhombs in

Figure 17. A Russian white nephrite carving depicting a woman holding a lotus flower, measuring approximately 30 × 19 × 5 cm. Photo by Yu Ming.

white nephrite from Russia could be regarded as a diagnostic microstructure, and the orange peel effect could be used as a powerful and reliable way to distinguish Russian material from white nephrite originating from other localities, which is possible using only a 10× loupe.

CL imaging revealed the pseudomorphs, veins, and pseudo-rhombs of the Russian white nephrite. The strong pink luminescence of the netlike Tr-I made Tr-II and Tr-III more distinguishable, both of which exhibited pale pink to violet luminescing colors (again, see figure 13). CL imaging strongly supported our proposed model for the formation of this microstructure by fluid flow and precipitation and has further implications for identifying the origin and understanding the details of the formation of Russian white nephrite. The distinct CL characteristics of distribution, color, and intensity observed between Tr-I and Tr-II + Tr-III imply variations in their formative fluid properties or other growth conditions.

This microstructure, as well as the appearance of the orange peel effect on the polished surface of Russian white nephrite, has significant implications for understanding this nephrite's special properties and usage. The fissures and central domains within the pseudo-rhombs indicate that the nephrite material might easily become colored naturally in the presence of various dissolved metal oxides, which could explain a feature that Russian white nephrite often has: a thick "skin" with color variation. Such skin makes the white nephrite highly desirable for expressive carvings (e.g., Wang and Shi, 2020; figure 17). The thick colored layer may have geological and gemological implications that need further investigation to fully understand. Conversely, this characteristic may also allow this material to be deliberately dyed in the laboratory or factory, potentially causing problems with its identification.

CONCLUSIONS

White nephrite from Russia has a distinctive orange peel effect and a fissure-like surface, both of which can be attributed to a well-preserved isogranular pseudomorph microstructure formed through a unique metasomatic process. This microstructure features a three-dimensional net pattern that reflects its specific formation conditions.

A distinctive three-stage metasomatism model of dolomite replacement by tremolite for this Russian white nephrite with a unique microstructure of individual pseudomorphs was proposed. In the early stage, the Tr-I veins precipitated out during fluid flow, establishing a vein net for the pseudo-rhombs. In the middle stage, Tr-II formed on the foundation of the vein net, growing toward the inner domains inside the pseudo-rhombs. Finally, in the later stage, the Tr-III possibly filled the central parts of the pseudo-rhombs (the less compact parts of the domains). These complicated and independent pseudomorphs together create the distinctive microstructure of the Russian white nephrite.

The results of this study will contribute to not only understanding the microstructure of Russian white nephrite, but also to supporting the origin traceability of white nephrite.

ABOUT THE AUTHORS

Dr. Meiyu Shih (cvc5005@hotmail.com) obtained a PhD from the School of Gemology, China University of Geosciences in Beijing (CUGB), and is currently a lecturer at Quanzhou Liming Vocational University in Fujian, China. Dr. Guanghai Shi (shigh@cugb.edu.cn, corresponding author) is a professor at the School of Gemology, State Key Laboratory of Geological Processes and Mineral Resources, CUGB. Dr. Biqian Xing (xingbq@cnaes.edu.cn) obtained a PhD from the School of Gemology, CUGB, and is currently an assistant professor at the China National Academy of Educational Sciences in Beijing.

ACKNOWLEDGMENTS

Yu Ming is gratefully appreciated for providing the studied samples and the image in figure 17, Zuojiang Chen for providing the image in figure 1, and Ye Yuan and Qingqing Deng for helping with the experiments. The authors would like to thank George E. Harlow, Yan Li, and an anonymous reviewer for their thoughtful suggestions, which substantially improved this manuscript. This research was supported by the National Key Research and Development Project of China (grant no. 2022YFC2903302) and the National Science Foundation of China (grant no. 42273044).

REFERENCES

Blazek M.C. (1979) Classification of pseudomorphs. *Rocks & Minerals*, Vol. 54, No. 5, pp. 194–197, http://dx.doi.org/10.1080/00357529.1979.11764723

Bradt R.C., Newnham R.E., Biggers J.V. (1973) The toughness of jade. *American Mineralogist*, Vol. 58, No. 7-8, pp. 727–732.

Brodie K., Fettes D., Harte B., Schmid R. (2002) Towards a unified nomenclature of metamorphic petrology: 5. Structural terms including fault rock terms. Recommendations by the IUGS Subcommission on the Systematics of Metamorphic Rocks, https://www.ugr.es/~agcasco/personal/IUGS/pdf-IUGS/scmr_struc2_structuraltermsincludingfaultrockterms.pdf

Brown W.L., Macaudiére J. (1984) Microfracturing in relation to atomic structure of plagioclase from a deformed meta-anorthosite. *Journal of Structural Geology*, Vol. 6, No. 5, pp. 579–586, http://dx.doi.org/10.1016/0191-8141(84)90067-1

Burtseva M.V., Ripp G.S., Posokhov V.F., Murzintseva A.E. (2015) Nephrites of East Siberia: Geochemical features and problems of genesis. *Russian Geology and Geophysics*, Vol. 56, No. 3, pp. 402–410, http://dx.doi.org/10.1016/j.rgg.2015.02.003

Cha L. (2011) Metaphor and metonyms of jade in Chinese culture. *Journal of Chinese Language and Literature*, No. 23, pp. 93–95, http://dx.doi.org/10.3969/j.issn.1672-8610.2011.23.040 [in Chinese].

Chen D., Yu M., Luo W., Wang C. (2020) Sub-microstructures of nephrite from five sources based on multispectral imaging and effect enhancement. *Asian Journal of Advanced Research and Reports*, Vol. 12, No. 3, pp. 13–24, http://dx.doi.org/10.9734/AJARR/2020/v12i330288

Deer W.A., Howie R.A., Zussman J. (2013) Tremolite-ferro-actinolite $\square Ca_2(Mg, Fe^{2+})_5[Si_8O_{22}](OH,F)_2$. *An Introduction to the Rock-Forming Minerals*, Mineralogical Society of Great Britain and Ireland, pp. 150–153, http://dx.doi.org/10.1180/DHZ

Gao K., Shi G.H., Wang M.L., Xie G., Wang J., Zhang X.C., Fang T., Lei W., Liu Y. (2019a) The Tashisayi nephrite deposit from South Altyn Tagh, Xinjiang, northwestern China. *Geoscience Frontiers*, Vol. 10, No. 4, pp. 1597–1612, http://dx.doi.org/10.1016/j.gsf.2018.10.008

Gao S., Bai F., Heide G. (2019b) Mineralogy, geochemistry and petrogenesis of nephrite from Tieli, China. *Ore Geology Reviews*, Vol. 107, pp. 155–171, http://dx.doi.org/10.1016/j.oregeorev.2019.02.016

Gao K., Fang T., Lu T., Lan Y., Zhang Y., Wang Y., Chang Y. (2020) Hydrogen and oxygen stable isotope ratios of dolomite-related nephrite: Relevance for its geographic origin and geological significance. *G&G*, Vol. 56, No. 2, pp. 266–280, http://dx.doi.org/10.5741/GEMS.56.2.266

Hansen R. (2022) *Gemstones: A Concise Reference Guide*. Princeton University Press, New Jersey.

Harlow G.E., Sorensen S.S. (2005) Jade (nephrite and jadeitite) and serpentinite: Metasomatic connections. *International Geology Review*, Vol. 47, No. 2, pp. 113–146, http://dx.doi.org/10.2747/0020-6814.47.2.113

Hobbs B.E., Means W.D., Williams P.F. (1976) *An Outline of Structural Geology*. Wiley, New York.

Holland T.J.B. (2009) AX: A program to calculate activities of mineral endmembers from chemical analyses (usually determined by electron microprobe). University of Cambridge, http://ccp14.cryst.bbk.ac.uk/ccp/web-mirrors/crush/astaff/holland/ax.html

Hou H., Wang Y., Liu Y.F. (2010) Study of gemological characteristic of Korea nephrite jade. *Northwestern Geology*, Vol. 43, No. 3, pp. 147–153 [in Chinese].

Hu W., Di J.R., Yang Y. (2011) An analysis of characteristics of "water line" in nephrite from Qinghai Province. *Journal of Gems and Gemmology*, Vol. 13, No. 4, pp. 14–18 and 25, http://dx.doi.org/10.3969/j.issn.1008-214X.2011.04.005 [in Chinese].

Jiang Y., Shi G., Xu L., Li X. (2020) Mineralogy and geochemistry of nephrite jade from Yinggelike deposit, Altyn Tagh (Xinjiang, NW China). *Minerals*, Vol. 10, No. 5, article no. 418, http://dx.doi.org/10.3390/min10050418

Kushnir A.R.L., Kennedy L.A., Misra S., Benson P., White J.C. (2015) The mechanical and microstructural behavior of calcite-dolomite composites: An experimental investigation. *Journal of Structural Geology*, Vol. 70, pp. 200–216, http://dx.doi.org/10.1016/j.jsg.2014.12.006

Leake B.E., Woolley A.R., Arps C.E.S., Birch W.D., Gilbert M.C., Grice J.D., Hawthorne F.C., Kato A., Kisch H.J., Krivovichev V.G., Linthout K., Laird J., Mandarino J.A., Maresch W.V., Nickel E.H., Rock N.M.S., Schumacher J.C., Smith D.C., Stephenson N.C.N., Ungaretti L., Whittaker E.J.W., Youzhi G. (1997) Nomenclature of amphiboles—Report of the subcommittee on Amphiboles of the International Mineralogical Association Commission on New Minerals and Mineral Names. *European Journal of Mineralogy*, Vol. 9, No. 3, pp. 623–651.

Ling X., Schmädicke E., Wu R., Wang S., Gose J. (2013) Composition and distinction of white nephrite from Asian deposits. *Neues Jahrbuch für Mineralogie Abhandlungen*, Vol. 190, No. 1, pp. 49–65, http://dx.doi.org/10.1127/0077-7757/2013/0229

Liu Y., Deng J., Shi G.H., Sun X., Yang L. (2011a) Geochemistry and petrogenesis of placer nephrite from Hetian, Xinjiang, Northwest China. *Ore Geology Reviews*, Vol. 41, No. 1, pp. 122–132, http://dx.doi.org/10.1016/j.oregeorev.2011.07.004

Liu Y., Deng J., Shi G.H., Yui T.-F., Zhang G., Abuduwayiti M., Yang L., Sun X. (2011b) Geochemistry and petrology of nephrite from Alamas, Xinjiang, NW China. *Journal of Asian Earth Sciences*, Vol. 42, No. 3, pp. 440–451, http://dx.doi.org/10.1016/j.jseaes.2011.05.012

Manutchehr-Danai M. (2009) *Dictionary of Gems and Gemology*. Springer-Verlag, Berlin and Heidelberg.

Read P.G. (2008) *Gemmology*, 3rd ed. The Crowood Press, Wiltshire, UK.

Pei X.X., Qian Z., Shi G.H. (2011) A mineralogical study of the Chuncheon nephrite, South Korea. *Acta Petrologica et Miner-*

alogica, Vol. 30, No. Z1, pp. 89–94 [in Chinese with English abstract].
Shi G.H., Wang X., Chu B., Cui W. (2009) Jadeite jade from Myanmar: Its texture and gemmological implications. *Journal of Gemmology*, Vol. 31, No. 5, pp. 185–195.
Shi G.H., Jia R., Santosh M., Liang H., He H. (2024) First report of a nephrite deposit from Somaliland, Africa: Characterization and geological and archeological implications. *Geological Society of America Bulletin*, Vol. 136, No. 1-2, pp. 661–672, http://dx.doi.org/10.1130/B36826.1
Shih M.Y., Yuan Y., Shi G.H. (2024) Comparative analysis of LDA, PLS-DA, SVM, RF, and voting ensemble for discrimination origin in greenish-white to white nephrites using LIBS. *Journal of Analytical Atomic Spectrometry*, Vol. 39, pp. 1560–1570, http://dx.doi.org/10.1039/D3JA00464C
Tullis J., Yund R. (1992) The brittle-ductile transition in feldspar aggregates: An experimental study. *International Geophysics*, Vol. 51, pp. 89–117, http://dx.doi.org/10.1016/S0074-6142(08)62816-8
Verkouteren J.R., Wylie A.G. (2000) The tremolite-actinolite-ferro–actinolite series: Systematic relationships among cell parameters, composition, optical properties, and habit, and evidence of discontinuities. *American Mineralogist*, Vol. 85, No. 9, pp. 1239–1254, http://dx.doi.org/10.2138/am-2000-8-917
Wang J. (2022) The changes in the nephrite industry - talk with experts. *China Collections*, No. 3, pp. 62–65 [in Chinese].
Wang M.Y., Shi G.H. (2020) The evolution of Chinese jade carving craftsmanship. *G&G*, Vol. 56, No. 1, pp. 30–53, http://dx.doi.org/10.5741/GEMS.56.1.30
Wang S.Q., Sun L.H. (2013) Visual identification of tremolite features of five origins in today's nephrite jade market. *Proceeding of the 2013 China Gems Jewelry Academic Conference*, Beijing, China, pp. 139–141 [in Chinese].
Xu S., Nieto-Samaniego Á.F., Alaniz-Álvarez S.A. (2020) Column-normal fracture features of the basaltic joints in Santa Maria Regla, Hidalgo State, Mexico. *Journal of South American Earth Sciences*, Vol. 101, article no. 102611, http://dx.doi.org/10.1016/j.jsames.2020.102611
Yang S.-Y., Jiang S.-Y., Mao Q., Chen Z.-Y., Rao C., Li X.-L., Li W.-C., Yang W.-Q., He P.-L., Li X. (2022) Electron probe microanalysis in geosciences: Analytical procedures and recent advances. *Atomic Spectroscopy*, Vol. 43, No. 2, pp. 186–200, http://dx.doi.org/10.46770/AS.2021.912
Yui T.-F., Kwon S.-T. (2002) Origin of a dolomite-related jade deposit at Chuncheon, Korea. *Economic Geology*, Vol. 97, No. 3, pp. 593–601, http://dx.doi.org/10.2113/97.3.593
Zhang P., Zhao Q.-Y. (2012) Comparative analysis on gemmological characteristics of white nephrite gravel from Xinjiang and Russia. *Superhard Material Engineering*, Vol. 5, No. 24, pp. 48–53 [in Chinese].
Zhang X.C., Shi G.H., Zhang X.M., Gao K. (2022) Formation of the nephrite deposit with five mineral assemblage zones in the central western Kunlun Mountains, China. *Journal of Petrology*, Vol. 63, No. 11, article no. egac117, http://dx.doi.org/10.1093/petrology/egac117
Zhang X.H., Wu R.H., Wang L.Y. (2001) Research on petrologic character of nephrite jade from Baikal Lake Region in Russia. *Journal of Gems and Gemmology*, Vol. 3, No. 1, pp. 12–17, http://dx.doi.org/10.3969/j.issn.1008-214X.2001.01.003 [in Chinese].
Zhou Z.Y., Liao Z.T., Chen Y., Li Y.J., Ma T.T. (2008) Petrological and mineralogical characteristics of Qinghai nephrite. *Rock and Mineral Analysis*, Vol. 27, No. 1, pp. 17–20 [in Chinese with English abstract].
Zhou D., Shi G., Liu S., Wu B. (2021) Mineralogy and magnetic behavior of yellow to red Xuanhua-type agate and its indication to the forming condition. *Minerals*, Vol. 11, No. 8, article no. 877, http://dx.doi.org/10.3390/min11080877

CONGRATULATIONS

This year, readers from all over the world took the 2025 *Gems & Gemology* Challenge, testing their knowledge by answering questions listed in the Spring 2025 issue. Participants who earned a score of 75% or higher received a GIA Certificate of Completion. Those who earned a perfect score are listed below.

G&G Challenge Winners

Australia
Barbara Wodecki

India
Raju Jain

Malaysia
Arnold Cheong
Gam Peih Yinn

Ukraine
Nataliya Vovk

United States
Younga Choi
Elly Etheridge
Martin Harmon
Jessica Kramer
Steffano Minetto
Jana Miyahira-Smith
Jane No
Teresa Tolbert
Kate Trunnell
Flora Walters
Kate Waterman
Thomas Wendt
Cathy (Yingying) Zhong

Answers

See pages 82–83 of the Spring 2025 issue for the questions.

1 (b), 2 (a), 3 (d), 4 (c), 5 (a), 6 (b), 7 (d), 8 (c), 9 (b), 10 (a), 11 (b), 12 (d), 13 (a), 14 (b), 15 (d), 16 (a), 17 (d), 18 (a), 19 (d), 20 (b), 21 (a), 22 (c), 23 (a), 24 (b), 25 (a)

A Legacy of Gemological Innovation.

GIA Colored Stone Reports

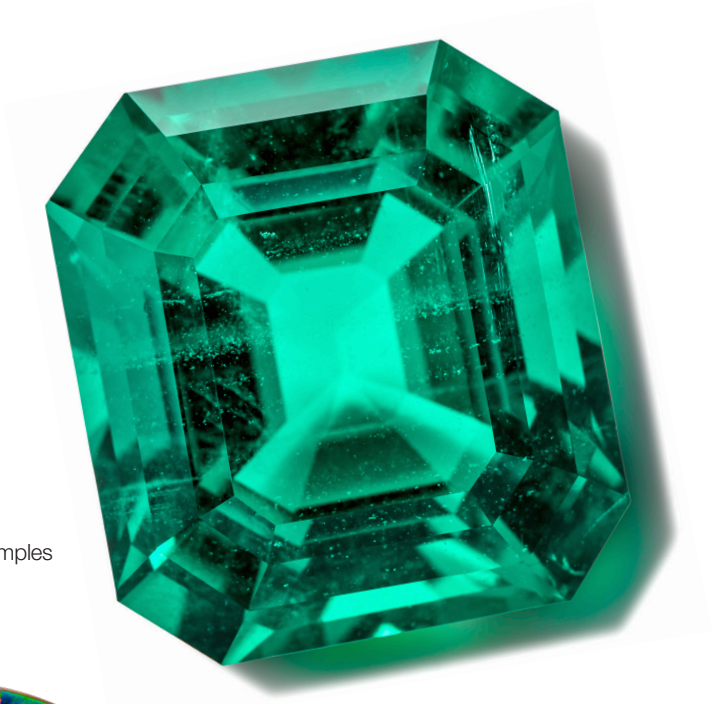

- 28,000+ gem reference samples and 100+ field expeditions

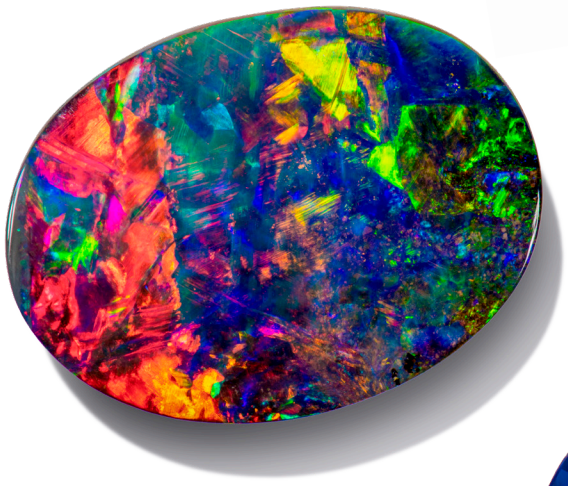

- 70+ research scientists and expert gemologists

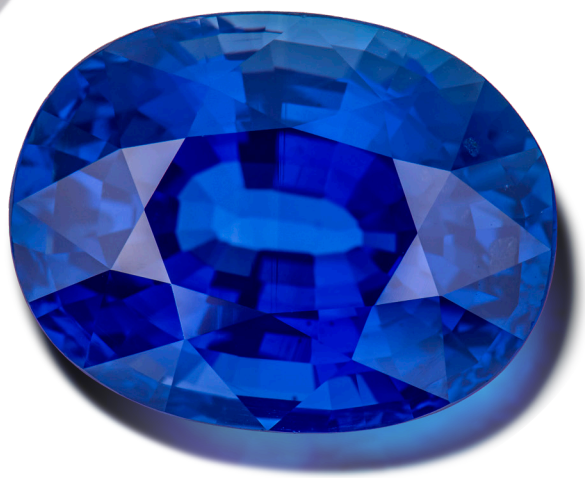

- A global network of colored stone laboratories

Our renowned field gemology and research scientists build a strong foundation, with extensive global expeditions and an unrivaled collection of gem specimens.

Our expert gemologists provide critical insights, precisely identifying colored stone treatments and origins.

Our respected reports help your customers feel secure with accurate information and confident in their purchase.

Get Your Report

GIA.edu/ColoredStones

Lab Notes

Editors

Thomas M. Moses | Shane F. McClure
Sally Eaton-Magaña | Artitaya Homkrajae

Figure 1. This 37.41 ct rough diamond has distinct pink and colorless zones. Photos by Tebogo Hambira.

DIAMONDS

Extraordinary Large Bicolor Natural Rough Diamond

Rough pink diamonds are rarely found, and although the cause of color has been correlated with plastic deformation, the precise mechanism and atomic configuration for the resulting color are topics of continuous research. Therefore, when GIA receives a diamond with distinct pink and colorless sections (figure 1), it is of scientific interest, particularly at an astounding weight of 37.41 ct. GIA has previously examined comparable type Ia pink and colorless bicolor rough, both reportedly from Australia, in much smaller specimens weighing less than 2 ct each (Spring 2021 Lab Notes, pp. 53–55).

Sourced from the Karowe mine in Botswana, this rare find was submitted to GIA's Botswana laboratory for the GIA Diamond Origin Report service. The stone measured 24.3 × 16.0 × 14.5 mm and examination showed mostly a sharp boundary between the pink and colorless zones (figure 2).

The Karowe mine recently has been a frequent source of noteworthy diamonds, including the second-largest rough diamond ever recovered at 2,488 ct ("GIA tests the world's second largest diamond," *GIA Research News*, August 15, 2025), nine diamonds weighing more than 1,000 ct each, and several other pink diamonds, such as the 62 ct type IIa "Boitumelo" ("Lucara recovers 62 carat fancy pink diamond 'Boitumelo' from the Karowe mine in Botswana," July 13, 2021, https://lucaradiamond.com/newsroom/news-releases/lucara-recovers-62-carat-fancy-pink-diamond-boitum-122825/).

Fourier-transform infrared absorption, visible/near-infrared (Vis-NIR) absorption, and photoluminescence (PL) spectroscopy along with deep-UV imaging were collected from both the pink and the colorless portions of the submitted diamond in order to better characterize its properties. The diamond was identified as type IIa with no observable differences in the IR spectra in the two sections. Vis-NIR absorption showed the 550 nm absorption band in the spectrum collected from the pink section; unsurprisingly, it was absent from the colorless section (figure 3). There were minor differences in features detected within the PL spectra collected with 457, 633, and 830 nm lasers, along with deep-UV fluorescence imaging when comparing data collected between the pink and colorless portions. However, the full peak width at half-maximum of the H3 center (NVN^0; 503.2 nm) was significantly narrower in the pink section (0.61 nm) than in the colorless section (1.12 nm).

The 514 nm PL spectra did show some differences (figure 4). The pink zone displayed an undulating broad

Editors' note: All items were written by staff members of GIA laboratories.

GEMS & GEMOLOGY, Vol. 61, No. 3, pp. 290–301.

Figure 2. This boundary shows a sharp transition from pink to colorless zones. Photomicrograph by Wanling Tan; field of view 4 mm.

photoluminescence band centered at ~670 nm, commonly seen in the PL spectra of pink diamonds, that was not apparent in the colorless spectrum (S. Eaton-Magaña et al., "Comparison of gemological and spectroscopic features in type IIa and Ia natural pink diamonds," *Diamond and Related Materials*, Vol. 105, 2020, article no. 107784). Additionally, the 514 nm PL spectrum from the colorless zone showed a series of features from 790–840 nm; although this series of features is uncharacterized, it is often observed in the 514 nm PL spectra of rough IIa diamonds and occasionally faceted diamonds.

Nearly all natural pink diamonds derive their color from the 550 nm absorption band, which is generally accepted as a byproduct in the diamond when stress, such as mountain-building events, results in plastic deformation of the stone. From what is understood about pink diamond formation, the

Figure 3. Comparison of Vis-NIR absorption spectra collected from the pink and colorless sections. Spectra are offset vertically for clarity.

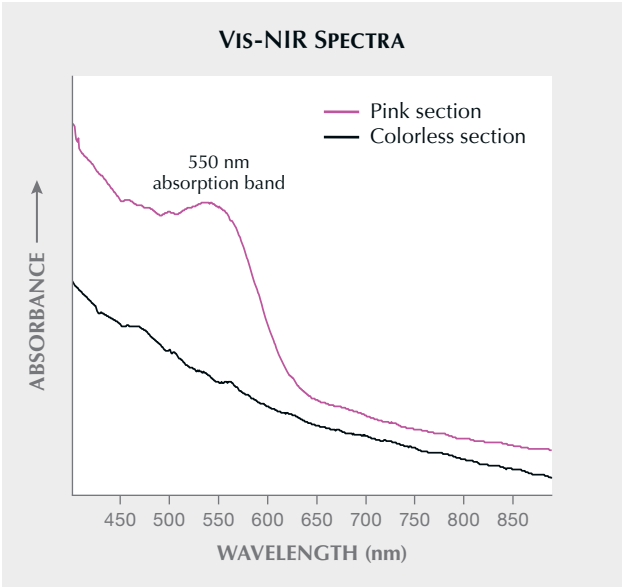

Figure 4. Comparison of 514 nm PL spectra collected at liquid nitrogen temperature from the pink and colorless sections. Spectra are offset vertically for clarity and are scaled such that the second-order diamond Raman features are equal.

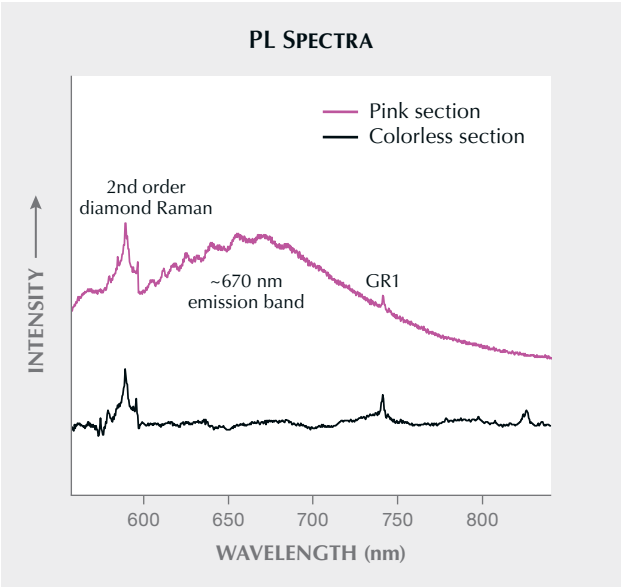

pink section likely was initially colorless and then plastically deformed resulting in its pink color; it is assumed that the colorless section formed at a later time after the stress-causing event. The distinctive appearance of this bicolor rough diamond displaying two attractive colors, its large size, and its potential to yield more information about pink diamond formation make this diamond quite noteworthy.

Sally Eaton-Magaña, Kgotlaetsho Baatshwana, and Norma-Jean Osi

Pink Diamond with Mottled Appearance

A 1.10 ct Fancy Deep brownish orangy pink round diamond was recently submitted to GIA's New York laboratory for analysis (figure 5). This diamond was multi-treated—a combination of high-pressure, high-temperature (HPHT) annealing, irradiation, and subsequent moderate temperature heating—with the intent to create nitrogen vacancy (NV) centers and thus achieve the desirable pink color. Prior to treatment, we assume this diamond was probably a less desirable brownish color (this has not been verified).

When viewed face-up, the diamond exhibited a mottled appearance. Further examination with a gemological microscope revealed that these patterns extended from a shallow depth to the polished surface. An uneven distribution of pink color created the mottled appearance—a very unusual feature for a treated pink diamond.

Figure 5. A 1.10 ct Fancy Deep brownish orangy pink diamond. Photo by Towfiq Ahmed.

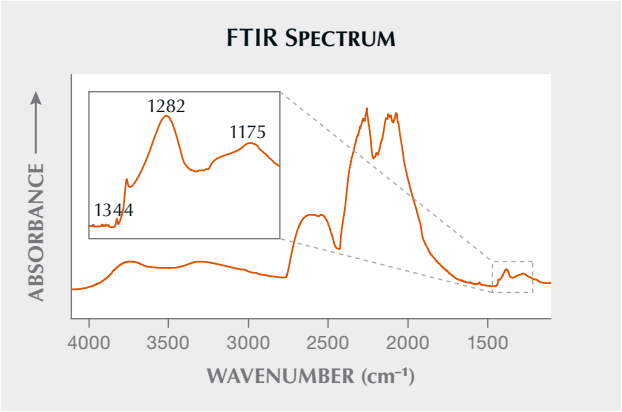

Figure 6. Mid-infrared spectrum showing the one-phonon region, A and B aggregated nitrogen at 1282 cm^{-1} and 1175 cm^{-1}, respectively, with type Ib (isolated nitrogen) at 1344 cm^{-1}.

The mid-infrared spectrum of this diamond (figure 6) shows it is a type IaAB with A aggregated nitrogen at 1282 cm^{-1} and B aggregated nitrogen at 1175 cm^{-1} distributed throughout the diamond crystal structure. Isolated single nitrogen impurities were detected at 1344 cm^{-1} (likely the result of HPHT annealing). An uneven distribution of nitrogen aggregates may have resulted in a variable NV center distribution and thus the subtle color distribution.

The visible/near-infrared (Vis-NIR) absorption spectrum obtained from this diamond has typical spectral features of a treated diamond exposed to laboratory irradiation and heat treatments. These features include the 594 nm peak indicative of irradiation, the NV^0 and NV^- centers causing the pink color, and the H2 center indicative of heat treatment (figure 7). Deep-UV fluorescence images, as observed using the DiamondView instrument, show a combination of yellow and orange fluorescence; both of these fluorescence colors can be created by NV centers and the observed color can vary

Figure 7. Vis-NIR absorption spectrum showing the 594 nm, NV^0 and NV^- (attributed to the pink color), and H2 centers, indicative of treatment.

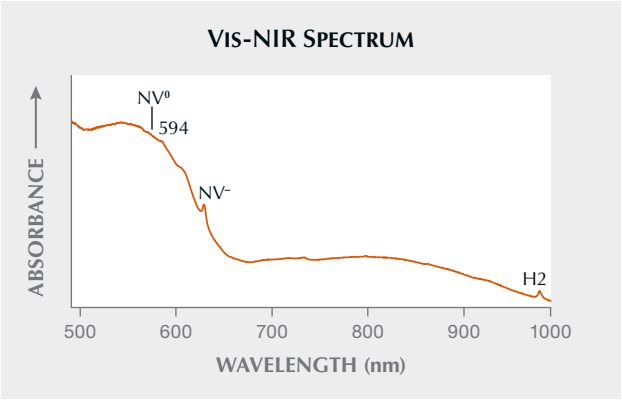

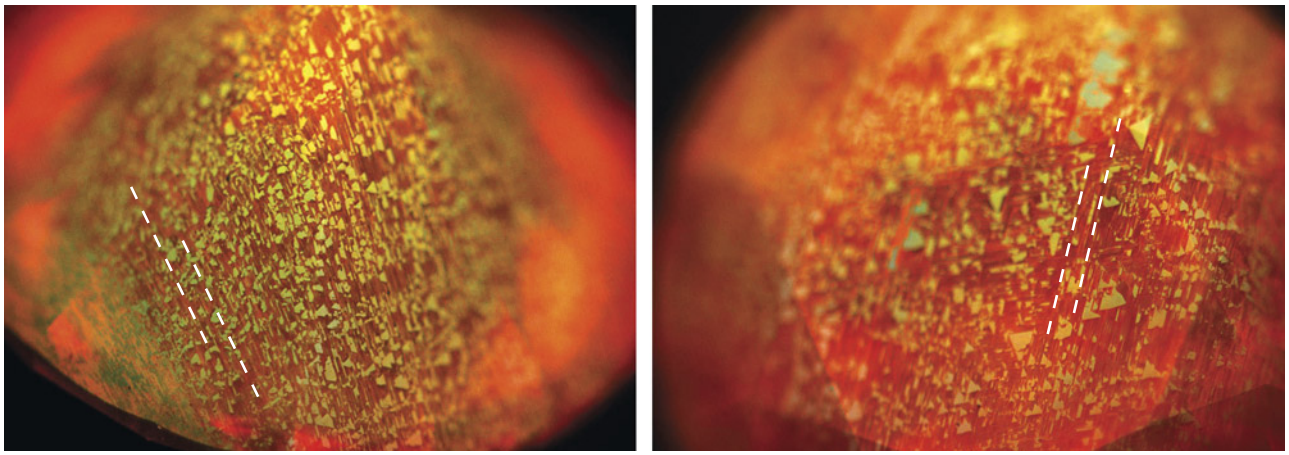

Figure 8. DiamondView images of pavilion and crown facets. The yellow and orange fluorescence, attributed to the NV^0 and NV^- nitrogen vacancy centers, follows the patterns dictated by the deformation of the crystal structure. Images by Paul Johnson.

based on the ratio of the negative to neutral NV center intensities. The NV center distribution and the variation in the ratio of the NV centers are assumed to be related to the nitrogen aggregate distribution, which could explain the mottled color distribution. However, no IR mapping to chronicle the nitrogen aggregate distribution and no photoluminescence mapping of the NV centers to confirm their distribution was performed.

After formation within the earth, the crystal structure of a diamond can be subjected to plastic deformation, which can impart a brown color to the crystal. Such deformation, which is common in brown diamonds (R. Tappert and M.C. Tappert, *Diamonds in Nature: A Guide to Rough Diamonds*, Springer, 2011), appears to resemble the fluorescence patterns observed in the DiamondView images shown in figure 8. These DiamondView images also show a striking pattern in the diamond following the deformation lines on the octahedral crystal faces. Such plastic deformation may have contributed to the mottled pattern observed on the diamond, with the nitrogen vacancy centers created by treatment appearing to follow these deformation lines.

This is a notable example of treatments used to enhance the color of a natural diamond.

Dimitry Krugolets and Paul Johnson

Starburst Cloud Inclusions in Diamond

Recently, the Carlsbad laboratory examined a 2.50 ct Faint yellow-green round brilliant diamond with several randomly distributed yellow zones consisting of stacks of clouds with four-sided star patterns near the girdle (figure 9). The clouds were clusters of micro-inclusions, with the center of each cloud containing more intensely colored particles in a cross pattern. When viewed from a different

Figure 9. Viewed through the pavilion, trails of starburst-patterned clouds were observed in patches near the girdle in a 2.50 ct diamond; in the center of each cloud were more intensely colored particles appearing to form a cross pattern. Photomicrographs by Forozan Zandi; fields of view 1.26 mm (left) and 2.34 mm (right).

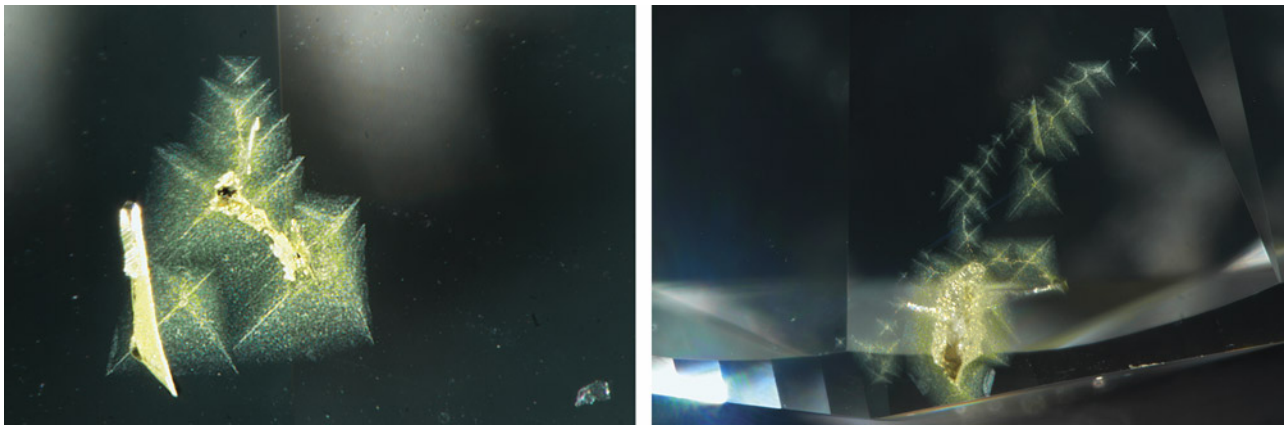

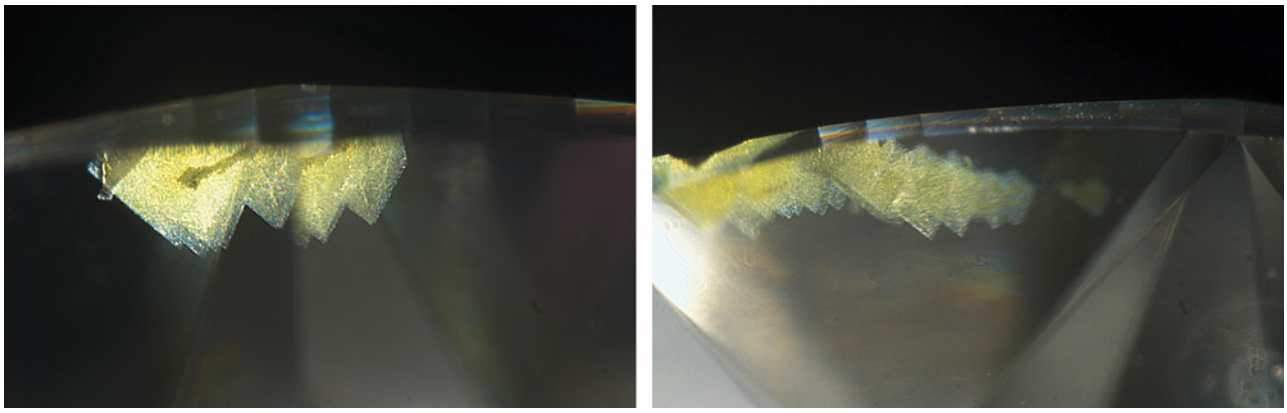

Figure 10. The same clouds appeared as a row of triangular spikes when viewed from a different direction through the pavilion. Photomicrographs by Forozan Zandi; fields of view 1.42 mm (left) and 1.58 mm (right).

direction, the same clouds appeared as a row of bright yellow overlapping triangles (figure 10). The uniqueness of these clouds triggered an in-depth investigation.

The body of the diamond exhibited blue fluorescence to long-wave (365 nm) UV radiation, and with a deep-UV (<230 nm) imaging microscope, the authors were able to discern that the cloud patches showed weak yellow fluorescence (figure 11).

The diamond's ultraviolet/visible/near-infrared absorption spectrum revealed cape absorption features at 415 (N3 center) and 478 (N2 center) nm. In addition, broad absorption bands centered at 730 and 836 nm, as well as a peak at 563 nm, were indicative of hydrogen-related defects (C.M. Breeding et al., "Naturally colored yellow and orange gem diamonds: The nitrogen factor," Summer 2020 *G&G*, pp. 194–219). The infrared absorption spectrum indicated that the diamond was type Ia with high abundance of both nitrogen and hydrogen.

Figure 11. When exposed to deep-UV excitation, the bulk of the diamond showed blue surface fluorescence, whereas the yellow color zones and the cross patterns with visibly darker particles showed weak yellow surface fluorescence. Image by Sally Eaton-Magaña.

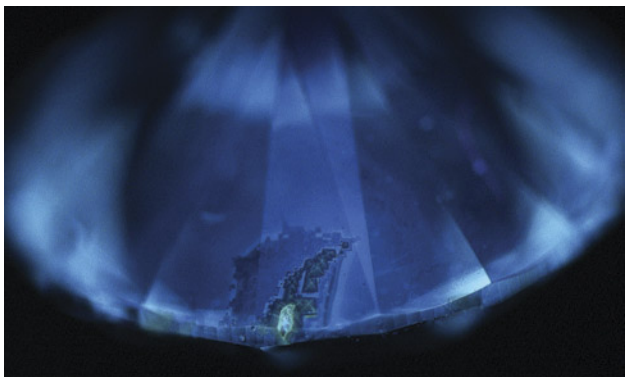

While hydrogen-related defects might cause brownish or greenish components to the diamond bodycolor, they are not responsible for the bright yellow color zones in this diamond. Generally, yellow color in diamond is caused by cape defects, H3 defects, isolated nitrogen (C-center), or a 480 nm absorption band (Breeding et al., 2020). However, patchy yellow color zones are more often associated with C-centers or a 480 nm absorption band (e.g., Breeding et al., 2020; M.Y. Lai et al., "Spectroscopic characterization of rare natural pink diamonds with yellow color zones," *Diamond and Related Materials*, Vol. 148, 2024, article no. 111428).

Photoluminescence (PL) spectra were collected on the bright yellow color zones and the surrounding areas, and neither the H3 center (at 503.2 nm) nor the characteristic PL features associated with the 480 nm absorption band (Lai et al., 2024) were detected. This finding suggests that these were not the causes for the yellow color zones in this diamond. The NV^- center at 637 nm, a common feature of diamonds colored by isolated nitrogen, was detected only within the bright yellow color zones, indicating that the yellow color was likely due to the presence of C-centers located in a confined region on the surface of the diamond.

Previously, a yellow overgrowth layer that formed on top of a near-colorless diamond in the late stage of diamond growth was reported (e.g., M.Y. Lai et al., "Yellow diamonds with colourless cores – Evidence for episodic diamond growth beneath Chidliak and the Ekati Mine, Canada," *Mineralogy and Petrology*, Vol. 114, 2020, pp. 91–103). However, the composition and formation of the clouds of micro-inclusions coincident with the yellow color zones in this diamond are currently unclear and require further investigation. This diamond with starburst-patterned clouds and patchy yellow zones highlights the crucial role of *in situ* analytical techniques in gemstone identification, where the causes of color zones can be determined based on well-resolved spectroscopic features.

Forozan Zandi, Mei Yan Lai, and Sally Eaton-Magaña

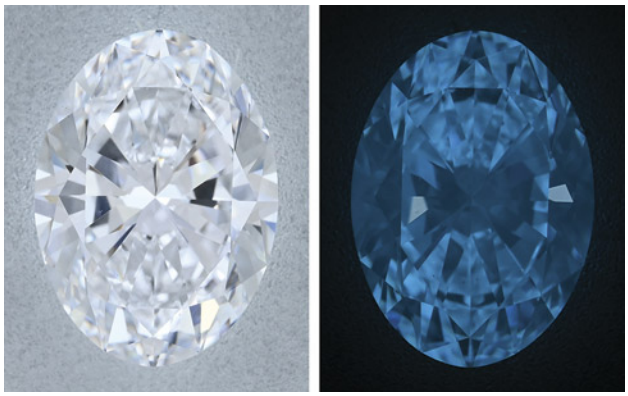

Figure 12. The 2.50 ct diamond under white LED lighting of 6500 K (left) and in a dark environment around 10 s after deep-UV excitation to showcase its phosphorescence (right). Photos by Nick "Ka Chun" Chan.

Type IIa/IaB Diamond Showing Transient Type IIb Responses

Recently, the Dubai laboratory encountered a strongly phosphorescent natural type IIa/IaB diamond, which showed a transient response, shifting to type IIb after deep-ultraviolet (<230 nm) excitation. The 2.50 ct oval-shaped diamond was graded as D color with VS_1 clarity and received Excellent grades on both polish and symmetry. Although instances of strong phosphorescence (Winter 2017 Gem News International, pp. 476–478; Summer 2021 Gem News International, pp. 177–178) and similar transient responses in natural diamonds (J. Li et al., "A diamond with a transient 2804 cm^{-1} absorption peak," *Journal of Gemmology*, Vol. 35, No. 3, 2016, pp. 248–252; Winter 2018 Gem News International, pp. 453–455) have been reported previously, this diamond's size and quality make it notable.

Strong and long-lived phosphorescence such as the blue phosphorescence observed in this diamond is typical of high-pressure, high-temperature (HPHT) laboratory-grown diamonds. As the necessary ingredients for observed phosphorescence, neutral boron and neutral isolated nitrogen can be present in HPHT-grown diamonds in abundance. However, when observed in natural diamonds, particularly those with a D color grade, phosphorescence is usually weak and fleeting. The fact that this diamond exhibited a strong and long-lasting phosphorescence (figure 12) with a duration of more than one minute prompted further investigation.

Photoluminescence (PL) spectra obtained using 830 nm laser excitation at liquid nitrogen temperature showed a very weak 883.1/884.6 nm doublet, a feature that is related to nickel impurities. In addition, 514 nm laser excitation produced a spectrum with a weak nickel-related broad band centered at ~640 nm (W. Wang et al., "Natural type Ia diamond with green-yellow color due to Ni-related defects," Fall 2007 *G&G*, pp. 240–243) and a sharp 694 nm peak ascribed to Ni-N complexes (C.M. Breeding et al., "Natural-color green diamonds: A beautiful conundrum," Spring 2018 *G&G*, pp. 2–27). These characteristics all indicated the presence of nickel, but compared to those commonly seen in HPHT-grown diamonds, the PL intensities of these nickel-related features were much lower. DiamondView imaging further ruled out the possibility of an HPHT-grown diamond due to the absence of typical growth sectors.

While possible to observe nickel impurities in natural diamonds, it is rarely coupled with strong phosphorescence, warranting a more thorough investigation. A Fourier-transform infrared (FTIR) spectrum (figure 13) was re-collected immediately after

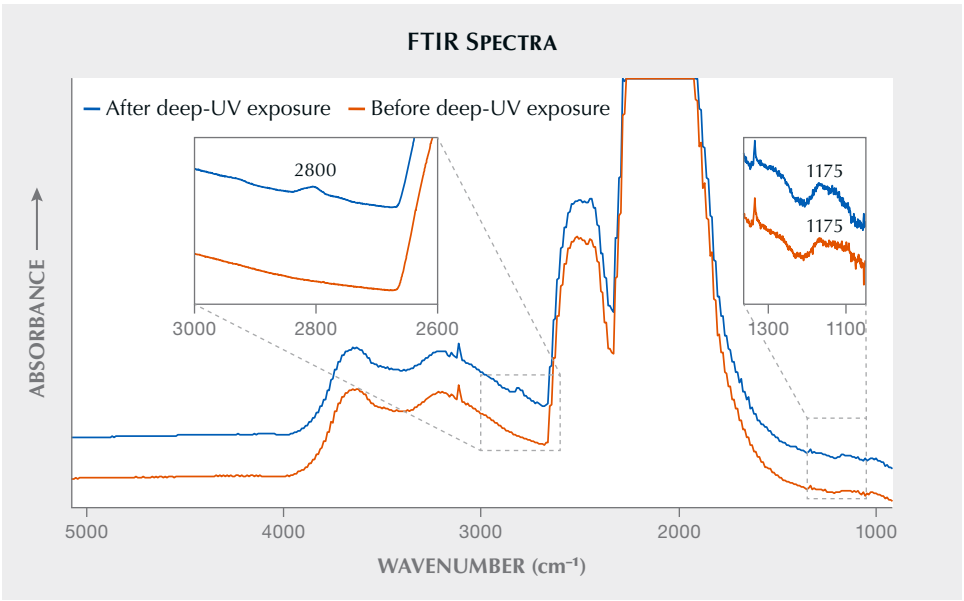

Figure 13. FTIR spectra show a change in diamond type before and after deep-UV exposure. Immediately after deep-UV exposure, an absorption at ~2800 cm^{-1} was observed, indicating an uncompensated boron concentration at ~3 ppb. Spectra are normalized for comparison and offset vertically for clarity.

deep-UV exposure. An absorption at 2800 cm^{-1} was induced which correlated to an ~3 ppb concentration of uncompensated boron, and then it slowly decayed and became undetectable within a few minutes, a timeframe longer than the duration in which observable phosphorescence dissipated. The weak nitrogen B-center at 1175 cm^{-1}, on the other hand, remained unaffected by deep-UV exposure. This transient response suggested that boron had been made uncompensated upon deep-UV exposure and then became detectable under FTIR spectroscopy. A mechanism has been suggested by Dean (P.J. Dean, "Bound excitons and donor-acceptor pairs in natural and synthetic diamond," *Physical Review*, Vol. 139, 1965, pp. A588–A602), and a decay model has also been proposed and studied (J. Zhao et al., "Phosphorescence and donor-acceptor pair recombination in laboratory-grown diamonds," *Physical Review B*, Vol. 108, 2023, article no. 165203).

For PL analysis, the sample was transferred immediately after deep-UV exposure to the PL system. Each PL spectrum was re-collected shortly after deep-UV exposure, but no noticeable changes were seen before and after deep-UV irradiation. Unlike typical type IIb natural diamonds, there were no detectable 648.2 cm^{-1}, 3H, or other characteristic type IIb emissions.

This example demonstrates the intertwined relationships and complexity of features observed in both natural and laboratory-grown diamonds. Reliance on a single observable screening feature such as strong phosphorescence might lead to misidentification. Advanced gemological testing and thorough identification processes are fundamentally important to ensure an accurate gem identification result.

Nick "Ka Chun" Chan and Satyaprasad Pradhan

Prismatic Bicolor DUMORTIERITE Crystal

Dumortierite is an orthorhombic, fibrous aluminum borosilicate mineral ($Al_7BO_3(SiO_4)_3O_3$) that typically forms slender prismatic crystals with spectacular color and pleochroism. The crystals can vary in color from brown, blue, and green to rarer violet and pink. These color variations are caused by the substitution of iron and other trivalent elements for aluminum. Dumortierite typically occurs in high-temperature, aluminum-rich regional metamorphic rocks resulting from contact metamorphism as well as in boron-rich pegmatites, with several reported sources, including Austria, the United States (Nevada), Madagascar, and Russia. A few reports of the mineral's occurrence have been published in the literature, which may be of general interest to mineralogists (e.g., A.B. Peck, "Dumortierite as a commercial mineral," *American Mineralogist*, Vol. 11, No. 4, 1926, pp. 96–101). Because perfect dumortierite crystals are very rare, small crystals surrounded by quartz and andalusite are more typically observed. Dumortierite has been reported to commonly occur as a blue mineral inclusion in quartzite (Spring 2015 Gem News International, pp. 100–102).

Recently, GIA's Bangkok laboratory received a 63.17 ct partially polished rough crystal with a prismatic shape and hexagonal cross section, measuring approximately 26.70 × 17.24 × 15.23 mm. The sample exhibited a uniform gray-blue color externally, with a strongly zoned bicolor core running along the length of the crystal featuring a pinkish orange center surrounded by a rim of gray-blue (figure 14). The color zoning was reminiscent of watermelon tourmaline's appearance, but in a different crystal form and color. The bicolored zoning observed in this dumortierite may be the result of a change in trace element composition during the crystal's growth.

Figure 14. A 63.17 ct (26.70 × 17.24 × 15.23 mm) prismatic bicolor dumortierite rough crystal, viewed from the side (left) along with a cross-section view (right), displaying a pinkish orange core and a gray-blue outer layer. Photos by Lhapsin Nillapat.

A refractive index of 1.67–1.69, a hydrostatic specific gravity of 3.38, and Raman spectroscopy identified this stone as dumortierite. The stone displayed strong chalky green fluorescence throughout the surface under short-wave (254 nm) ultraviolet radiation. Microscopic observation revealed a strong, partially hexagonal growth feature along the crystal outline with a zoned pinkish orange core and a gray-blue outer layer. The partially hexagonal polished cross section displayed triangular sectors under cross-polarizing filters. Fluid inclusions and fingerprints as well as intersecting cleavage planes were also present in the stone.

As the cause of blue color in dumortierite has been previously reported to be mainly from Fe^{2+}-Ti^{4+} intervalence charge transfer (A.N. Platonov et al., "Fe^{2+}-Ti^{4+} charge-transfer in dumortierite," *European Journal of Mineralogy*, Vol. 12, No. 3, 2000, pp. 521–528), energy dispersive X-ray fluorescence was also performed on the stone to obtain elemental information and to support its identification. High aluminum and silicon, which are among the main components of dumortierite, were detected along with small peaks of other elements, such as silver, titanium, chromium, and iron.

This dumortierite rough crystal is remarkable for its vivid, clearly separated bicolor zones and its rarity, and to the author's knowledge, is the most significant example reported in the literature due to its size, color, and shape.

Ungkhana Atikarnsakul

Quench-Crackled and Dyed LABORATORY-GROWN SAPPHIRE

One common process used to alter gemstones is the "quench-crackle and dye" treatment, in which a heated stone is quenched in room-temperature water, inducing fractures that allow dye to penetrate the stone and change the appearance of its color. This technique was introduced in the 1990s (S.F. McClure and C.P. Smith, "Gemstone enhancement and detection in the 1990s," Winter 2000 *G&G*, pp. 336–359) and is typically applied to quartz, cubic zirconia, glass, and other synthetic gemstones due to their low cost and high availability.

The Carlsbad laboratory recently received a 12.65 ct laboratory-grown colorless sapphire that showed signs of treatment (figure 15). At first glance, the overall face-up color of this stone suggested it was a Paraíba tourmaline or a low-quality emerald. With the unaided eye, the color-causing dye-filled fractures were faintly visible. The refractive index, specific gravity, and other basic gemological tests identified the material as sapphire. Along with the lack of natural inclusions, testing with X-ray fluorescence revealed the absence of both gallium and iron, confirming that the stone was laboratory-grown. Visible/near-infrared (Vis-NIR) absorption spectroscopy displayed a broad band around 650 nm that did not match natural color-causing components found in corundum (figure 16).

Figure 15. Face-up appearance of a quench-crackled and dyed laboratory-grown colorless sapphire, measuring 13.10 × 12.73 × 7.51 mm. Photo by Adriana Gudino.

This explains the unnatural color of this sapphire. With a microscope, the fractures within this stone displayed characteristic weblike fractures induced by quenching. Unlike naturally occurring fractures, the fractures

Figure 16. A comparison of the Vis-NIR spectra of a natural colorless sapphire, a natural bluish green sapphire, and the bluish green laboratory-grown sapphire demonstrates that the color in the latter results from the dye seen in figure 17. Spectra are offset vertically for clarity.

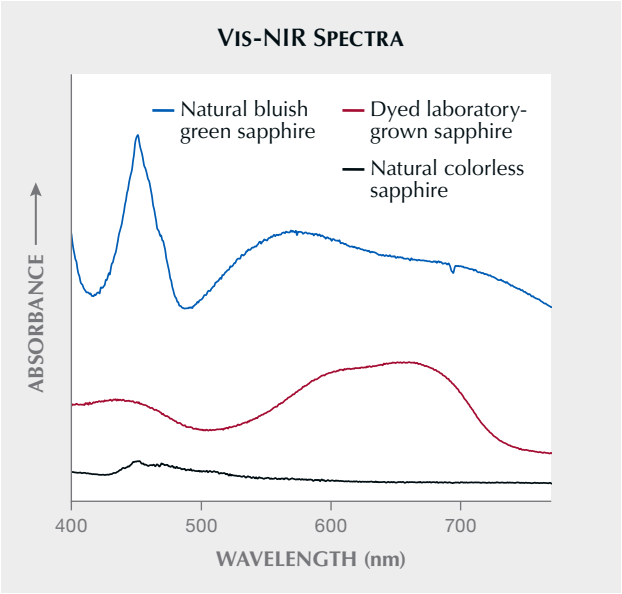

Figure 17. Dye concentrations along shallow, weblike induced fractures evenly spaced across the surface of a colorless laboratory-grown sapphire. Photomicrograph by Jamie Price; field of view 5.50 mm.

produced by this type of treatment have uniform spacing and depth, as shown in figure 17.

Jamie Leigh Price

PEARLS

Two Assembled Pearls

Recently, GIA's Mumbai laboratory received an intriguing pair of mounted pearl earrings, which were later unmounted for identification and concluded as assembled pearls. Both button-shaped pearls were partially drilled and exhibited a light cream hue. Pearl A measured 12.19 × 11.88 × 7.38 mm and weighed 7.40 ct, and pearl B measured 12.58 × 12.06 × 9.18 mm and weighed 9.37 ct (figure 18).

The face of each pearl appeared smooth and showed typical fine overlapping aragonite platelets, while each base exhibited prominent layering of materials used in the assembly process. The inner layers revealed a concentric acicular core with significant cracks typically seen in a natural pearl growth structure. This was surrounded by a layer of yellowish translucent material consisting of brown bubble-like spots, likely the adhesive material used in bonding the inner core with the outer nacreous dome (figure 19).

Real-time X-ray microradiography (RTX) imaging of the two pearls revealed similar unusual internal compositions (figure 20). The inner cores were distinctly rounded and exhibited growth features consistent with those of natural pearl. The outer domes appeared more button shaped, featuring a straight profile that flared outward toward the base and lacked a defined growth structure. These features suggested they may be blister materials, as indicated by the visible dark conchiolin layer and open skirts. However, whether these nacre domes were shell blisters, blister pearls, or cut whole pearls, and whether they were naturally formed or cultured could not be determined.

Figure 18. Two partially drilled button-shaped light cream assembled pearls weighing 7.40 and 9.37 ct, respectively, mounted in a pair of earrings. Photo by Gaurav Bera.

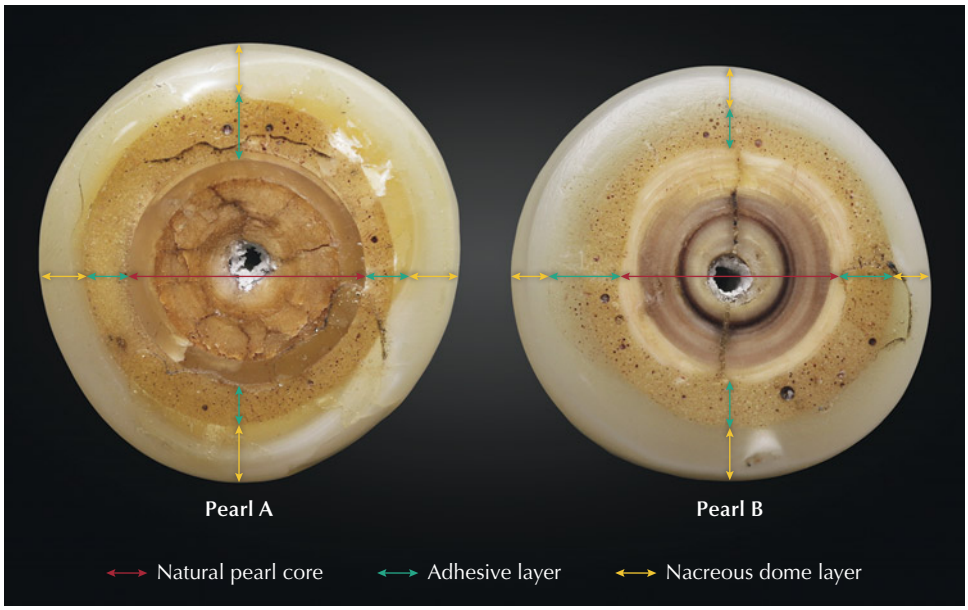

Figure 19. The base of pearl A measuring 12.19 × 11.88 mm and pearl B measuring 12.58 × 12.06 mm, showing the layering of different materials used in the assembly process. Photos by Gaurav Bera.

Therefore, their exact identity remains inconclusive (Fall 2015 Lab Notes, p. 318). Notably, each pearl showed a wide opening at the end of its drill hole. RTX imaging indicated that pearl A was partially drilled and pearl B was fully drilled prior to assembly. Both surface evidence and RTX imaging suggest that these natural cores had been bonded with the nacre domes using a radiolucent adhesive material. The natural cores and nacre domes may or may not belong to the same pearl. In addition, both pearls presented a significant internal void, which is a typical characteristic of assembled pearls or materials such as mabe pearl.

When exposed to X-ray fluorescence, the faces of the pearls displayed a very weak greenish reaction, while the bases showed a weak greenish yellow reaction for the outer nacre domes and the inner cores remained inert. Energy-dispersive X-ray fluorescence analysis on the face of each pearl revealed no trace of manganese and high strontium levels of 1353 ppm and 1532 ppm, respectively, indicating a saltwater origin. Under long-wave (365 nm) ultraviolet radiation, the top surface of both pearls exhibited a moderate bluish reaction, while the inner bottom layers displayed a weak yellowish green to light orangy red. A weaker overall reaction was observed under short-wave (254 nm) ultraviolet radiation.

The specific type of assembled pearl observed in this pair of earrings, in which natural pearl cores are used to simulate the appearance of natural pearl growth, is uncommon. Such items require comprehensive laboratory testing for accurate identification, as once mounted, these assembled pearls can easily deceive the human eye.

Roxane Bhot Jain, Abeer Al-Alawi, and Chunhui Zhou

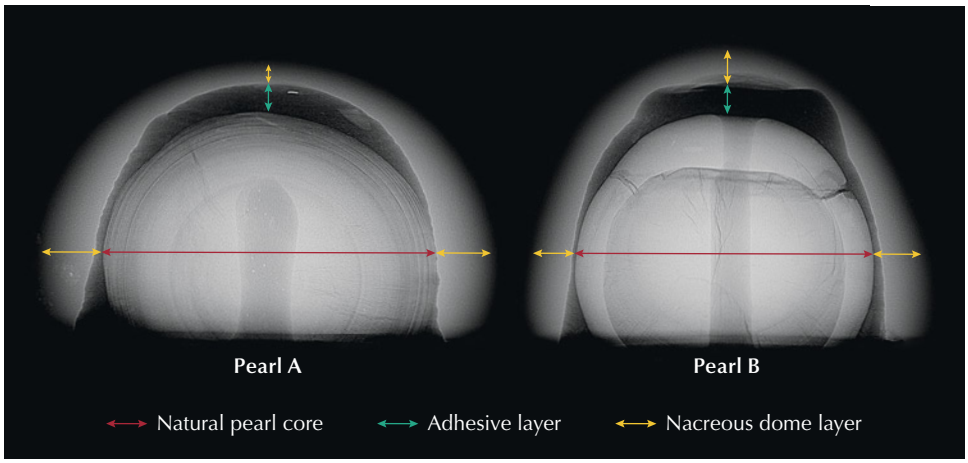

Figure 20. RTX imaging of both pearls revealing natural pearl cores (indicated by red arrows), void formations along with the radiolucent adhesive material (green arrows), and button-shaped nacreous domes (yellow arrows).

Figure 21. A dark gray and brown hollow natural pearl (2.89 ct, 11.13 × 10.47 × 10.16 mm) with a surface opening (indicated with arrow). The four fragments next to the pearl were recovered from its opening. Photos by Gaurav Bera.

Low-Heft Hollow Natural Pearl with an Opening

Pearls with low heft are always of interest as they usually exhibit a large size relative to their weight, and it is often difficult to ascertain whether they are hollow or have been filled. GIA's Mumbai laboratory recently received for identification a dark gray and brown semi-baroque pearl weighing 2.89 ct and measuring 11.13 × 10.47 × 10.16 mm (figure 21). Chemical analysis using energy-dispersive X-ray fluorescence determined no measurable manganese but a strontium content of 934 ppm, indicating a saltwater origin. Under long-wave (365 nm) and short-wave (254 nm) ultraviolet radiation, the pearl was inert.

The pearl contained a surface opening measuring approximately 2.46 × 1.94 mm, forming a window into the pearl where light brown fragments could be observed (figure 22, left). During transport and through the course of testing, four angular-shaped fragments with slightly rounded edges emerged from the opening, each weighing approximately 0.01 ct (figure 22, right), suggesting they had fractured within the pearl.

Real-time X-ray microradiography (RTX) revealed a large void with a dark gray radiolucent material inside, surrounded by a lighter gray outer rim of nacre (figure 23, left). The structure was more apparent using X-ray

Figure 22. Left: Opening in the pearl's surface with fragments visible. Right: A fragment that was dislodged from the pearl. Photomicrographs by Keaton Talker; fields of view 6.40 mm (left) and 3.00 mm (right).

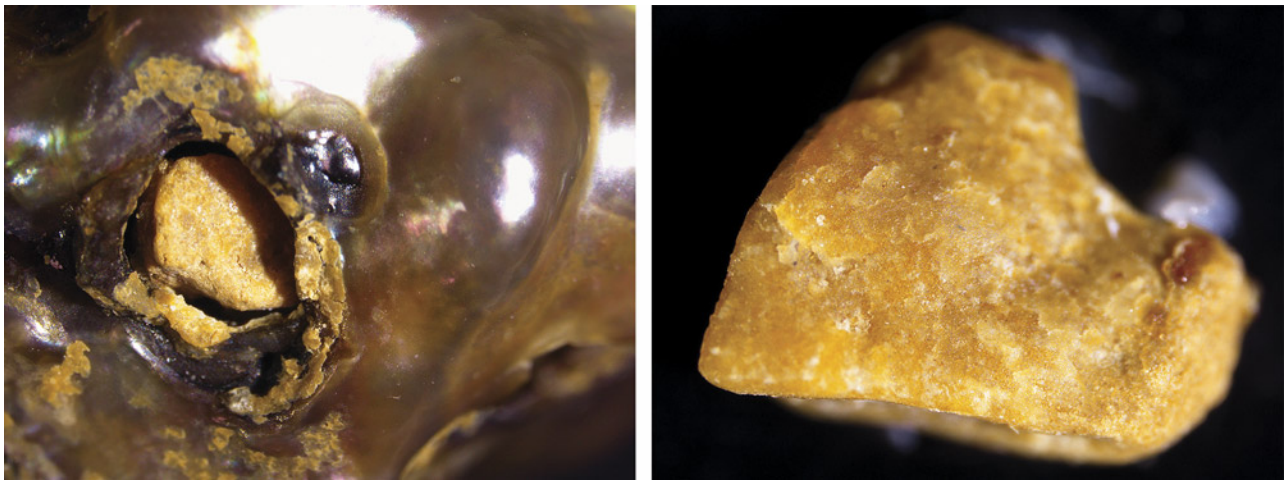

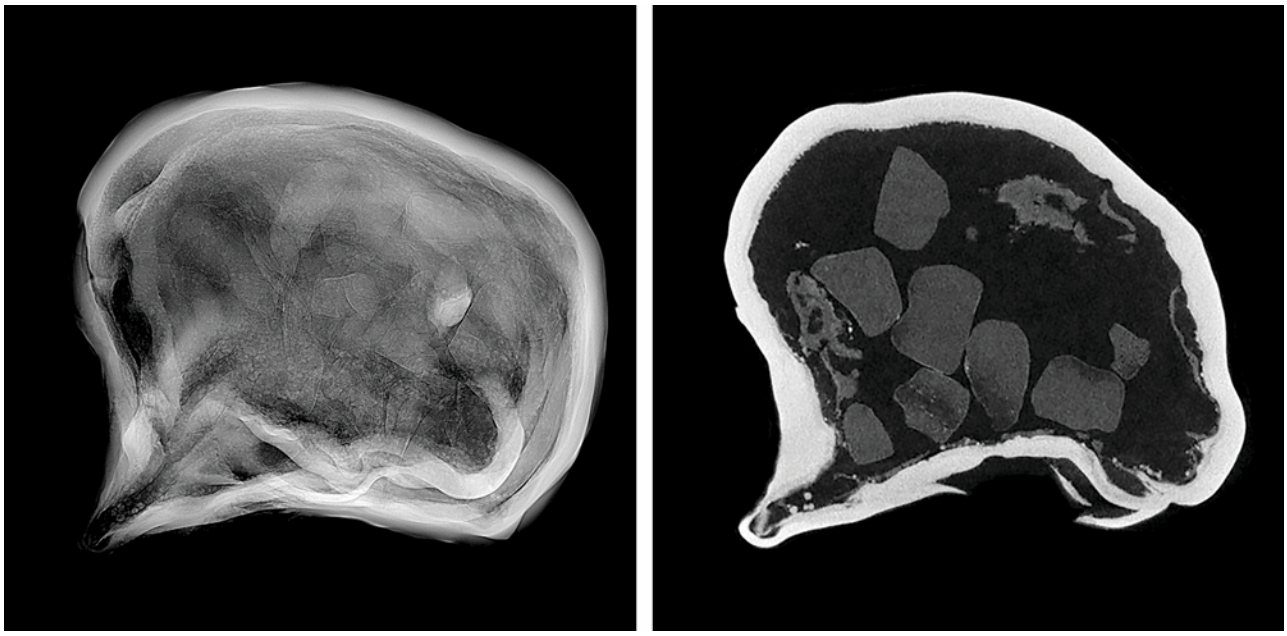

Figure 23. RTX image (left) and µ-CT image (right) of the 2.89 ct pearl with faint radiolucent material visible in the hollow void.

computed microtomography (µ-CT) imaging (figure 23, right), where many radiolucent fragments were visible inside the large void.

Further microscopic observation suggested that the dislodged fragments were made of an organic-rich resinous substance that appeared brownish yellow, similar to the fragments inside the opening and the organic material around it. However, due to the fragile nature of the pearl, Raman spectroscopy to conclusively identify this material was not possible.

Although some hollow pearls are intentionally filled with foreign materials to increase their weight and durability (Summer 2019 Lab Notes, pp. 251–254), the material inside this pearl appeared to be an organic-rich substance that naturally formed within the pearl. In addition, the void's shape followed the outline of the pearl, which has been previously observed in natural pearls ("Pearls with unpleasant odors," *GIA Research News*, March 23, 2009). The opening on the pearl's surface provided a rare glimpse into its natural filling, allowing the observation of organic-rich material as it became dislodged—a fascinating and significant occurrence.

Nishka Vaz and Abeer Al-Alawi

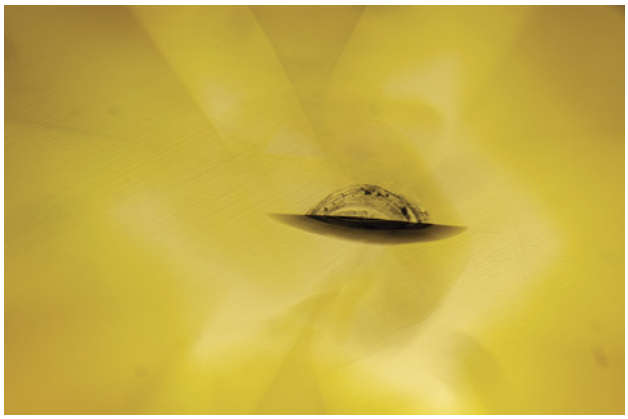

Figure 1. This diamond feather and its reflection resemble a UFO flying across the sun. Photomicrograph by Michaela Damba; field of view 3.57 mm.

"UFO" in Diamond

The author recently examined a 3.03 ct Fancy Deep brownish orangy yellow diamond featuring a small feather on the table and very strong yellow color zoning in a stellate pattern. When held table to culet, the diamond displayed a feather that, with its reflection, appeared as a caricature of an unidentified flying object soaring across the sun (figure 1).

Feathers are common inclusions that impact the clarity grade of a diamond. This diamond received a clarity grade of SI_1 based on its etch channels and several feathers. Color zoning does not impact the clarity grade, but it can affect the overall color grade of a diamond.

Michaela Damba
GIA, Carlsbad

Cristobalite Stars and Snowflakes in Devitrified Glass

Recently, the authors examined a 3.04 ct transparent green oval mixed cut stone. Basic gemological testing suggested this stone was glass, which was further supported with Fourier-transform infrared and Raman spectroscopy showing characteristic features of artificial glass.

Although artificial glass is one of the most common gem simulants, microscopic observation revealed a unique inclusion scene. In addition to gas bubbles, many six-pointed star-shaped platelets were observed (figure 2). These star-shaped platelets exhibited a dendritic pattern, which could be seen clearly when observed in brightfield illumination (figure 3). In this lighting environment, the stars more closely resembled snowflakes. Additional inclusions were also observed, taking the form of three-dimensional lattices with spikes at each tip (figure 3). All inclusions were identified as cristobalite by Raman spectroscopy.

Cristobalite, a crystallized form of silica, is a common inclusion in artificial glass formed by devitrification (e.g., E.J. Gübelin and J.I. Koivula, *Photoatlas of Inclusions in Gemstones, Volume 1*, ABC Edition, Zurich, 1986, p. 430; G. Bosshart, "Cobalt glass as a lapis lazuli imitation" Winter 1983 *G&G*, pp. 228–231). Devitrification is the process by which an amorphous material changes to a crystalline state. Crystalline inclusions produced by this

About the banner: Prismatic tourmaline crystals intersect in this goshenite beryl from Governador Valadares, Minas Gerais, Brazil. Photomicrograph by Nathan Renfro; field of view 11.28 mm.

Gems & Gemology, Vol. 61, No. 3, pp. 302–307.

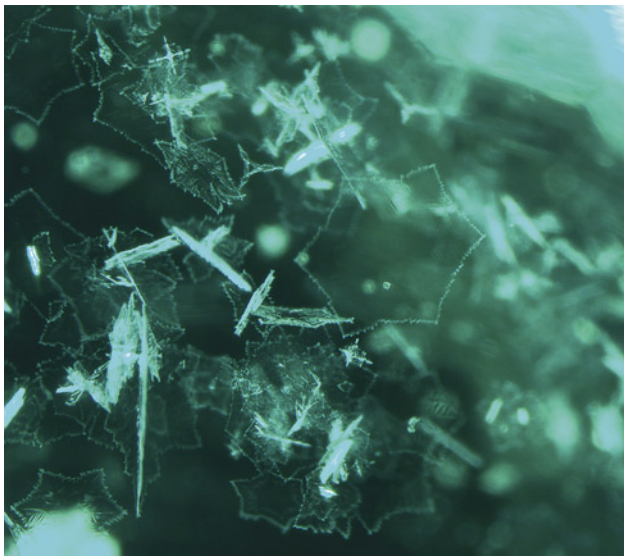

Figure 2. Many six-pointed star-shaped platelets and round gas bubbles are observed in this artificial glass. Photomicrograph by Kanako Otsuka; field of view 2.51 mm.

process can give a natural appearance to glass simulants (e.g., Summer 2018 *G&G* Micro-World, pp. 230–231). However, this artificial glass, which was likely made to imitate emerald, has a unique beauty that would not exist in natural gemstones.

Kanako Otsuka and Kazuko Saruwatari
GIA, Tokyo

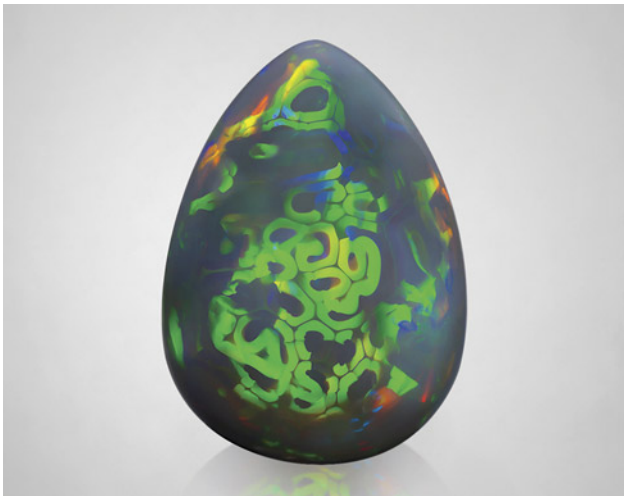

Figure 4. A natural 47.77 ct Ethiopian opal with an unusual play-of-color pattern. Photo by Nuttapol Kitdee.

Natural Opal with Unusual Play-of-Color Pattern

Ethiopian opal was first discovered in the early 1990s and is capable of producing spectacular play-of-color in a variety of patterns and bodycolors. Some Ethiopian opals exhibit macroscopic finger-like structures called digit patterns: columnar zones of interpenetrating play-of-color within a network of common opal (B. Rondeau et al., "Play-of-color opal from Wegel Tena, Wollo Province, Ethiopia," Summer 2010 *G&G*, pp. 90–105).

Recently, the author encountered a 47.77 ct gray Ethiopian opal displaying attractive play-of-color in an unusual pattern (figure 4). Basic gemological observation and properties confirmed that the stone was a natural non-

Figure 3. Brightfield illumination reveals a dendritic pattern in the star-shaped platelets, which bear a striking resemblance to snowflakes. Smaller three-dimensional crystal inclusions are also observed in the artificial glass. Photomicrograph by Kanako Otsuka; field of view 1.58 mm.

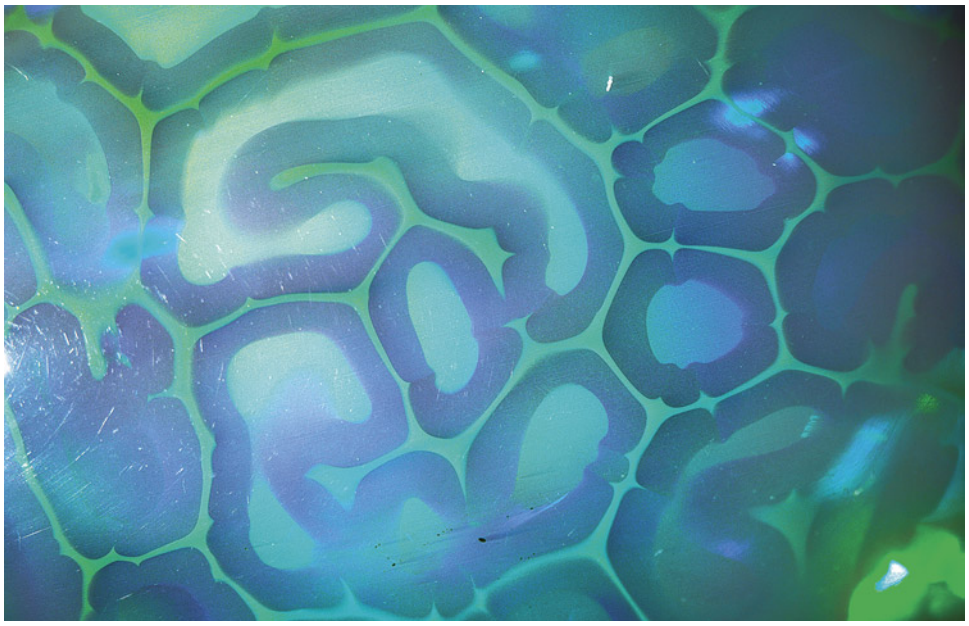

Figure 5. The turtle shell–like pattern of the natural opal as seen in oblique reflected light. Photomicrograph by Ungkhana Atikarnsakul; field of view 14.4 mm.

hydrophane opal. Interestingly, the play-of-color pattern in this specimen was confined to distinct "cells" separated by greenish-colored opal, resembling a turtle-shell structure on the top of the cabochon (figure 5). This is one of the most extraordinary patterns in natural opal that the author has examined.

Ungkhana Atikarnsakul
GIA, Bangkok

"Melon" Pearl

Non-nacreous pearls are characterized by the absence of iridescent layers of nacre and are recognized for their distinctive surface characteristics. For some non-nacreous pearls, their unique look is attributed to the calcite structure's patterning on the surface. Such structures can result in a wide range of surface appearances, predominantly featuring a cellular pattern, in contrast to nacreous pearls, which typically display overlapping aragonite platelets.

Recently, the authors examined a parcel of non-nacreous yellow, gray, brown, and black pearls of various shapes reportedly sourced from *Pinctada radiata* mollusks fished from Bahrain. Among the samples, an oval non-nacreous black pearl with grayish yellow areas at its center, weighing 0.085 ct and measuring 2.46 × 2.25 mm, stood out for its fascinating surface appearance (figure 6, left). When viewed under magnification, its subsurface revealed a reticular netted structure characterized by a spiky veined cellular pattern (figure 6, right). Although the authors have previously encountered similar surface textures, this particular pattern was intriguing, as it closely resembled the netted tissue found on the surface of a melon.

Pfokreni Nipuni and Abeer Al-Alawi
GIA, Mumbai

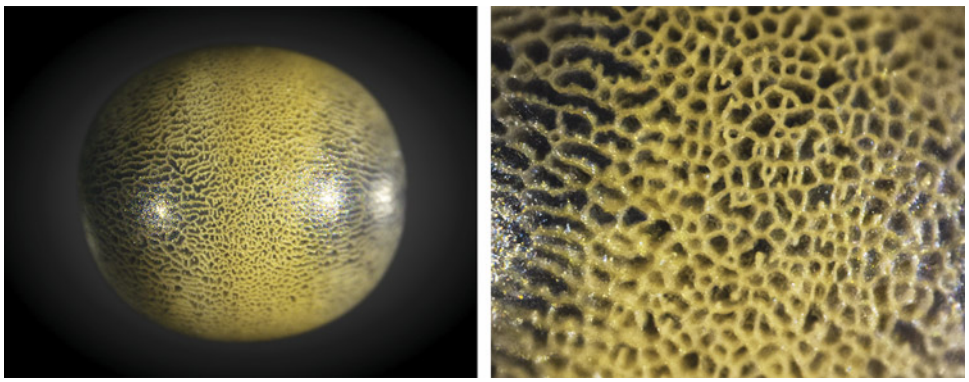

Figure 6. Left: A non-nacreous 0.085 ct pearl with a unique netted surface resembling the exterior of a melon. Right: The reticular netted cellular structure on the pearl's surface. Photomicrographs by Pfokreni Nipuni; fields of view 4.0 mm (left) and 1.0 mm (right).

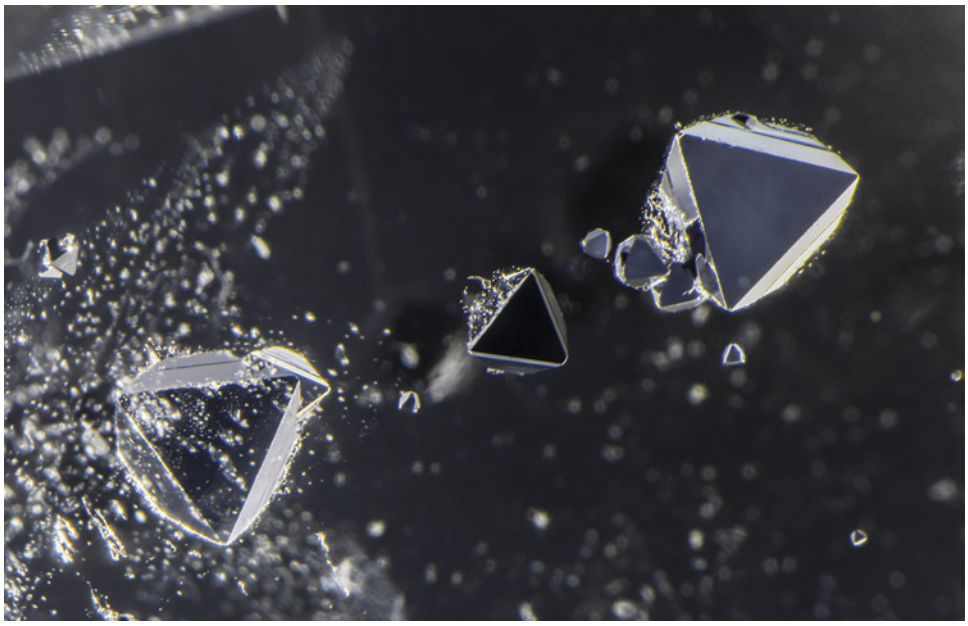

Figure 7. Octahedral gersdorffite inclusions in quartz appearing as triangles. Photomicrograph by Nathan Renfro; field of view 8.16 mm.

Gersdorffite in Quartz

While examining a 59.32 ct transparent colorless freeform shield-shaped step cut from Kara-Oba in the Karagandy Province of Kazakhstan, we noticed something curious. Using optical microscopy, X-ray powder diffraction, and standard gemological testing, we identified the sample as transparent rock crystal quartz and its eye-visible inclusions as the isometric nickel arsenic sulfide, gersdorffite.

What made this quartz subject particularly interesting to study was the euhedral morphology of the opaque, silvery gray, highly reflective, cubically modified octahedral crystals of gersdorffite. From one side of the quartz host, the inclusions with octahedral faces reflected as triangles (figure 7). Through the opposite side of the host, the faces of the very same inclusions appeared as hexagons (figure 8). In this sample, the perceived shape of the inclusions—triangles or hexagons—depends entirely on viewing direction.

John I. Koivula and Nathan Renfro
GIA, Carlsbad

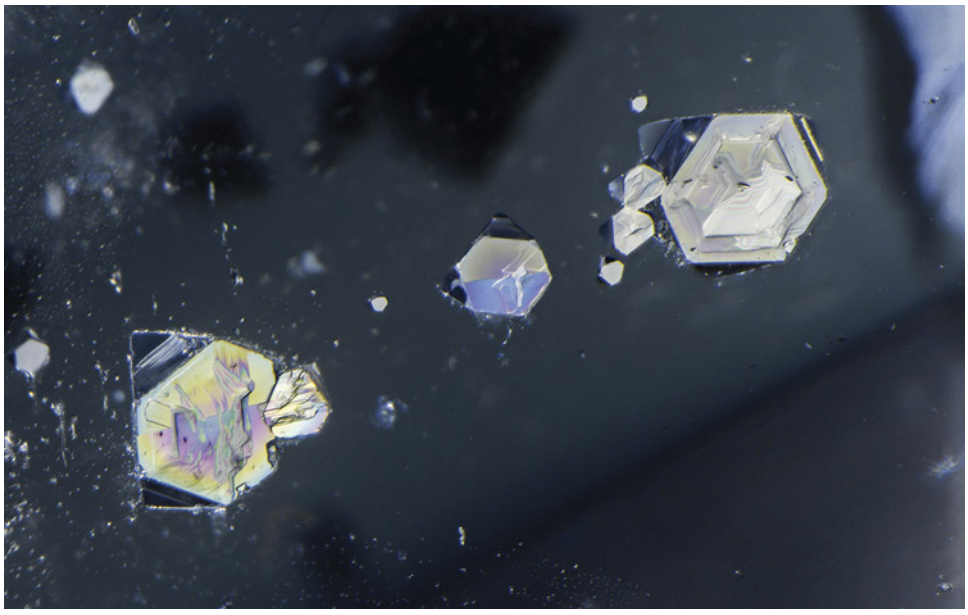

Figure 8. When viewed from the opposite side of the quartz host, the same gersdorffite inclusions display as hexagons. Photomicrograph by Nathan Renfro; field of view 8.11 mm.

Figure 9. Sea urchin–like 3D radial fissures in a heated Mong Hsu ruby. Photomicrograph by Taku Okada; field of view 1.70 mm.

Sea Urchin–Like 3D Radial Fissures in a Heated Mong Hsu Ruby

The author recently examined a 1.34 ct red stone with a three-dimensional radial inclusion resembling a sea urchin, or *uni* in Japanese (figure 9). The stone was identified as a heated ruby from Mong Hsu, Myanmar, based on trace element chemistry, chalky fluorescence under short-wave (254 nm) UV radiation, and the altered state of diagnostic inclusions (A.C. Palke et al., "Geographic origin determination of ruby," Winter 2019 *G&G*, pp. 580–613). Mong Hsu rubies rarely contain such large crystals, indicating that this was an aggregate of tension fissures and not a crystal at all. These fissures likely formed when an isolated, relatively small inclusion expanded during heating. If an inclusion has a thermal expansion coefficient greater than that of corundum, fissures may form around the inclusion during heating, such as common discoidal decrepitation fissures. The fissures usually develop in the direction of maximum compression stress of the residual strain inside the ruby (e.g., T.L. Anderson, *Fracture Mechanics: Fundamentals and Applications*, Third Edition, CRC Press, 2005). In this case, the radial fissures developed almost isotropically in three dimensions, suggesting that the surroundings of the inclusion were in a quasi-hydrostatic pressure state with almost no differential stress. The unexpected local stress state in the ruby formed the fissure aggregates in this exciting and unusual shape.

Taku Okada
GIA, Tokyo

Suspended Pargasite Crystal in Pink Spinel

A 1.33 ct pink spinel containing a distinct mineral inclusion located near the stone's surface was recently examined by the author. Raman analysis identified the inclusion as a pargasite ($NaCa_2(Mg_4Al)(Si_6Al_2)O_{22}(OH)_2$) crystal. This euhedral prismatic crystal displayed chamfered terminations, rhombohedral pinacoids, and a near-colorless bodycolor (figure 10). Reflected light highlighted a central feature, possibly a growth hillock, which gave the appearance of two connected pargasite crystals. While pargasite inclusions are more commonly found in corundum than in spinel, few have been documented exhibiting such remarkable morphology.

Hannah Wiggins
GIA, New York

Figure 10. A prismatic pargasite crystal against the pink faceted background of its spinel host. Photomicrograph by Tyler Smith; field of view 1.76 mm.

Figure 11. Weighing 2.34 ct and measuring 7.71 mm in the largest dimension, this partially etched diamond octahedron hosts a yellow-orange almandine-pyrope garnet crystal. Photo by Diego Sanchez.

Quarterly Crystal: Almandine-Pyrope Garnet in Diamond

The authors recently examined a collection of African diamond crystals that hosted various mineral inclusions. This Quarterly Crystal, chosen from that collection, is a 2.34 ct transparent near-colorless partially etched diamond octahedron measuring 7.71 × 7.39 × 4.92 mm, which came from the Republic of South Africa (figure 11). During routine testing, the near-colorless octahedron fluoresced a strong blue when exposed to long-wave (365 nm) ultraviolet radiation.

The diamond crystal hosts a transparent yellow-orange inclusion situated near its center. Laser Raman microspectroscopy identified this included crystal as an almandine-pyrope garnet. The yellow-orange color is typical of this type of inclusion. In addition to the garnet, light grayish green transparent birefringent omphacite crystals and opaque black sulfide and graphite crystals (some forming rosettes) were also present.

As inclusions in diamonds, transparent almandine-pyrope crystals are generally a medium to deep yellow-orange color with a vitreous luster. As shown in figure 12, such inclusions typically form as somewhat rounded protogenetic mineral crystals. Geologically, the presence of an almandine-pyrope garnet inclusion is an indicator that the host diamond formed in a rock type known as eclogite.

John I. Koivula and Nathan Renfro

Figure 12. This yellow-orange transparent crystal of almandine-pyrope garnet is a very rare inclusion in diamond. The example shown here has a typical somewhat rounded habit. Photomicrograph by Nathan Renfro; field of view 3.84 mm.

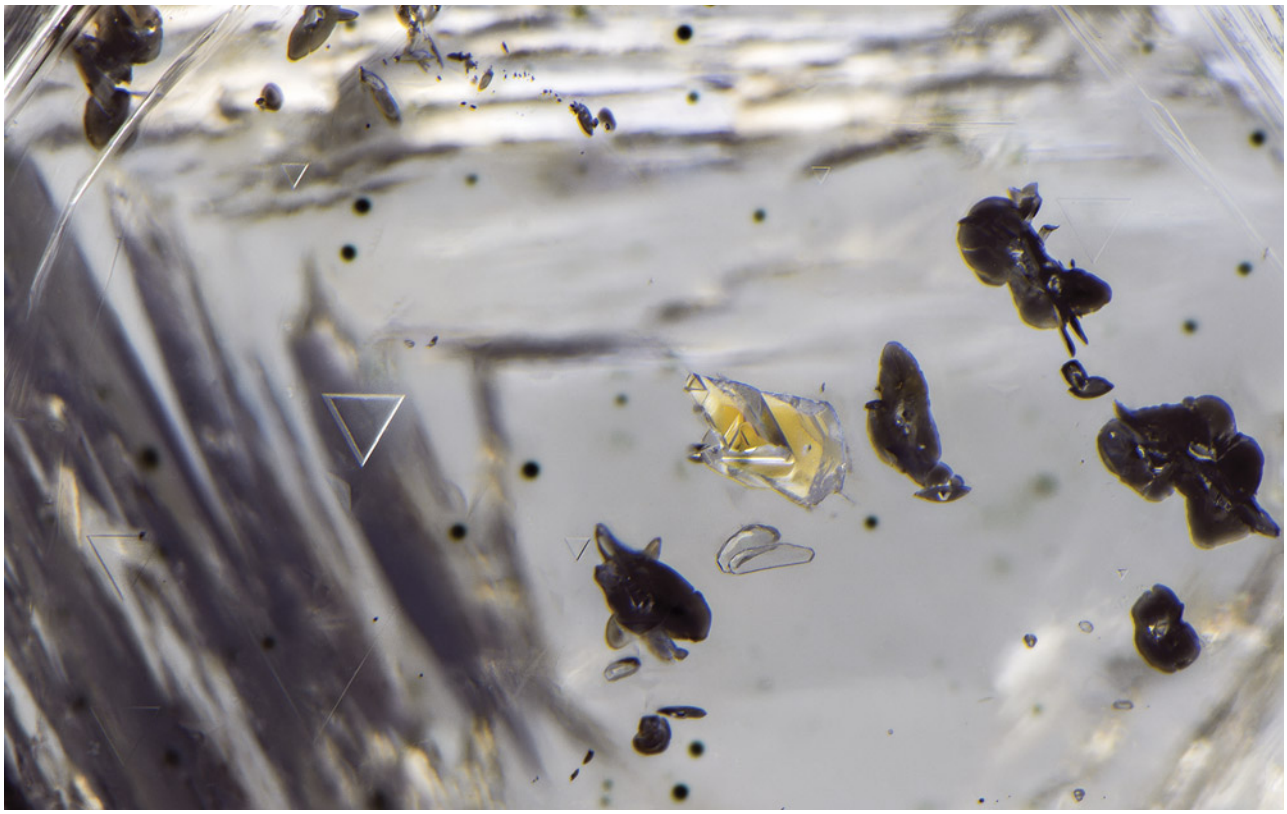

Editor: Evan M. Smith

Raw Brilliance: Nature's Diamond Sculptures

The basic shape of a rough diamond is all around us, from black diamonds on ski slopes to the familiar red diamonds in a standard deck of playing cards. These symbols are the silhouette of an octahedron, which is the archetypal diamond crystal. Indeed, the octahedron appears regularly within parcels of mined diamonds, but accompanying it are many other nuanced shapes, all sculpted by natural processes. GIA scientists recently had the opportunity to examine a suite of 264 rough diamonds handpicked over several years by Pintu Dholakia of Hari Krishna Exports for their unusual or interesting nature. Here we showcase some of these specimens to discuss their morphology and highlight their striking appearances.

Sculpted by Natural Growth, Breakage, and Resorption in the Earth

Diamonds form deep in the mantle when carbon-bearing fluids migrate and interact with solid rocks. Chemical reactions or other changes can decrease the solubility of carbon, forcing it to form solid crystals of diamond. In the simplest case, a growing diamond will take the shape of an octahedron. However, variations in growth conditions can lead to other shapes. By growing diamond crystals in different ways, nature can build diverse rough diamond shapes—as an artist might press clay together to create a masterpiece. Examples include variations of cubes (cuboids, cuboctahedra, re-entrant cubes with concave cube faces and protruding corners), spheres called ballas, and twinned triangular plates called macles (figure 1).

Despite its status as the hardest natural substance, diamond is not invincible. Natural stresses that squeeze or shear a diamond in the mantle or during transport to Earth's surface in a kimberlite eruption can lead to fracture and cleavage. A diamond has four symmetrical planes within its crystal structure along which it can cleave, meaning that it can break apart with nearly perfect flat, smooth surfaces (see figure 1A). In addition to breakage, the shape and surface of a diamond can be refashioned by a process known as resorption. During resorption, hot fluids or magma in the earth partially etch away a diamond's outer surface. Resorption affects the overall shape, turning sharp-edged octahedral crystals into rounded forms, and can also modify the surface texture through the creation of features including negative trigons, hillocks, and lustrous glossy surfaces (Robinson, 1979; Harris et al., 2022). Removing material from a diamond by breakage and resorption is akin to an artist taking a hammer and chisel to a block of marble. Mother Nature engages in both additive sculpture, by crystal growth, and subtractive sculpture, through breakage and resorption. The incredible array of natural diamond sculptures attests to the dynamic processes occurring deep beneath our feet over millions or billions of years.

Nature's Windows

Geologists sometimes refer to diamonds as metaphorical windows into the mantle, but occasionally diamonds do emerge resembling windowpanes of glass. The transparent plate-like forms shown in figure 2 were created entirely by natural processes. Diamond can form excellent plates by cleavage, breaking along flat planes of weakness in the crystal structure. A single cleave may liberate the face of an octahedral crystal, for example, to make a flat plate shape. The 2.22 ct hexagonal-shaped specimen shown in tweezers in figure 2 was produced in this way. Examination using deep-UV luminescence shows that one side is the original exterior surface of the crystal, while the opposing face represents a cleave crosscutting multiple

Editor's note: Questions or topics of interest should be directed to Evan Smith (evan.smith@gia.edu).

Gems & Gemology, Vol. 61, No. 3, pp. 308–314.

Figure 1. Examples of rough diamonds with shapes governed by various combinations of growth, breakage, and resorption: a diamond broken cleanly along a flat plane by cleavage (A); irregular broken fragments smoothed by resorption (B and C); cuboctahedron (D), ballas (E), and re-entrant cuboid (F) shapes produced during diamond growth; two macles resulting from twinned crystal growth, along with two fragments resulting from macle breakage (G); and an elongate fragment representing an edge broken from an octahedron crystal, with the former octahedron corners forming the ends (H). Specimens range from 1.08 to 28.08 ct, with the largest specimen measuring 27 mm in length. Photo by Evan M. Smith.

growth layers. Despite its incredible transparency, small negative trigons (not shown) decorate all sides of this diamond, testifying to its natural unpolished state. In addition to cleavage, twinning can produce flat transparent plates. Macle twinned diamonds tend to grow as flat triangular plates (again, see figure 2, left). Natural transparent diamond plates can therefore form by either growth or breakage.

Figure 2. Left: Transparent plate-shaped rough diamonds ranging from 0.99 to 9.67 ct. Ruled lines have 2.8 mm spacing. Right: The top left specimen (2.22 ct) against the sky. Photos by Evan M. Smith.

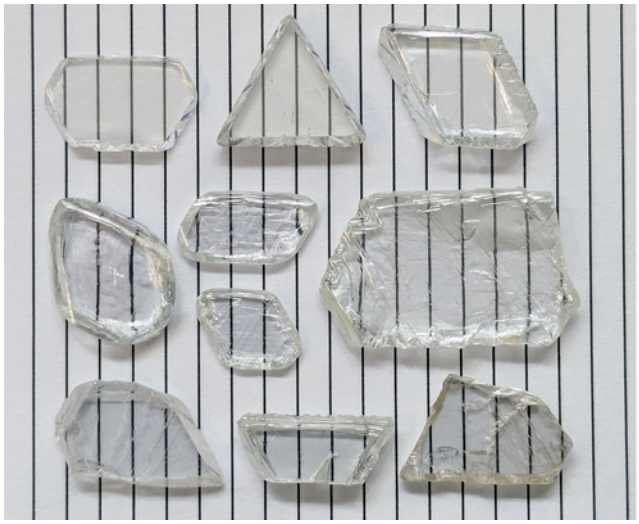

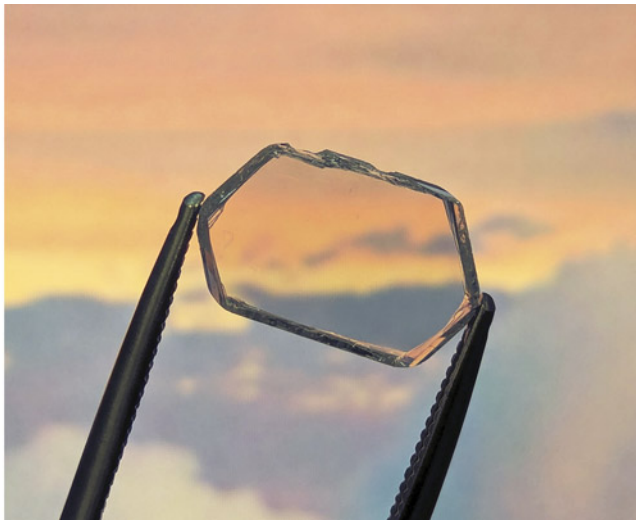

Figure 3. Elongate rough diamonds reminiscent of baguette cuts, ranging from 1.84 to 7.10 ct in weight and 16 to 24 mm in length. Photo by Evan M. Smith.

These shapes are evocative of portrait-cut diamonds, one of the earliest faceting styles, which some jewelers have recently repopularized. Portrait cuts possess two relatively large parallel facets and a thin profile and were originally intended for use as stylish protective covers for painted portraits. In a similar sense, diamond windows serve as transparent yet robust physical barriers in devices such as high-power laser systems and synchrotron beamlines. Diamond windows can have high transmission across the ultraviolet, visible, far-infrared, and microwave regions of the electromagnetic spectrum, which, combined with their thermal and chemical resistance and high strength, make them ideally suited for some modern high-tech applications.

Raw Baguettes

The elongated diamond forms shown in figure 3 are reminiscent of baguettes, both the cut style and the loaves of bread, though their shapes arise through crystal growth or natural breakage in the mantle. Whereas macle twinning provides a viable pathway to grow a natural plate-shaped diamond, there is no such straightforward mechanism to grow an elongate single crystal of diamond. That is not to say that it is impossible for a diamond to crystallize as an elongate rod, but the examples here appear to have been shaped by breakage. In nearly all cases, the direction of elongation is not random but is aligned with the internal crystal structure due to breakage that occurred along cleavage planes. Some are further sculpted by resorption, creating smooth, glossy finishes.

Among the specimens in figure 3, breakage has produced elongate diamonds in at least three distinct ways. The first is depicted in figure 4, with the faces of the octahedron parallel to the four different orientations of cleavage planes within a diamond crystal structure. Cleaving a plate from an octahedron (like those in figure 2) and then cleaving one of the edges off that plate along a cleavage plane of a different orientation can generate a fragment that is elongated in a <110> crystallographic direction.

The second and third ways that natural breakage has produced elongate rough diamonds are less intuitive and involve macle twins, as illustrated in figure 5. In the second mechanism, an edge is broken off a macle (figure 5A). The breakage surface is not planar because of the change in crystal structure orientation across the twin plane. If this break occurs purely by cleavage, the broken surface will be re-entrant, or angled inward, leaving sharp edges that are likely to be rounded off by resorption. Some broken fragments have more irregular or curved breaks (such as the two broken macles in figure 1).

In the third mechanism (figure 5B), the breakage produces a fragment that is elongate in a direction

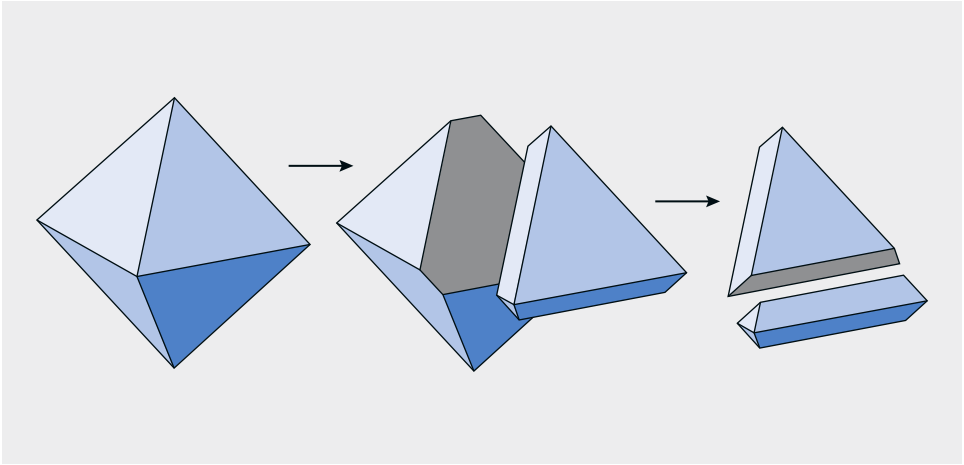

Figure 4. Three-part illustration showing how an octahedron (left) may cleave to yield an elongate parallel-sided fragment. The initial cleave (middle) produces a flat plate-shaped fragment. Cleaving an edge off the plate (right) creates an elongate fragment (as seen in figure 1H).

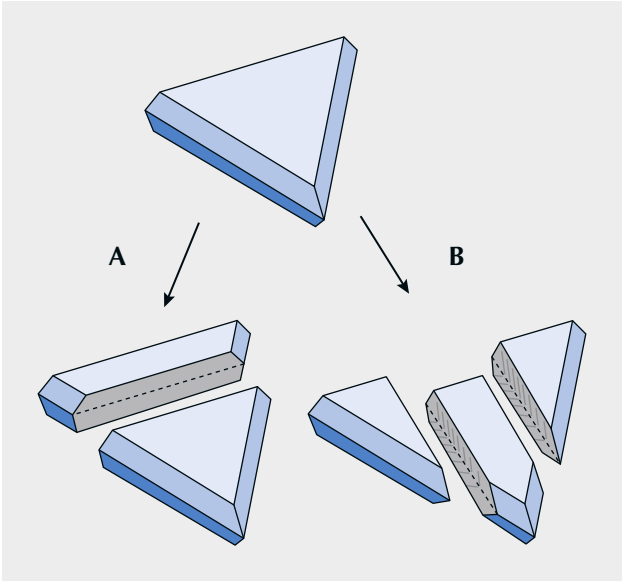

Figure 5. Illustration showing two ways (A and B) that a macle can fracture to yield an elongate parallel-sided fragment. Each fragment will still have a twin plane running through it (dashed line). In B, the breakage surfaces develop a chevron pattern that "points" toward the original point of the macle.

perpendicular to a macle edge. In this case, the breakage surfaces are parallel to {110} planes. Although they are not perfectly planar breaks, it is possible that the diamond is effectively cleaving because diamond does possess a rarely seen cleavage in this orientation (Brookes et al., 1990; Smith et al., 2017). Unlike diamond's typical {111} cleavage planes, there are three possible {110} planes that transect the twin plane and will align perfectly between both portions of a macle twin. Alternatively, these broken surfaces could develop by the combined action of multiple {111} cleavage planes, creating finely stair-stepped breakage surfaces that average out to a {110} plane. Some of these broken surfaces develop a characteristic chevron pattern.

Diamonds Resembling Animals and Objects

The complex sculpted forms of natural diamonds are fertile ground for lively imaginations. Depending on the lighting and viewing angle, some may resemble animals or familiar objects. Perceiving familiar shapes in inanimate forms such as clouds or rough diamonds is called pareidolia.

In some cases, these forms have arisen predominantly by growth (additive sculpting), while in other specimens, breakage or resorption (subtractive sculpting) has been more important. For example, in figure 6C, the small colorless "dog" on the left, resembling a West Highland white terrier, is an irregular octahedral crystal with stepped surfaces,

Figure 6. Rough diamonds resembling animals: parrot, 5.99 ct (A); sitting cat, 5.68 ct (B); small dogs, 2.15 and 3.66 ct, respectively (C); yellow bird, 5.69 ct (D); rabbit, 2.79 ct (E; white rabbit for comparison created using Adobe Photoshop Generative AI). Photos by Evan M. Smith.

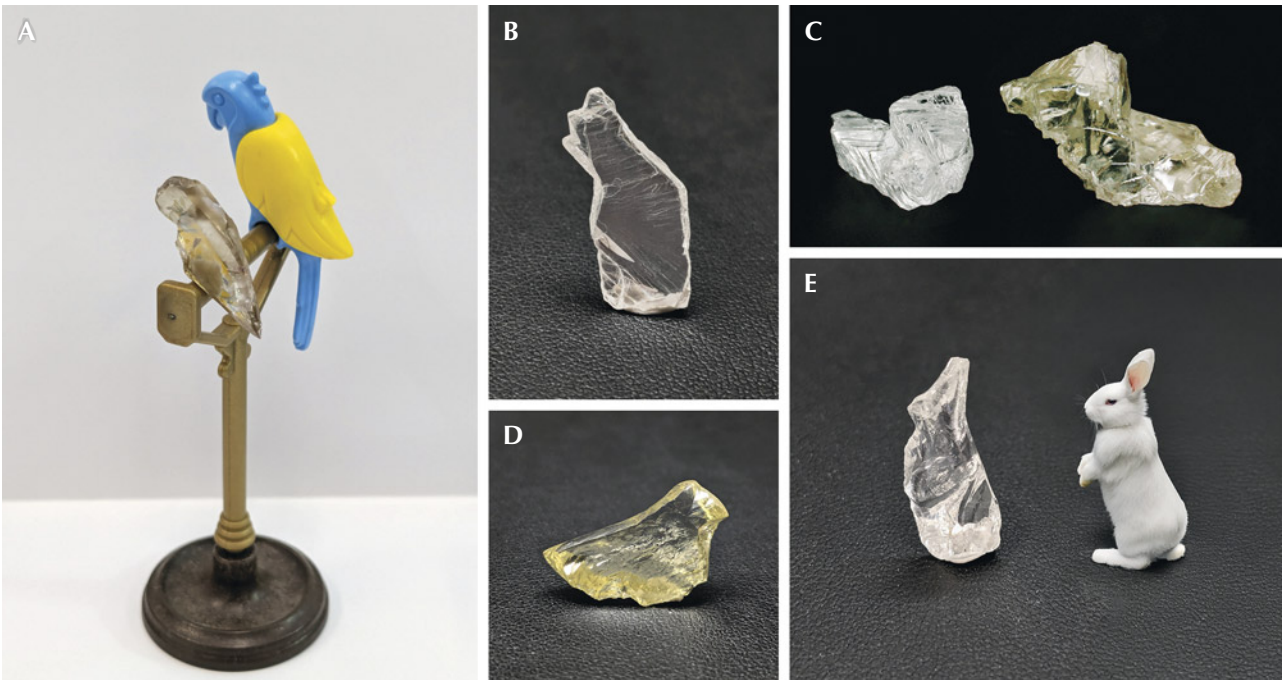

which grew in this shape. The yellow "dog" on the right, however, resembling a dachshund, likely looked much different before being sculpted into this shape by breakage and resorption. The two "raindrops" in figure 7B are another example of contrasting formation, with the right dominated by growth and the left dominated by breakage. Coincidentally, the resulting "raindrops" are of equal weight.

One of the most unusual morphologies in the collection is the "mortar" (pictured with non-diamond pestle) shown in figure 7A. This bowl-like specimen consists of a colorless, gemmy cuboid that is broken in half, revealing an octahedral-shaped internal cavity. The cuboid faces are convex and rounded between the protruding corners. The hollow central portion looks as though an octahedron has been plucked out, leaving a depression in the shape of the apex of a square-based pyramid. One possible explanation suggests that an inclusion formed a discontinuous layer partially separating the inner core from the outer diamond rim (Harris and Stachel, 2024). The inclusion could have weakened the diamond, leading to breakage, after which the core and inclusion would have been released or etched away.

Superdeep Diamonds

All mined diamonds originate at great depths and are transported to Earth's surface by kimberlites or related mantle-sourced volcanic eruptions. Most diamonds crystallize in the base of old, thick parts of continental plates, at approximately 150–200 km deep. Some rare diamonds (estimated 1–2% of mined diamonds) originate from even greater depths, ranging from 300 to 800 km (Stachel et al., 2005; Shirey et al., 2024). Known as sublithospheric or superdeep diamonds, these curious crystals can carry mineral inclusions that provide invaluable insights into Earth's interior. Superdeep diamonds possess highly irregular shapes (figure 8) resulting from stressful growth conditions and multiple episodes of breakage and resorption during the torturous journey to Earth's surface.

The depth of crystallization is mostly based on inclusion mineralogy. Rocks and minerals undergo changes with increasing depth inside Earth as pressure and temperature increase. Some high-pressure minerals, such as

Figure 7. Rough diamonds resembling objects: mortar, 1.95 ct, with a pestle carved from a toothpick (A); raindrops, 3.23 ct each (B); campfire flame, 2.70 ct, backlit using orange light and placed with raw baguettes from figure 3 as firewood (C); gummy bear, 9.18 ct (D; colored gummy bears for comparison created using Adobe Photoshop Generative AI); fibrous diamond cuboids resembling dice, 22.45, 22.47, and 23.64 ct, respectively, shown with a superimposed 10 mm die (E). Photos by Evan M. Smith.

Figure 8. Superdeep diamonds, ranging from 1.27 to 12.97 ct, with typical irregular sculpted shapes resulting from extensive breakage and resorption. The top left specimen is 21 mm in length. Photo by Evan M. Smith.

ringwoodite, can only form at great depths, and when found as inclusions in a diamond, they indicate that the diamond must have crystallized at a depth where that particular mineral was stable. Combinations of multiple minerals also constrain the depth of diamond formation. The diamond at the center of figure 8 contains an inclusion identified as the mineral breyite ($CaSiO_3$; figure 9), which is a calcium silicate that signifies an original depth of diamond growth deeper than 360 km (Anzolini et al., 2016).

Other diamonds in figure 8 have been deemed superdeep on the basis of iron-rich metallic inclusions consistent with those found in a variety of superdeep diamonds referred to as CLIPPIR (Cullinan-like, Large, Inclusion-Poor, Pure, Irregular, and Resorbed) (Smith et al., 2016; Smith et al., 2017). All specimens in figure 8 are tentatively classified as CLIPPIR diamonds. Here purity refers to the low nitrogen concentration of these diamonds, being either type IIa, with no nitrogen detectable by Fourier-

Figure 9. This 2.13 ct superdeep diamond (left; and shown at the center of figure 8) has an irregular shape and strongly resorbed surface marked by many square etch pits or tetragons, which arise from resorption of {100} cube-orientation surfaces. The inclusion (right; red arrow) is a colorless crystal of breyite surrounded by a black graphitic fracture. Photos by Evan M. Smith; fields of view 14.52 mm (left) and 1.58 mm (right).

transform infrared spectroscopy, or type IaB, with very low (<20 ppm) concentrations of nitrogen in the form of B-centers. The specimens in figure 8 are all type IIa except for the top right and top left diamonds. The CLIPPIR acronym also calls out the characteristic morphology, being irregular in shape and highly resorbed, which are common traits across all superdeep diamonds.

In addition to CLIPPIR diamonds, the superdeep geological category encompasses type IIb (boron-bearing, often blue) diamonds as well as those typically less gemmy diamonds associated with the Juína region of Brazil and the Kankan region of Guinea (Smith et al., 2018; Shirey et al., 2024). All three varieties of superdeep diamonds can be found across multiple deposits worldwide, indicating that the processes that create these diamonds are not singular but repeat through time and space (Smith et al., 2025).

Concluding Remarks

The beauty of natural rough diamonds is easily overlooked, with most people only encountering diamonds after faceting. But given the opportunity to take a closer look, it is hard not to admire the myriad of morphologies among rough diamonds. Natural processes of crystal growth, breakage, and resorption can sculpt almost anything, from the ideal octahedron to irregular shapes resembling animals and familiar objects. The shape of each rough diamond is a testament to unseen geological activity inside our dynamic planet.

ACKNOWLEDGMENTS

GIA gratefully acknowledges the generosity of Pintu Dholakia of Hari Krishna Exports for lending these specimens for scientific examination and for display at GIA-AGS Converge. They are part of a broader collection of notable rough diamonds assembled by Dholakia.

REFERENCES

Anzolini C., Angel R.J., Merlini M., Derzsi M., Tokár K., Milani S., Krebs M.Y., Brenker F.E., Nestola F., Harris J.W. (2016) Depth of formation of $CaSiO_3$-walstromite included in super-deep diamonds. *Lithos*, Vol. 265, pp. 138–147, http://dx.doi.org/10.1016/j.lithos.2016.09.025

Brookes C.A., Brookes E.J., Howes V.R., Roberts S.G., Waddington C.P. (1990) A comparison of the plastic deformation and creep of type I, type II and synthetic diamonds at 1100°C under conditions of point loading. *Journal of Hard Materials*, Vol. 1, No. 1, pp. 3–24.

Harris J., Stachel T. (2024) A Russian doll diamond in the making. *International Kimberlite Conference: Extended Abstracts*, Vol. 12, http://dx.doi.org/10.29173/ikc4050

Harris J.W., Smit K.V., Fedortchouk Y., Moore M. (2022) Morphology of monocrystalline diamond and its inclusions. *Reviews in Mineralogy and Geochemistry*, Vol. 88, No. 1, pp. 119–166, http://dx.doi.org/10.2138/rmg.2022.88.02

Robinson D.N. (1979) Surface textures and other features of diamonds. Ph.D. thesis, University of Cape Town, 382 pp.

Shirey S.B., Pearson D.G., Stachel T., Walter M.J. (2024) Sublithospheric diamonds: Plate tectonics from Earth's deepest mantle samples. *Annual Review of Earth and Planetary Sciences*, Vol. 52, pp. 249–293, http://dx.doi.org/10.1146/annurev-earth-032320-105438

Smith E.M., Chinn I., Timmerman S. (2025) Large irregular Type IIa and Type IIb diamonds: Valuable sublithospheric gems that elude conventional indicators. *Mineralogy and Petrology*, Vol. 119, pp. 305–325, http://dx.doi.org/10.1007/s00710-025-00901-9

Smith E.M., Shirey S.B., Nestola F., Bullock E.S., Wang J., Richardson S.H., Wang W. (2016) Large gem diamonds from metallic liquid in Earth's deep mantle. *Science*, Vol. 354, No. 6318, pp. 1403–1405, http://dx.doi.org/10.1126/science.aal1303

Smith E.M., Shirey S.B., Richardson S.H., Nestola F., Bullock E.S., Wang J., Wang W. (2018) Blue boron-bearing diamonds from Earth's lower mantle. *Nature*, Vol. 560, No. 7716, pp. 84–87, http://dx.doi.org/10.1038/s41586-018-0334-5

Smith E.M., Shirey S.B., Wang W. (2017) The very deep origin of the world's biggest diamonds. *G&G*, Vol. 53, No. 4, pp. 388–403, http://dx.doi.org/10.5741/gems.53.4.388

Stachel T., Brey G.P., Harris J.W. (2005) Inclusions in sublithospheric diamonds: Glimpses of deep Earth. *Elements*, Vol. 1, No. 2, pp. 73–78, http://dx.doi.org/10.2113/gselements.1.2.73

Protect Your Customers and Your Business.

GIA®

The most effective defense against diamond deception.

In under two seconds, the easy-to-use **GIA iD100®** can identify a diamond as natural with 100% accuracy.

Speed, precision, and convenience – the ideal tool to add to your protocol.

Learn More

GIA.edu/iD100

GEM NEWS INTERNATIONAL

Contributing Editors
Gagan Choudhary, *IIGJ-Research & Laboratories Centre, Jaipur, India* (gagan.choudhary@iigjrlc.org)
Guanghai Shi, *School of Gemmology, China University of Geosciences, Beijing* (shigh@cugb.edu.cn)

COLORED STONES AND ORGANIC MATERIALS

***Palaeoclavaria burmitis* inclusions in Burmese amber.** Biological inclusions represent an extraordinary and scientifically valuable aspect of amber. Beyond an aesthetic and commercial appeal, these inclusions provide significant insights into ancient ecosystems. Among global amber sources, Burmese amber is particularly renowned for its abundance and diversity of biological inclusions. These inclusions encompass a wide range of organisms, including fauna (ants, bees, beetles, scorpions, lizards, small birds, and snails), flora (leaves, bark, and stems), and fungi.

Recently, during a visit to the Mandalay Gem Market in Myanmar, the authors encountered several high-quality amber specimens containing fossilized fungi and acquired two amber cabochons weighing 131.85 and 130.37 ct and measuring 59.04–39.91 × 21.97 mm and 53.73–40.35 × 21.08 mm, respectively (figure 1). Both specimens displayed a transparent yellow-orange bodycolor.

Standard gemological testing revealed specific gravity values of 1.05 and 1.04, with a spot refractive index of 1.50 for both. Neither sample reacted with acetone. Fourier-transform infrared (FTIR) spectroscopy exhibited characteristic absorption peaks at approximately 2923, 2852, 1720, 1450, 1150, 1030, and 813 cm^{-1}, with the notable absence of the 887 cm^{-1} peak typical of copal. These findings confirmed that the specimens were natural amber, exhibiting diagnostic features consistent with Burmese amber (L.N. Nang et al., "Characteristics of newly discovered amber from Phu Quoc, Vietnam," Summer 2022 *G&G*, pp. 184–194). Each piece contained a cluster of approximately 20–25 fungal fruiting bodies. Based on morphological characteristics, these inclusions were identified as *Palaeoclavaria burmitis*—an extinct fungal species observed only in Burmese amber (G.O. Poinar and A.E. Brown, "A non-gilled hymenomycete in Cretaceous amber," *Mycological Research*, Vol. 107, No. 6, 2003, pp. 763–768) (figure 2, left).

Figure 1. Two amber specimens (131.85 and 130.37 ct, respectively) containing Palaeoclavaria burmitis *fungal inclusions. Photo by Ta Quan Ngoc.*

Within the amber, the *Palaeoclavaria burmitis* inclusions were preserved with a granular gray outer surface and an interior ranging in color from light gray to black (figure 2, right). The fruiting bodies measured ~1–3 mm in diameter and reached heights of ~2–4 mm. Notably, nearly colorless siliceous crystalline structures were observed within the fungal tissues—a diagnostic feature indicative of fossilization through silicification replacement. These

Editors' note: Interested contributors should send information and illustrations to gandgeditorial@gia.edu.

Gems & Gemology, Vol. 61, No. 3, pp. 316–330.

Figure 2. Left: Lateral view of Palaeoclavaria burmitis *fungal inclusions in the 131.85 ct Burmese amber sample. Right: Cross section of the* Palaeoclavaria burmitis *inclusions showing a siliceous crystalline structure. Photos by Le Ngoc Nang; field of view 4 mm (right).*

crystalline clusters exhibited a higher degree of crystallinity than the surrounding material, forming microcrystalline quartz or chalcedony—types of silica crystallization commonly found in siliceous fossils as well as in silica precipitates from magmatic sources (especially within chalcedony masses).

FTIR spectroscopy of the fungal interior confirmed the presence of silica, indicated by absorption peaks at 1006, 775, and 693 cm^{-1} (B.C. Smith, "Inorganics III: Even more spectra, and the grand finale," *Spectroscopy*, Vol. 39. No. 3, 2024, pp. 11–15), along with organic compound bands at 1431 and 1625 cm^{-1} and water at a peak of 3622 cm^{-1} (figure 3) (R.H. Ellerbrock and H.H. Gerke, "FTIR spectral band shifts explained by OM–cation interactions," *Journal of Plant Nutrition and Soil Science*, Vol. 184, No. 3, 2021, pp. 388–397). These data suggest that the fungi underwent siliceous replacement fossilization—a separate process from the surrounding amber's polymerization.

Figure 3. FTIR spectrum confirming the presence of siliceous material, along with organic compounds and water.

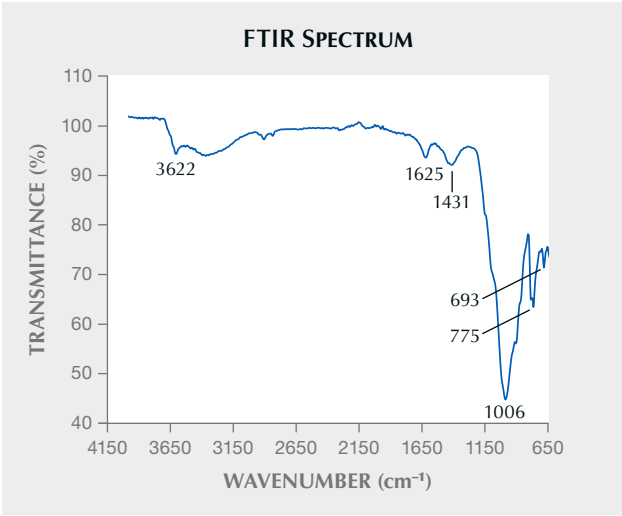

Fungi belong to a unique biological kingdom, distinct from both plants and animals, and are rarely fossilized outside of the amber environment. According to a comprehensive study by Poinar Jr. (G. Poinar Jr., "Fossil fleshy fungi ('mushrooms') in amber," *Fungal Genomics & Biology*, Vol. 6, No. 2, 2016, article no. 1000142), each amber deposit contains a unique assemblage of fungal taxa. Fungi identified in Dominican amber include *Aureofungus yaniguaensis*, *Protomycena electra*, *Coprinites dominicana*, *Favolaschia* sp., *Xylaria antiqua*, *Ganoderma* sp., and *Paleomorchella dominicana* sp. nov.; *Gerontomyces lepidotus* in Baltic amber; and *Palaeoagaracites antiquus*, *Palaeogaster micromorpha*, and *Palaeoclavaria burmitis* in Burmese amber. These fungal taxa differ markedly in geological age, geographic distribution, and morphology. As such, they serve as reliable paleobiological markers for determining the provenance and geological age of amber specimens with high accuracy.

Le Ngoc Nang
Liu Gemological Research and Application Center
Ho Chi Minh City, Vietnam

Ta Quan Ngoc
Bong Cam Thach Myanmar
Ho Chi Minh City, Vietnam

Trapiche pattern formation of grossular garnets. The sixfold rotational symmetric pattern, called trapiche, is commonly reported in hexagonal or trigonal crystal system minerals such as beryl, corundum, tourmaline, and quartz, but also can be found in diamond, spinel, and garnet having a cubic crystal system (J. Bergman, "Trapiche: The rising star," *InColor*, No. 31, 2016, pp. 32–44). Recently, three near-colorless transparent tablets with six-rayed black inclusions arranged in a snowflake-like pattern forming a

trapiche structure were submitted to GIA's Tokyo laboratory for identification (figure 4A). Standard gemological properties, Raman spectra, and chemical analyses using energy-dispersive X-ray fluorescence identified the stones as grossular garnets, composed mainly of $Ca_3Al_2Si_3O_{12}$. The arms and cores were black due to irregular black inclusions, and the samples also contained numerous colorless transparent inclusions (figure 4B). In cross-polarized light, the largest stone, weighing 1.00 ct, showed a clear concentric hexagonal light and dark pattern (figure 4C). The three submitted samples were very similar to the recently reported trapiche grossular garnets from Zhejiang Province, China (Y. Wang et al., "Trapiche garnets in Chun'an, Zhejiang Province, China: New constraints from their gemology, geochemistry, and geochronology," *Crystals*, Vol. 15, No. 3, 2025, article no. 201; T. Hainschwang, "Trapiche grossular from China," *Journal of Gemmology*, Vol. 39, No. 5, 2025, pp. 418–421; Summer 2025 GNI, pp. 208–210).

Typical idiomorphism of single crystal gemstones, such as hexagonal prismatic emeralds, octahedral diamonds, and rhombic dodecahedral garnets, is the thermodynamic equilibrium shape in which the sum of all surface energies is minimized (Wulff's theorem). Since the distance between the euhedral facets and the center is shorter than that between the apexes and the center, it is clear that the euhedral facets grow slower than the apexes. This slower crystal growth for the flat euhedral facets as compared to the apexes relates to the fact that they are smooth at the atomic level and have fewer defects (e.g., Y. Saito, *Statistical Physics of Crystal Growth*, World Scientific, Singapore, 1996). A smooth surface is one in which the constituent atoms in a crystal structure (i.e., the lattice points that represent molecular groups) are most densely packed. The densest plane can be determined primarily by the mineral's Bravais lattice type. The seven crystal systems are further classified into 14 types of Bravais lattices by considering four unit cell lattice patterns: primitive, body-centered, face-centered, and base-centered. Snowflakes and emeralds (beryls) have primitive hexagonal lattices, diamonds have face-centered cubic (fcc) lattices, and garnets have body-centered cubic (bcc) lattices (figure 5, first column). A primitive hexagonal lattice often forms a hexagonal prism or plate consisting of two basal pinacoids {0001} and six prism faces $\{10\bar{1}0\}$. An fcc lattice has the {111} plane where the lattice points are densest and often forms a euhedral octahedron. On the other hand, the densest plane for a bcc lattice is the {110} and often forms a euhedral rhombic dodecahedron (Bravais' empirical law; figure 5, second column).

The critical nuclei, which are the earliest stages of crystal growth and are the smallest crystals nucleated, have the shapes of small equilibrium euhedral crystals that depend on the Bravais lattices (figure 5, third column; e.g., Saito, 1996). Immediately after the critical nuclei are formed, or after a certain amount of growth, if the driving force for growth (such as supersaturation of gemstone components in the magma or fluid) increases, the gems will grow rapidly.

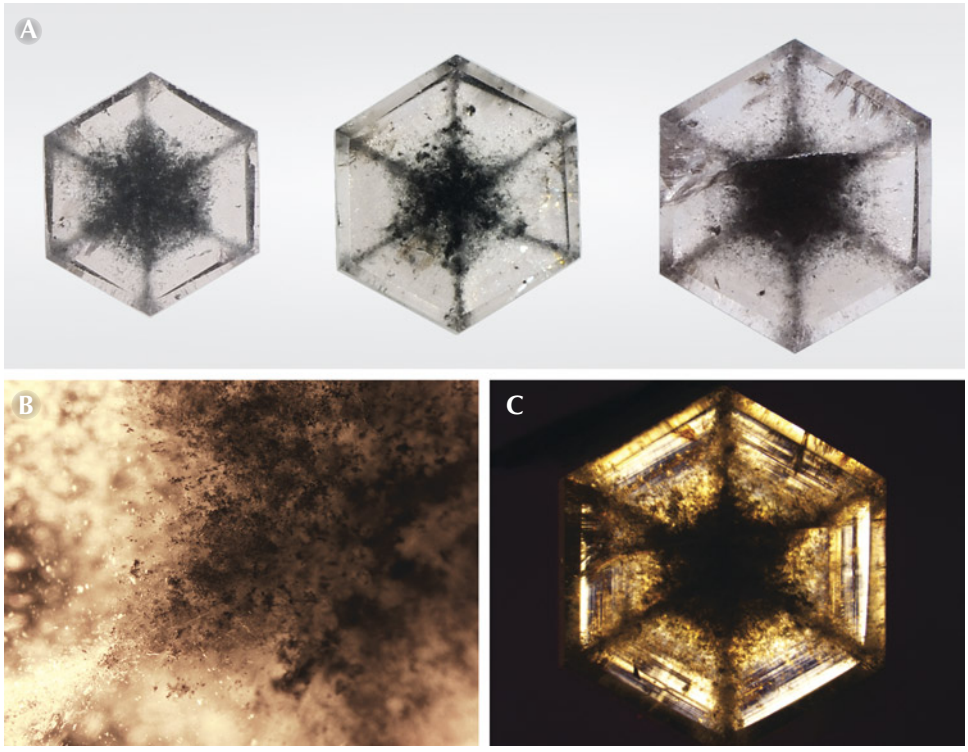

Figure 4. A: Three near-colorless transparent grossular garnet tablets with black inclusions arranged in snowflake-like patterns: 0.46, 0.68, and 1.00 ct, respectively. B: Black and colorless inclusions in the 0.46 ct sample; field of view 1.10 mm. C: Concentric hexagonal light and dark growth pattern of the 1.00 ct stone in cross-polarized light. Photos by Shunsuke Nagai (A) and Taku Okada (B and C).

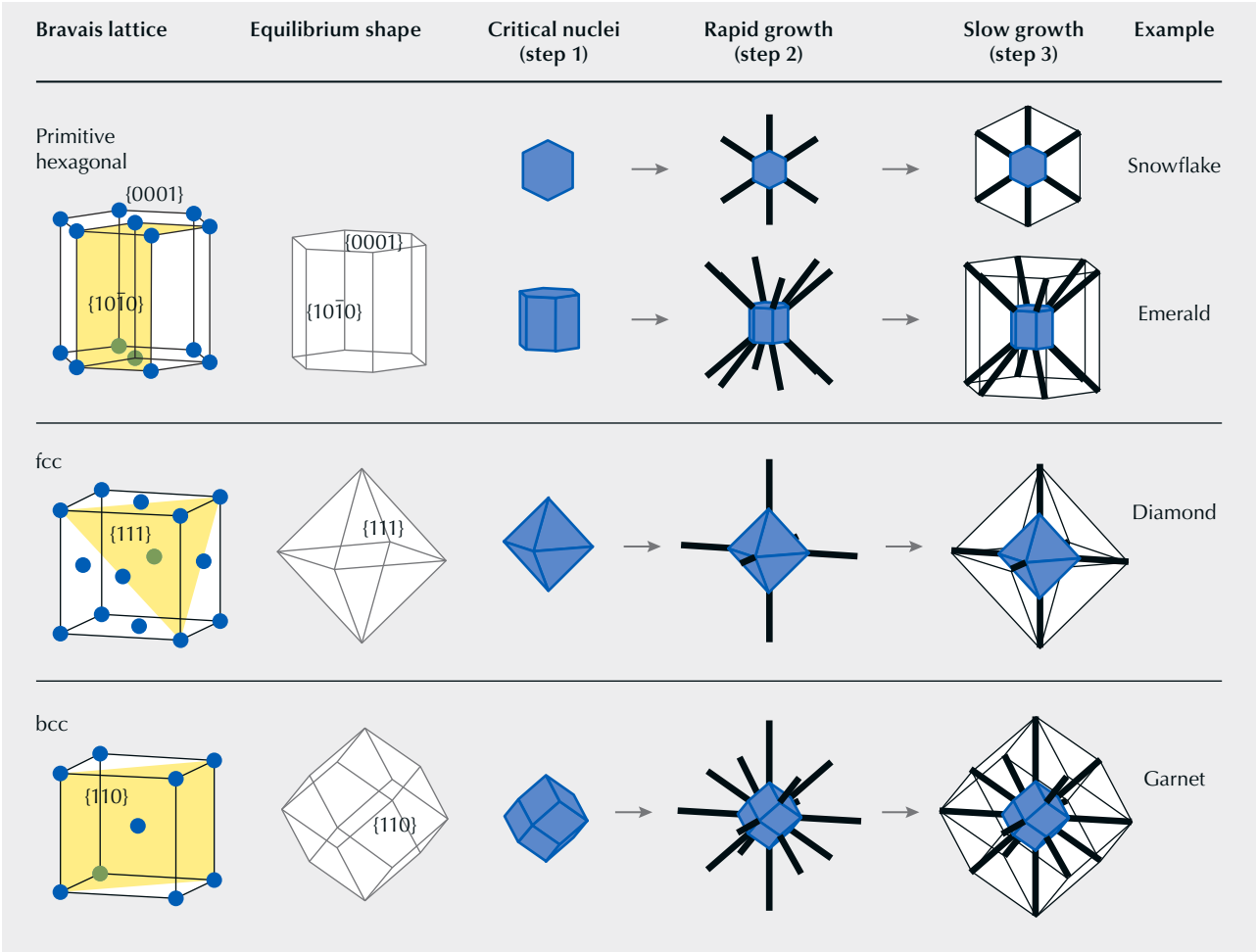

Figure 5. According to Bravais' empirical law, a primitive hexagonal lattice forms a hexagonal prism, a face-centered cubic (fcc) lattice forms an octahedron, and a body-centered cubic (bcc) lattice forms a rhombic dodecahedron as an equilibrium euhedral shape, respectively (modified from M. Tachibana, Beginner's Guide to Flux Crystal Growth, *NIMS Monographs, Springer, Tokyo, 2017). The shape of the critical nuclei corresponds to the equilibrium euhedral shape. In rapid growth, the sharpest corners of the euhedral crystal grow preferentially along the extension of each axial diagonal. Note that the size of the euhedral core crystal may or may not be observable. In slow growth, equilibrium euhedral shapes are again formed as the external shapes.*

In general, the sharpest corners of a euhedral crystal will preferentially grow faster due to the greater supersaturation as well as the "rough" interface (figure 5, fourth column). At this time, the tiny inclusions suspended in the magma or fluid will not be expelled from the gems and will instead be trapped inside and solidified. In fact, Monte Carlo simulations showed that branched dendritic crystals formed in the early stages of garnet growth when the gem's component was highly supersaturated in fluid (D.E. Wilbur and J.J. Ague, "Chemical disequilibrium during garnet growth: Monte Carlo simulations of natural crystal morphologies," *Geology*, Vol. 34, No. 8, 2006, pp. 689–692). These Monte Carlo simulations explain processes that are also reflected in the growth processes and shapes of snowflakes (e.g., K.G. Libbrecht, *Snow Crystals: A Case Study in Spontaneous Structure Formation*, Princeton University Press, Princeton, New Jersey, 2022).

Trapiche emerald and garnet and stellate diamond crystals seem to rapidly grow into a dendritic shape, incorporating the surrounding impurities into six axial diagonals consisting of the 12 vertices of a hexagonal prism in the case of emerald, three axial diagonals consisting of the six vertices of an octahedron in the case of diamond, and seven axial diagonals consisting of the 14 vertices of a rhombic dodecahedron in the case of garnet (figure 5, fourth column). During this rapid growth phase, the fastest growth is along the sector boundaries (the axial diagonals), forming a 3D internal structure such as the six axial diagonal black

lines seen in the rough trapiche emeralds reported by Schmetzer (Spring 2019 GNI, pp. 156–158). Alternatively, axial thickening may occur, incorporating impurities, as seen in diamond, where six thick "hydrogen clouds" are separated by a central core (Summer 2024 Lab Notes, pp. 212–214). Then, when the growth rate slows down due to a decrease in supersaturation or a change in temperature or pressure, the crystal approaches equilibrium with the surrounding environment, and the densest faces grow slowly, forming an equilibrium euhedral crystal again (figure 5, fifth column). These growth processes correspond to the formation of a central core by slow growth on a smooth surface (step 1), the formation of a skeleton structure by fast adhesive growth on a rough interface (step 2), and the formation of an outer shape by slow growth on a smooth surface (step 3) as the driving force for growth changes (I. Sunagawa et al., "Texture formation and element partitioning in trapiche ruby," *Journal of Crystal Growth*, Vol. 206, No. 4, 1999, pp. 322–330; I. Pignatelli et al., "The texture and chemical composition of trapiche ruby from Khoan Thong, Luc Yen mining district, Northern Vietnam," *Journal of Gemmology*, Vol. 36, No. 8, 2019, pp. 726–746).

We do not know how the submitted trapiche tablets were physically sliced from the euhedral crystals, but our observations and growth model indicate that they were sliced along the {111} planes (figure 6), and are central portions of garnet single crystals in which black inclusions have been distributed along the seven axial diagonals of a rhombic dodecahedron. Our model differs from the reporting in Wang et al. (2025), but is consistent with the latest detailed report in Wu et al. (Summer 2025 GNI, pp. 208–210). In the case of an octahedral diamond with an fcc lattice, the hydrogen clouds included along the three <100> axes connecting the rapidly growing vertices appear as four lines when viewed along the <100> axis but six lines when viewed along the <111> axis (e.g., W. Wang and W. Mayerson, "Symmetrical clouds in diamond – The hydrogen connection," *Journal of Gemmology*, Vol. 28, No. 3, 2002, pp. 143–152). Since the "essential symmetry" of the cubic crystal system is four three-fold axes of symmetry along four equivalent <111> axes, the six-rayed "star" or trapiche pattern seen in such cubic gemstones is a pseudo six-fold rotational symmetry observable only through inclusions produced by three-fold rotation-inversion symmetry. By conducting thought experiments based on crystallography and crystal growth theory to study the trapiche pattern formation process in garnets exhibiting the complicated euhedral rhombic dodecahedron, to our knowledge we have explained the apparent six-fold symmetry that can appear in cubic gemstones and established a growth model that can be applied to trapiche pattern formation in gems of various crystal systems and Bravais lattice types.

Taku Okada and Kazuko Saruwatari
GIA, Tokyo

Figure 6. The seven axial diagonals in a rhombic dodecahedron viewed from different angles. Left: The blue lines are the three equivalent <100> axes, and the red lines are the four equivalent <111> axes. Center: Cutting along the two yellow dotted lines perpendicular to a <111> axis gives a uniform regular hexagonal plate. Right: The black snowflake-like pattern in trapiche garnets corresponds to three equivalent <111> axes (red lines) excluding the central <111> axis. Three equivalent <100> axes (blue lines) intersecting at higher angles may produce the black core.

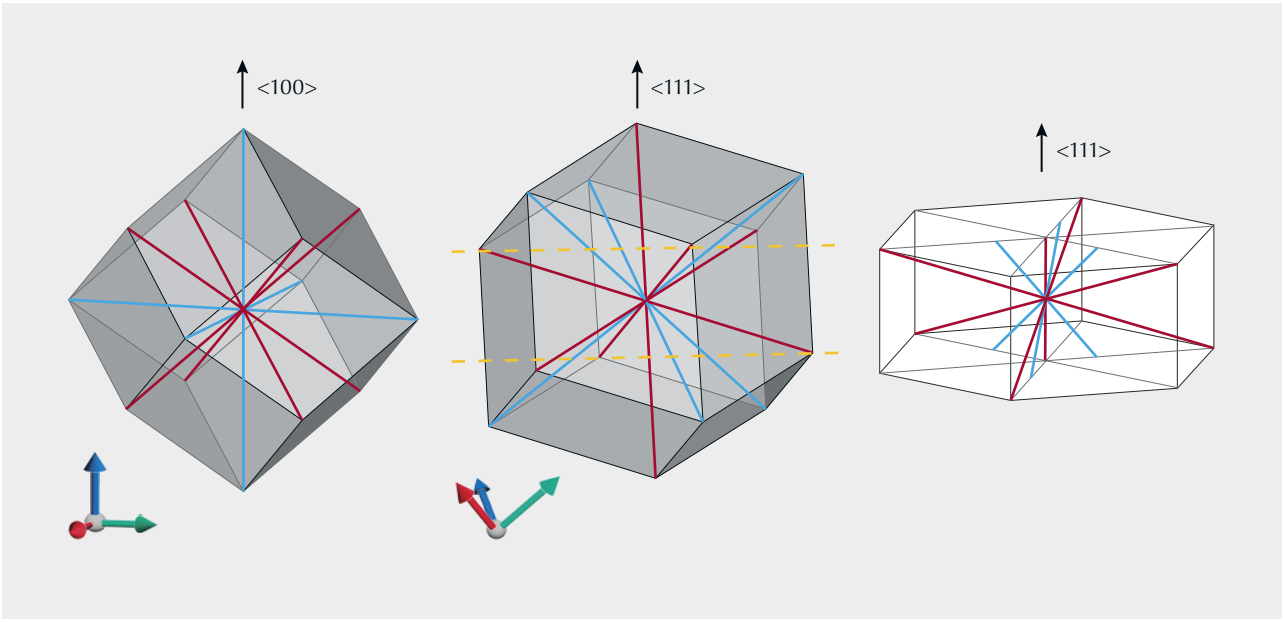

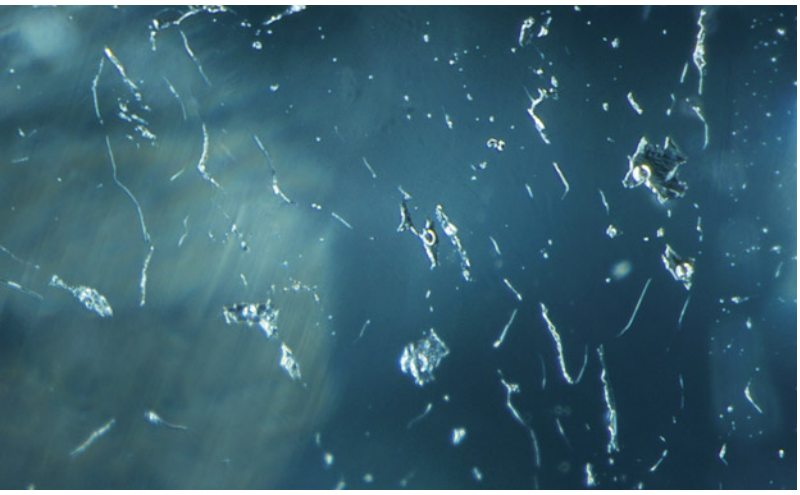

Figure 7. Immiscible two-phase fluid inclusions in a 0.48 ct Paraíba tourmaline. All circular phases were identified as gaseous CO_2 by confocal Raman spectroscopy. Photomicrograph by Kazuko Saruwatari; field of view 1.10 mm.

Gaseous carbon dioxide phases in Paraíba tourmaline. Recently, the authors encountered immiscible two-phase fluid inclusions in several Paraíba tourmaline stones. One stone weighed 0.48 ct and contained many two-phase inclusions (figure 7). Confocal Raman spectroscopy using a 100× objective lens detected carbon dioxide peaks of various intensities at around 1285 and 1388 cm^{-1} in the circular phases, identifying them as gaseous CO_2 (L. Li et al., "In situ Raman spectral characteristics of carbon dioxide in a deep-sea simulator of extreme environments reaching 300°C and 30MPa," *Applied Spectroscopy*, Vol. 72, No. 1, 2017, pp. 48–59) (figure 8), while no specific peaks were observed in the matrix phases. The most likely candidate for the matrix phase was liquid water (H_2O; e.g., H. Beurlen et al., "Geochemical and geological controls on the genesis of gem-quality 'Paraíba tourmaline' in granitic pegmatites from northeastern Brazil," *Canadian Mineralogist*, Vol. 49, No. 1, 2011, pp. 277–300), but it was difficult to detect because the Raman modes of O-H in tourmaline overlap with the two main O-H stretching modes at 3657 and 3756 cm^{-1} of liquid H_2O (M.L. Frezzotti et al., "Raman spectroscopy for fluid inclusion analysis," *Journal of Geochemical Exploration*, Vol. 112, 2012, pp. 1–20).

It is generally known that natural H_2O-CO_2 fluid inclusions can collapse when heated to approximately 350°C (R.J. Bodnar, "Introduction to aqueous-electrolyte fluid systems," in I. Samson et al., *Fluid Inclusions: Analysis and Interpretation*, Mineralogical Association of Canada, Short Courses Vol. 32, 2003, pp. 81–99), which is lower than the conventional heating temperature of Paraíba tourmaline (Spring 1990 Gem News, p. 103). The immiscible coexistence of small amounts of gaseous CO_2 and possible liquid H_2O phases, and the absence of many tension fissures, may be evidence that the Paraíba tourmaline did not undergo heat treatment. To verify this, further heating experiments are needed.

Kazuko Saruwatari and Taku Okada

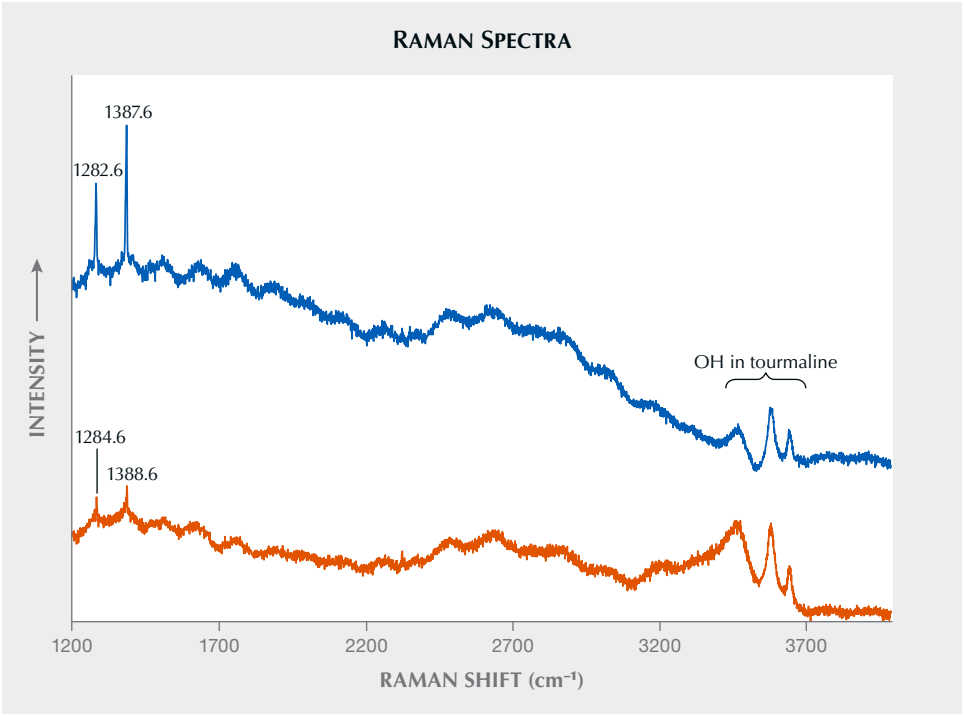

Figure 8. Raman spectra of two gas phases shown in figure 7. The upper Raman spectrum displays stronger CO_2 fermi doublets at 1282.6 and 1387.6 cm^{-1}, while the lower Raman spectrum shows weaker CO_2 fermi doublets at 1284.6 and 1388.6 cm^{-1}. The three broad peaks between 3200 and 3700 cm^{-1} are hydroxyl (OH) peaks of the tourmaline host. Spectra are offset vertically for clarity.

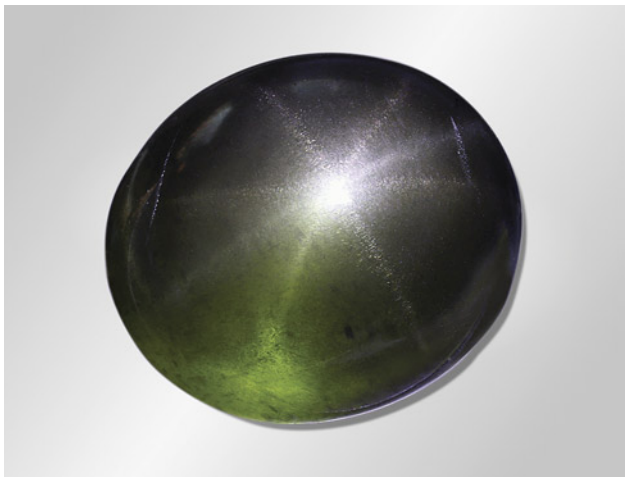

Figure 9. Eight-rayed star peridot from Myanmar weighing 34.16 ct. Photo by Karola Sieber.

Large peridot from Myanmar with an eight-rayed star. Peridot is the gemstone variety of the mineral olivine, a solid solution series with the end members forsterite (Mg_2SiO_4) and fayalite (Fe_2SiO_4). Peridot crystallizes in the orthorhombic system. Its main commercial sources include the Mogok region in Myanmar, the San Carlos area in the U.S. state of Arizona, and, more recently, the Yanbian Chaoxianzu area in China's Jilin Province.

Star peridot is rare and mostly occurs with a four-rayed star (L.B. Benson, Jr., "Highlights at the Gem Trade Lab in Los Angeles," Spring 1960 *G&G*, p. 3), though extremely rare six-rayed (R.T. Liddicoat, Jr., "Highlights at the Gem Trade Lab in Los Angeles: Rare star peridot," Spring 1970 *G&G*, p. 150) and eight-rayed (M.P. Steinbach, *Asterism: Gems with a Star*, MPS Publishing and Media, 2016; M.P. Steinbach, *Star Gems: A Fascinating World*, MPS Publishing and Media, 2023) star peridots have been identified.

Figure 10. Short reflective needles create one of the four-rayed stars in the eight-rayed star peridot. Photomicrograph by Liviano Soprani; field of view 3 mm.

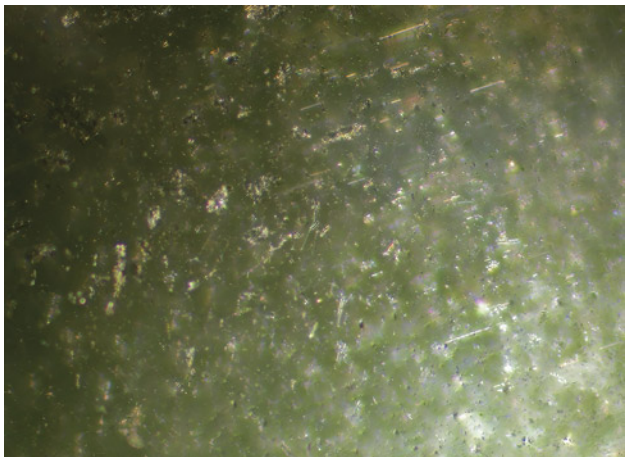

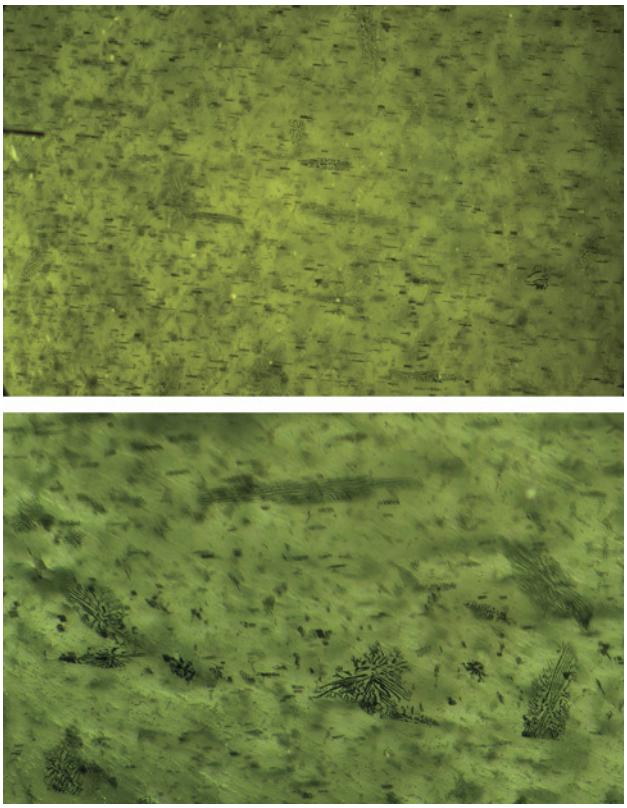

Figure 11. Top: Dark short needles and elongated particle clouds are responsible for the second four-rayed star, oriented at a 45-degree angle to the first star. Bottom: Skeletal inclusions, likely of dissolved magnetite. Photomicrographs by Liviano Soprani; fields of view 2.5 mm (top) and 2.0 mm (bottom).

In the case of the apparent eight-rayed star, it was proposed that the phenomenon was caused by diasterism, in which the star is viewed in transmitted light.

During the 2023 Hong Kong Gem and Jewellery Fair, author MPS purchased an eight-rayed star peridot reportedly from Myanmar weighing 34.16 ct (figure 9). The oval cabochon measured 17.61 × 15.48 × 13.82 mm and exhibited eye-visible dark inclusions. The stone was identified as peridot by Raman spectroscopy. Compared to the eight-rayed star mentioned above (examined in transmitted light), this star was readily visible in reflected light, a phenomenon called epiasterism. To our knowledge, eight-rayed star peridots exhibiting epiasterism have not been previously described.

Microscopic analysis revealed two sets of inclusions, each creating a four-rayed star oriented 45-degrees apart, forming an eight-rayed star. The first set consisted of short light-colored reflective needles (figure 10) (see Spring 2020 GNI, pp. 159–160). The second set was comprised of thicker black acicular inclusions and elongated clouds of dark particles (figure 11, top). Such needles and dendritic inclusions were previously described in a four-rayed star peridot from Myanmar and identified as magnetite by Raman

spectroscopy (Fall 2020 Lab Notes, pp. 422–423). Several of these inclusions were observed in this studied stone as well and are most likely skeletal magnetite (figure 11, bottom).

The eight-rayed star, made up of light- and dark-colored needle-like inclusions, resembles a combination of the four-rayed stars observed in two smaller stones studied for comparison (figure 12). A 2.89 ct lighter colored star peridot with sharp reflective needles and a 3.56 ct darker colored star peridot with dark cloud-like particles showed nearly identical inclusions to those described in the eight-rayed sample, and the colors of the stones are similar.

To the authors' knowledge, an eight-rayed star peridot with a star system made up of two different sets of inclusions has not been described before, and the authors feel privileged to report on this rarity.

Martin P. Steinbach
Steinbach–Gems with a Star
Idar-Oberstein, Germany

Lore Kiefert
Gemmology Consulting
Heidelberg, Germany

Jeanette Fiedler
Deutsches Diamant Institut
Pforzheim, Germany

Figure 12. Similar inclusions observed in a 2.89 ct lighter colored four-rayed star peridot (top) and a 3.56 ct darker colored four-rayed star peridot (bottom) studied for comparison. Photomicrographs by Lore Kiefert; fields of view approximately 2.0 mm (top) and 1.8 mm (bottom).

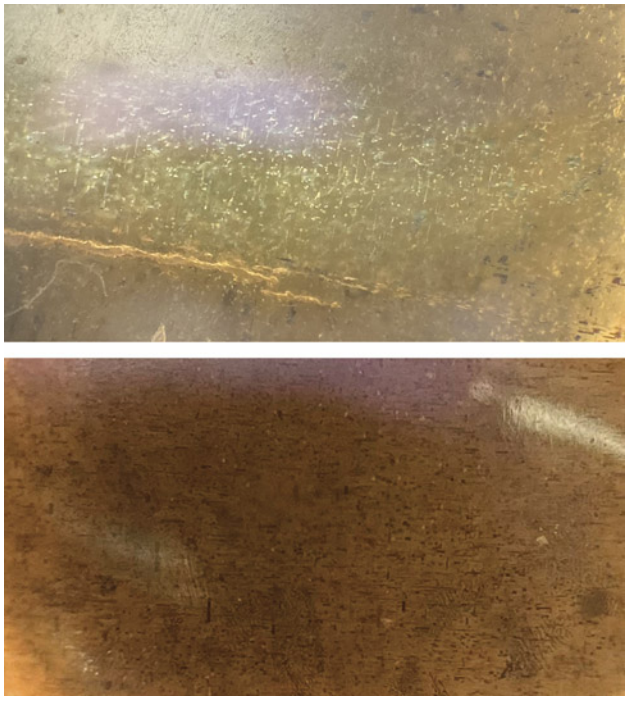

Blue color in quartz caused by elbaite inclusions. Blue color in quartz is usually caused by micro-inclusions of dumortierite (Spring 2015 GNI, pp. 100–102). Although other blue minerals, such as chrysocolla, apatite, and chlorapatite, have been reported as inclusions in quartz, they have not been known to impart a blue bodycolor to quartz (Spring 2015 GNI, pp. 89–90; Summer 2017 *G&G* Micro-World, pp. 241–242; Spring 2022 *G&G* Micro-World, p. 62).

Recently, three semitransparent to opaque quartz spheres weighing 4.85, 5.40, and 5.50 ct, and measuring 9.04, 9.26, and 9.28 mm in diameter, respectively (figure 13, top), were submitted for identification to the National Gemstone Testing Center (NGTC) in Shenzhen, China. Under fiber-optic transmitted illumination, the specimens each exhibited a blue color associated with numerous needle-like blue inclusions.

The spot refractive index of the specimens was approximately 1.55, while hydrostatically calculated specific gravity (SG) values spanned from 2.50 to 2.65. Standard

Figure 13. Top: Three quartz spheres weighing 4.85, 5.50, and 5.40 ct, respectively, colored by blue needle-like inclusions. Bottom: Abundant needle-like blue mineral inclusions in the 5.50 ct quartz sphere, with some displaying triangular cross sections; field of view 1.75 mm. Photos by Rong Liang.

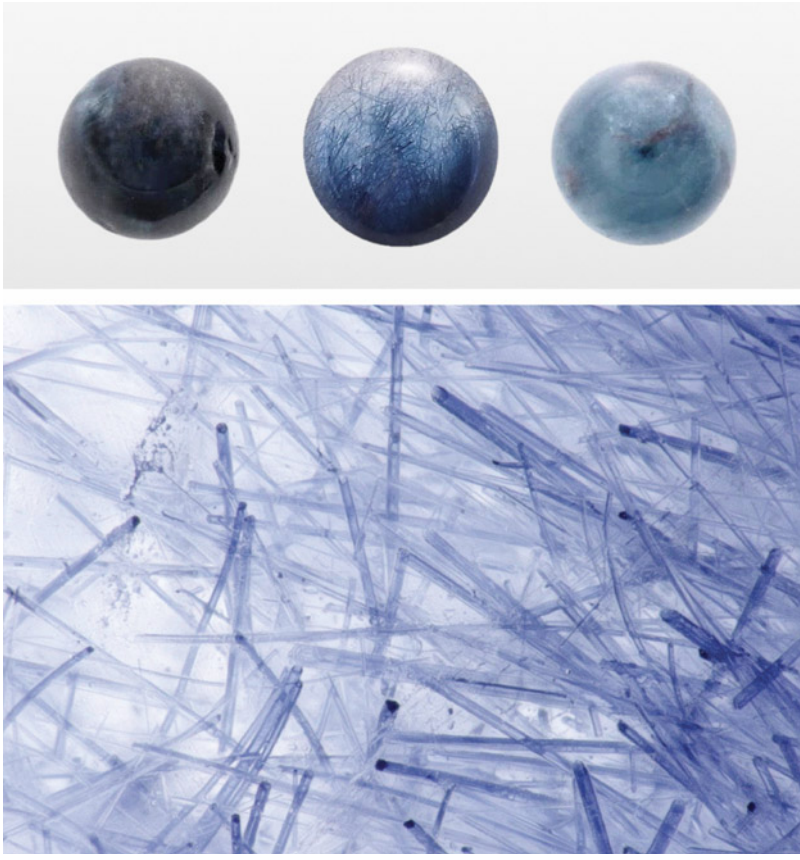

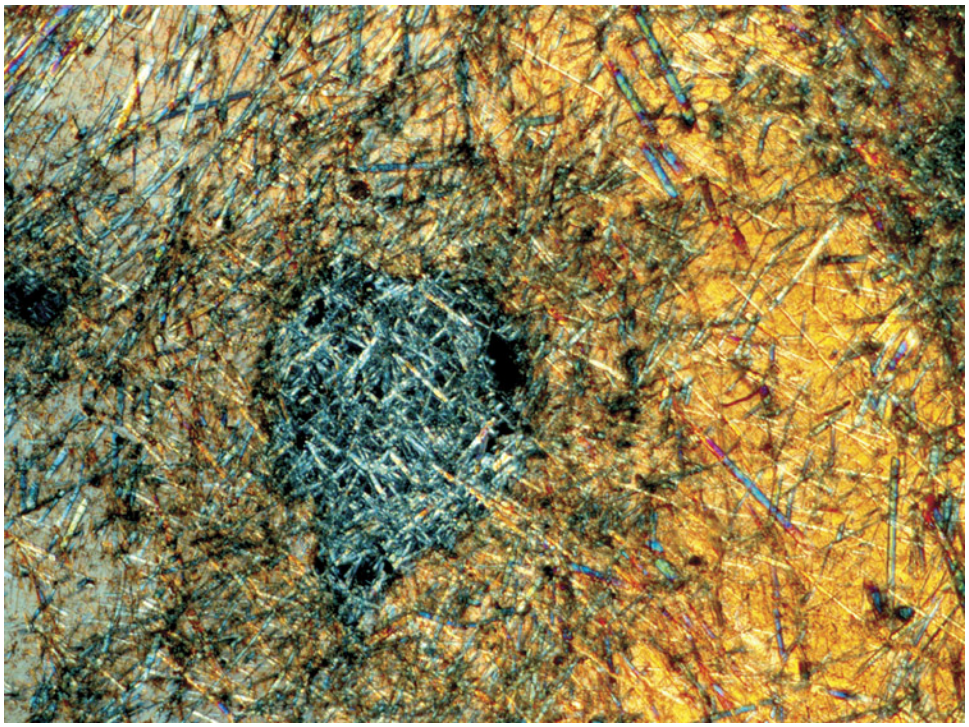

Figure 14. Under cross-polarized light, numerous prismatic inclusions are distributed within the 4.85 ct sphere. Photomicrograph by Rong Liang; field of view 2.15 mm.

gemological testing, along with Fourier-transform infrared (FTIR) spectroscopy, identified the host material as quartz. Microscopic examination revealed abundant needle-like mineral inclusions and healed fractures. These inclusions were either clustered or randomly distributed, with some displaying a triangular cross-sectional morphology (figure 13, bottom). The samples' surfaces showed resin-impregnated fractures contrasting with the inherent vitreous

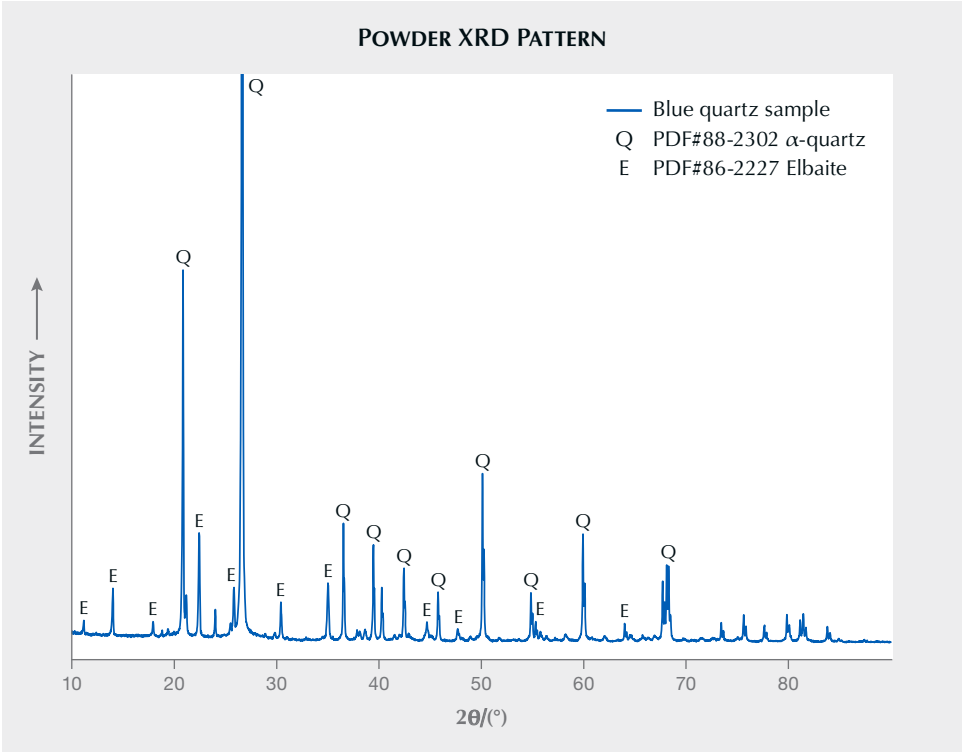

Figure 15. Powder XRD pattern of the 4.85 ct quartz sample, displaying characteristic peaks of α-quartz and elbaite.

luster of the quartz matrix. Semitransparent zones of the samples maintained full brightness in cross-polarized illumination while being rotated 360° in all directions, whereas the inclusion-dense areas remained opaque. Due to the optical behavior being obscured by numerous inclusions, thin sections were prepared from inclusion-rich areas of all three samples. Both the residual bulk material and the thin sections were subsequently examined by a combination of analyses, including polarizing microscopy, Raman spectroscopy, FTIR, laser-induced breakdown spectroscopy (LIBS), energy-dispersive X-ray fluorescence (EDXRF), and X-ray diffraction (XRD).

In cross-polarized light, the entire quartz host went extinct at the same time, confirming the quartz was a single crystal. In the thin section from the left sphere in figure 13, seven voids (0.3 to 0.6 mm in diameter) and three fractures (0.01 to 0.04 mm in width) were observed within the quartz matrix. Some of these voids were filled with acicular minerals (figure 14). This sample's lower SG of 2.50 compared to quartz's theoretical value is likely attributed to these voids and fractures. Under plane-polarized light, the blue acicular inclusions displayed strong pleochroism, transitioning from deep blue to pale blue.

Raman spectroscopy of the inclusions detected peaks at 225, 267, 370, 640, and 707 cm^{-1}, consistent with elbaite (R100137) in the RRUFF database (B. Lafuente et al., 2015, https://rruff.info/about/downloads/HMC1-30.pdf). XRD also identified their mineralogical phase as elbaite, revealing that one specimen (figure 13, top, left stone) exhibited an elbaite content of approximately 20 wt.% (figure 15). Since black tourmaline is a common type of inclusion in quartz, this case of blue elbaite inclusions responsible for the blue bodycolor in these quartz samples is rare.

LIBS identified lithium, sodium, magnesium, calcium, aluminum, silicon, iron, and boron in these inclusions (figure 16). The LIBS and EDXRF analyses detected iron but not copper or manganese, suggesting that the blue color was primarily attributable to iron, potentially by an Fe^{3+}-Fe^{2+} intervalence charge transfer.

FTIR revealed organic absorption peaks at 3036, 3057, 2958, 2928, and 2870 cm^{-1}. Raman peaks at 639, 1110, 1184, and 1605 cm^{-1} confirmed the presence of epoxy resin in the fractures and voids, indicating resin infiltration for structural stabilization and to improve transparency.

The systematic differentiation of single-crystal versus polycrystalline aggregates is critical to gemological classification. This is one case study in which sample morphology or inclusion density complicates identification, but thin section polarized microscopy observation and related analyses provided simple yet effective methods for determining the mineral phases.

Rong Liang, Ying Ma, Huihuang Li, Rongxiang Du, and Muyu Chen
National Gemstone Testing Center
Shenzhen, China

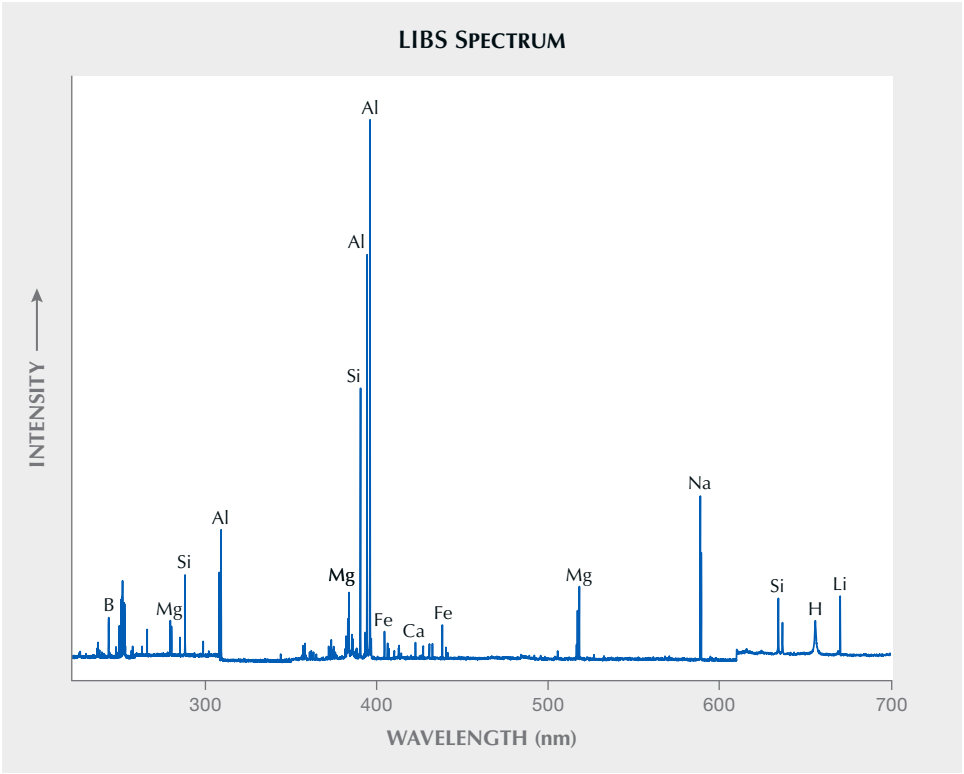

Figure 16. LIBS spectrum of an elbaite inclusion in the 5.50 ct quartz sample using a 266 nm laser showed characteristic emission lines of boron, magnesium, silicon, aluminum, iron, calcium, sodium, hydrogen, and lithium.

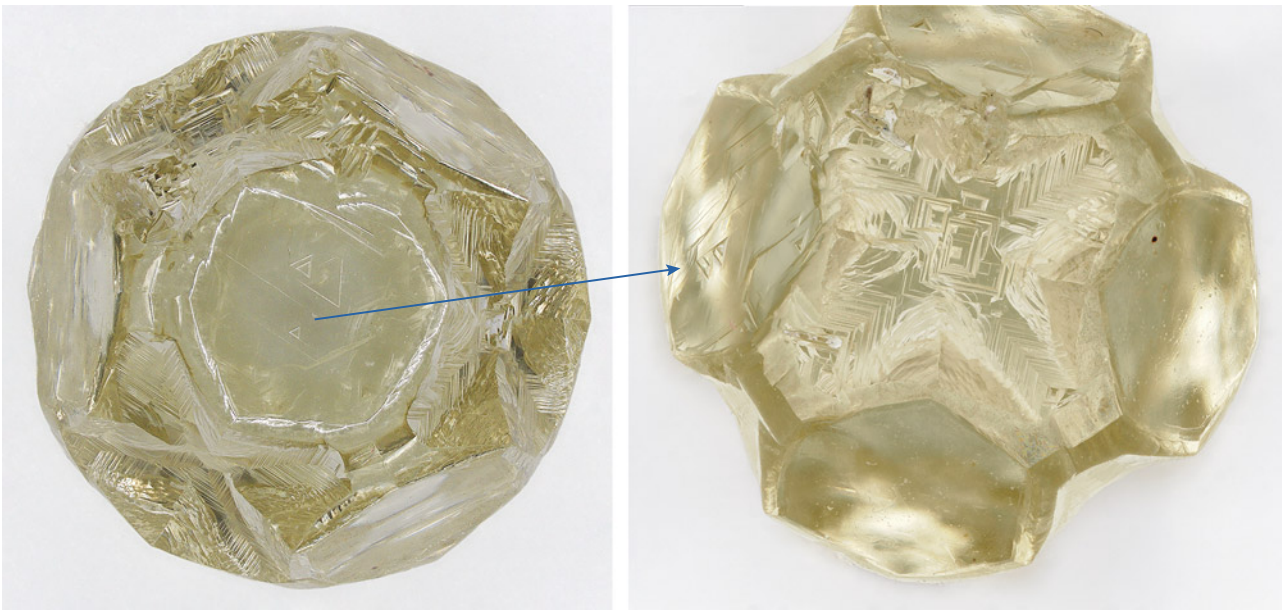

Figure 17. Left: This 3.49 ct yellow diamond with a diameter of ~7 mm exhibits a unique shape due to a combination of growth and dissolution features. Right: Tetragonal etch pits suggesting dissolution on cubic faces of initial habit. Photos by Cristiano Ferraris.

DIAMONDS

Unusual yellow diamond with a complex growth history. A rare yellow 3.49 ct diamond from a private collector exhibiting an unusual form due to a combination of growth and dissolution features was recently studied by the authors (figure 17). Microscopic examination highlighted the absence of solid inclusions and the presence of brown stains near the surface (figure 18, left). The stains were due to natural irradiation causing the formation of GR1 defects, implying that the stains were initially green and turned brown after the annealing process (S. Eaton-Magaña et al., "Low-temperature annealing and kinetics of radiation stains in natural diamond," *Diamond and Related Materials*, Vol. 132, 2023, article no. 109649).

Ultraviolet/visible/near-infrared spectroscopy indicated absorption features at 415, 373, 383, 392, and 404 nm related to N3 and N2 defects. A small percentage of yellow diamonds with these defects also contain hydrogen-related defects (C.M. Breeding et al., "Natural-color green diamonds: A beautiful conundrum," Spring 2018 *G&G*, pp. 2–27). In fact, the infrared spectrum of this stone showed the absorption peaks at 3107 and 1405 cm^{-1} characteristic of N_3VH^0 defects. With the sharp 3107 cm^{-1} peak, the hydrogen concentration was enough to classify the diamond as "hydrogen-rich" (T. Hainschwang et al., "A defect

Figure 18. Brown stains near the surface (left) and a trigon on the octahedral face (right) of the diamond. Photomicrographs by Cristiano Ferraris; fields of view 2.43 mm (left) and 1.82 mm (right).

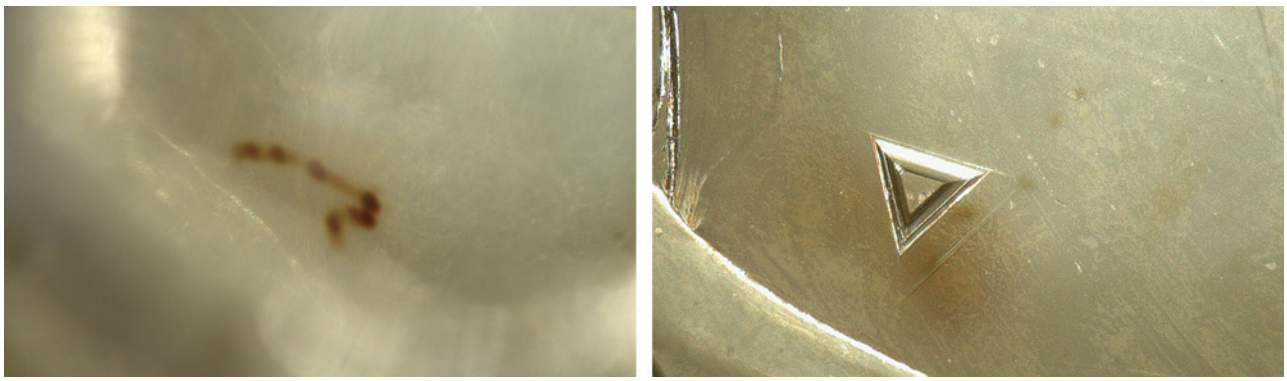

study and classification of brown diamonds with non-deformation-related color," *Minerals*, Vol. 10, No. 10, 2020, article no. 914). The peak at 1377 cm^{-1} indicated that the diamond also contained platelets (i.e., extended planar defects considered byproducts of nitrogen aggregation) (J.P. Goss et al., "Extended defects in diamond: The interstitial platelet," *Physical Review B*, Vol. 67, No. 16, 2003, article no. 165208).

While its color and size were impressive, the unique shape of the diamond, a result of growth and dissolution events, attests to the specimen's complex history. The yellow diamond's well-developed octahedral faces were marked by the presence of shallow trigons (figure 18, right) and separated by slightly curved resorbed faces. Tetragonal etch pits were clearly recognizable in this diamond (figure 17, right). This type of pit has been observed in diamonds from Botswana (C.M. Welbourn et al., "A study of diamonds of cube and cube-related shape from the Jwaneng mine," *Journal of Crystal Growth*, Vol. 94, No. 1, 1989, pp. 229–252) and are referred to as "re-entrant cubes," indicating dissolution processes that modified the initial cuboctahedral mixed habit. Unfortunately, the geological and geographical provenances of the yellow diamond are unknown, making the reconstruction of the formation conditions more difficult. However, trigon features (such as size and shape) can provide information about fluid composition and temperature during dissolution event(s) (Y. Fedortchouk et al., "Diamond destruction and growth during mantle metasomatism: An experimental study of diamond resorption features," *Earth and Planetary Science Letters*, Vol. 506, 2019, pp. 493–506), helping to determine if this occurred during kimberlite transport or mantle storage (K.V. Smit and S.B. Shirey, "Diamonds are not forever! Diamond dissolution," Spring 2020 *G&G*, pp. 148–155). A possible formation history of this exceptional diamond has been recently proposed by authors IP and CF (I. Pignatelli and C. Ferraris, "A rare yellow diamond: Reconstruction of the possible geological history," *Crystals*, Vol. 15, No. 5, 2025, article no. 461) on the basis of non-destructive analyses.

Isabella Pignatelli
Université de Lorraine, Centre de Recherches Pétrographiques et Géochimiques (CRPG)
Nancy, France

Cristiano Ferraris
Institut de Minéralogie, de Physique des Matériaux et de Cosmochimie, Museum National d'Histoire Naturelle
Paris, France

Dominik Schaniel
Université de Lorraine, CNRS, Laboratoire de Cristallographie, Résonance Magnétique et Modélisation
Nancy, France

Diamond ring prize from an arcade-style claw game. In Tokyo, the author recently had the opportunity to play a coin-operated claw game (figure 19A) for 100 yen (approximately US$0.70). The prizes offered were gold-colored rings set with natural diamond, cubic zirconia, or white topaz. After 24 attempts, the ring shown in figure 19 (C and D) was captured. The label on the box noted the following:

Figure 19. A: The arcade-style claw game. B: The diamond ring prize packaged in a paper box. C and D: The diamond ring shown from two angles: front view and back view. Photos by Mari Sasaki (A) and Shunsuke Nagai (B–D).

adjustable-size brass ring with 18K gold plating, natural diamond of approximately 0.01 ct, made in Japan, along with the names of the manufacturer and distributor (figure 19B).

The ring itself, weighing 1.28 g, had a simple open-band design, with a diameter of about 18 mm and a width ranging from 5.6 to 2.4 mm. For closer inspection, the stone was removed, which damaged the ring's prongs and surrounding areas of metal. The small melee stone weighed 0.0119 ct—consistent with the "approximately 0.01 ct" packaging claim—and measured around 1.37–1.38 mm in diameter and 0.88 mm in depth (figure 20). Internal fractures were observed in the brownish orange-yellow stone, which exhibited poor clarity. The crown featured a table surrounded by eight facets, while the pavilion also displayed eight facets, suggesting a single-cut stone, with visible chips on the girdle and culet.

Standard gemological testing, including photoluminescence and ultraviolet/visible spectroscopy, confirmed that the stone was indeed a natural untreated diamond. Energy dispersive X-ray fluorescence spectroscopy revealed that the metal was a gold-plated alloy of copper, zinc, and nickel, matching the gold-plated brass description on the package.

Interestingly, the promotional poster inside the machine described the diamonds as "transparent" and "colorless," which was clearly not the case with this ring. The tested sample featured on the poster may have been colorless, but colored diamonds could have been mixed in during mass production. Japanese regulations limit the market value of claw machine prizes to around 1,000 yen (approximately US$7) (Summer 2024 GNI, pp. 256–257), making it impossible for each prize to include a gem report confirming its features.

In a previous attempt with another machine, the author won a 0.06 ct "yellow diamond" for about 800 yen (approximately US$5.60). Testing indicated it was a treated, artificially irradiated, natural brownish greenish yellow diamond. Though a prize may be labeled simply as "diamond," considering the possibility of treatments is advised.

Mari Sasaki
GIA, Tokyo

TREATMENTS

Low-temperature heat treatment of corundum and the behavior of the 3161 cm^{-1} infrared band. The 3161 cm^{-1} infrared (IR) band can be observed in variously colored natural corundum, most commonly in yellow sapphire. The presence of this feature is used frequently as supporting evidence to conclude that a sapphire has not been heat treated (C.M. Breeding and N.J. Ahline, "Infrared spectroscopy and its use in gemology," Winter 2024 *G&G*, pp. 474–492). This 3161 cm^{-1} band is often present with other less intense side bands known as the "3161 cm^{-1} series" and includes features at ~3355, 3242, 3100 (shoulder), 2460, and 2420 cm^{-1} (C.P. Smith and C. van der Bogert, "Infrared spectra of gem corundum," Fall 2006 *G&G*, pp. 92–93). The exact origin of the 3161 cm^{-1} band is not well understood, although it is thought to be related to stretching vibrations of hydroxyl groups caused by interstitial H^+ ions present as charge compensation for Fe^{2+} substituting for Al^{3+} in the corundum structure (M.C. Jollands et al., "Vibrational properties of OH groups associated with divalent cations in corundum (α-Al_2O_3)," *European Journal of Mineralogy*, Vol. 35, No. 5, 2023, pp. 873–890).

As previously reported by Atikarnsakul and Emmett (Fall 2021 GNI, pp. 286–288), the intensity of the 3161 cm^{-1} band does not change after heating at 700°C in air, but it disappears or significantly decreases in intensity after heating at 900°C and above. Additionally, the prominent broad band at around 3000 cm^{-1} together with the 2625 cm^{-1} band, or the so-called "3000 cm^{-1} band series," can be created in some heated yellow sapphires containing low iron concentrations after heating at 900°C and higher. This series is related to stretching modes of hydroxyl groups in corundum doped with Mg^{2+} (N. Fukatsu et al., "Incorporation of hydrogen into magnesium-doped α-alumina," *Solid State Ionics*, Vol. 162–163, 2003, pp. 147–159). The 3000 cm^{-1} band series can also be observed in high iron yellow sapphires from basalt-related deposits without artificial heat treatment (Fall 2016 GNI, pp. 325–327). Moreover, a combination of the 3161 cm^{-1} series and the 3000 cm^{-1} series has been

Figure 20. Table (left) and pavilion (right) views of the removed 0.0119 ct melee stone. Photos by Shunsuke Nagai.

Figure 21. Color-calibrated photos of studied natural corundum crystals from various deposits ranging from 0.44 to 1.28 ct before (left) and after heating at 850°C (right). At this heating temperature, stronger yellow/orange coloration can be created. Photos by Sasithorn Engniwat.

reported in a few untreated Rock Creek sapphires from the state of Montana (J.L. Emmett et al., "Yellow sapphire: Natural, heat-treated, beryllium-diffused, and synthetic," Fall 2023 *G&G*, pp. 268–297).

In this study, 10 natural corundum samples of various colors from GIA's colored stone reference collection were selected to analyze the thermal behavior of the 3161 cm^{-1} IR feature starting with its strong intensity prior to any heating (figure 21). These untreated stones were from various deposits: Madagascar (samples C1, C2, C5, C6, and C7), Myanmar (sample C3), Sri Lanka (samples C4 and C8), and Mozambique (samples C9 and C10). The stones were heated in air to 650°, 700°, 750°, 800°, 850°, and 900°C for 5 hours at each temperature. At the end of each heating session, the samples were rapidly cooled to room temperature, and color-calibrated photos and Fourier-transform infrared absorption (FTIR) spectra were collected. The light yellow zones exhibited a stronger yellow color after heating at 800°–850°C (samples C1 to C8). Additionally, when present, blue color zones became less saturated after heating at 800°C (samples C7 and C8).

For comparison, unpolarized FTIR spectra were recorded at the identical sample area after heating at each experimental temperature. Figure 22 shows FTIR spectra of sample C1 before heating and after heating at 750°, 800°,

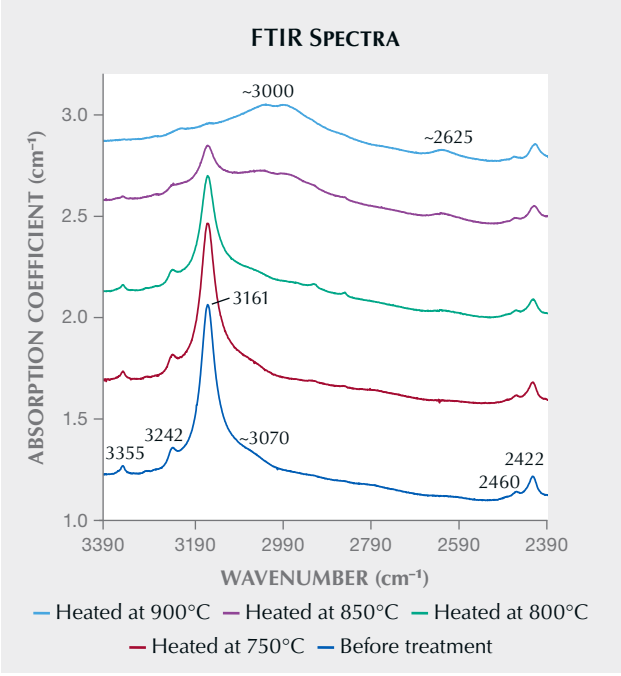

Figure 22. FTIR spectra of sample C1 before heat treatment and then heated at 750°, 800°, 850°, and 900°C for 5 hours at each temperature. After heating at 850°C, both the 3161 cm^{-1} series and the 3000 cm^{-1} band series were present in the same spectrum. Spectra are offset vertically for clarity.

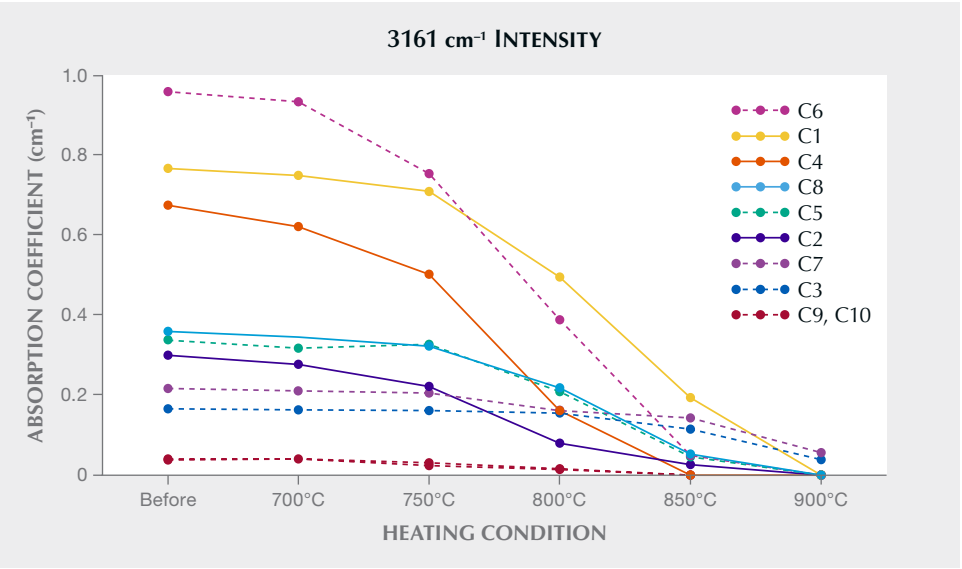

Figure 23. Variation in the 3161 cm⁻¹ IR band intensity of the samples with no treatment and after 5 hours of heat treatment at 700°, 750°, 800°, 850°, and 900°C. Solid lines represent the samples that produced the 3000 cm⁻¹ band after heat treatment, and dashed lines show those that did not produce any features after heat treatment.

850°, and 900°C. An insignificant to slight decrease in the 3161 cm⁻¹ band intensity was observed after heating at 750°C or lower (figure 23). When heating between 800° and 850°C, the 3161 cm⁻¹ intensity reduced significantly in all samples (figure 23), and the 3000 cm⁻¹ band series was created in some samples, resulting in a combination of the 3161 cm⁻¹ and the 3000 cm⁻¹ band in the same spectrum (figure 22, purple line). After heating at 900°C, the 3161 cm⁻¹ band either disappeared entirely or was still present but at a much lower intensity.

These experimental results and the previous work cited above indicate that natural corundum from different deposits possibly formed under various growth conditions such as temperature. Geological origin should also be taken into consideration when using the 3161 cm⁻¹ and/or the 3000 cm⁻¹ IR band to identify the presence of heat treatment.

Wasura Soonthorntantikul
GIA, Bangkok

Aaron C. Palke
GIA, Carlsbad

ERRATUM

In the Summer 2025 Colored Stones Unearthed section titled "Gem Granitic Pegmatites," a citation was incorrectly omitted on p. 192. In the second column, the first full paragraph should begin with "According to London (2008, p. 4), the name *pegmatite*…." We apologize for this error.